Advanced Modelling and Evolutionary Multiobjective Optimization of Motor Drive for Aerospace Applications

by Benjamin Cheong, MEng

Thesis submitted to The University of Nottingham
for the degree of Doctor of Philosophy, Sept 2019



Abstract

The More-Electric Aircraft (MEA) and hybrid/all-electric propulsion concepts have been introduced to improve the efficiency and reduce the environmental impact of air travel. Within the MEA concept, it is proposed to replace heavy pneumatic, mechanical or hydraulic driven elements with electrical systems, and to this end, an increasing number of motor drives is required on-board. Likewise, within hybrid/all-electric propulsion concepts, motor drives play a pivotal role in handling the drivetrain electromechanical power conversions. However, the greatest challenge concerning the wide employment of motor drives is in achieving high power density and high efficiency in their design.

The main goal of this PhD thesis is to develop advanced models and multiobjective optimisation techniques for motor drive system-level weight and efficiency optimisation. This holistic approach considers all components within a typical motor drive, i.e. the electrical machine, and the power converter with its associated cooling system and passive filter components. The novel contribution of this work is in combining a comprehensive knowledge of machine and converter modelling, with modern optimisation algorithms to form a practical system-level motor drive design and optimisation tool.

The first part of the thesis presents a computationally-efficient analytical model developed for a surface permanent magnet machine, to evaluate its multiphysics

operation and performance. Detailed finite-element analysis and experimental tests are carried out to validate the model's accuracy. A similar analytical model is also developed for the power converter, to predict its performance and size the associated cooling system and passive components. The model's accuracy is also verified using time-domain simulations and experimental results. Next, the machine and converter models (component-level) are integrated into one system-level model, to comprehensively evaluate the motor drive's performance and weight. To model extra losses in the electrical machine due to power converter pulse width modulations, a physics-based harmonic loss model is also proposed and incorporated within the system-level model.

Owing to the availability and capability of modern computing, researchers and engineers are increasingly turning to evolutionary algorithms to solve complex optimisation problems. The second part of the thesis discusses the application of evolutionary multiobjective optimisation (EMO) algorithms for an optimisation-based motor drive design, with the system-level model at its core. In particular, three popular EMO algorithms, namely the Non-dominating Sorting Genetic Algorithm-II (NSGA-II), Speed Multiobjective Particle Swarm Optimization (SMPSO), and Generalized Differential Evolution 3 (GDE3), are considered, and practical guidelines for their implementations are provided. For illustration, a motor drive optimisation case study is presented for a benchmark prototype motor drive, while visualisation plots are employed to analyse the optimisation results. Finally, the three EMO algorithms are compared against each other, and the SMPSO algorithm is found to be most competitive for a multiobjective motor drive optimisation problem.

This thesis is dedicated to my Lord and Saviour Jesus Christ who gave me strength to complete this work.

Acknowledgements

First and foremost, my heartfelt gratitude goes to Professor Patrick Wheeler, for this opportunity to do my Ph.D. at the Power Electronics, Machines and Control Group, and for his great trust over the years, going all the way back since I was an undergraduate here at the University. I also wish to thank Professor Pericle Zanchetta, Professor Mikiel Galea, Dr. Paolo Giangrande, and Dr. Xiaochen Zhang for their kind supervision over the years, and for offering help whenever I needed it. I would like to also express my appreciation to Professor Rolando Burgos and Professor Dushan Boroyevich, from CPES in Virginia Tech, for the opportunity to do a nine-months research exchange at their world-leading research group.

I would also like to thank Dr. Tom Cox and Professor Braham Ferreira for being my Ph.D. examiners, for their interest in this research and for their time in reviewing this thesis.

Many thanks to all my PEMC and CPES colleagues that I've met along this Ph.D. journey, for their valuable help and support. Especially, I want to thank Dr. Zhen Huang, Dr. Zhenyu Wang, Dr. Guo Xu, and Dr. Francesco Cavazzana for their friendship and the good times we've shared. I would like to thank John Hinchliffe and Colin Blackburn for leading a very capable team of technicians, that offered me tremendous help as I was setting up my experimental work.

There are many people outside the university that were instrumental and I would like to acknowledge them. I would like to thank my college physics teacher Mr. Lim,

who first ignited my passion for science and engineering. Being away from home, I am also grateful to all my friends and 'family' at Solid Rock and Cornerstone Church, for encouraging me in my faith, and for all the good memories that I will dearly cherish for the rest of my life.

I sincerely want also to thank my dear family (Dad, Mum, Priscilla and Abigail) for their continuous love and prayers, and for everything that I am and have.

Last but not least, a very special thanks to my girlfriend Charlene for her love, understanding, and kind support. Thank you so much, dear, for always being there, for cheering me up, and for believing in me.

Contents

Abstract ii

Acknowledgements v

Contents vii

List of Publications xi

List of Acronyms xiii

1 Introduction 1

1.1 Motivation . . . 1

1.1.1 Flight Electrification . . . 1

1.1.2 Role of Motor Drives in Aerospace . . . 4

1.1.3 Multiobjective Optimisation-based Design . . . 6

1.2 Problem Statement . . . 10

1.3 Research Objectives . . . 11

1.4 Summary of Research Contributions . . . 12

1.5 Thesis Outline . . . 13

2 State of the Art: Modelling and Optimisation of Motor Drives 15

2.1 Considered Motor Drive Topologies . . . 15

2.1.1 Electrical Machine . . . 16

2.1.2 Power Converter . . . 19

2.2 Motor Drive Modelling and Optimisation . . . 22

2.2.1 Component Level 22
2.2.2 System Level 29
2.3 Chapter Summary 31

3 Electrical Machine Modelling **33**
3.1 Input Parameter Definitions 34
3.2 Geometrical and Winding Models 36
3.3 Electromagnetic Model 39
3.3.1 Open-circuit Air-gap Magnetic Field 39
3.3.2 Armature-reaction Air-gap Magnetic Field 41
3.3.3 Machine Inductance 42
3.3.4 Flux and Flux Densities 44
3.3.5 Fundamental Magnetic Losses 45
3.3.6 Electromagnetic Torque 46
3.4 Thermal Model 47
3.5 Machine Model Verifications 51
3.5.1 Prototype Machine 52
3.5.2 Finite Element Analysis 53
3.5.3 Experimental Analysis 58
3.6 Chapter Summary 63

4 Power Converter Modelling **65**
4.1 Input Parameter Definitions 66
4.2 Modulation and Control Analysis 67
4.2.1 Converter Modulation 67
4.2.2 Control Strategies 75
4.3 Semiconductor Losses and Heat-sink Model 83
4.3.1 Semiconductor Losses 83
4.3.2 Semiconductor Heat-sink Model 86
4.4 Passive Components Modelling 90

4.4.1 Boost Inductor . . . 91
4.4.2 DC-link Capacitor . . . 96
4.5 Model Verifications . . . 99
4.5.1 Time-domain Simulation Study . . . 99
4.5.2 Experimental Analysis . . . 104
4.6 Chapter Summary . . . 108

5 System-level Motor Drive Modelling 109
5.1 Motor Drive System-level Model . . . 110
5.2 Machine Harmonic Losses . . . 112
5.2.1 Proposed Model . . . 113
5.2.2 Experimental Analysis . . . 115
5.3 Analysis of System-level Model . . . 118
5.3.1 Experimental Setup . . . 118
5.3.2 Impact of Converter Modulation . . . 119
5.3.3 Impact of Load Profile Operating Points . . . 122
5.4 Chapter Summary . . . 124

6 Evolutionary Multiobjective Optimisation 126
6.1 Description of EMO Algorithms . . . 127
6.1.1 Non-dominated Sorting Genetic Algorithm II . . . 128
6.1.2 Speed Multiobjective Particle Swarm Optimisation . . . 129
6.1.3 Generalised Differential Evolution 3 . . . 131
6.2 Practical Guidelines for Applying EMO . . . 133
6.2.1 Modelling . . . 133
6.2.2 Search Space Definition . . . 134
6.2.3 Performance Space Mapping . . . 135
6.2.4 Constraint Handling . . . 135
6.3 Case Study: GDE3 Optimisation of Motor Drive . . . 137
6.3.1 Benchmark System . . . 137

6.3.2 Optimisation Setup . . . 138
6.3.3 Analysis of Optimisation Results . . . 140
6.3.4 Verification of Design Solutions . . . 144
6.3.5 Effect of Fixed Input Parameters . . . 144
6.4 Comparison of EMO algorithms . . . 154
6.4.1 Test Functions . . . 154
6.4.2 Motor Drive Optimisation Problem . . . 155
6.5 Chapter Summary . . . 159

7 Conclusions **160**
7.1 Further Work . . . 163

Appendix A Machine Model **165**
A.1 Geometrical and Winding Model . . . 165
A.2 Electromagnetic Model . . . 169

Appendix B Converter Model **176**
B.1 Phase Average Duty-cycle Reference . . . 176
B.2 Device Average and RMS Currents . . . 178

Bibliography **181**

List of Publications

The findings of this thesis have been partly published in the publications listed as follows:

1. B. Cheong, P. Giangrande, X. Zhang, P. Wheeler, P. Zanchetta and M. Galea, "Evolutionary Multiobjective Optimization of a System-Level Motor Drive Design", (Submitted to the 'IEEE Transactions on Industry Applications')

2. B. Cheong, P. Giangrande, X. Zhang, M. Galea, , P. Zanchetta and P. Wheeler, "Fast and Accurate Model for Optimization-based Design of Fractional-Slot Surface PM Machines", The 22nd international Conference on Electrical Machines and Systems (ICEMS), 11-14 August 2019, Harbin, China, 2019

3. B. Cheong, P. Giangrande, X. Zhang, M. Galea, P. Zanchetta and P. Wheeler, "Fast and Accurate Multiphysics Model for Optimization-based Design of VSBBC", The 45th Annual Conference of the IEEE Industrial Electronics Society (IECON), 14-17 October 2019, Lisbon, Portugal, 2019

4. B. Cheong, P. Giangrande, X. Zhang, P. Wheeler, P. Zanchetta and M. Galea, "System Level Motor Drive Modelling for Optimization-based Designs", The 21st European Conference on Power Electronics and Applications (EPE), 2-6 September 2019, Genoa, Italy, 2019

5. B. Cheong, P. Giangrande, M. Galea, P. Zanchetta and P. Wheeler, "Integrated motor drive design for weight optimization", 2017 IEEE Energy Conversion Congress and Exposition (ECCE), Cincinnati, Ohio, USA, 2017

6. B. Cheong, P. Giangrande, M. Galea, P. Zanchetta and P. Wheeler, "Integrated design of motor drives using random heuristic optimization for aerospace applications", 2017 SAE AeroTech Congress and Exhibition, AEROTECH 2017, 26-28 September 2017, Fort Worth, Texas, USA, 2017

7. A. Baraston, Q, Li, B. Cheong, J. Schanen, L. Gerbaud, P. Zanchetta, D. Boroyevitch, "Design by Optimization of a Three-phases AFE under EMC constraints", 2017 ELECTRIMACS, 4-7 July 2017, Toulouse, France, 2017

List of Acronyms

AC Alternating Current.

AFE Active Front-End.

ATRU Auto Transformer Rectifier Unit.

BEMF Back Electro-Motive Force.

BLDC Brushless DC.

CSPI Cooling System Performance Index.

DC Direct Current.

DE Differential Evolution.

DPWM1 60°-Clamping Discontinuous Pulse-Width Modulation.

EHA Electro Hydrostatic Actuators.

EMO Evolutionary Multiobjective Optimization.

FE Finite Element.

FFT Fast Fourier Transform.

GA Genetic Algorithm.

GDE3 Generalized Differential Evolution 3.

IGBT Insulated Gate Bipolar Transistors.

IPM Interior Permanent Magnet.

LPTN Lumped Parameter Thermal Network.

MEA More Electric Aircraft.

MMF Magneto-Motive Force.

MOSFET Metal Oxide Semiconductor Field Effect Transistors.

NSGA-II Non-dominating Sorting Genetic Algorithm-II.

PI Proportional-Integral.

PM Permanent Magnet.

PSO Particle Swarm Optimization.

PWM Pulse-Width Modulation.

SMPSO Speed Multiobjective Particle Swarm Optimization.

SPM Surface Permanent Magnet.

SR Switched Reluctance.

SVM Space Vector Modulation.

VSBBC Voltage Source Back-to-Back Converter.

Chapter 1

Introduction

1.1 Motivation

The global aviation industry produces 2% of global man-made CO_2 emissions, and its environmental impact is expected to increase further into the foreseeable future considering the 4.5% annual growth rate in passenger air traffic [1]. For this reason, the International Air Transport Association (IATA) has adopted the ambitious target of reducing global aviation CO_2 emissions of 50% by 2050, while the European Commission's Flightpath 2050 targets a 75% reduction in CO_2 emissions per passenger kilometre by 2050 [2]. Increasingly stringent regulations to reduce CO_2 emissions, and an increasing focus on reducing operating costs have become strong incentives for airlines to improve on the fuel efficiency performance of their aircraft.

1.1.1 Flight Electrification

Flight electrification allows new and exciting opportunities for aircraft optimisation to help reduce its environmental impact. At a high level, flight electrification can be categorised into two trends [3]:

- An evolutionary trend towards more-electric configurations, for conventional mechanical, pneumatic, and hydraulic systems

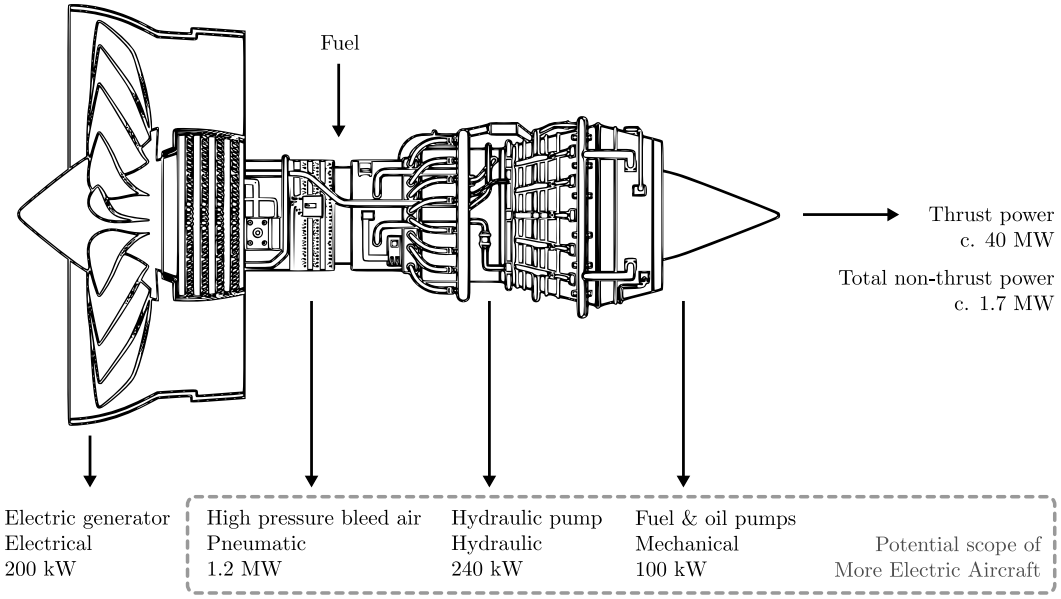


Figure 1.1: The More Electric Aircraft concept considering an A330-sized aircraft, according to [6].

- A disruptive trend towards hybrid-electric and all-electric propulsion.

Power is generated on traditional aircraft via gas turbines, and the majority of this power is used for propulsion thrust. The remaining power is used to power electrical, mechanical, pneumatic, and hydraulic loads on-board. The replacement of non-electrical systems, with electrical components and equipment, to improve aircraft fuel efficiency is commonly known as the More Electric Aircraft (MEA) concept [4]. The MEA concept is shown in Fig. 1.1. Other significant benefits from the MEA concept are weight reduction, improved reliability, and simplified maintenance. While an increasing amount of MEA-related research is still on-going, aircraft programmes, such as the Airbus A380 and Boeing 787, have already exhibited greater use of electrical power onboard [5].

The MEA concept considers the electrification of all on-board systems except for propulsion. Going a step further, hybrid-electric concepts for aircraft are also being researched, where a combination of the thermal engine (gas turbine or internal combustion engine) and electrical power generation or storage system drives either a

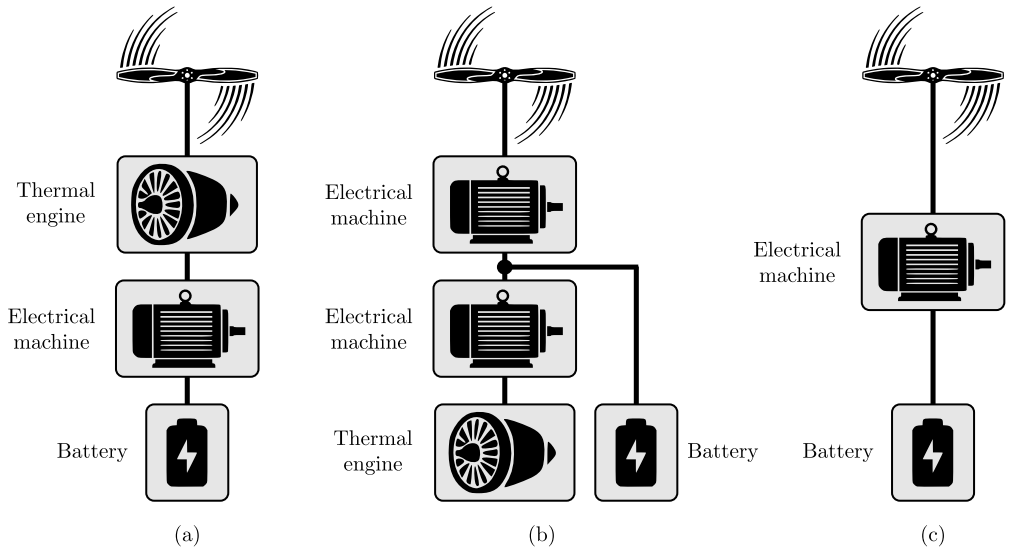


Figure 1.2: Electrical propulsion concepts: (a) parallel hybrid-electric (b) series hybrid-electric (c) all-electric configurations.

fan or propeller for propulsion. All-electric concepts, on the other hand, wholly rely on electrical power generated in fuel cells or stored in batteries. These configurations are shown in Fig. 1.2.

In parallel hybrid-electric concepts, both the electrical machine and thermal engine are mechanically connected to the fan or propeller on the same shaft. During periods of high output demand, such as 'take-off', electrical power complements the thermal engine in delivering additional propulsion thrust. When less output is required, i.e. during cruising, the batteries can be recharged from the thermal engine. An advantage of this configuration is that only one electrical machine is needed as it operates as both a motor and a generator.

For series hybrid-electric configuration, all fossil fuel energy in the thermal engine is transformed into electrical energy via a generator, and it is fed into a grid with energy storage elements. The generated electrical energy is then distributed to multiple fans or propellers driven by electric motors and is used to recharge the batteries. With this configuration, the thermal engine is always operating at optimal power and speed across the entire flight profile, allowing high efficiencies to be

attained. Other inherent advantages of this configuration include flexibility in the location of the engine and generator set, and simplicity in the mechanical drivetrain.

Lastly, the all-electric concept, where the thermal engine is completely removed, and electrical energy generation or storage system provides all the propulsion energy, is also being considered. This simple configuration emits no pollutants and is very attractive for high population density areas. However, the highest achievable energy storage density of current battery technology greatly limits its range and, thus, its suitability for medium or long-range flights.

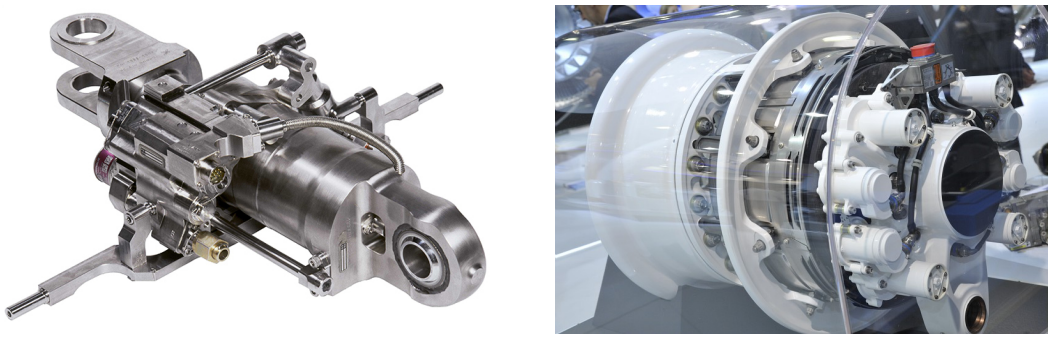
The mentioned hybrid-electric and all-electric propulsion configurations are similar to what has already been adopted by the marine and automotive sector over the past two decades, and in many ways, aerospace is pursuing a path already set in these industries. Despite their similarities, however, there are several key differences: low volume and weight is important for marine and automotive applications but is extremely critical for aerospace, and aerospace has much stricter safety regulations compared to the marine and automotive industry.

1.1.2 Role of Motor Drives in Aerospace

The motor drive is a key enabling technology to the realisation of all the mentioned flight electrification concepts to convert power between mechanical and electrical forms.

For MEA concepts, motor drives form an essential part of the electric compressors, pumps, braking and actuation systems. For example, Fig. 1.3(a) shows an electro-hydraulic servo-actuator used to actuate spoiler surface position of an Airbus A380 aircraft, while Fig. 1.3(b) shows an electric braking system on-board a Boeing 787 aircraft, replacing conventional hydraulic pistons with electromechanical actuators.

For hybrid and all-electric concepts, on the other hand, motor drives are a key part of the drivetrain to supply mechanical power for propulsion and to generate electricity on-board. Photos of a series hybrid-electric powertrain, developed for a



(a) (b)

Figure 1.3: More-electric aircraft motor drives application: (a) A380 electrohydraulic servoactuator [7] (b) Boeing 787 electrical braking system [8].



(a) (b)

Figure 1.4: Hybrid-electric and all-electric aircraft motor drives application: (a) series hybrid-electric powertrain [9] (b) all-electric power train [10].

Pipistrel plane under the project HYPSTAIR, and an all-electric powertrain, built for an Extra 330LE two-seater acrobatic plane by Siemens, are shown in Fig. 1.4.

The most basic motor drive consists of a power converter and an electrical machine. The converter employs power electronic devices to switch and regulate electrical power going into the machine, while the machine converts this electrical power into mechanical power. For aerospace applications, power density and efficiency are of exceptionally high priority in motor drive designs in order to achieve high overall aircraft efficiency.

1.1.3 Multiobjective Optimisation-based Design

Engineering design, in general, is an enveloping process that includes *analysis* and *optimisation* as subprocesses. *Analysis* provides an understanding of the real-world system and models it to take in a set of input design parameters and, correspondingly, calculate and output values of interests, such as performance and weight. *Optimisation* provides insight into possible designs that are optimal as defined with a set of objective values.

The traditional design approach for motor drives relies heavily on 'rule-of-thumbs' and sizing equations formulated by experienced engineers, combining elements of analysis and optimisation. With this approach, significant simplifications and assumptions are usually in place, especially for complex problems that have many design variables, constraints, and objective values.

With increasing availability and capability of computational power these days, an optimisation-based design approach can be employed instead. In this approach, modern optimisation algorithms are 'taught' about the real-world system by models, to automatically perform the design, such that the best performance can be obtained. In contrast to the traditional design approach, sizing equations are no longer necessary, thus reducing the number of simplifications and assumptions needed to arrive at good design [11].

For most motor drive designs, there are more than one important objective values, and they are typically coupled such that improvements in one objective value results in poorer performance in another. Consequently, there is often not one unique solution but a set of compromised solutions. According to [12], a general multiobjective optimisation problem can be formally defined as a problem of finding a set of input parameters $\vec{x}$ which minimises a set of objective functions $\vec{f}(\vec{x})$ for an evaluation function F, subject to o number of inequality constraints $g_i(\vec{x})$ and p

number of equality constraints $h_j(\vec{x})$. Mathematically, this can be written as:

$$\begin{aligned} \text{find} \quad & \vec{x} = [x_1,\ x_2,\ ...,\ x_m] \quad \text{for} \quad \vec{f}(\vec{x}) = F(\vec{x}) \ , \\ \text{such that} \quad & \vec{f}(\vec{x}) = \min\Big[f_1(\vec{x}),\ f_2(\vec{x}),\ ...,\ f_n(\vec{x})\Big] \ , \\ \text{subject to} \quad & g_i(\vec{x}) \leq 0 \quad \text{for} \quad i = \{1, ..., o\} \\ \text{and} \quad & h_j(\vec{x}) = 0 \quad \text{for} \quad j = \{1, ..., p\} \end{aligned} \tag{1.1}$$

The set of compromised multiobjective solutions can be found using the *Pareto Optimality Theory* [13]. This theory states that solutions $\vec{x}^*$ for a minimisation problem are considered to be Pareto optimal if there are no other feasible solutions $\vec{x}$ which would decrease an objective function without causing a simultaneous increase in at least another objective function. This theory can be mathematically written as:

$$\begin{aligned} & \vec{x}^* \in D \quad \Longleftrightarrow \quad \nexists \quad \vec{x} \in D \ , \\ \text{such that} \quad & f_i(\vec{x}) < f_i(\vec{x}^*) \quad \forall \quad i = \{1, ..., n\} \end{aligned} \tag{1.2}$$

The mathematical definitions above are shown in Fig. 1.5. The search space is formed by all possible combination of input parameters, which can be mapped onto the performance space (or objective function space) via an evaluation function. In performance space, the Pareto front is a set of objective functions for the Pareto optimal solutions, and they represent the best achievable performances for a multiobjective optimisation problem.

Optimisation Methods

The formulation of engineering design problems varies from problem to problem. Some problems involve linear terms for objective function and constraints while others have non-linear terms for them. Unfortunately, there is no single problem-solving method (optimisation algorithm) that will work for all problems equally efficiently. This explains why there are many available algorithms, each suitable for

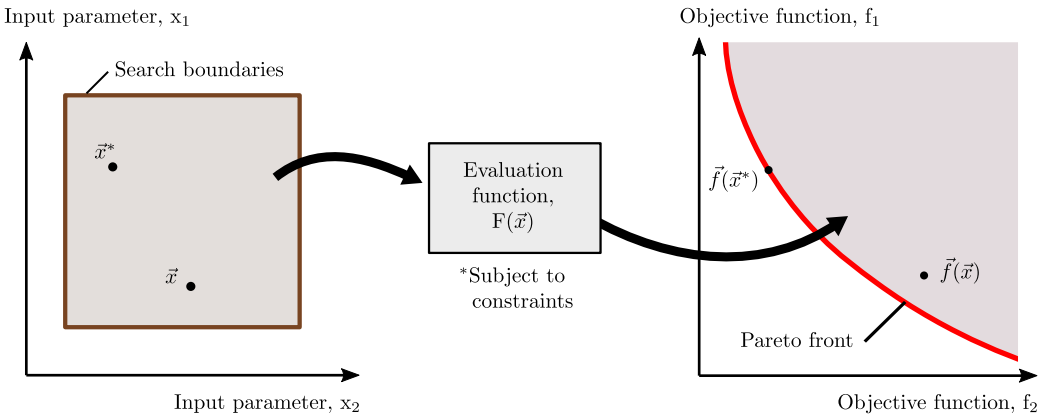


Figure 1.5: Illustration of a typical multi-objective optimisation problem (left: search space, middle: evaluation function, right: performance space).

a particular type of problem. In general, optimisation algorithms can be divided into two categories: deterministic algorithms, and stochastic algorithms, as shown in Fig. 1.6 [14].

Deterministic algorithms follow a strict procedure and has 'repeatable' solutions while stochastic algorithms incorporates an element of randomness. A third type of algorithm has a mixture of deterministic and stochastic algorithms, but as it contains a random component, it is often classified as a type of stochastic algorithm in the optimisation literature.

Most classical algorithms are deterministic, for example: Simplex method in linear programming [15]. Further, within the pool of deterministic optimisation algorithms, some employ gradient information, for example: the well-known Newton-Raphson algorithm [16] or Sequential Quadratic Programming [17]. Generally, gradient-based methods work extremely well for smooth unimodal problems. On the other hand, gradient-free algorithms are better if there is discontinuity in the objective function, for example: Hooke-Jeeves pattern search [18] and Nelder-Mead downhill simplex [19].

According to [12], stochastic algorithms can be divided into two types: heuristic

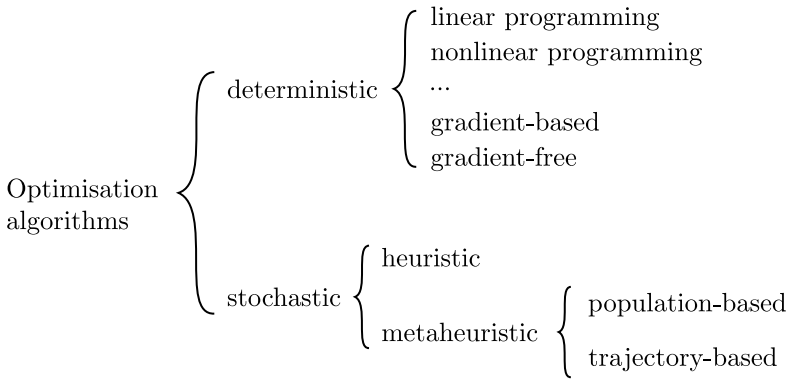


Figure 1.6: Classification of optimisation algorithms.

and meta-heuristic. The term 'heuristic' refers to a 'trial and error' approach towards problem solving, to produce good enough solutions in a reasonable time frame. The simplest heuristic method is the pure Random search method which randomly samples the search space for solutions. This strategy, however, is not efficient for many multiobjective problems and is hence rarely used for practical designs. Nevertheless, further developments over the heuristic algorithms, by incorporating clever simplifications and problem domain knowledge, lead to the term 'meta-heuristic' algorithms and generally provide good solutions to computationally complex problems.

Most meta-heuristic algorithms are nature-inspired and can be classified as population-based or trajectory-based. Evolutionary algorithms, such as genetic algorithms (GA) [20], are population-based as they are characterised by a population of solution candidates that evolve towards optimal trade-offs. On the other hand, simulated annealing [21] is an example of a trajectory-based method as it is characterised by a single solution moving through the search space in a piecewise style.

For complex multiobjective engineering optimisation problems, the use of evolutionary algorithms are particularly attractive as they require little knowledge about the problem being solved and are less susceptible to the shape or continuity of the Pareto-front, easy to implement, robust, and can utilise parallelism for solving [12].

1.2 Problem Statement

With a global push towards flight electrification, lighter and more efficient motor drives beyond current state-of-art are needed. Research and development activities in power electronics and machine technology can be grouped into two distinct vectors: innovation vector, where novel components, topologies, and control schemes are introduced; and optimisation vector, where activities improve on available technological building blocks using advanced modelling, virtual prototyping, and machine-converter integration. Both vectors aim at enhancing motor drive performance, where innovation unlocks new opportunities for optimisation and optimisation identifies performance barriers of available technologies to stimulate further innovations [22].

Within the optimisation vector, it is common to see components of a motor drive, such as the machine or converter, being designed and optimised independently from each other. As a result, cross-coupling effects and various interactions between these components are neglected, leading to poor compatibility and subpar performance when they operate together in a system. To achieve optimal performance, the motor drive design has to be approached from a system-level perspective, and its components need to be design and optimised together. The challenge here, however, is in developing suitable models for the system-level design, which can account for the complex and multiphysics component interactions in a motor drive operation. Besides, these models need also to be fast and accurate for them to be effectively used in an optimisation-based design.

Evolutionary algorithms are particularly promising for complex optimisation problems with many design variables, constraints, and objective values, and their use for engineering designs, including that of motor drives, is increasingly popular. Nevertheless, practical aspects relating to their implementation such as design variable selection, constraint handling mechanisms, multiobjective consideration, and choice of optimisation algorithms are often overlooked, resulting in inefficient utilisation of computational resources, and, in worst-case scenario, un-converging solutions.

1.3 Research Objectives

In this thesis, a holistic optimisation-based design approach for motor drives, considering machine and converter component and system-level designs, is presented. In particular, advanced analytical models for a motor drive, which employs a Surface Permanent Magnet (SPM) machine and Voltage Source Back-to-Back Converter (VSBBC), are proposed together with an optimisation-based design framework, making use of Evolutionary Multiobjective Optimization (EMO) algorithms. This work combines an in-depth knowledge of machine modelling, converter modelling, and modern evolutionary optimisation techniques, and should serve as a useful guideline for motor drive engineers, not limited to the aerospace industry, to design optimal weight and efficiency motor drives.

1.4 Summary of Research Contributions

Novel contributions from this work are summarised in the following points:

- A SPM machine component-level model for use in an optimisation-based design. Machine electromagnetic performance is characterised based on its air-gap magnetic field distribution, and its thermal behaviour is predicted using a simplified Lumped Parameter Thermal Network (LPTN). The model is fast, simulating on a normal PC in approximately 3×10^{-2} seconds, and its accuracy is validated against Finite Element (FE) and experimental analysis.

- A VSBBC component-level model for use in an optimisation-based design. In particular, the model evaluates the converter in terms of input current ripples, transient performance, losses, and volume. The model is fast, taking an average of approximately 1×10^{-4} seconds to run on a normal PC, while its performance analysis and loss calculations are verified to be accurate using time-domain simulations and experimental loss measurements.

- A comprehensive system-level motor drive model, integrating the machine and converter component-level models, with extra considerations of machine-converter interactions. A new machine harmonic loss model is proposed to account for effects of converter Pulse-Width Modulation (PWM) on machine losses. Meanwhile, effects of converter DC-link voltage on motor drive loss distributions at different operating points are also studied.

- Practical guidelines for the implementation of EMO algorithms in optimisation-based motor drive designs, relating to search space definition, performance space mapping, and constraint handling techniques. Using a case study, visualisation plots to aid the interpretation of optimisation results are also proposed. Three popular EMO algorithms (NSGAII, SMPSO, and GDE3) are benchmarked for motor drive optimisations, and SMPSO is found to be most competitive.

1.5 Thesis Outline

This thesis is structured into seven chapters, covering topics related to the optimisation-based design of motor drives. Chapter 2 discusses the suitable machine and converter topologies for aerospace motor drive applications and presents a review of previous work done on the modelling and optimisation of motor drives at component and system levels.

In Chapter 3, the development of an SPM machine analytical model is detailed. A set of input parameters are firstly defined, followed by a modelling approach for its geometry, winding, electromagnetic performance, and thermal performance. This chapter concludes with finite element analysis and experimental verifications using a prototype machine to validate the accuracy of the proposed model.

Similarly, Chapter 4 presents the development of analytical models for a back-to-back converter. A set of input parameters are defined at first, followed by modulation and control analysis of the converter operation. Next, analytical loss calculations for the switching devices and a simple heat-sink sizing method are discussed. The passive component sizing methods are also provided with detailed procedures. In the final section of this chapter, time-domain simulations and experimental tests on a prototype converter are performed to validate the model's accuracy.

Chapter 5 addresses an approach towards motor drive system-level modelling, integrating machine and converter models from previous chapters. A new machine harmonic loss model is also proposed to account for extra losses due to pulsed converter voltage. The system-level model is employed to evaluate performance and loss distributions within the motor drive, under different converter modulation parameters and load operating points. The analytical evaluation is validated by loss measurements on an experimental back-to-back motor drive setup, to confirm the system-level model's accuracy.

Next, Chapter 6 presents the system-level design of a motor drive design using evolutionary optimisation techniques. Firstly, the operating principles of three state-

of-art EMO algorithms are reviewed. Subsequently, practical guidelines are given for a motor drive optimisation setup, regarding search space definition, performance space mapping, and constraints handling. A multiobjective optimisation case study is performed for a motor drive to illustrate these concepts, and new visualisation methods are proposed to aid interpretation of the optimisation results. Lastly, the EMO algorithms are benchmarked against each other, in terms of their performance and suitability for motor drive optimisations.

To conclude the thesis, Chapter 7 summarises the contributions and findings, and suggests potential future work to extend this research, in the area of multiobjective motor drive optimisation.

Chapter 2

State of the Art: Modelling and Optimisation of Motor Drives

The previous chapter has provided an introduction and background to this thesis by introducing flight electrification concepts, the role of motor drives in them, and an optimisation-based approach for motor drive designs. This chapter will focus on how the work carried out in this thesis relates to relevant work already done and published by others in this research area. The contents in this chapter are subdivided into two parts: firstly, machine and converter topologies for aerospace motor drive applications are briefly discussed; secondly, a comprehensive summary of past work in areas of machine and converter component and system-level modelling and optimisation is presented.

2.1 Considered Motor Drive Topologies

The motor drive serves as a vital linking component between an electrical source and a mechanical load, and it consists of an electrical machine and power converters. For aerospace applications, power density and efficiency of the motor drive are key metrics in the selection of suitable machine and converter topologies, as is discussed in this section.

2.1.1 Electrical Machine

The most important electrical machines in industry are squirrel cage induction machines, traditional field-winding Alternating Current (AC) synchronous machines, Permanent Magnet (PM) synchronous machines, Brushless DC (BLDC) machines, Direct Current (DC) machines, and Switched Reluctance (SR) machines.

For the aerospace industry, there are strict requirements for electrical machines to have high power and torque density, while other desirable traits include reliability, efficiency, and availability [23]. Onboard a more electric aircraft, several types of machine topologies have been used or proposed, such as BLDC and SR machines, due to their lightweight and robust nature [24, 25]. An example of a BLDC application is in Electro Hydrostatic Actuators (EHA) technology to operate flight control surfaces for military and commercial aircraft, with an example shown in Fig. 2.1. This provides many advantages, such as 'power on demand', ease of integration into the aircraft system, and simplified maintenance [26].

Compared to other topologies, PM synchronous machines offer the highest power density and efficiency, due to low torque ripples, absence of rotor copper loss, and replacement of field windings by high-energy rare-earth magnets to provide excitation [27]. Additionally, with the possibility of fault-tolerant designs and high performance control, PM synchronous machines have been a popular candidate for aerospace actuation, generation, and environmental control system application over the recent years [28, 29]. Fig. 2.2 shows an example of a prototype 60-slot 50-pole PM machine, for an airborne wind-turbine application, with a power density of ≈6.2 kW/kg and efficiency of ≈95% [30].

Conventional internal rotor PM machines are categorised into Surface Permanent Magnet (SPM) and Interior Permanent Magnet (IPM) types, according to the magnet locations. As shown in Fig. 2.3, SPM machines have magnets mounted on the rotor iron surface, while for IPM machines, their magnets are buried inside the rotor iron. Compared to IPM machines, SPM machines provides an advantage of having low

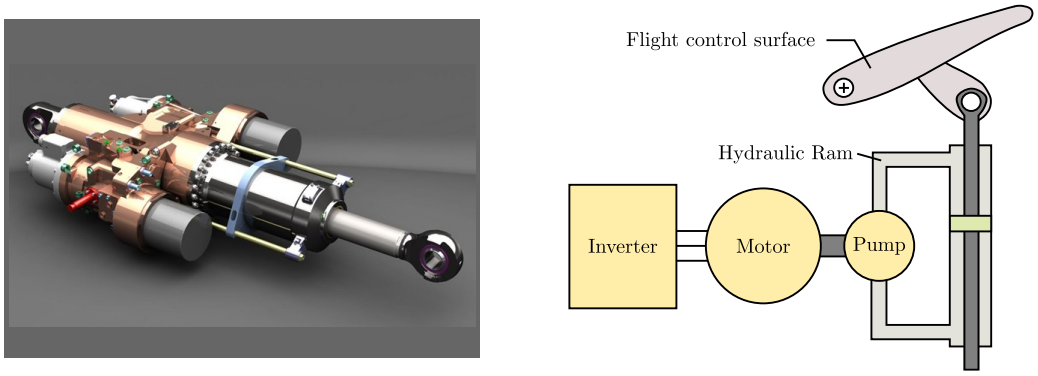


Figure 2.1: (a) Photo of Moog Electro Hydrostatic Actuators (EHA) with dual-redundant in-built brushless DC motor [26] (b) basic schematic of EHA system.

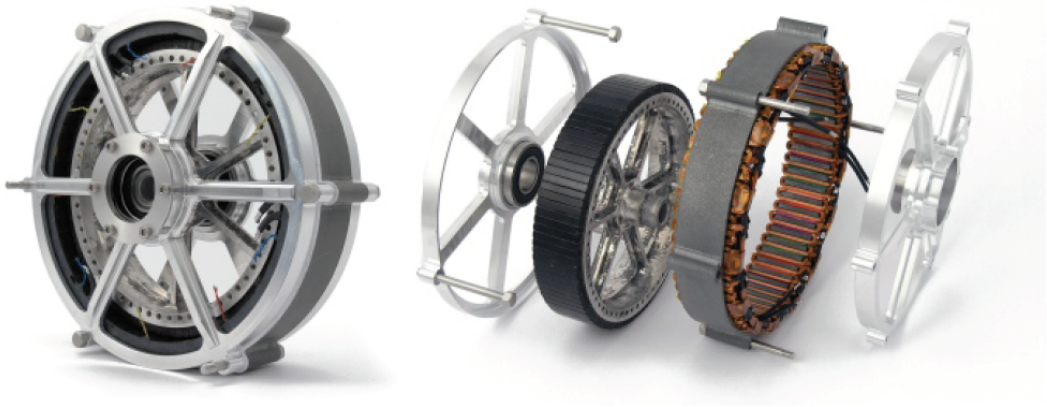


Figure 2.2: Photos of a high power density 60-slot 50-pole PM machine designed for an airborne wind turbine application [30].

leakage flux and better utilisation of the permanent magnet material. For these reasons, the SPM machine is an attractive option, especially for low-speed high-torque drives, where losses in rotor surface magnets are low due to low rotor speeds [31].

PM machines can be classified as distributed and concentrated winding machines, depending on their stator winding configurations, as shown in Fig. 2.3. Due to their shorter end-windings, it is often advantageous for PM machines to employ concentrated windings for lower copper losses. For concentrated winding machines, design for fault-tolerance in aerospace applications generally favours single-layer windings, due to their higher self-inductances and physical separation of phase

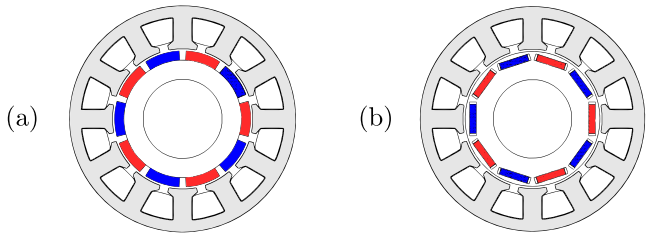


Figure 2.3: PM machine rotor topologies: (a) surface PM (b) interior PM.

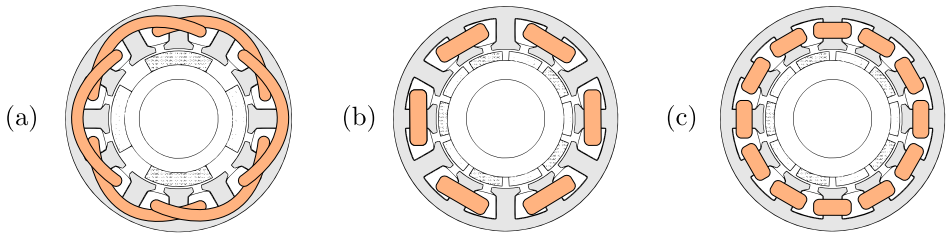


Figure 2.4: PM machine stator topologies: (a) distributed winding (b) concentrated winding (single-layer) (c) concentrated winding (double-layer).

windings. However, for higher torque density, double-layer windings are usually preferred [32].

If the machine's number of slots per pole per phase is a fraction, it is known as a fractional-slot machine. Interestingly, many desirable attributes can be obtained by having concentrated windings on a fractional-slot machine. They include high power density, high efficiency, low cogging torque, flux-weakening capability, and fault tolerance [33]. Based on literature study performed, recent high power density machine, which are designed for aerospace applications, have always favoured a fractional slot concentrated winding configuration, for the mentioned reasons.

In the remaining parts of this thesis, the chosen machine topology, considering a high power density aerospace application, is a fractional-slot concentrated-winding double-layer SPM machine.

2.1.2 Power Converter

Onboard a more-electric aircraft, loads are supplied by an variable frequency AC-distribution bus directly fed by a generator [34]. Power converters are thus required to produce, from the three-phase input AC voltage with constant or variable voltage and frequency, an output AC voltage or current to the machine with a controllable amplitude and angular frequency.

For example, the Boeing 787 aircraft electrical system architecture is shown in Fig. 2.5. Each gas turbine drive two starter/generators, which power a three-phase 230 VAC mains bus, with a variable frequency of 360 - 800 Hz. An Auxiliary Power Unit (APU) can also generate power into the AC bus, in case of an emergency. Although some loads are directly connected to the bus, a majority of the electrical loads require rectification into either the ±270 VDC, 115 VDC, or 28 VDC bus. In particular, for adjustable-speed motors, for the hydraulic pumps, environmental control system, etc, an Auto Transformer Rectifier Unit (ATRU) is employed to generate the required DC bus [35].

A number of ATRU topologies have been proposed during the last decade and they can be categorised into 12-pulse, 18-pulse rectifier type, etc., according to the pulse numbers in the line current every fundamental cycle [37]. An example of the 12-pulse ATRU is shown in Fig. 2.6(a). The transformer unit placed on the AC-side are used primarily for phase-shifting, to enhance input current quality. This choice of topology is due to its simplicity, robustness, and high reliability [38]. Despite the advantages, this topology requires a large and heavy line frequency auto-transformer unit at its input. Moreover, the intermediate DC-link voltage with this topology is dependent on the line-to-line voltage of the grid and can not be increased to a higher voltage.

It is possible to use other AC-AC conversion topologies, such as the voltage source back-to-back converter (VSBBC), for reduction in input filter sizes and to allow voltage boosting capability. Although they allow bi-directional power flow, i.e.

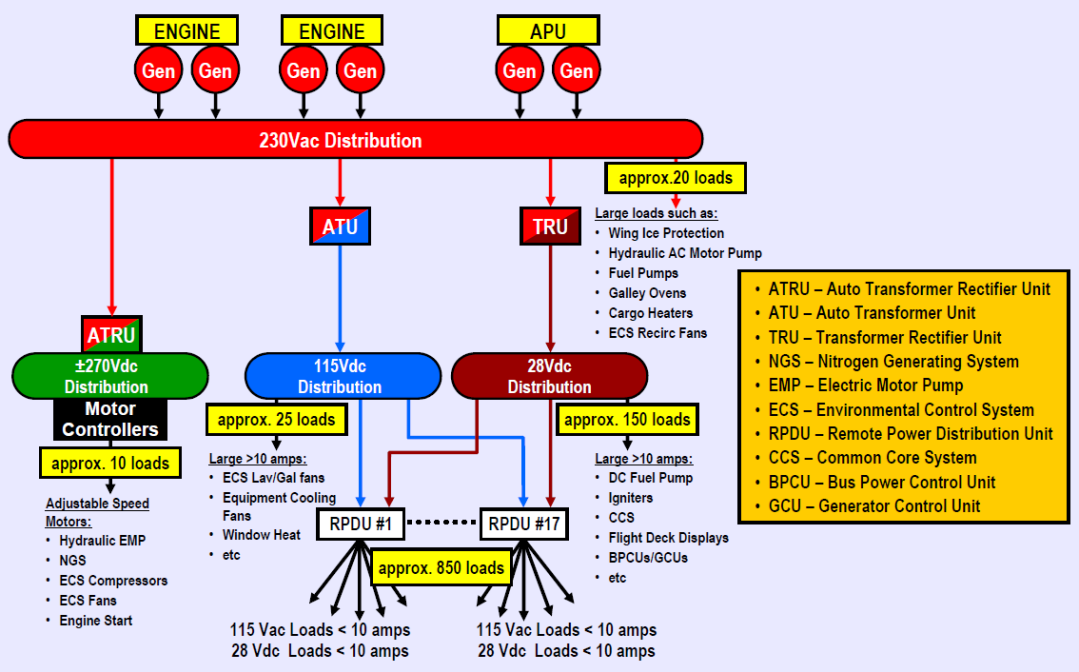


Figure 2.5: Modern More Electric Aircraft (Boeing 787) electrical power system architecture according to [36].

energy regeneration back to the grid which is currently not allowed [39], a braking circuit (also known as dynamic brake chopper) can be placed at the DC-link to quickly dissipate this energy for compliance with electrical power quality regulations. It is worth mentioning that this braking circuit is also needed for uni-directional topologies, such as the diode rectifier-inverter configuration, to prevent the DC-link voltage from rising, in the event of energy regeneration [40].

Conventional braking circuits are made of a large resistor with an active semiconductor switch to control the energy dissipation. This resistor is typically rated for worst-case operation, which is why it is heavy and bulky. Wheeler et al. [41] showed that by allowing regeneration for aerospace actuator applications, the impact on network power quality is almost negligible, and braking circuits can be omitted to reduce total system weight and volume. It is thus foreseen for future aircraft systems, that regeneration of energy into the main bus might be allowed.

The two-level VSBBC, depicted in Fig. 2.6(b), is arguably the most popular and

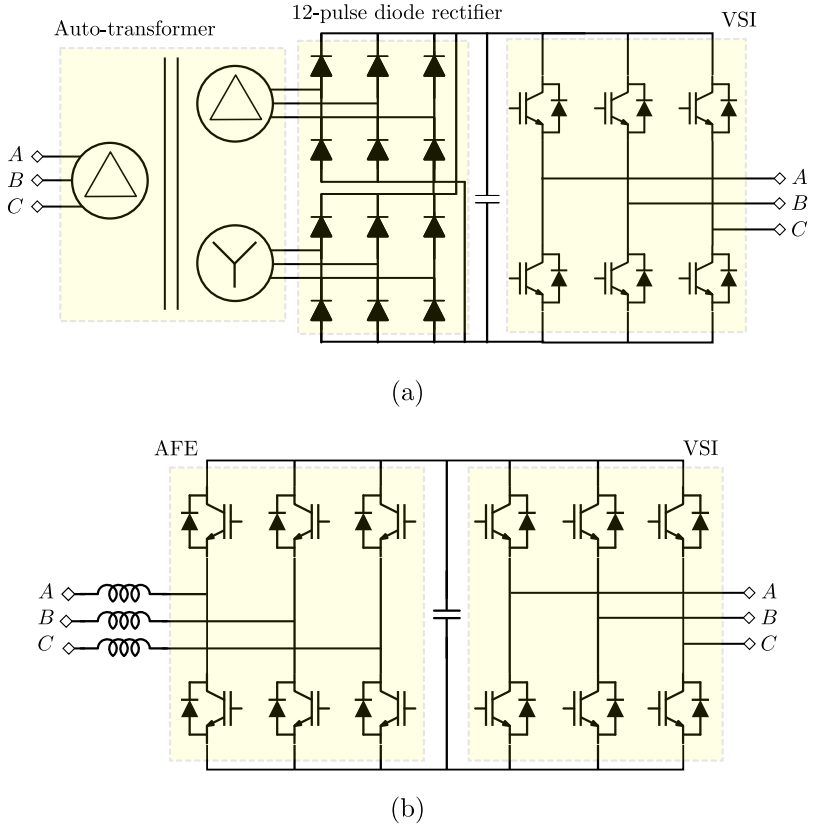


Figure 2.6: AC-AC power conversion topologies: (a) 12-pulse diode rectifier and voltage source inverter (b) two-level voltage-source back-to-back converter.

widely used bi-directional topology for AC-AC power conversion. This topology consists of an input and output two-level converter, connected via a DC-link and decoupled by a DC-link capacitor. The input stage converter, better known as the Active Front-End (AFE) rectifier, interfaces with the variable frequency AC grid to regulate input power factor and DC-link voltage, while the output VSI converter is connected to the machine, to control its speed and torque.

This back-to-back configuration can also be implemented with multi-level converters, to bring additional benefits, in terms of converter efficiency, lower machine harmonic losses, and smaller filtering components [42]. However, multi-level power conversion requires more switching devices and is more involved in terms of control and implementation. Matrix Converters can also be employed for AC-AC power

conversion, but compared to the two-level VSBBC, they are less flexible because of their increased control complexity and smaller possible motor drive operating range (due to their lack of boost capability and limited output voltage range) [43].

Aerospace electrification concept, in general, calls for a reduction in size and weight, and thus a high power density of the electrical power systems are desirable. In particular, active rectifiers allow a reduction of weight, as compared to conventional passive multi-pulse rectifier systems, while improving input current quality to meet stringent aircraft power quality requirements. Therefore, considering an aerospace application, a two-level VSBBC topology is selected for modelling in the remaining parts of this thesis.

2.2 Motor Drive Modelling and Optimisation

Motor drive design optimisation can generally be split into two independent parts: modelling and optimisation. Modelling techniques include the use of analytical equations, lumped parameter models, and numerical analysis [44, 45], while optimisation techniques are generally categorized into two types: deterministic, where solutions are searched for systematically, and stochastic, where the search space is explored randomly [12].

2.2.1 Component Level

Over the recent two decades, with drastic improvements in computing performance, many combinations of modelling and optimisation techniques have been presented for the component level design of electrical machine and power converters.

Machine Modelling and Optimisation

Practising machine designers know that although experience in obtaining good designs are not to be underestimated, the multi-variable, non-linear and complex nature

of how machine geometry relates to its performance makes it almost impossible to optimise, without the help of a proper optimisation strategy.

Bianchi et al. [46] were one of the first to present a Genetic Algorithm (GA) based design procedure for the constrained optimisation of an SPM machine. However, only one objective function (cost) and two design variables (machine bore diameter and axial length) were considered. Similarly, Wieczorek et al. also presented the use of GA for efficiency optimisation of induction machine designs, but they focused only on the optimisation technique and did not provide information about the machine models employed [47].

In contrast to the stochastic GA, Messine et al. proposed the use of a global deterministic Branch and Bound algorithm associated with interval arithmetic, for a slotless PM machine design optimisation, to minimise its mass and volume [48]. In their paper, the authors argued that their approach is advantageous as it has a guaranteed fast convergence towards a global optimum. In a later publication [49], the PM machine model was improved to consider more details, such as magnetic and thermal properties, along with discrete parameters, related to machine structure and choice of materials. Finally, in [50], the authors described the use of the Branch and Bound algorithm for the improved model. A limitation of this work is that the models employed are based on traditional sizing equations, which inherently carry many assumptions, and no experimental verifications were reported.

Sudhoff et al. [20] presented a structured analytical modelling approach to SPM machine design, using single or multiobjective GAs, for it's mass and efficiency optimisation. The modelling approach begins with a physical description of the machine, followed by its electromagnetic characterisation, in terms of flux density, torque, and power loss. The proposed advantage here is the elimination of traditional sizing equations for machine. In a later publication [51], the authors published more details of the model and extended it to also include core losses, inductance estimations, and axial flux leakage compensation. Different setups of the optimisation problem were also studied by the authors in [52] to consider the effects of design

variable encoding methods etc. However, the authors have only considered integer slot distributed winding PM machines and assumed a fixed slot current density to account for machine thermal performance in this work.

In [53], Duan et al. proposed a reduced-dimension electromagnetic model for SPM machines, and applied a Particle Swarm Optimization (PSO) algorithm to optimise five performance indices (volume, weight, efficiency, magnet weights, and torque per ampere). As only a basic PSO was implemented, the five performance indices were combined into one single objective using weighting factors. This model is expanded by Semidey et al. [54] to also consider machine thermal behaviour and the effect of different load profiles using a finite-difference thermal model. The main limitation with both this work is that its fundamental electromagnetic model considers many assumptions. For example, the authors assumed that the best machine designs will have the highest possible current density, which is not necessarily valid from an efficiency point of view.

Gammeter et al. [55] employed a comprehensive set of electromagnetic and thermal analytical models for the design and optimisation of radial and axial flux PM machines in an airborne wind turbine application. For optimisation, the authors used an exhaustive (direct search) algorithm to evaluate the whole design space deterministically, and from the resulting Pareto front, a solution is selected for prototyping. The main limitation of this work, however, is in its direct search optimisation algorithm, which has a 'step-size' problem. If the chosen step-size is too small, this leads to excessive computational efforts, whereas if it is too large, optimal points might be missed.

A closed-form analytical model for fractional slot concentrated winding SPM machines was presented by Min et al. [56]. The model can accurately predict the electromagnetic performance of the SPM machine, in terms of its open-circuit and armature air-gap magnetic field distribution. The authors also demonstrated the effective use of this model in a PSO optimisation environment to optimise machine design for high power density and efficiency. The authors, in a later

publication [57], also proposed a faster analytical model named Schwarz-Christoffel subdomain and demonstrated its use with a Differential Evolution (DE) optimisation algorithm. Similar to [20], this work has only considered the machine electromagnetic performance, while machine thermal sizing simply assumes a maximum slot current density.

The machine modelling and optimisation work discussed so far have only considered the use of analytical models. For SPM machines, analytical modelling is, in most cases, sufficiently accurate, as saturation of the main magnetic flux path in the machine is typically avoided during the design. To study effects of machine non-linearities, several publications, such as Rottach et al. [58] and Beniakar et al. [59], have proposed the incorporation of magnetic reluctance networks within the machine optimisation. Although an increased modelling accuracy can be obtained, this approach requires additional computational time to solve the non-linear reluctance network equations and results in significantly longer computational time.

For IPM machines, it is complicated to use analytical models or magnetic reluctance networks to account for different rotor geometry and leakage fluxes due to local saturation at the rotor bridges. Therefore, most IPM machine optimisations incorporate FE analysis within the optimisation algorithm.

The challenge of including FE analysis is the drastic increase in computational load. Ionel and Demerdash, in particular, have introduced a 'computationally efficient' FE modelling method, which uses Fourier analysis and a minimum number of magnetostatic solutions to evaluate the performance of each potential solution [60, 61, 62]. This method was then employed by the authors in a DE optimisation environment to optimise different objective values. In a later publication, the authors also investigated the use of a combined multi-objective optimisation with differential evolution (CMODE) algorithm to improve the utilization of computational resources during the optimisation process [63].

Similarly, Zarko et al. [64] defined a way of handling constraint functions in a DE optimisation algorithm, which contains computationally intensive FE-based

calculations. By using normalised IPM rotor geometry parameters, the appearance of geometrically unfeasible candidates can be reduced, and by checking each solution's feasibility before evaluating it using finite element analysis, a significant amount of computational time can be saved.

The optimisation and comparison of three PM machine types (SPM, IPM and flux switching machine), using FE and multiobjective PSO, was also carried out by Van der Geest et al [65]. In this paper, the authors' main objectives to optimize were weight and efficiency, and they provided detailed analysis and inspection of the large quantity of data produced during the optimization, to gain insight of general trends. The main downside of this approach is the significant amount of time needed (one or two day runtime), as reported.

In this thesis, an analytical model is developed for the electromagnetic performance of a fractional slot concentrated winding SPM machine, while a LPTN is used to evaluate its thermal behaviour. Finite element analysis and experimental tests are carried out on a prototype SPM machine, to verify the accuracy of this model, in terms of modelling the machine's electromagnetic performance. More details on the model can be found in Chapter 3. Meanwhile, EMO algorithms are employed for optimisation as is discussed more in Chapter 6. Compared to previous work, the machine modelling approach presented in this thesis focuses on speed and modelling accuracy, as compared to finite element and experimental analysis.

Converter Modelling and Optimisation

For power electronics modelling, there is always a trade-off between modelling accuracy and computational intensity. Unlike machines, power converters FE analysis typically need to be carried out in 3-D and is time-consuming to perform. This modelling method is hence never used during design optimisation. In contrast, analytical models for power converters employ a set of algebraic or simple differential/integral equations, which are much faster to evaluate computationally, and are thus more frequently used in optimisations.

Very early on, Blaabjerg et al. [66] described a design optimisation tool for a three-phase VSI to maximise its efficiency, by varying gate-drive resistances, gate-drive supply, and load current. The authors developed a complete loss model for the inverter and deployed weight functions for the IGBT and diode losses. For optimisation, they employed a deterministic hill-climbing local optimisation algorithm. However, no sizing or volume-related converter modelling was mentioned in this work.

Busquets-Monge et al. [67] presented an approach to optimise the design of a single-phase boost power factor correction front-end converter and its electromagnetic interference (EMI) filter, for minimum total component cost. Cost data were approximated using curve-fits of known data and the optimisation method employed is a gradient-based deterministic approach. Again, this work did not consider any physical sizing of the converter.

Kolar et al. [68] reported a multi-objective design optimisation performed for a single-phase power factor correction (PFC) rectifier using very detailed analytical models to estimate the size of each converter component. The objective functions pursued here were efficiency and power density, and a deterministic global-local optimisation method was employed. In this optimisation method, the switching frequency was varied 'globally', while the components were optimised 'locally', based on requirements propagated from the global level. This work was extended to also consider cost as an objective function in a later publication [69].

The same global-local optimisation method was used in several other publications. Wang et al. [70] employed this technique to optimise footprint area and losses for different DC-AC converters, sweeping through a range of switching frequencies at a global level, and optimising component designs at a local level for each switching frequency. Similarly, the same technique was employed by these authors to optimise the design of a two-channel interleaved Vienna-type rectifier, as reported in [71].

Laird et al. [72] presented a design tool to optimise the selection of devices, heatsink and passive components for a three-phase VSI and its EMI filter, using a deterministic branching optimisation method. The method exploits the interdepen-

dency of design variables and performs optimisation at multiple levels. Variables with the most dependent variables branching from it are optimised in the outer loop, while others are optimised in various inner loops. Based on the authors' analysis carried out for a VSI design, the same conclusions from the global-local method were obtained, that is switching frequency should be optimised in the outermost loop and other parameters related to each component model in the inner loops.

The converter optimisation techniques described above are considered as deterministic, and, as explained before, they can suffer from a 'step-size' problem. Over recent years, there is an increasing amount of research interest in evolutionary approaches for the optimisation, as they can explore the search space more efficiently and are particularly useful for complex optimisation problems.

Wang et al. [73], proposed a design optimisation approach for a three-phase diode front-end rectifier, using GA to minimise cost and volume of the system. Similarly, Mirjahari et al. [74] described a design approach for a module-integrated inverter, employing a multiobjective variant of GA (NSGAII) to optimise reliability, efficiency, and volume. In this work, a 'reduced-order modelling' technique is applied to simplify the component models without losing much accuracy. From a broader perspective, looking at the grid and power distribution systems, D' Antonio et al. [75] detailed a multiobjective GA optimisation method for the design of a photovoltaic (PV) microgrid system, which is composed of several modular DC-DC converters. The objective functions are daily average deliverable power and total system mass, while four design variables that characterise solar power based microgrids (battery voltage, PV maximum power, PV maximum power point voltage, and the number of panels per string) are optimised.

This thesis considers only analytical models to represent the power converter and its components in the optimisation. Semiconductor loss models are used to estimate losses of switching devices, while physics-based curve-fitted models, obtained from commercially available products, are employed to size the heat-sink and passive components. The power converter models are detailed in Chapter 4, while EMO

algorithms used for converter optimisations are presented in Chapter 6.

2.2.2 System Level

Due to the close and synergetic interactions between machine and converter in a motor drive operation, their designs are to be inseparable, to achieve optimal drive performance. For instance, Lovelace et al. [76] looked at IPM motor drive cost optimisations, considering magnetic saturation and inverter costs, and they concluded that a larger and more expensive machine could be exchanged for low power electronics cost.

Despite the above, significantly more research in motor drive modelling and optimisation pay attention to improving performances at a component level rather than at a system level, as discussed previously. There is noticeably less literature for motor drive modelling and optimisation at a system level, where the design of machine and converter are coupled and considered together.

Roos et al. [77] presented a simultaneous design and optimisation of the SPM machine, mechanical gearhead, and converter power electronics for servo-application motor drives. This work also considered the impact of load profiles and aimed to design the smallest possible system. The main limitation with this work, however, is that overly simplified machine and converter models were employed and that no experimental verifications were carried out.

Interactions between machine and converter were investigated by Sarikhani et al. [78] in a drive optimisation environment. In this work, a multiobjective optimisation process, which employs a hybrid-GA-PSO optimiser and dynamic physics-based phase variable machine model obtained from FE analysis, was proposed. For torque ripple evaluation, the authors incorporated FE analysis within the optimisation, slowing down the process considerably.

An SPM motor drive sizing optimisation methodology for a specific torque-speed operating profile was proposed by Aubry et al. [79], for wave energy conversion

applications. In this paper, the sizing parameters of the machine and current rating of the power converter were optimised together using a multiobjective variant of PSO, to lower system cost and maximise electrical energy. However, no details on experimental validation was presented, to validate the accuracy of the models employed.

De Andrade et al. [80] presented two optimal design approaches for a motor drive, coupling the design of a high-speed PM machine, VSI and input filters. In this work, the complete integrated optimisation approach showed significant improvements over the local and sequential optimisation approach. A multiobjective GA is also employed to minimise the combined weight and losses of the system. Nevertheless, the authors have only discussed the optimisation approach in the paper, without providing details about the models employed.

Rottach et al. [81] developed a comprehensive design tool to perform integrated optimisation of a helicopter electromechanical actuator drive, for minimum weight. A particular emphasis was placed on the consideration of machine non-linearities as part of the optimisation, using magnetic reluctance network models. PSO algorithm was employed in this work to optimise the main machine geometry and mechanical gear ratio, while an exhaustive search algorithm was used to optimise the detailed slot-opening and tooth-tip shape. However, only a basic tuning and implementation of the optimisation algorithm was considered, resulting in less effective utilisation of computational resource during its search.

Lei et al. [82] proposed a system-level design optimisation method for a PM transverse-flux machine motor drive system. In this paper, the motor and control design are optimised together to achieve steady and dynamic performances, using single-level and multi-level implementations of the DE algorithm. This work was later extended to consider also the robustness of the optimisation, i.e. taking into account noise factors and uncertainties [83]. However, in this work, the authors did not consider power converter volume or weight sizing as part of the optimisation.

Zarko et al. [84] presented the use of a mixed-integer distributed ant colony

optimisation for the multiobjective optimisation design of a traction motor drive system, to minimise its total volume and losses in a single driving cycle. Notably, in this work, an IPM analytical machine model based on 2-D maps of parameters calculated with FE analysis, and neutral point clamped three-level VSI averaged model are employed to represent the drive.

Overall, to the best of the author's knowledge, there is no literature available for the optimisation of an AC-AC motor drive with a back-to-back converter. Unique to this converter topology is the optimisable intermediate stage DC-link voltage, which significantly affects switching device losses and machine operating range, as is discussed in Chapter 5. A motor drive system-level optimisation, using EMO algorithms, is detailed in Chapter 6.

2.3 Chapter Summary

This chapter has presented an overview of different machine and converter topologies suitable for high power-density aerospace motor drive applications. Comparing the different topologies, the selected topology for further investigations in this work is that of a fractional-slot concentrated-winding double-layer SPM machine controlled by a two-level VSBBC.

A detailed review was also carried out and discussed for the research area of motor drive modelling and design optimisation. An observation made is that significantly more related work has been undertaken for machine and converter component level, as compared to the motor drive at a system level. Besides, the system-level optimisation of a back-to-back converter together with the machine design, specifically considering the intermediate DC-link voltage as a design variable, was also not found anywhere in literature. Finally, another contribution from this review points to the fact that proper application and setup of EMO algorithms for motor drive optimisation is often overlooked, resulting in an inefficient utilisation of computational resources. These findings further motivate the need for a holistic optimisation-based design

approach for motor drives at a system level, along with practical guidelines on the implementation of EMO algorithms, as is presented in this thesis.

Chapter 3

Electrical Machine Modelling

The problem of designing optimal electrical machines is challenging due to the complexity and multiphysics nature of their operation. Computational methods to evaluate their performances include the use of analytical models, LPTN models, and FE models. FE models are most time-consuming to solve although they are most accurate, while lumped parameter models are faster to solve, in comparison, but are difficult to set up. Analytical models are fastest to solve and simple to use, but their accuracy depends on their simplifications and assumptions. For the SPM machine topology, analytical models for their electromagnetic performance can be very accurate due to their consistent rotor shape and minimal leakage flux. Simplified LPTN models, on the other hand, are suitable for its thermal modelling due to machine slot symmetries.

This chapter presents a detailed multiphysics SPM machine model suitable for use in an optimization-based design. Compared to other models, the proposed model is remarkably systematic and straightforward, consisting of only three main parts, as shown in Fig. 3.1. Besides, it is versatile, to consider many input parameters, fast, to take only an average of only 0.03 seconds to run on a regular PC, and accurate, as verified by FE analysis and experimental tests.

Section 3.1 firstly defines a comprehensive set of input parameters for the machine model, and Section 3.2 describes a systematic method to parametrise the machine

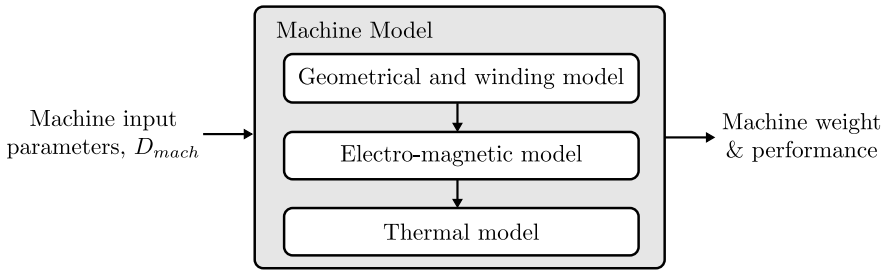


Figure 3.1: Organisation/flowchart of machine model.

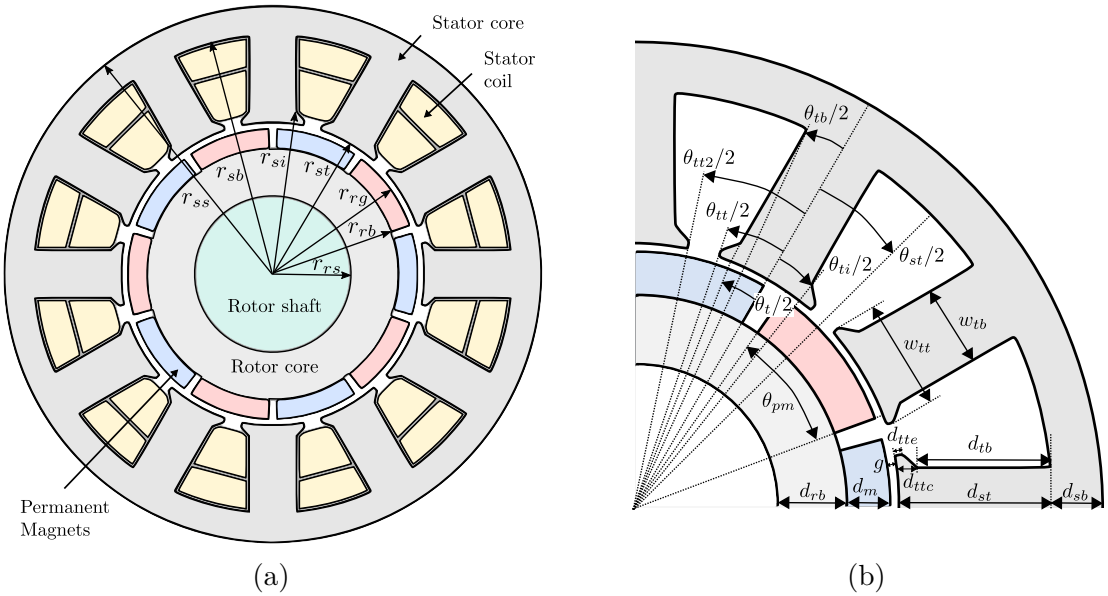
geometry and winding properties. Next, Section 3.3 presents different analytical modelling techniques to characterise the machine's electromagnetic performance, with high accuracy and speed. Section 3.4 follows on to propose the use of a simplified LPTN model to evaluate machine thermal behaviour. Finally, Section 3.5 focuses on model validation using FE and experimental analysis performed for a prototype SPM machine.

3.1 Input Parameter Definitions

To evaluate the machine's performance, it is useful to consider it as a simple model with an input-output form. A set of input parameters D_{mach} is firstly defined for the machine model:

$$D_{mach} \ni \{D_{mat},\ D_{geo},\ N_{ts},\ w_{dia},\ n_{wpc},\ \omega_e,\ i_d,\ i_q,\ T_{amb}\} \tag{3.1}$$

where D_{mat} is a set of vectors consisting of selected stator and rotor core, winding, and PM material information, D_{geo} is a set of machine geometrical parameters, N_{ts} is the number of coil turns in series per phase, w_{dia} is the wire diameter, n_{wpc} is the number of wires per conductor, ω_e is the electrical speed, $\hat{i}_d$ and $\hat{i}_q$ are the peak d and q-axis machine currents, respectively, and T_{amb} is the ambient temperature.



(a) (b)

Figure 3.2: Cross-sectional diagram of a surface permanent magnet machine: (a) full stator geometry (b) detailed slot and tooth.

With reference to Fig. 3.2, the geometrical parameters contained in D_{geo} are:

$$D_{geo} \ni \{p,\ S_s,\ r_{rs},\ d_{rb},\ d_m,\ g,\ d_{ttc},\ d_{tte},\ d_{tb},\ d_{sb},\ \theta_t,\ \theta_{tt},\ \theta_{pm},\ l\} \tag{3.2}$$

where p is the number of pole pairs, S_s is the slot number, r_{rs} is the inner shaft radius, d_{rb} is the rotor back-iron thickness, d_m is the magnet thickness, g is the air-gap thickness, d_{ttc} is the tooth-tip thickness at the centre, d_{tte} is the tooth-tip thickness at the edge, d_{tb} is the depth of tooth base, d_{sb} is the stator back-iron thickness, θ_t is the tooth fraction, θ_{tt} is the tooth-tip fraction, θ_{pm} is the magnet fraction, and l is the machine lamination stack length.

Together, input parameters in Eqs. (3.1) and (3.2) provide essential information for a full evaluation of the machine's electromagnetic and thermal behaviour.

3.2 Geometrical and Winding Models

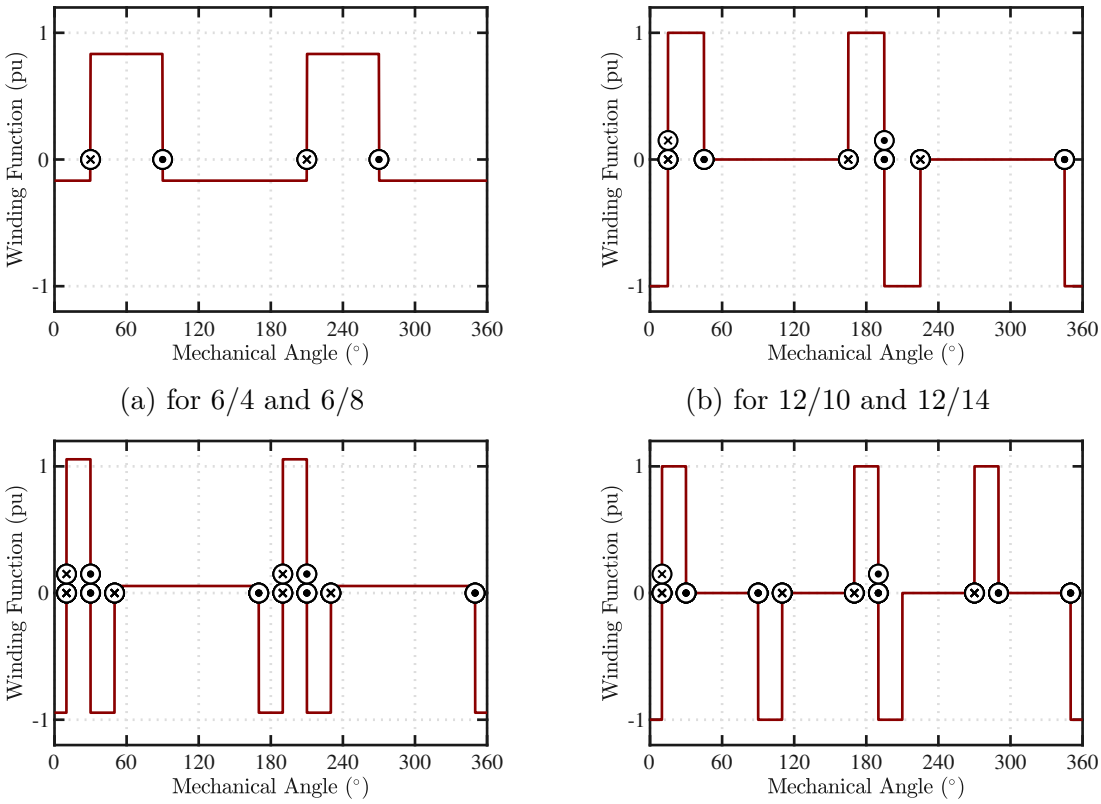
Figure 3.2 illustrates the cross-section of a SPM machine, which, in this example, has a 12-slot 10-pole configuration. For machines with a non-magnetic and non-conductive sleeve around the rotor magnets, the sleeve is considered to be a part of the air-gap. The surface magnets are considered here to have a curved uniform height and are mounted directly onto the rotor back-iron. For simplicity, trapezoidal slots, with curved-bottom stator slot shape and no corner radius, are assumed.

For geometrical modelling, this work adopts the approach proposed by Sudhoff et al. [11]. For a fixed topological shape, as shown in Fig. 3.2, a systematic set of equations governing all the geometrical relationships is developed. Given the geometrical parameters in Eq. (3.2), the full machine geometry can be computed, together with other quantities of interest, such as slot area and volumes.

Fractional-slot concentrated-winding configurations offer unique advantages, as discussed previously in Section 2.1.1. Based on recommendations from Mitcham et al. [85], if similar slot and pole numbers are selected for these machines, additional merits of high torque density and low cogging torque can be gained. Further, to prevent excessive vibration and noise, slot-pole combinations with unbalanced magnetic pull are to be avoided. For these reasons, this thesis considers only the slot-pole combinations of 6/4, 6/8, 12/10, 12/14, 18/14, 18/16, 18/20, and 18/22.

The choice of winding layout significantly affects the flux linkage between the stator windings and the magnetic flux flowing within the machine. In most cases, winding layouts which result in the highest fundamental winding factor $k_{w,v}$ are used to obtain maximum air-gap magnetic flux linkage.

To calculate $k_{w,v}$, the method proposed by Farshadnia et al. [86] is employed. Phase winding function W_m^* is firstly defined as the air-gap Magneto-Motive Force (MMF) produced by a single-phase winding coil around the stator, of 1 turn and carrying 1 A of current. By applying a Fourier series transformation on W_m^* across the angular circumference, amplitude $\hat{W}_{m,n}^*$ can be found for individual n^{th} harmonic



(a) for 6/4 and 6/8

(b) for 12/10 and 12/14

(c) for 18/16 and 18/20

(d) for 18/14 and 18/22

Figure 3.3: Phase winding function plot of optimal winding layouts for the considered slot-pole combinations.

components. Fundamental winding factor $k_{w,v}$ is calculated as

$$k_{w,v} = \frac{\hat{W}^*_{m,v}}{\hat{W}^{*(\text{base})}_{v}} = \frac{\hat{W}^*_{m,v} m v \pi}{2 S_s} \tag{3.3}$$

where v is the operating harmonic, $\hat{W}^{*(\text{base})}_{v}$ is the amplitude of v^{th} order harmonic component of a base winding function, and m is the number of phases. The base winding function is a hypothetical winding function created by a phase winding with S_s/m number of turns and spans π radians around the stator circumference. Phase winding functions for the optimal winding layouts of the considered slot-pole combinations are plotted in Fig. 3.3, and their Fourier series expressions and fundamental winding factors are given in Table 3.1.

Table 3.1: Fourier series expression of phase winding functions and the calculated fundamental winding factors.

Slot-pole combinations	**Slot per pole per phase,** S_{pp}	**Fourier series expression of phase winding function,** $\boldsymbol{W^*_{m,n}}$	**Fundamental winding factor,** $\boldsymbol{k_{\mathrm{w,v}}}$
6/4, 6/8	1/2, 1/4	$\frac{P}{c}\frac{2}{n\pi} \cdot \sin\left(\frac{n\pi}{S_s}\right)$	0.866
12/10, 12/14	2/5, 2/7	$\frac{P}{c}\frac{2}{n\pi} \cdot \sin\left(\frac{n\pi}{S_s}\right) \cdot \left[2\cos\left(\frac{7n\pi}{S_s}\right)\right]$	0.933
18/16, 18/20	3/8, 3/10	$\frac{P}{c}\frac{2}{n\pi} \cdot \sin\left(\frac{n\pi}{S_s}\right) \cdot \left[1-2\cos\left(\frac{2n\pi}{S_s}\right)\right]$	0.945
18/14, 18/22	3/7, 3/11	$\frac{P}{c}\frac{2}{n\pi} \cdot \sin\left(\frac{n\pi}{S_s}\right) \cdot \left[1+2\cos\left(\frac{10n\pi}{S_s}\right)\right]$	0.902

* c is the denominator of S_{pp}.

Unlike integer-slot distributed-windings, the fractional-slot concentrated-winding MMF is rich with spatial harmonics. Their winding functions are, therefore, important for calculations of their armature reaction magnetic field and machine inductances in later sections.

Based on previous input parameters from Section 3.1, other winding-related quantities of interest, such as slot fill-factor and phase resistance, are also calculated at this stage. The maximum slot fill-factor (space-factor) primarily depends on the slot-liner insulation requirements and practical manufacturability. For low-voltage machines, the maximum slot fill-factor is typically between 0.5 to 0.6, while for high-voltage machines, slot insulation takes more space and this factor is typically between 0.3 to 0.45 [31]. The geometrical and winding model equations are provided in Section A.1.

As winding losses are a function of phase resistance and current, they tend to increase with the winding temperature. For simplification, a conservative approach is employed in this work, where phase resistances assuming maximum allowed winding

temperature are used for loss computations. Also, it is important to note that winding high-frequency AC losses (due to skin-effect) are not considered here, as they are assumed to be negligible compared to fundamental losses.

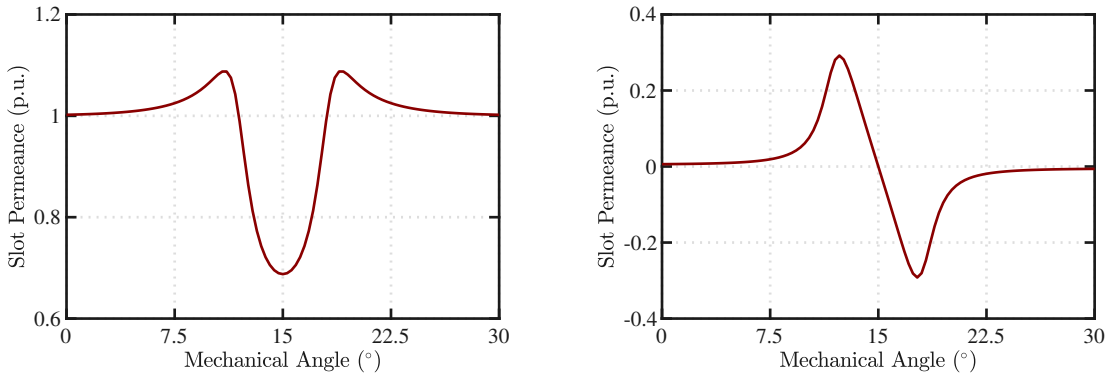
3.3 Electromagnetic Model

Knowledge of the field distribution is needed to evaluate machine electromagnetic performance, as it reveals where the flux is concentrated, where electric potential is created, and where force is produced. Although accurate field calculations can be performed using an FE analysis, it is very time-consuming. Alternatively, analytical models are faster and can also be employed to compute the magnetic fields in an SPM machine, as will be discussed in this section.

3.3.1 Open-circuit Air-gap Magnetic Field

The SPM machine open-circuit air-gap magnetic field is firstly computed with the technique proposed by Zhu et al. [87, 88]. Although the technique was first applied to brushless DC motors, it is equally applicable to brushless permanent magnet AC motors, as it is a general analytical technique for instantaneous air-gap magnetic field distribution in radial-field topologies. For a slotless machine, its magnetic field is modelled in 2-D polar coordinates, by solving the governing Laplacian/quasi-Poissonian field equations within the air-gap region. The assumptions here are that stator and rotor cores feature infinite permeability such that fluxes going through the stator and rotor surfaces are perfectly radial, and that magnetic flux is uniformly distributed across the magnet material. Detailed derivations of the slotless machine magnetic field flux density are given in Table A.5.

Stator slotting effect in the air-gap, due to stator slot-openings, is undesirable as it reduces the fundamental magnetic flux and distorts the field solution. Unlike integer-slot distributed-winding machines, fractional-slot concentrated-winding machines have smaller slot numbers for the same pole numbers and, consequently, larger



(a) (b)

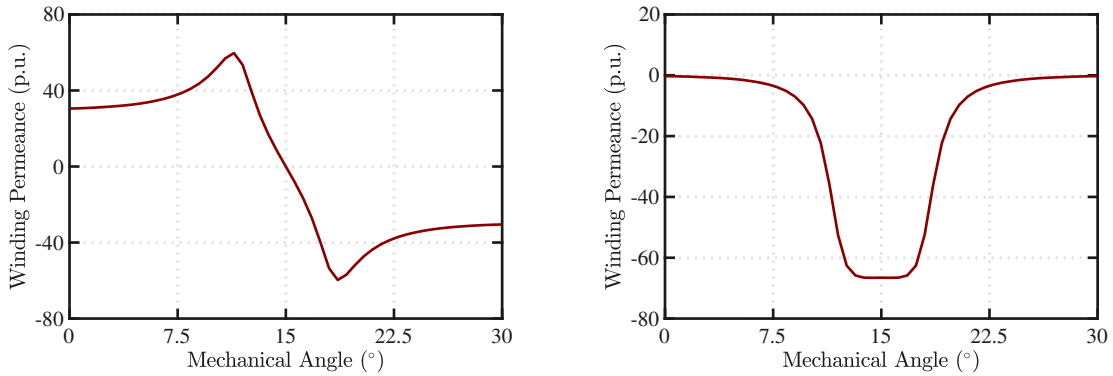
Figure 3.4: Complex relative air-gap permeance of a slot-opening in the middle of the air-gap: (a) real component (b) imaginary component.

slot-opening to pole-pitch ratios. Slotting effect is, thus, more pronounced and needs to be considered for the latter machine topology.

Slotting effects are traditionally accounted for using an equivalent air-gap length calculated by the Carter factor. In terms of computation time and implementation, this method is fast and simple to use. However, it does not capture the radial and tangential magnetic field variations.

As an alternative, this thesis employs a complex permeance method, based on the conformal transformations of the stator slot-openings, to consider slotting effects [89]. This method is more accurate than the Carter factor method and its closed-form solutions reduce computation time significantly, as concluded by Ramakrishnan et al. [90]. In this method, a complex relative permeance function is derived and applied as a masking function on the slotless machine air-gap magnetic field. An example of the slot-opening complex permeance functions is shown in Fig. 3.4, while detailed equations for its derivation are given in Table A.6.

Next, magnet flux flowing into or out of the stator is found by integrating air-gap flux density over a tooth pitch, and the induced winding flux linkages can subsequently be calculated from this flux information. By taking a negative derivative of the induced flux linkages' variation against time, not only the fundamental component, but the full open-circuit Back Electro-Motive Force (BEMF) waveform can be



(a) (b)

Figure 3.5: Complex relative permeance function for a slot-opening with current-carrying conductors in the middle of the air-gap (in cylindrical form): (a) radial component (b) tangential component.

obtained. Detailed derivation of these functions are given in Table A.7.

3.3.2 Armature-reaction Air-gap Magnetic Field

Armature-reaction can be defined as the effects of magnetic flux created by the armature winding, which is located inside the stator for a PM machine. A similar approach, proposed by Zhu et al. [91], is employed to calculate the armature-reaction air-gap magnetic field, where the Laplacian equation is solved in the air-gap region for current sheets of uniform current-density, distributed along the stator core air-gap surface. These current sheets have lengths equal to the slot-opening, and they represent slots containing current-carrying conductors. Again, the technique was first applied to brushless DC motors but it is also applicable to brushless permanent magnet AC motors with concentrated windings.

Subsequently, a conformal mapping technique, proposed by Zarko et al. [92], is applied to compute complex relative permeance functions for these current sheets. An example of the complex relative permeance function, for a slot-opening with current-carrying conductors, is plotted in Fig. 3.5.

The single-coil air-gap magnetic field is found by assembling field solutions of positive and negative current-carrying coil sections and shifting the waveform in

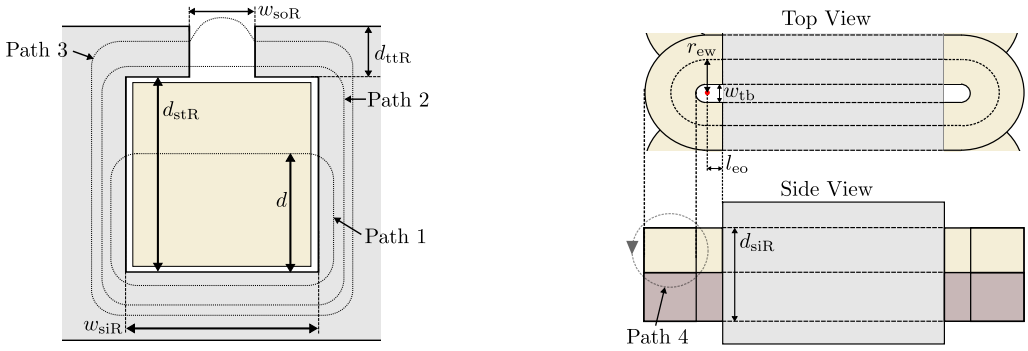
amplitude, to ensure that average radial flux density around the air-gap circumference equals to zero. For slot-openings without current-carrying conductors, the open-circuit complex relative permeance functions from Section 3.3.1 are employed. To obtain the total armature-reaction air-gap magnetic field, field solutions from coils of all phases are super-positioned. Detailed equations for this derivation are provided in Table A.8.

3.3.3 Machine Inductance

Machine inductance is a key parameter in the analysis of machine and converter interactions. When calculating inductance, the three important magnetic field regions to consider are air-gap region, slot region, and end-winding region. Portions of the machine made of soft magnetic materials do not contribute to inductance, assuming that their high relative permeability is maintained. Magnet flux also does not contribute to inductance because coil inductance only relates its current to flux linkages created by itself. In an inductance analysis, the magnets are simply blocks of material with a relative permeability of μ_r [93].

Armature winding magnetising flux is defined as armature flux that crosses the air-gap, and its fundamental component electromagnetically links with the rotor magnetic fields to produce torque. This flux entering or exiting the stator is obtained by integrating armature-reaction air-gap magnetic flux density over each stator tooth surface. Subsequently, the induced magnetising flux linkage and corresponding magnetising inductance is found by multiplying this flux distribution with the phase winding functions from Section 3.2. Detailed equations for the flux computation are given in Table A.9.

Armature winding leakage flux, on the other hand, is the armature flux that does not cross the air-gap. The induced leakage flux linkage and corresponding leakage inductance are calculated using the energy method, also known as the principle of virtual work. In this principle, stored magnetic energy W_ϕ in a closed volume of



(a) (b)

Figure 3.6: The four main leakage flux paths considered in this work, around the (a) stator slot and (b) end-winding area.

V is equal to the field energy, which is created by the enclosed current-carrying conductors. The magnetic inductance of this closed volume L_V can be calculated as:

$$L_V = \frac{2W_\phi}{i^2} = \frac{1}{\mu i^2} \int_V B^2 \mathrm{d}V \tag{3.4}$$

where i is the winding current, μ is the magnetic permeability of enclosed volume, and B is the magnetic field flux density. Assuming an infinite stator permeability, slot inductances depend on the enclosed volume of air at the slot opening or coil within the slot. In this work, the leakage flux is considered to only flow in four main paths, as illustrated in Fig. 3.6:

- Path 1: Horizontally across inner slot walls.
- Path 2: Horizontally between tooth tips at slot opening.
- Path 3: Fringing between tooth tips at slot opening.
- Path 4: Circularly around end winding coils

Slot leakage inductances, due to flux flowing in paths 1, 2, and 3, are computed with leakage permeance factors proposed by Ponomarev et al. [94], with rectangular slot approximations as depicted in Fig. 3.6(a). In this approximation, rectangular

inner slot width w_{siR} is fixed as the top width of the trapezoidal shape, while rectangular slot depth d_{stR} is varied to ensure that slot area is kept the same.

The concentrated-winding machine end-sections are considered as half solenoids when viewed from the top, as illustrated in Fig. 3.6(b). Their inductances L_{sol} are calculated using well-known inductance equations for solenoids [94]:

$$L_{sol} = \frac{N_t^2 \mu_0 \mu_{env} A_{sol}}{l_{sol}} \tag{3.5}$$

where N_t is the number of winding turns per coil, A_{sol} is the cross-sectional area of the solenoid, μ_{env} is the relative permeability of the environment, and l_{sol} is the solenoid's axial length. In this work, for simplification, μ_{env} is assumed to be that of air, which is 1. Nevertheless, due to the presence of high-permeability iron parts in the machine housing and stator lamination stack ends, this representation is inexact and it is expected to underestimate the actual end-winding inductance. For a more accurate representation of the end-winding inductance, analytical equations, parametrised with 3-D FE modelling results, can be implemented instead [95].

Finally, synchronous inductance L_s is obtained as a sum of magnetising inductance L_m and all leakage inductances L_l. Detailed equations for the inductance calculations are provided in Table A.10.

3.3.4 Flux and Flux Densities

With the large effective air-gap of SPM machines, the rotor core flux consists mainly of the magnet flux. Flux density distribution at the rotor core surface is integrated across the surface area of a magnet pole, to calculate the magnet flux flowing into or out of the rotor core.

Stator core flux, however, consists of both magnet flux and a considerable amount of armature-reaction flux, as shown in Section 3.3.3. At any time instant, armature-reaction flux distribution due to each phase is estimated with the phase winding function, phase inductance, instantaneous phase currents, and the number of coil-

turns in series per phase. Flux flowing through each stator tooth can be found by super-positioning the total armature-reaction flux and magnet flux flowing into or out of the stator core. For double-layer windings, stator tooth flux is assumed to split equally in opposite tangential directions as it enters the back-iron.

Rotor back-iron, stator tooth, and stator back-iron flux densities are computed by dividing the total flux flowing through these parts over the area perpendicular to the direction of its flow. Flux density in the main magnetic path is typically constrained by a maximum value, to avoid magnetic saturation of the core material. Detailed equations for the flux and flux density calculations are given in Table A.11.

3.3.5 Fundamental Magnetic Losses

In general, under no-load conditions, magnetic losses contribute to a large share of the machine losses, as compared to mechanical losses. However, they are difficult to model accurately because they are microscopically dependent on the magnetic material properties, and they are related to magnetic flux density, which is non-uniform, time-varying, and non-linear.

To estimate fundamental magnetic losses in a soft ferromagnetic material, a two-terms approach, based on the modified Steinmetz equation, is employed [96]. Assuming a sinusoidally varying stator flux density with an amplitude of $\hat{B}$ and frequency of f, the specific loss parameter W_{loss}, with units W/kg, can be estimated for a certain part of the machine as:

$$W_{loss}(f, \hat{B}) = K_{hys} f^{\alpha} \hat{B}^{\beta} + K_{eddy}(K_{sf} f \hat{B})^2 \tag{3.6}$$

where K_{sf} is the lamination sheets stacking factor, K_{hys}, α, β, and K_{eddy} are Steinmetz coefficients for the material, obtained by curve-fitting manufacturers loss data. Fundamental iron losses are then calculated by multiplying W_{loss} with the mass of the considered part. Magnetic losses from the stator tooth and back-iron are calculated separately, as their flux density values and variation characteristics are

different.

As air-gap magnetic flux fundamental component rotates synchronously with the rotor, no fundamental magnetic losses are produced in the rotor back-iron and magnets. However, for fractional-slot concentrated-winding machines, some eddy-current losses can be induced in the rotor back-iron and magnets, by their rich air-gap flux density spatial harmonics. Due to limitations in time, these rotor spatial harmonic losses are not considered in this thesis, due to the complexity involved in their modelling and measurements [97]. It is important to note that these losses become increasingly dominant in high-speed applications.

3.3.6 Electromagnetic Torque

To calculate torque, an energy method can be employed, which is based on the principle of energy conservation. According to this principle, since energy cannot be created or destroyed, electrical input energy is equal to the sum of output mechanical energy, stored magnetic energy, and losses in the form of heat energy. Average torque T_m is thus calculated as:

$$T_m = \frac{P_{out}}{\omega_{rm}} = \frac{P_{in} - P_w - P_{ir,fund} - P_{ml}}{\omega_{rm}} \tag{3.7}$$

where P_{out} is the output mechanical power, ω_{rm} is the mechanical speed in radians, P_{in} is the input electrical power, P_w is the winding loss, $P_{ir,fund}$ is the fundamental iron loss, and P_{ml} is the mechanical loss. P_{in} can be determined as:

$$P_{in} = \frac{3}{2}(\hat{v}_q\hat{i}_q + \hat{v}_d\hat{i}_d) \tag{3.8}$$

where p is the machine pole pair number, $\hat{v}_d$ and $\hat{v}_q$ are the peak d and q-axis voltages, respectively, and $\hat{i}_d$ and $\hat{i}_q$ are the peak d and q-axis currents, respectively.

3.4 Thermal Model

The main thermal limitations in electrical machines are typically the winding insulation life and magnet demagnetisation. Copper winding insulation is sensitive to operating temperatures and its life expectancy roughly halves for every increase of 10°C, according to the Arrhenius law [98]. Magnets, on the other hand, have decreased remanent flux densities as temperature increases, and they can ultimately irreversibly lose their magnetisations above a certain temperature, which is known as the Curie temperature. For machine designs, a thermal analysis is needed to prevent machine performance derating due to over-temperatures.

In this work, a simplified LPTN with a reduced number of parameters is employed, exploiting machine slot symmetries to consider only a section of the machine [99]. Power loss produced in different parts of the machine are considered to inject heat flow into the relevant nodes, and the resulting node potential represents its physical temperature.

The LPTN structure is illustrated in Fig. 3.7(a), while its parameters are described in Table 3.2. The main assumption with this thermal network model is that heat flux is conducted outwardly in the radial direction only, i.e. no heat is transferred axially through the housing front/end covers. Further, as only the steady-state temperatures are of interest, thermal capacitances are also omitted to speed up the analysis. Using an open-source Matlab based tool [100], closed symbolic solutions are derived to estimate the winding and magnet temperatures in the thermal network.

Besides, the main sources of losses incorporated within this LPTN are winding conduction losses, stator back-iron losses, and stator teeth losses. As mentioned previously in Section 3.3.5, rotor spatial harmonic losses are not considered in this thesis, due to its complexity and mechanical losses on the shaft are also not included in the consideration. For these reasons, the magnet temperature is expected to be higher than predicted by this LPTN model.

Obtaining accurate values for the LPTN thermal resistances is challenging as

Table 3.2: Description of LPTN symbols.

Parameters	**Description**
V_1:	Ambient temperature
I_1:	Copper losses in stator winding
I_2:	Iron losses in stator backiron
I_3:	Iron losses in stator tooth
I_4:	Magnet eddy current losses
I_5:	Iron losses in rotor backiron
R_1:	Convection from housing to ambient
R_2:	Radiation from housing to ambient
R_3:	Conduction in stator backiron (outer) + conduction in housing
R_4:	Conduction in slot liner + conduction in stator backiron (inner)
R_5:	Conduction in stator tooth (outer)
R_6:	Conduction through winding insulation
R_7:	Conduction through slot liner (side)
R_8:	Conduction in stator tooth (inner) + convection from tooth to air-gap
R_9:	Conduction in magnet (outer)
R_{10}:	Conduction in magnet (inner) + conduction in rotor (outer)
R_{11}:	Conduction in rotor (inner), shaft + convection from shaft to ambient

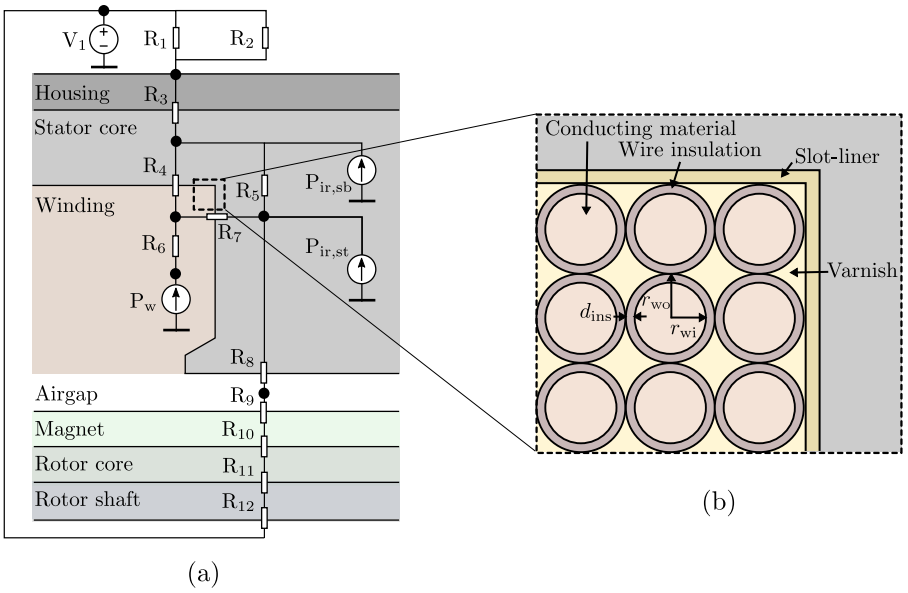


Figure 3.7: (a) Simplified LPTN with reduced number of parameters (b) Inhomogeneous slot area consisting of conducting material, insulation material, and varnish.

it is difficult to measure and separate the cooling effects as a result of conduction, convection, and radiation heat transfer.

Conduction heat transfer is the main mechanism by which power losses inside the machine are transferred to its surface. This heat transfer mechanism takes place within a body of material as a function of temperature difference, and its thermal resistance $R_{\mathrm{th,cond}}$ is a reciprocal function of the material's thermal conductivity k_{th}. Radial conductive thermal resistances $R^{(\mathrm{rad})}_{th,cond}$ are calculated using well-known heat transfer equations for hollow cylinders [101] according to Eq. (3.9), while tangential conductive thermal resistances $R^{(\mathrm{tan})}_{th,cond}$ are computed using parallel 2-D heat conduction equations according to Eq. (3.10).

$$R^{(\mathrm{rad})}_{th,cond} = \frac{1}{2\pi k_{th} l_{ax}} \log\left(\frac{r_o}{r_i}\right) \tag{3.9}$$

$$R^{(\mathrm{tan})}_{th,cond} = \frac{l_{tan}}{k_{th} A_{tan}} \tag{3.10}$$

where l_{ax}, r_o, r_i, l_{tan}, and A_{tan} are the axial length, outer radius, inner radius, tangential length, and heat transfer area of the cylinder wall, respectively.

Conduction heat transfer inside the slots with winding bundles is complicated, as the slot area is inhomogeneous, typically containing conductive material, insulation material, and varnish. However, the method proposed by Pyrhonen et al. [31] is used to homogenise the slot area and represent it as a 'lumped' effective material with anisotropic properties. Assuming that the round wire conductors are placed side-by-side, as illustrated in Fig. 3.7(b), the slot conductive thermal resistance $R_{th,cond}^{(\text{slot})}$ can be approximated as:

$$R_{th,cond}^{(\text{slot})} = k_{th,ins}\left(\frac{r_{wi}}{d_{ins}} + \frac{d_{ins}}{r_{wo}}\right) \tag{3.11}$$

where $k_{th,ins}$, d_{ins}, r_{wi}, and r_{wo} are the thermal conductivity, thickness, inner diameter, and outer diameter of the insulation material, respectively. It is important to note that Eq. (3.11) is only a loose approximation, as in practice, with random-wound machines, the round wire conductors are randomly placed.

Convection through air or liquid at the outer machine surface is usually the most significant heat transfer mechanism, and it is an effective method to remove heat from the machine to its ambient surrounding. Convection heat transfer takes place between solid surfaces and moving fluid, and are of two types: natural convection, where fluid circulation is purely due to thermal gradients, and forced convection, where an external pump or fan drives the fluid movements. Convective thermal resistance can be estimated as:

$$R_{th,conv} = \frac{1}{h_{conv}A_{hs}} \tag{3.12}$$

where h_{conv} is the convective heat transfer coefficient, and A_{hs} is the housing cylindrical surface area. It is important to note that convection losses are strongly influenced by the environment, i.e. air pressure due to changes in altitude, or the movement of

air/fluid surrounding the machine for aerospace applications. As a simplification, the changes in environment factors are not considered and a constant convection heat transfer coefficient is assumed.

Radiation heat transfer also takes place at the outer machine surface, in the form of electromagnetic radiation. Radiative thermal resistances can be estimated, again, using a heat transfer coefficient:

$$R_{th,rad} = \frac{1}{h_{rad} A_{hs}} \tag{3.13}$$

where h_{rad} is the radiative heat transfer coefficient. For temperature differences on the order of 10°C, the proportion of radiation heat transfer is typically comparable to that obtained by natural convection, especially when the outer machine surface is anodised and painted black for high emissivity [102].

In practice, h_{conv} and h_{rad} are difficult to determine accurately as they are strongly correlated to the ambient operating conditions. In this thesis, heat transfer models to find these coefficients are not included, but, instead, they are fixed to approximate values, obtained using a commercial electrical machine thermal analysis software MotorCAD [103]. For natural-air convection-cooling with axial-fins rounded and black anodised housing, the convection and radiation heat transfer coefficients are calculated from MotorCAD to be $h_{conv} \approx 6$ $\mathrm{Wm^{-2}K^{-1}}$ and $h_{rad} \approx 6$ $\mathrm{Wm^{-2}K^{-1}}$, respectively, similar to values obtained from the empirical equations in [104].

3.5 Machine Model Verifications

Due to budget and time constraints, Finite-Element (FE) analysis and experimental tests to validate the developed machine model are carried out on a prototype 12-slot 10-pole SPM machine, originally designed and built for servo applications. Key parameters for the prototype machine are listed in Table 3.3. A limitation of using this prototype test machine, as opposed to a typical aerospace machine, is its lower

Table 3.3: Key parameters of prototype 12-slot 10-pole SPM machine.

Parameter	**Symbol**	**Value**	**Unit**
Rated mechanical speed	w_{m}	1500	rpm
Rated output power	P_{o}	1300	W
Rated rms phase current	I_{ph}	9.3	A
Number of turns per coil	N_{t}	30	-
Stack length	l	54	mm
Stator air-gap radius	r_{st}	34	mm
Stator outer radius	r_{ss}	61	mm
Stator and rotor material	-	M235-35A	-
Permanent magnet material	-	NdFe38-EH	-

power density, reliability, and lack of in-built fault-tolerance characteristics. However, as the main objective of this verification is to validate different assumptions in the models before employing them in an optimisation-based design, these limitations are not considered to be too significant.

In this section, details of the prototype hardware are firstly presented, followed by a comparison of predictions from the analytical model and results from the FE analysis and experimental tests.

3.5.1 Prototype Machine

Several photos of the machine stator and rotor, before and after assembly, are shown in Fig. 3.8. The laminated stator core with its double-layer concentrated-winding can be seen in Fig. 3.8(a) and Fig. 3.8(b). From Fig. 3.8(b), a slight offset in the end-winding length can be observed. This is necessary for the process of inserting winding bundles into the stator slots. In Fig. 3.8(c), the rotor magnets' axial segmentation,

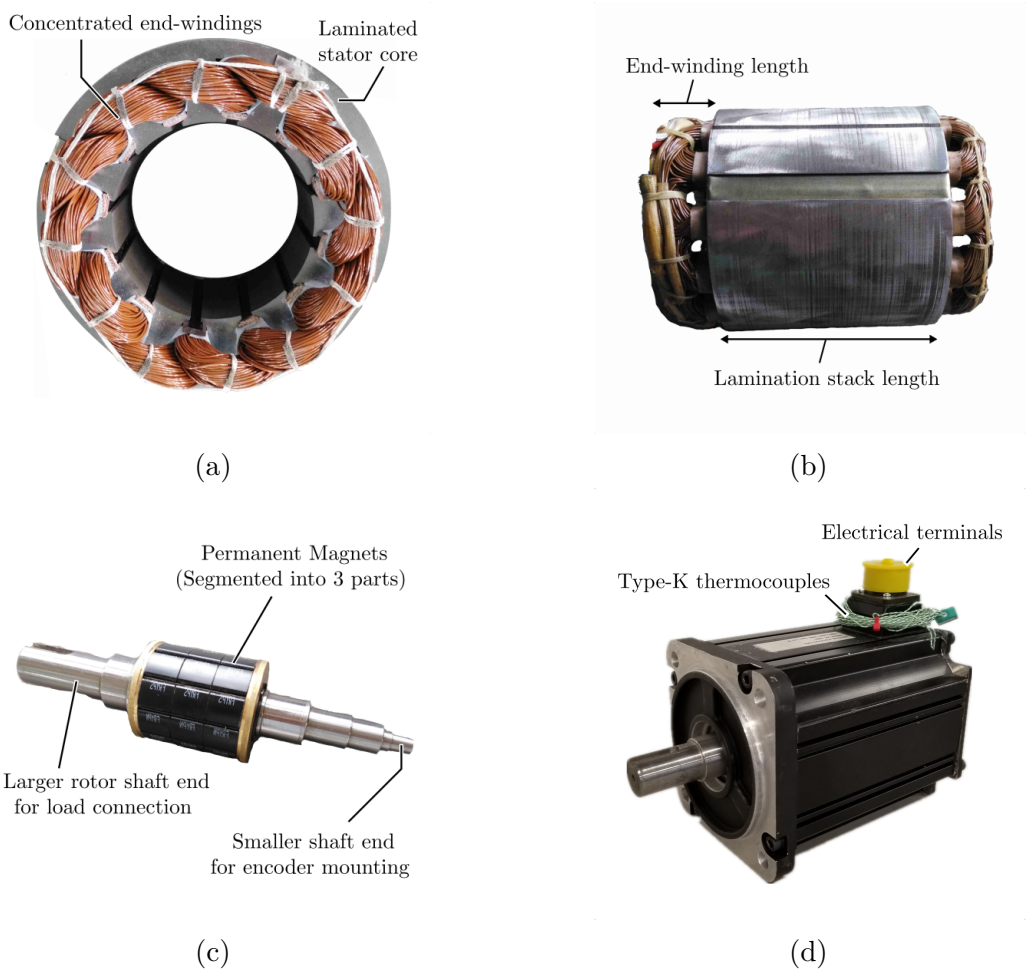


Figure 3.8: Photos of the prototype machine: (a) front view and (b) side view of stator after windings were inserted into the core; (c) rotor with axially-segmented magnets before assembly; (d) fully-assembled machine in black anodised housing.

to reduce PM eddy-current losses, can be seen. Finally, in Fig. 3.8(d), the fully-assembled machine in its black-anodised housing is shown. Type-K thermocouples are embedded within the final machine assembly to monitor winding temperatures.

3.5.2 Finite Element Analysis

In the analytical models, local saturation effects are neglected and the soft magnetic material is assumed to be infinitely permeable. Other assumptions were also made regarding magnetic flux paths for leakage inductance calculations and boundary

conditions for the air-gap magnetic field calculation. 2-D FE analysis, under static and transient-with-motion conditions, using Infolytica MagNet is thus useful to check the validity of these assumptions for the prototype machine.

To create the FE models in Infolytica MagNet, a Matlab script is written to interface and populate the machine design parameters in Infolytica MotorSolve, which contains ready-made templates for rotor and stator designs. The MotorSolve design (full geometric model) is then exported into Magnet for solving and further post-processing.

Figures 3.9 to 3.11 show static 2-D FE field solutions for the machine under open-circuit, pure armature excitation, and rated load conditions, respectively, for a particular time instant. For pure armature excitation condition, the magnet material's magnetisation is set to zero in the FE software. As shown in the figures, the air-gap flux density components extracted from the field solutions, under all three operating conditions, generally match well with the analytical model's predictions but exhibit some discrepancies in the tangential component. This is due to the shape deformation of magnets and current carrying conductor slot openings, as a result of the conformal mapping. The analytical model's predictions of non-current carrying conductor slot opening effects, especially, are shown to be very accurate, allowing reductions in fundamental air-gap flux density, due to wide slot-openings of fractional slot concentrated winding machines, to be taken into consideration.

From the static field solution under rated load conditions in Fig. 3.11(c), the flux densities at point A, B, and C are also compared against analytical predictions. The analytical model predicted a stator tooth flux density (Point A) of 1.46 T, while the FE computed a value of 1.40 T (4.1 % difference); for the stator back-iron (Point B), the analytical prediction was 1.15 T, whereas the FE calculation was 1.13 T (1.7 % difference); finally, in the rotor back-iron (Point C), the analytical prediction was 0.71 T, while the FE prediction was 0.65 T (8.5 % difference). The differences can be explained by local saturations, tooth tip fringing flux, and non-uniform flux density distributions, which are neglected in the analytical model.

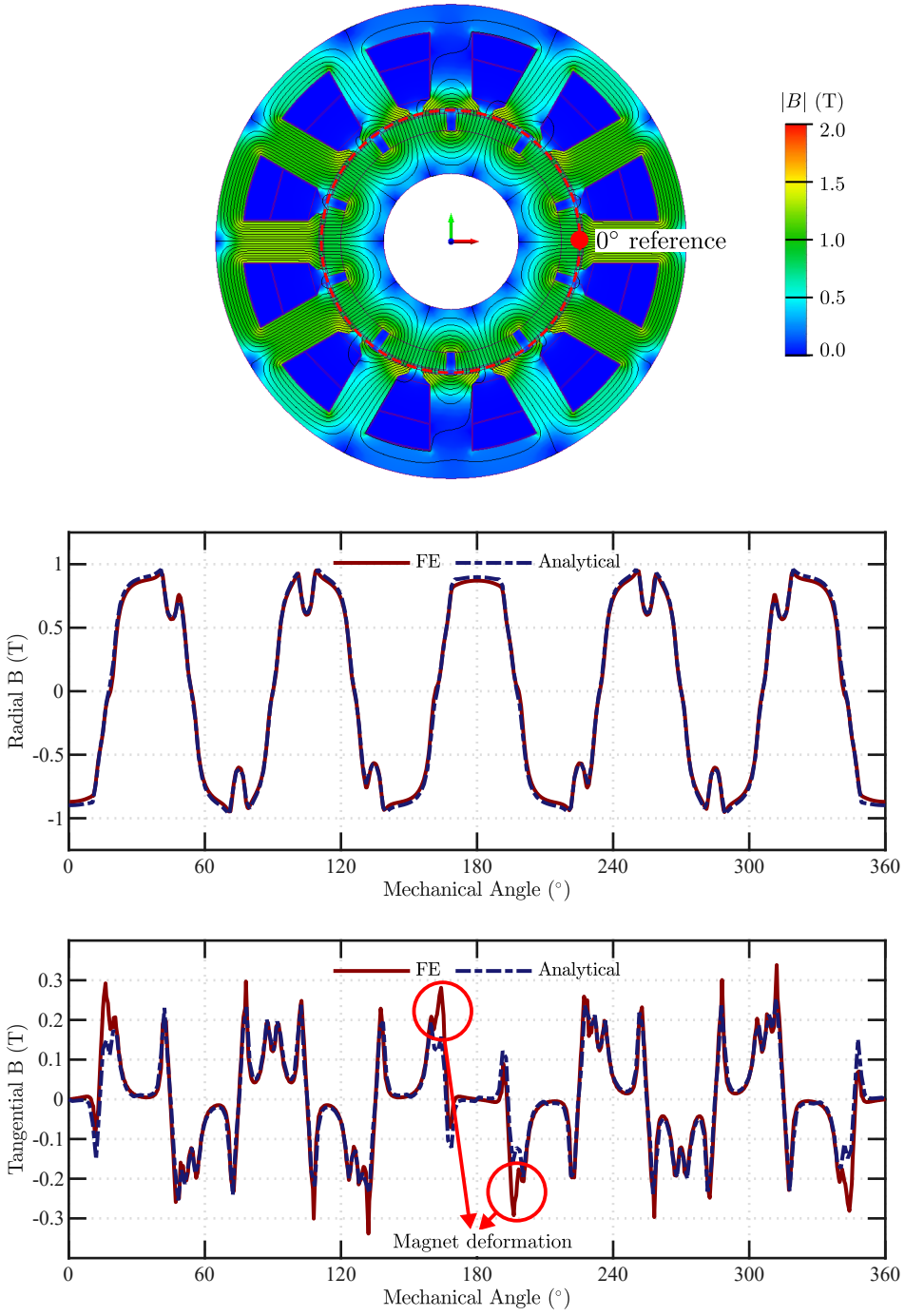


Figure 3.9: Flux density plots and air-gap magnetic field radial and tangential flux density components based on static 2-D FE analysis under open-circuit conditions. For flux density component plots, the analytical waveforms are included for comparison.

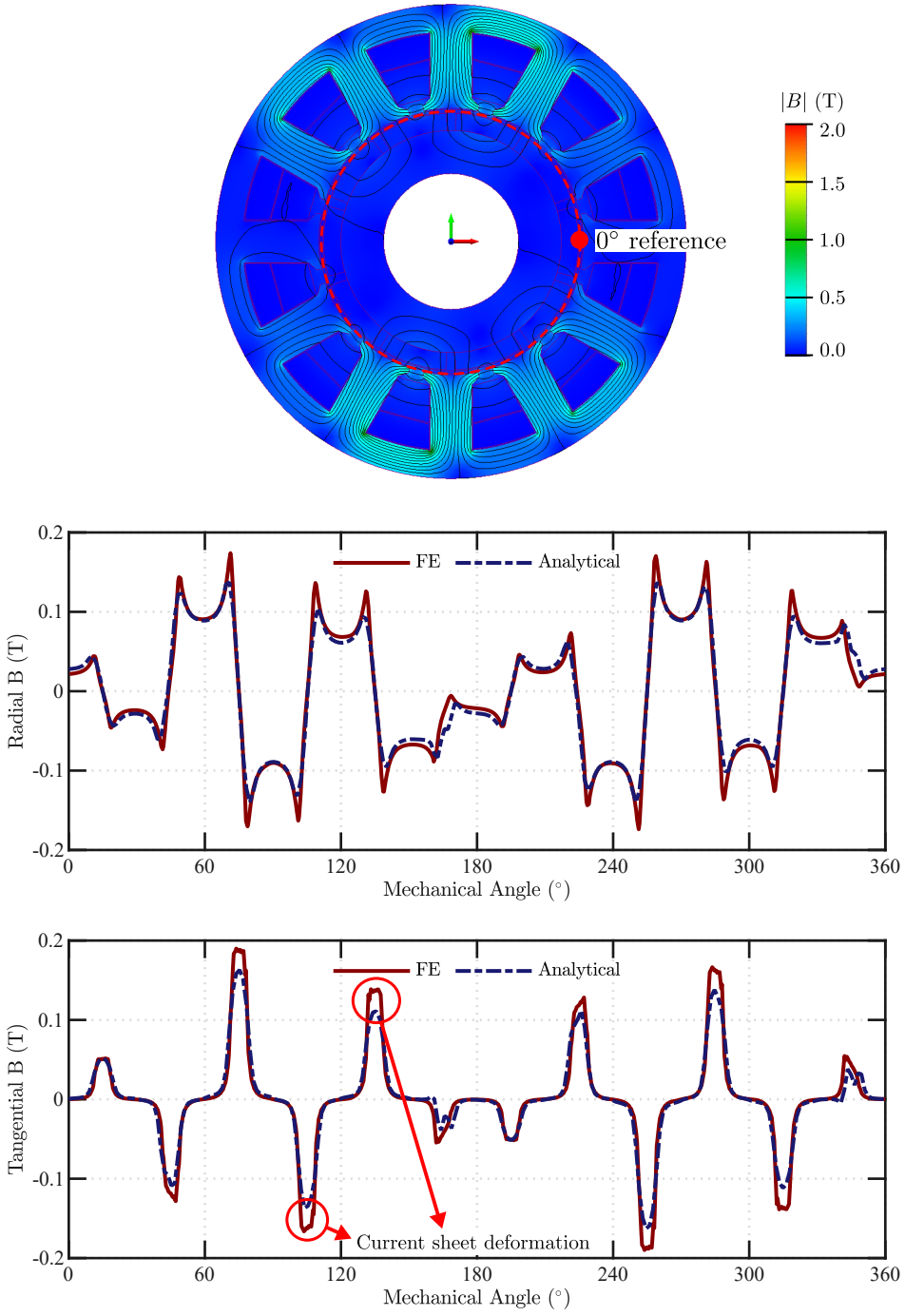


Figure 3.10: Flux density plots and air-gap magnetic field radial and tangential flux density components based on static 2-D FE analysis under pure armature excitation. For flux density component plots, the analytical waveforms are included for comparison.

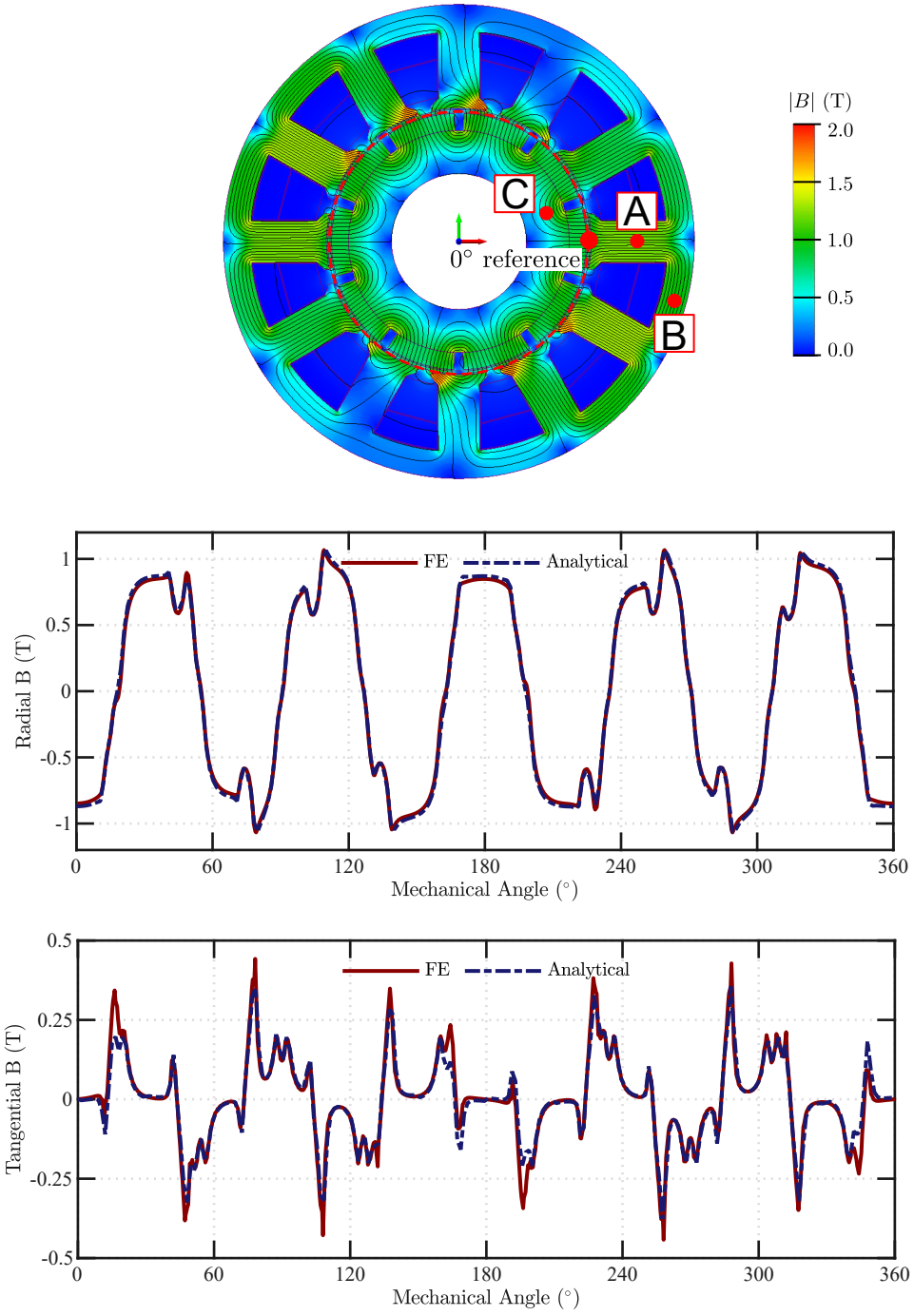


Figure 3.11: Flux density plots and air-gap magnetic field radial and tangential flux density components based on static 2-D FE analysis under rated load conditions. For flux density component plots, the analytical waveforms are included for comparison. Flux densities at points A, B, and C are compared against analytical predictions.

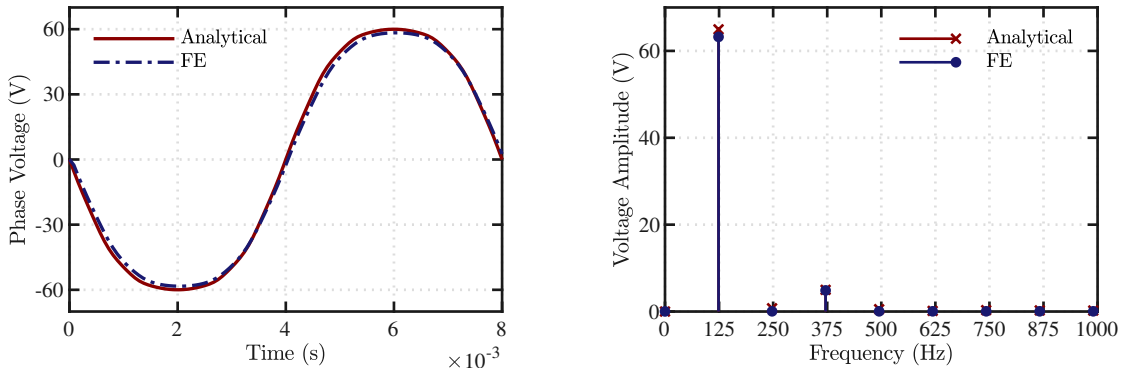


Figure 3.12: Comparison of analytical predictions against transient with motion FE solutions under open-circuit conditions: (a) phase voltage against time and (b) FFT of phase voltage waveform.

The machine BEMF and electromagnetic torque are computed in FE using a transient-with-motion analysis. At rated speed and open-circuit conditions, Fig. 3.12(a) compares the BEMFs from the analytical model and FE analysis, revealing a good match. By performing a Fast Fourier Transform (FFT) analysis on the waveforms, as seen in Fig. 3.12(b), their fundamental components are compared, and a small difference of 2.0 % in their amplitudes is obtained. At rated speed and rated load conditions, the analytical model predicts a mean torque of 8.49 Nm, while the mean torque obtained from the FE analysis is 8.41 Nm (1.0 % difference).

Finally, machine inductances are calculated from the transient-with-motion results. The analytically predicted end-winding inductances are added to the 2-D FE model's electrical circuit. The inductance value calculated by the analytical model is 2.22 mH, while the FE analysis gives 2.28 mH (2.7 % difference). This good match confirms the validity of assumptions made regarding the leakage flux paths around the stator windings.

3.5.3 Experimental Analysis

Apart from the FE analysis, the analytical model is also validated experimentally. A photo of the test bench, with the prototype machine, high-precision torquemeter,

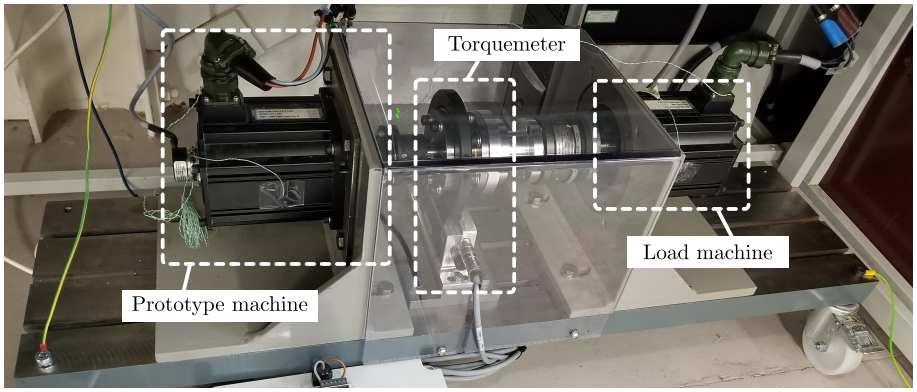
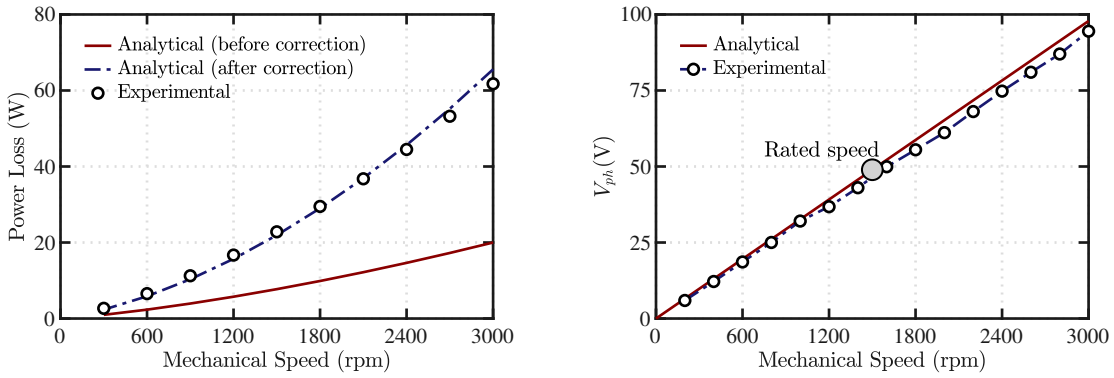


Figure 3.13: Photo of test bench for experimental analysis of prototype machine.

and associated load machine, is shown in Fig. 3.13.

Stator DC resistances are measured using a Valhalla Scientific 4300B Digital Micro-Ohmmeter at ambient temperature. Initially, the analytical model underestimates the phase resistance as the end-winding offset length was neglected. When an offset end-winding length is included, the predicted and measured resistances are found to match better. At room temperature (20°C), the analytical model predicts a phase resistance of 202.5 mΩ, while experimentally, it is measured to be 232.8 mΩ. The remaining differences are due to the random wound coil bundles in the prototype machine, extra terminal contact resistances, and overly-simplified end-winding geometry in the analytical model.

Machine inductances are also measured under static conditions, using a QuadTech 1730 LCR Digibridge high-performance passive component tester. The rotor is electrically aligned to the d-axis using a low voltage DC-supply, and it is mechanically locked in position before the d-axis inductance is measured. The d-axis inductance is calculated by the analytical model to be 2.22 mH, while experimentally, it is determined as 2.29 mH. Due to the low test current of the measuring equipment, the measured inductance value is expected to be lower than this value, especially when the machine is loaded. This is because soft magnetic material's permeability is low at low excitation, thus reducing the measured inductance. Instead, a better approach is to excite the machine with a variable magnitude AC current source and



(a) (b)

Figure 3.14: Comparison between analytical prediction and experimental values for (a) no-load power loss against speed (b) open-circuit back-electromotive force (rms, phase) against speed.

measure the corresponding input RMS voltage. However, due to a lack of time and suitable equipment in the lab, the more accurate inductance measurement test was not carried out.

For measurements of the machine's fundamental magnetic loss, its rotor shaft is allowed to rotate freely, i.e. it is decoupled from any external loads. A power converter is employed to control the machine's speed up to several speed set-points. At each speed set-point, the input power is measured with a Kinetiq PPA2530 precision power analyser, which has a bandwidth of 2 MHz and watts accuracy of 0.08%. For consistent measurements, the machine is left running at its maximum speed (3000 rpm) for 45 minutes, before the power measurements are taken, consecutively, as speed is stepped down in steps of 300 rpm. This is because bearing friction losses are usually high at first, and as bearing grease heats up to its operating temperature, these friction losses are significantly lowered.

As no load is connected to the machine and its stator current is close to zero, winding losses are negligible. The analytical model loss predictions, therefore, contain only fundamental magnetic losses. However, when machine no-load losses are compared against the analytical values, as shown in Fig. 3.14(a), they are observed to be much larger.

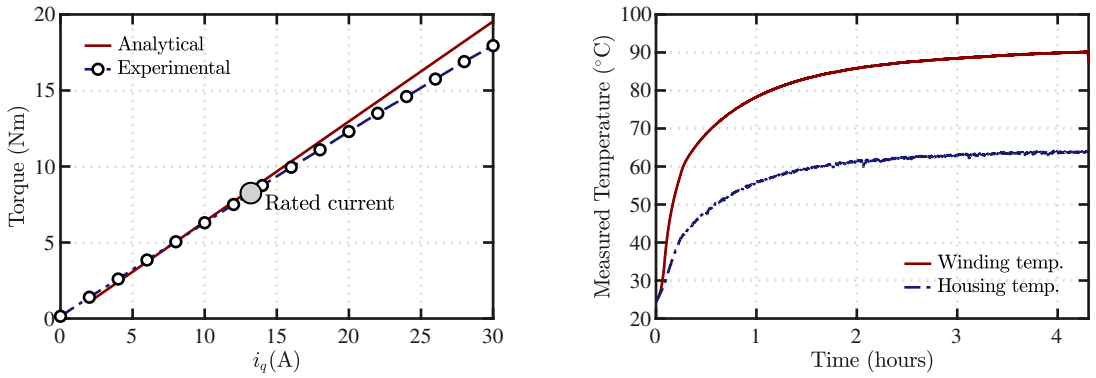
One of the reasons for this deviation is because a significant amount of no-load losses are, contrary to expectations, actually mechanical. A precise modelling of bearing friction and windage losses is complicated, and these losses are typically determined experimentally, using a dummy rotor without magnets. In this thesis, these mechanical losses are estimated using empirical constants and mechanical loss relationships found in [31]:

$$P_{ml} = k_{fric}\omega_{\mathrm{m}} + k_{wind}\omega_{\mathrm{m}}^2 \tag{3.14}$$

where k_{fric} is the friction loss coefficient and k_{wind} is the windage loss coefficient, calculated to be 2×10^{-3} W/rpm and 3.3×10^{-6} W/rpm^2, respectively, while ω_{m} is the mechanical speed in rpm. In Eq. (3.14), the first term represents bearing friction losses, while the second term is for windage losses.

The other reason for the observed deviation in no-load losses is that the analytical magnetic loss calculations employ manufacturer loss density data, obtained from Epstein tests performed on single lamination sheets. As explained by Al-Timimy et al. [105], core material machining process has a significant impact on the assembled machine's iron losses and can cause them to be much larger than losses measured for single lamination sheets. Based on the authors findings, to correct the analytical iron loss estimations, a correction factor $k_{\mathrm{corr,ir}}$= 1.5 can be added to Eq. (3.6) for fundamental magnetic loss calculations [27]. With the mechanical losses and correction factor included, the corrected loss predictions are again compared to the experimental measurements and a much better match is obtained.

For open-circuit and rated-load tests, the prototype machine is coupled to an external load machine, with a high-precision torquemeter installed on the shaft between both machines, as shown in Fig. 3.13. Firstly, the prototype machine's input terminals are disconnected from the power converter, and its BEMFs are measured at different mechanical speeds, controlled by the external load machine. The measuring equipment used is a Picotech TA057 differential oscilloscope voltage



(a) (b)

Figure 3.15: Comparison between analytical prediction and experimental values for (a) torque against i_q current; (b) Plot of machine temperatures against time under rated load conditions.

probe (bandwidth of 25 MHz), and a Yokogawa DLM2024 mixed-signal oscilloscope (bandwidth of 200 MHz). The measurements for the BEMFs match very well with the analytical model, as shown in Fig. 3.14(b).

Next, the prototype machine is reconnected to the power converter and it is operated under current control, as the load machine regulates its speed. At rated speed, the machine torque is measured for different i_q current set-points, and its torque-current relationship is plotted in Fig. 3.15(a). The measurements are shown to match well with the analytical predictions, up to the rated operating point. Beyond this point, the output torque begins to deviate from the analytical predictions, as expected due to magnetic saturations in the machine.

Lastly, to validate the thermal models, type-K thermocouples are employed to measure the winding and stator housing surface temperatures. From non-operating to rated load conditions, the temperature measurements are recorded and plotted against time in Fig. 3.15(b). At steady-state (i.e. defined to be when temperature change is less than 2 °C/hour), recorded temperatures for the stator housing surface and winding temperatures are 59.5 °C and 85 °C, respectively, while analytical predictions are 64.0 °C and 90.2 °C, respectively. This is a very good match, considering the rough approximations for thermal resistances in the LPTN model.

Table 3.4: Comparison of key performances predicted by the analytical model, calculated in finite element, and measured for the prototype machine.

Key performance metrices	**Analytical Model**	**FE Calculations**	**Measured Results**	**Unit**
Phase resistance	202.5	217.4	232.8	mΩ
Inductance	2.22	2.28	2.29*	mH
Rated speed open-circuit BEMF (rms, phase)	48.93	47.96	46.32	V
Rated output torque	8.49	8.41	8.33	Nm

* Less accurate as it was measured using a passive component tester.

A comparison of key performance metrics, predicted by the analytical model, calculated by finite element software, and experimentally measured for the prototype machine, is summarised in Table 3.4. Overall, a reasonably accurate match is obtained for the various aspects of machine performance evaluated, thereby validating the machine modelling approach employed in this work.

3.6 Chapter Summary

This chapter presented a fast and accurate multiphysics model for the SPM machine. To evaluate electromagnetic performance, the model computes the machine's air-gap magnetic field distribution under open-circuit and pure armature-reaction conditions. The field distributions are employed to calculate the BEMF, inductance, flux densities, magnetic losses, and torque. For thermal behaviour analysis, a simplified LPTN model is included, exploiting machine slot symmetries to reduce its number of parameters. The combination of different modelling techniques results in a fast evaluation of the machine performance, taking only an average of 0.03 seconds to run on a normal PC. The model's accuracy is finally verified using FE analysis and

experimental measurements, for a prototype 12-slot 10-pole SPM machine.

The developed model allows for a computationally efficient evaluation of the SPM machine electromagnetic and thermal performance due to its simple structure. Versatility is also a key feature of the model making it easy for it to be combined with the converter model proposed in the following chapter.

Chapter 4

Power Converter Modelling

As well as the machine, the power converter, with its associated cooling system and passive components, also forms a considerable proportion of the motor drive's total weight and volume, and their losses are a significant part of the total system losses. The main challenge in power converter modelling is in accounting for its multiphysics operation and the complex interactions between its components. For example, converter modulation affects semiconductor losses and heat-sink volume, while also producing high-frequency switching harmonics, which need to be managed with filter components.

In Chapter 3, a detailed machine model and its validation was discussed. This chapter follows up by presenting a back-to-back converter model and its validation. The focus is to evaluate converter performance quickly and accurately, and thus, a simple structure of the converter model is considered, as shown in Fig. 4.1.

To begin with, Section 4.1 defines a set of input parameters for the model, and Section 4.2 presents an in-depth modulation and control analysis for the converter in motor drive applications, considering its operation and electrical properties. Next, in Section 4.3, semiconductor loss models and a simple heat-sink sizing model are presented. In Section 4.4, sizing models for the main converter passive components are also proposed. Finally, Section 4.5 presents a time-domain simulation study and the experimental tests carried out to validate the model's accuracy.

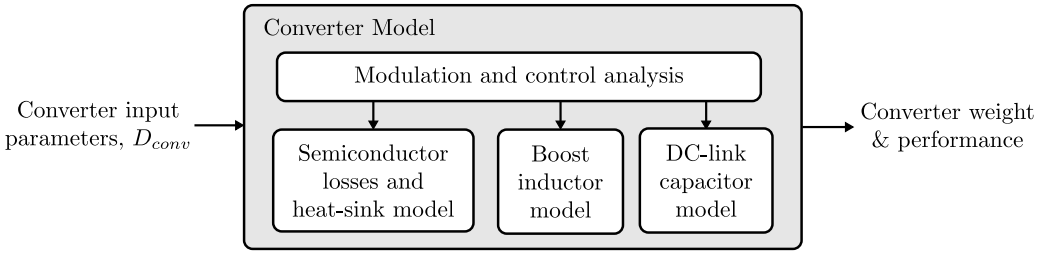


Figure 4.1: Organisation/flowchart of converter model.

4.1 Input Parameter Definitions

For the purposes of converter analysis, it is useful to consider it as a simple model with an input-output form. The main task of the model is to represent the real converter system by considering the coupled impact of different input parameters on its output performance. In this work, the considered set of input parameters for the converter model is:

$$D_{conv} \ni \left\{D_{mat},\ D_{grid},\ D_{mach},\ V_{dc},\ f_{sw}^{(\mathrm{VSI})},\ f_{sw}^{(\mathrm{AFE})},\ C_{dc},\ L_b,\ T_{amb}\right\} \tag{4.1}$$

where D_{mat} is a set of vectors consisting of switching device, cooling system, inductor core material, and capacitor type information, D_{grid} and D_{mach} are sets of grid and motor-related parameters, respectively, V_{dc} is the intermediate DC-link voltage, $f_{sw}^{(\mathrm{VSI})}$ and $f_{sw}^{(\mathrm{AFE})}$ are the switching frequencies of VSI and AFE, respectively, C_{dc} is the DC-link capacitance, L_b is the converter boost inductance, and T_{amb} is the ambient temperature. The grid-related parameters contained in D_{grid} are:

$$D_{grid} \ni \{\hat{v}_g,\ \omega_{ge},\ R_g\} \tag{4.2}$$

where $\hat{v}_g$, ω_{ge}, and R_g are the peak voltage, electrical frequency, and phase resistance of the input grid, respectively. On the other hand, the motor-related parameters

contained in D_{mach} are:

$$D_{mach} \ni \left\{\omega_e,\ \hat{i}_d,\ \hat{i}_q,\ R_{ph},\ L_{ph},\ \hat{\Psi}_d\right\} \tag{4.3}$$

where ω_e, $\hat{i}_d$, $\hat{i}_q$, R_{ph}, L_{ph}, and $\hat{\Psi}_d$ are electrical frequency, peak dq-axis currents, resistance, inductance, and peak d-axis flux linkage of the machine at converter output, respectively. These input parameters provide the required information for further evaluation of the converter's performance.

4.2 Modulation and Control Analysis

This section considers the modulation and control strategies that are typically employed for two-level back-to-back voltage source converters.

4.2.1 Converter Modulation

Converter modulation is the process of switching semiconductor devices within a power converter from one state to another, and it significantly affects the converter operation, electrical properties, and semiconductor losses [106]. In this section, a mathematical model for the fixed switching frequency modulation of two-level voltage source converters is first discussed, followed by an analysis of the currents passing through different components.

For the two-level converter shown in Fig. 4.2(a), a switching function j can be defined for each phase leg. When j_i is 'p', the high-side switch of phase leg i is turned on, while its complementary low-side switch is turned off. When j_i is 'n', the opposite is true. A combination of switching functions for all three phases is known as the converter switching state k. For example, when switches S_{pA}, S_{nB}, and S_{nC} are turned on, k is (pnn).

Two-level converters with three phases have $2^3 = 8$ number of switching states and they can be plotted as stationary vectors on a complex plane. This plot is also

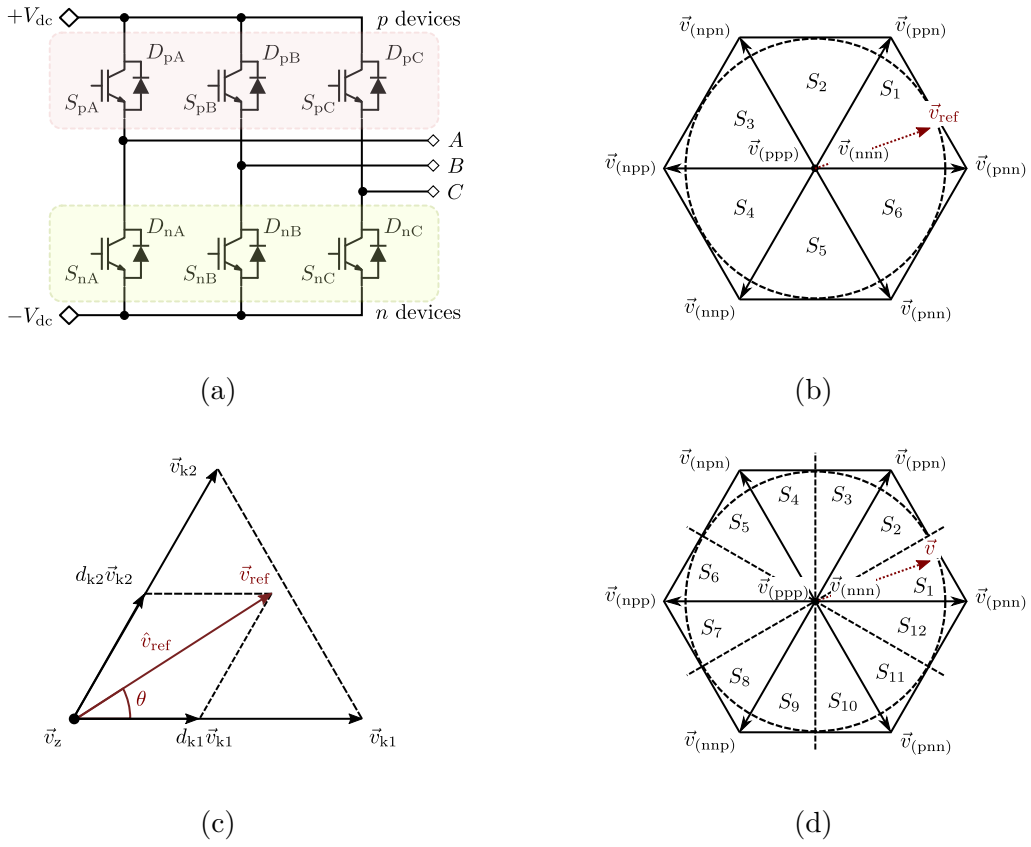


Figure 4.2: (a) Circuit diagram of a two-level voltage source converter. (b) Standard space vector diagram with 6 sectors and 8 switching states. (c) Magnified view for Sector 1 of space vector diagram. (d) Modified space vector diagram with 12 sectors for the DPWM1 modulation.

known as the *space-vector* diagram, as shown in Fig. 4.2(b). The stationary vectors can be written, in a complex form, as:

$$\vec{v}_k = \frac{2}{3} V_{dc} \left[\left(s_a - \frac{1}{2} \right) + \left(s_b - \frac{1}{2} \right) e^{j\frac{2\pi}{3}} + \left(s_c - \frac{1}{2} \right) e^{j\frac{4\pi}{3}} \right] \tag{4.4}$$

where V_{dc} is the DC-link voltage, s_i is '1' when j_i is 'p', and '0' when j_i is 'n'. Based on this equation, the switching states $\vec{v}_{\text{ppp}}$ and $\vec{v}_{\text{nnn}}$ have zero magnitude, and hence they are known as zero vectors, while the others have a magnitude of $2/3V_{dc}$ and are known as active vectors.

At any point in time, an arbitrary target output voltage vector $\vec{v}_{ref}$ can be formed

by the summation or averaging of at least two active vectors within a switching time period T_{sw}. As shown in Fig. 4.2(c), the geometric summation of $\vec{v}_{ref}$ is:

$$\vec{v}_{ref} = \frac{1}{T_{sw}} \int_0^{T_{sw}} \vec{v}_k \mathrm{d}t = d_{k1}\vec{v}_{k1} + d_{k2}\vec{v}_{k2} + d_z\vec{v}_z \tag{4.5}$$

where d_{k1}, d_{k2}, and d_z are the relative turn-on times of active vectors $\vec{v}_{k1}$, $\vec{v}_{k2}$, and zero vectors $\vec{v}_z$, respectively. The required relative turn-on times for $\hat{v}_{\mathrm{ref}}$ are:

$$d_{k1}(\theta) = \frac{\sqrt{3}}{2} M \cos\left(\theta + \frac{\pi}{6}\right) = \frac{\sqrt{3}\ \hat{v}_{\mathrm{ref}}}{V_{\mathrm{dc}}} \cos\left(\theta + \frac{\pi}{6}\right) \tag{4.6}$$

$$d_{k2}(\theta) = \frac{\sqrt{3}}{2} M \sin(\theta) = \frac{\sqrt{3}\ \hat{v}_{\mathrm{ref}}}{V_{\mathrm{dc}}} \sin(\theta) \tag{4.7}$$

$$d_z(\theta) = 1 - d_{k1}(\theta) - d_{k2}(\theta) \tag{4.8}$$

where M is the modulation index to describe the relationship between $\hat{v}_{\mathrm{ref}}$ and V_{dc}, and θ is the instantaneous reference voltage vector angle.

After calculating the relative turn-on times for the switching state vectors, the sequence, in which they are realised within each switching period, is determined by the modulation scheme. Standard converter modulation schemes are mostly continuous, such as sinusoidal PWM and symmetrical Space Vector Modulation (SVM), or discontinuous, such as 60°-Clamping Discontinuous Pulse-Width Modulation (DPWM1). This work considers symmetrical SVM, due to its simple implementation, and DPWM1, due to its low switching losses.

Symmetrical SVM is based on the standard space vector diagram, where six sectors are defined based on two active vectors nearest to $\vec{v}_{ref}$, as it rotates around. With this modulation method, in each sector, the two active vectors and both zero vectors are utilised to output $\vec{v}_{ref}$ in the switching period. For example, in Sector 1, the two nearest active vectors are (pnn) and (ppn) and the determined switching states sequence is (nnn)-(pnn)-(ppn)-(ppp)-(ppn)-(pnn)-(nnn), involving six commutations per switching period.

For DPWM1, on the other hand, twelve sectors are defined in the space vector

diagram, by the two active vectors nearest to the $\vec{v}_{ref}$, and zero vectors, which alternate every $\pi/3$ interval. The twelve sectors space vector diagram can be seen in Fig. 4.2(d). The main difference between symmetrical SVM and DPWM1 is that, in each sector, the latter utilises the two active vectors and only one zero vector to realise $\vec{v}_{ref}$ in the switching period. For the same Sector 1 example, the DPWM1 switching states sequence is (pnn)-(ppn)-(ppp)-(ppn)-(pnn), where switch S_{pA} is effectively clamped. The number of commutations per switching period is therefore reduced from six to four. Further, if input or load power factor is close to unity, clamping periods coincide with when the switches conduct maximum current. The lower number of commutations per switching period and clamping of devices at maximum currents result in a significant reduction of switching losses.

In practical implementations of the modulation scheme on a digital microcontroller unit (MCU), duty-cycle phase references $d_{ph,ref}$, averaged over each switching period, are calculated and directly employed to modulate the phase leg switches appropriately. Analytical expressions for $d_{ph,ref}$ are provided in Section B.1.

For example, Fig. 4.3 shows the duty-cycle phase reference, phase voltage, and phase current waveforms of a VSI powering a resistive-inductive (RL) load, with unity modulation index and unity power factor operation.

Device Average and RMS Currents

Considering an alternating duty-cycle and phase current, device average and rms squared currents ($I_{S/D,avg}$ and $I^2_{S/D,rms}$), calculated over a fundamental period, are needed to determine the semiconductor conduction losses. The average current considers the DC-component of the current whilst rms current takes into account its time-varying function.

$$I_{S/D,avg} = \frac{1}{2\pi}\int_0^{2\pi} i_{\mathrm{S/D}}(\theta)\mathrm{d}\theta \tag{4.9}$$

$$I^2_{S/D,rms} = \frac{1}{2\pi}\int_0^{2\pi} i_{\mathrm{S/D}}(\theta)^2\mathrm{d}\theta \tag{4.10}$$

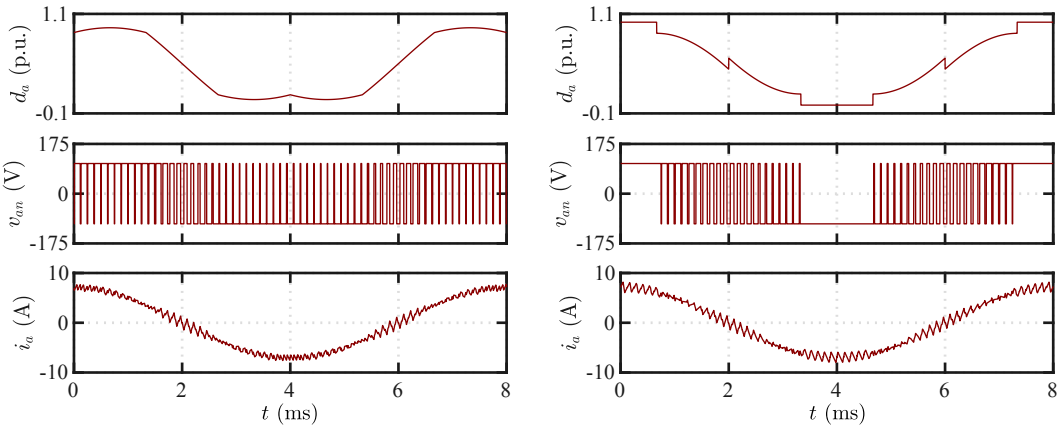


Figure 4.3: VSI duty-cycle phase reference (top), phase voltage (middle), and phase current (bottom) under (a) Symmetrical SVM (b) DPWM1 modulation schemes.

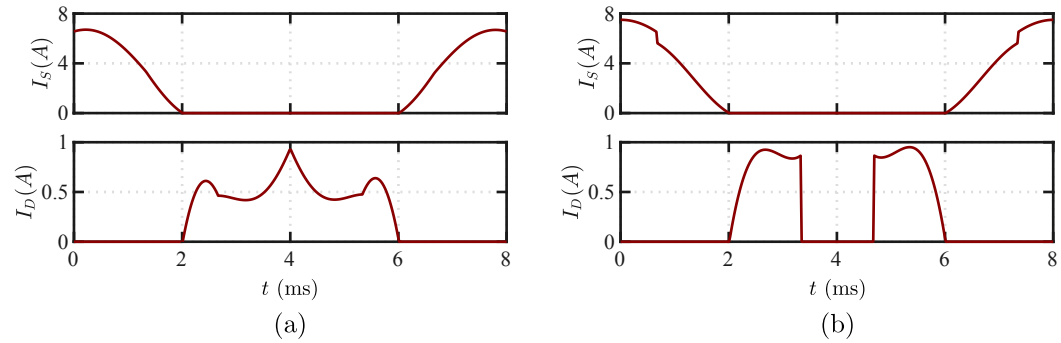


Figure 4.4: VSI device current averaged over each switching period for upper-leg IGBT (top) and upper-leg diode (bottom) under (a) Symmetrical SVM (b) DPWM1 modulation schemes.

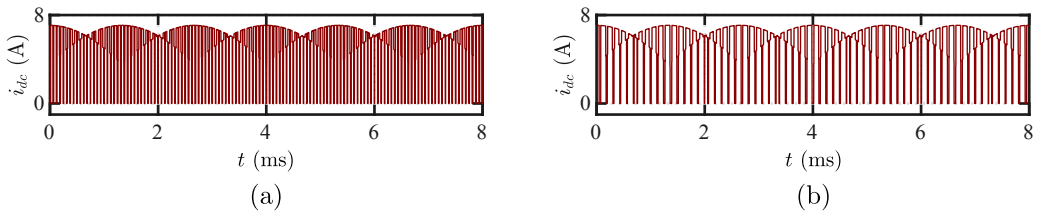


Figure 4.5: VSI DC-link current under (a) Symmetrical SVM (b) DPWM1 modulation schemes.

S where $i_{\mathrm{S/D}}$ is the device current averaged over each switching period, which can be calculated as:

$$i_{S/D}(\theta) = d_{ph,ref}(\theta) \cdot \hat{i}_{ph}(\theta) \tag{4.11}$$

where $\hat{i}_{ph}$ is the instantaneous phase current. An example of $i_{S/D}$ passing through upper leg devices of phase A for the same VSI-RL load operation is shown in Fig. 4.4. Closed-form analytical expressions for $I_{S/D,avg}$ and $I^2_{S/D,rms}$ can be derived, as presented in Section B.2 for VSI and AFE operations.

Maximum Input Current Ripple

When connecting the AFE to grid, boost inductors are needed at its input to attenuate switching ripples in the current waveform, to ensure power quality compliance with industry standards, such as the DO-160E electrical specifications for aerospace applications [39]. To meet further regulatory standards regarding high frequency conducted Electro-Magnetic Interference (EMI), an additional LC-filter is typically appended to the boost inductors, forming a cascaded second-order filter for high-bandwidth filtering. The LC-filter has to be designed carefully, to avoid resonances and instability issues [107]. In this work, only boost inductors are considered at the converter input.

Switching ripples in the currents are caused by discrete changes in the voltage drop across the boost inductors, as a result of the converter modulation. At any point in time, the peak-to-peak current ripple Δi_{pp} can be calculated as:

$$\Delta i_{\mathrm{pp}} = \frac{1}{L_b} \int_0^{t_{on}} V_L \mathrm{d}t \tag{4.12}$$

where L_b is the boost inductance, and V_L is the inductor voltage drop that is applied for a continuous 'turn-on' period of t_{on}. As V_L switches between $+V_{dc}/2$ and $-V_{dc}/2$ for a varying t_{on}, Δi_{pp} also varies significantly across the fundamental period.

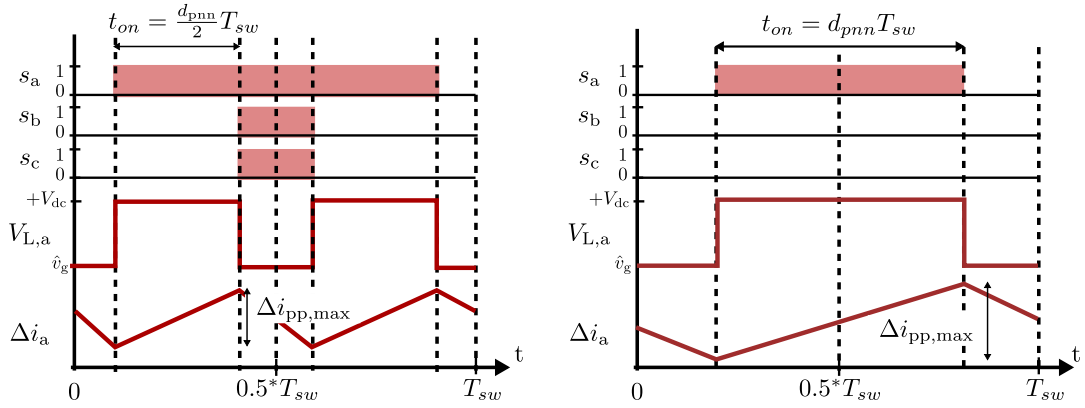


Figure 4.6: Current ripple and modulation analysis at $\theta_v = 0°$ for the (a) symmetrical SVM and (b) DPWM1 modulation scheme.

To simplify the analysis, phase A peak-to-peak current ripple at reference voltage vector angle $\theta = 0°$ is considered to be the maximum peak-to-peak current ripple $\Delta i_{\text{pp,max}}$. This simplification is justified, as for unity input power factor operation, $\theta = 0°$ corresponds to the phase A peak fundamental current, when inductance drop from its nominal value is expected to be most significant, especially for powder core inductors with soft magnetic saturation characteristics, leading to current ripples being largest at this time instant.

When $\theta = 0°$, the voltage drop across phase A inductor is

$$V_{L,a}(0°) = \hat{v}_{\text{pnn}} - \hat{v}_s = \frac{2}{3} V_{dc} - \hat{v}_s \tag{4.13}$$

where $\hat{v}_{\text{pnn}}$ is the voltage magnitude of switching state (pnn), and $\hat{v}_s$ is the peak AC-grid voltage. For symmetrical SVM, $V_{L,a}$ is applied for a continuous time period of $t_{on} = (d_{\text{pnn}}/2)T_{sw}$, while for DPWM1, it is $t_{on} = d_{\text{pnn}} T_{sw}$, due to their modulation sequences, as illustrated in Fig. 4.6.

DC-link Capacitor RMS Current

It is important to evaluate the DC-link capacitor rms current, for appropriate thermal sizing of the component. Figure 4.5 shows an example of the converter DC-link current for a VSI-RL load operation. Using the analytical method proposed by Kolar et al. [108], average and rms value of DC-link current over each fundamental period I_{dc} is found as:

$$I_{\text{dc,avg}} = \frac{3\sqrt{2}}{4} i_{ph} M \cos(\phi) \tag{4.14}$$

$$I_{\text{dc,rms}} = i_{ph} \sqrt{\frac{2\sqrt{3}}{\pi} M \left(\frac{1}{4} + \cos^2(\phi)\right)} \tag{4.15}$$

where i_{ph} is the rms phase current, and ϕ is the power factor angle. The DC-link capacitor rms current $I_{\text{c,rms}}$ is then calculated as the squared difference of $I_{\text{dc,rms}}$ and $I_{\text{dc,avg}}$, as:

$$I_{\text{c,rms}} = \sqrt{I_{\text{dc,rms}}^2 - I_{\text{dc,avg}}^2} = i_{ph} \sqrt{2M \left[\frac{\sqrt{3}}{4\pi} + \cos^2(\phi)(\frac{\sqrt{3}}{\pi} - \frac{9}{16}M)\right]} \tag{4.16}$$

The above calculations assume a sinusoidal current at the AC-side and a constant voltage at the DC-link, neglecting high-frequency switching harmonic components. They are, therefore, applicable to all modulation schemes, as their fundamental current and modulation index components are the same.

For the back-to-back converter considered in this work, 'worst-case' rms current stress on the DC-link capacitor $I_{\text{c,rms}}^{(worst)}$ is assumed to be an average of the rms currents from both converters:

$$I_{\text{c,rms}}^{(worst)} = \frac{I_{\text{c,rms}}^{(VSI)} + I_{\text{c,rms}}^{(AFE)}}{2} \tag{4.17}$$

This approach is conservative, as with appropriate synchronisation, the current ripples from the converters can be made to cancel out each other [109].

4.2.2 Control Strategies

Besides modulation, selected motor drive control strategies have a significant impact on converter performance. This section describes the control analysis of a back-to-back converter in motor drive applications. The simplicity and robustness of the back-to-back converter control, due to its two-stage implementation, makes it an attractive topology, as compared to direct AC-AC power conversion topologies.

VSI Machine Control

The VSI controller provides the converter modulators with appropriate target output voltage vectors, to meet the machine output torque and speed demand. For field-oriented vector control, the sinusoidal *abc* current and voltage components are transformed into constant *dq*-components in a rotating frame, to enable zero steady-state error tracking of the current references with simple Proportional-Integral (PI) compensators. Assuming that sampling, filtering, and PWM switching frequencies are at least an order of magnitude faster than the closed-loop current control bandwidth, only fundamental current and voltage components need to be considered in the controller design. For non-salient SPM machine control, the system is first modelled, in *dq*-form, as:

$$M_d \frac{V_{dc}}{2} = v_{sd} = R_s i_d + L_{ph} \frac{\mathrm{d}i_d}{\mathrm{d}t} - p\omega_r L_{ph} i_q \tag{4.18}$$

$$M_q \frac{V_{dc}}{2} = v_{sq} = R_s i_q + L_{ph} \frac{\mathrm{d}i_q}{\mathrm{d}t} + p\omega_r L_{ph} i_d + p\omega_r \Psi_d \tag{4.19}$$

$$T_e = \frac{3p}{2} i_q \Psi_d \tag{4.20}$$

$$\frac{\mathrm{d}\omega_r}{\mathrm{d}t} = \frac{1}{J}(T_e - T_{load}) \tag{4.21}$$

where R_s is the machine phase resistance, L_{ph} is the phase inductance, p is the number of pole pairs, Ψ_d is the d-axis flux linkage, J is the combined shaft inertia, T_{load} is the load torque, T_e is the machine torque, and ω_r is the mechanical speed. From the machine's point of view, M_d and M_q are considered as inputs, while i_d, i_q,

T_e, and ω_r are outputs.

In a cascaded control scheme, the overall system is treated as a cascaded combination of independent sub-plants, with the inner sub-plant closed-loop control bandwidths being at least an order of magnitude faster than the outer sub-plant open-loop time constant. For VSI control, machine current is controlled in the inner loop, and its speed in the outer loop. To ensure that converter voltage limits are not exceeded, a field-weakening strategy is required and, in this work, a 'direct current' field-weakening method is employed [110]. To prevent a *windup* effect caused by the integrator action of the controller when its output is limited, anti-windup controllers are also in place [111]. The overall VSI control scheme is shown in Fig. 4.7.

The q-axis current reference $i_q^{(\mathrm{ref})}$ is provided by the outer speed control loop, while d-axis current reference $i_d^{(\mathrm{ref})}$ is fed from the field-weakening controller and it is only non-zero when $|M|$ exceeds $M^{(\mathrm{lim})}$. When $i_d^{(\mathrm{ref})}$ is non-zero, a dynamically calculated limit, based on maximum allowable current $i^{(\mathrm{lim})}$, is placed on $i_q^{(\mathrm{ref})}$.

By implementing feed-forward terms, cross-coupling effects between the d- and q-axis components are removed, allowing the machine inner current sub-plants, from Eqs. (4.18) and (4.19), to be simplified into a first-order linear plant as:

$$\frac{i_{dq}}{M_{dq}} = \left(\frac{2}{V_{dc}}\right) \frac{1}{(L_{ph}/R_s) \ \cdot \ s + 1} = \left(\frac{2}{V_{dc}}\right) \frac{1}{\tau_i \ \cdot \ s + 1} \tag{4.22}$$

where τ_i is the current sub-plant time constant, which dictates its responsiveness. The current controller PI parameters are manually tuned based on its open-loop frequency response, for a desired phase margin at a specified cut-off frequency. An example of the inner current control $i_q/i_q^{(ref)}$ open and closed-loop frequency response is shown in Fig. 4.8(a).

Machine outer speed sub-plant time constant τ_ω is dictated by its rotor mechanical inertia. If inner current control dynamics are at least an order of magnitude faster than τ_ω, they can be ignored in the outer loop control design, and the speed sub-plant

can also be simplified into a first-order linear plant, as:

$$\frac{\omega_r}{i_q} = \frac{1}{(2J/3p\Psi_d) \cdot s} = \frac{1}{\tau_\omega \cdot s} \tag{4.23}$$

Figure 4.8(b) shows an example of the outer speed control $\omega_r/\omega_r^{(ref)}$ open and closed-loop frequency response.

AFE DC-link Voltage and Unity Power Factor Control

At the input stage, the AFE controller regulates the power factor at grid terminals, while maintaining a constant voltage at the converter DC-link. For controller design, the grid is assumed to be infinitely stiff, outputing a balanced, sinusoidal, and fixed frequency three-phase AC voltage, while the load at the DC-side of the converter is represented by a simple resistance. In a back-to-back converter, the AFE output impedance has to be lower than VSI input impedance, to ensure a stable operation [112]. Similar to the VSI control, a rotating-frame approach can also be implemented for the AFE, and the system can be written, in dq-form, as:

$$M_d \frac{V_{dc}}{2} = v_{td} = R_b i_d + L_b \frac{\mathrm{d}i_d}{\mathrm{d}t} - \omega_{ge} L_b i_q + v_{sd} \tag{4.24}$$

$$M_q \frac{V_{dc}}{2} = v_{tq} = R_b i_d + L_b \frac{\mathrm{d}i_q}{\mathrm{d}t} + \omega_{ge} L_b i_d + v_{sq} \tag{4.25}$$

$$\frac{3}{4}\left(M_d i_d + M_q i_q\right) = I_{dc} = -\frac{V_{dc}}{R_{dc}} - C_{dc}\frac{\mathrm{d}V_{dc}}{\mathrm{d}t} \tag{4.26}$$

where L_b is the boost inductance, R_b is the boost inductors' resistance, C_{dc} is the DC-link capacitance, and R_{dc} is the DC-link load resistance.

For a cascaded control, the AFE input current is controlled in the inner loop, and its DC-link voltage in the outer loop. To synchronise the AFE controllers to the grid, a phase-locked loop (PLL) is employed to track the rotating reference angle, which is controlled such that the q-axis voltage component V_{sq} is kept at zero [113]. An extra power control stage is also included to manage the real and reactive power exchange between the converter and grid. Based on power reference signals from the

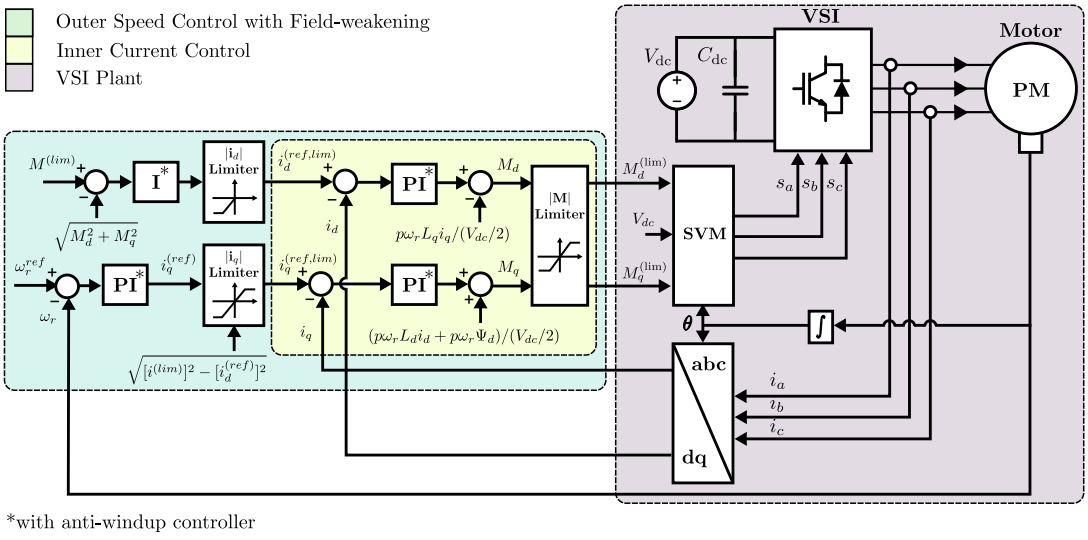


Figure 4.7: Structure of VSI control scheme, with inner current control and outer speed control with field-weakening.

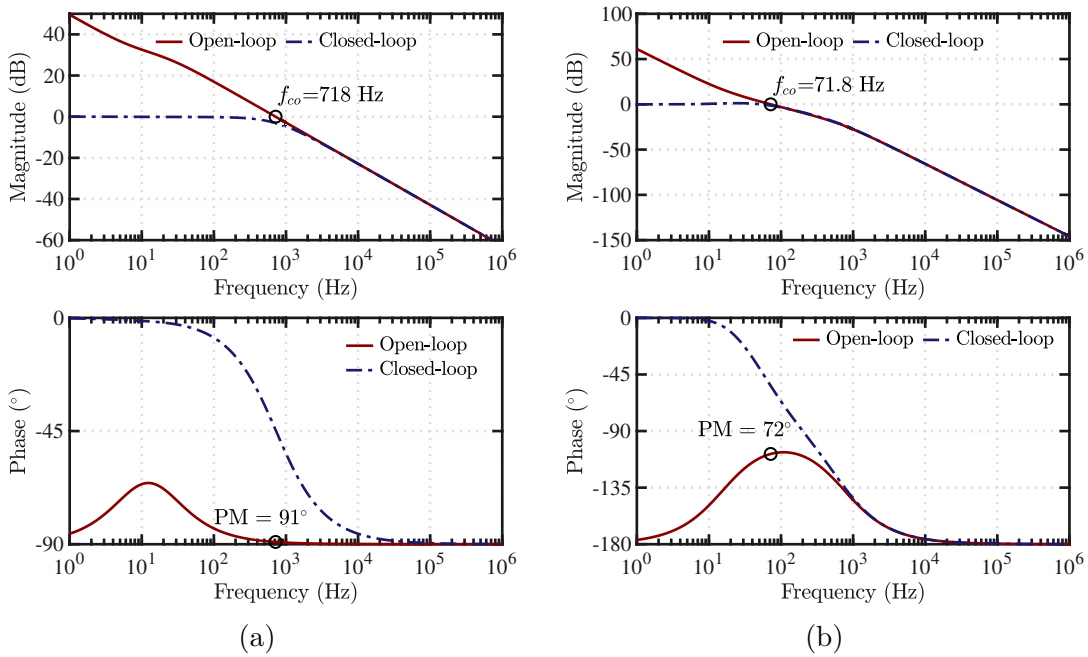


Figure 4.8: Examples of VSI open and closed-loop frequency response characteristics: (a) inner q-axis current control $i_q/i_q^{(\mathrm{ref})}$ (b) outer speed control $\omega_r/\omega_r^{(\mathrm{ref})}$.

outer loop controller, current references $i_d^{(\text{ref})}$ and $i_q^{(\text{ref})}$ are calculated and fed into the inner current controller. As V_{sq} is zero at steady-state, only the d-axis voltage component V_{sd} is used to calculate the current references, as:

$$i_d^{(\text{ref})} = \frac{2}{3V_{sd}} P^{(\text{ref})} \tag{4.27}$$

$$i_q^{(\text{ref})} = -\frac{2}{3V_{sd}} Q^{(\text{ref})} \tag{4.28}$$

where $P^{(\text{ref})}$ and $Q^{(\text{ref})}$ are the real and reactive power reference signals, respectively. For unity power factor operation at the grid terminal, $Q_{(\text{ref})}$ is typically set to zero. The overall AFE control scheme is shown in Fig. 4.9.

It is important to consider DC-link voltage variations in the AFE current controller design, to ensure its stable operation. By linearising the AFE model about a steady-state operating point, the following small-signal model is derived, in state-space form, as:

$$\frac{\mathrm{d}}{\mathrm{d}t}\begin{bmatrix} \tilde{i}_d \\ \tilde{i}_q \\ \tilde{v}_{dc} \end{bmatrix} = \begin{bmatrix} -\frac{R_b}{L_b} & \omega_{ge} & \frac{M_d}{2L_b} \\ -\omega_{ge} & -\frac{R_b}{L_b} & \frac{M_q}{2L_b} \\ -\frac{3}{4}\left(\frac{M_d}{C_{dc}}\right) & -\frac{3}{4}\left(\frac{M_q}{C_{dc}}\right) & -\frac{1}{R_{dc}C_{dc}} \end{bmatrix} \begin{bmatrix} \tilde{i}_d \\ \tilde{i}_q \\ \tilde{v}_{dc} \end{bmatrix} + \begin{bmatrix} \frac{V_{dc}}{2L_b} & 0 \\ 0 & \frac{V_{dc}}{2L_b} \\ -\frac{3}{4}\left(\frac{I_d}{C_{dc}}\right) & -\frac{3}{4}\left(\frac{I_q}{C_{dc}}\right) \end{bmatrix} \begin{bmatrix} \tilde{m}_d \\ \tilde{m}_q \end{bmatrix} + \begin{bmatrix} -\frac{1}{L_b} & 0 \\ 0 & -\frac{1}{L_b} \\ 0 & 0 \end{bmatrix} \begin{bmatrix} \tilde{v}_{sd} \\ \tilde{v}_{sq} \end{bmatrix} \tag{4.29}$$

where I_{dq}, M_{dq}, and V_{dc} are the steady-state current, modulation index, and DC-link voltage parameters, while ($\tilde{\cdot}$) represent their small-signal variations. With decoupling terms, the cross-coupling components between the d and q-axis can be

removed, and Eq. (4.29) can be rewritten as:

$$\frac{\mathrm{d}}{\mathrm{d}t}\begin{bmatrix}\tilde{i}_d\\ \tilde{i}_q\\ \tilde{v}_{dc}\end{bmatrix} = \begin{bmatrix}-\frac{R_b}{L_b} & 0 & \frac{M_d}{2L_b}\\ 0 & -\frac{R_b}{L_b} & \frac{M_q}{2L_b}\\ -\frac{3}{4}\left(\frac{M_d}{C_{dc}}\right) & -\frac{3}{4}\left(\frac{M_q}{C_{dc}}\right) & -\frac{1}{R_{dc}C_{dc}}\end{bmatrix}\begin{bmatrix}\tilde{i}_d\\ \tilde{i}_q\\ \tilde{v}_{dc}\end{bmatrix} + \begin{bmatrix}\frac{V_{dc}}{2L_b} & 0\\ 0 & \frac{V_{dc}}{2L_b}\\ -\frac{3}{4}\left(\frac{I_d}{C_{dc}}\right) & -\frac{3}{4}\left(\frac{I_q}{C_{dc}}\right)\end{bmatrix}\begin{bmatrix}\tilde{m}_d\\ \tilde{m}_q\end{bmatrix} + \begin{bmatrix}-\frac{1}{L_b} & 0\\ 0 & -\frac{1}{L_b}\\ 0 & 0\end{bmatrix}\begin{bmatrix}\tilde{v}_{sd}\\ \tilde{v}_{sq}\end{bmatrix} \quad (4.30)$$

Similar to the VSI, the AFE current controller PI parameters are also manually tuned, using the open-loop frequency response, to obtain a desired phase margin at a specified cut-off frequency. An example of the inner current control $i_d/i_d^{(ref)}$ open and closed-loop frequency response is shown in Fig. 4.10(a).

As mentioned previously, the DC-link voltage controller provides the power control stage with the real power reference signal to regulate the DC-link voltage. The control strategy is based on the principle of power balance [114] and the DC-side power balance dictates that:

$$P_{ext} - P_{dc} = \frac{\mathrm{d}E_c}{\mathrm{d}t} = \frac{\mathrm{d}}{\mathrm{d}t}\left[\frac{1}{2}(C_{dc}V_{dc}^2)\right] \quad \rightarrow \quad \frac{\mathrm{d}}{\mathrm{d}t}V_{dc}^2 = \frac{2}{C_{dc}}\left(P_{ext} - P_{dc}\right) \quad (4.31)$$

where P_{ext} and P_{dc} are the external load and converter DC-link power, respectively, and E_c is the instantaneous energy of the DC-link capacitor.

If V_{dc}^2 is regulated and a feed-forward power signal is used for P_{ext}, the DC-link voltage sub-plant can be simplified into a first-order linear system, as:

$$\frac{V_{dc}^2}{P_{dc}} = \frac{1}{(C_{dc}/2)\,s} = \frac{1}{\tau_v s} \quad (4.32)$$

where τ_v is the DC-link voltage sub-plant time constant. Figure 4.10(b) shows an example of the outer DC-link voltage control $V_{dc}^2/[V_{dc}^{(ref)}]^2$ open and closed-loop frequency response. It is important to note that this simplified model does not

account for the instantaneous power in the boost inductors and, thus, can result in poor dynamic performance [113]. To overcome this, advanced control methods are usually implemented but they are not considered in this work as the system is not sized here for transient operations.

DC-link Voltage Overshoot

In a back-to-back converter, the DC-link capacitor acts as an energy damper that absorbs and supplies power during output load transients. During a worst-case load transient (defined as an externally-triggered step removal of the rated output load), the d-axis current reference $i_d^{(\mathrm{ref})}$ of the AFE controller reacts almost immediately, owing to the implemented feed-forward power signal. This fast response in $i_d^{(\mathrm{ref})}$ saturates the AFE current controller output for some time, during which energy stored in the boost inductors continues to flow into the converter, causing the DC-link voltage to rise (or 'overshoot').

During the short period of time when the AFE current controller output is saturated, the boost inductors and DC-link capacitor act like an uncontrolled, second-order LC-circuit, as illustrated in Fig. 4.11, and the maximum DC-link voltage overshoot $V_{dc,max}$ is calculated as:

$$V_{dc,max} = \sqrt{(V_{dc} - \sqrt{3}\hat{v}_{sd})^2 + \frac{2L_b}{3C_{dc}}\left(\frac{P_0}{\hat{v}_{sd}}\right)^2} + \sqrt{3}\hat{v}_{sd} \tag{4.33}$$

where $\hat{v}_{sd}$ is peak grid-side d-axis voltage and P_0 is the output power delivered to load just before the transient. It is important to note that this method does not account for any delays, due to sampling and PWM dead-times. In practice, $V_{dc,max}$ is expected to be slightly larger than the calculated value using equation Eq. (4.33).

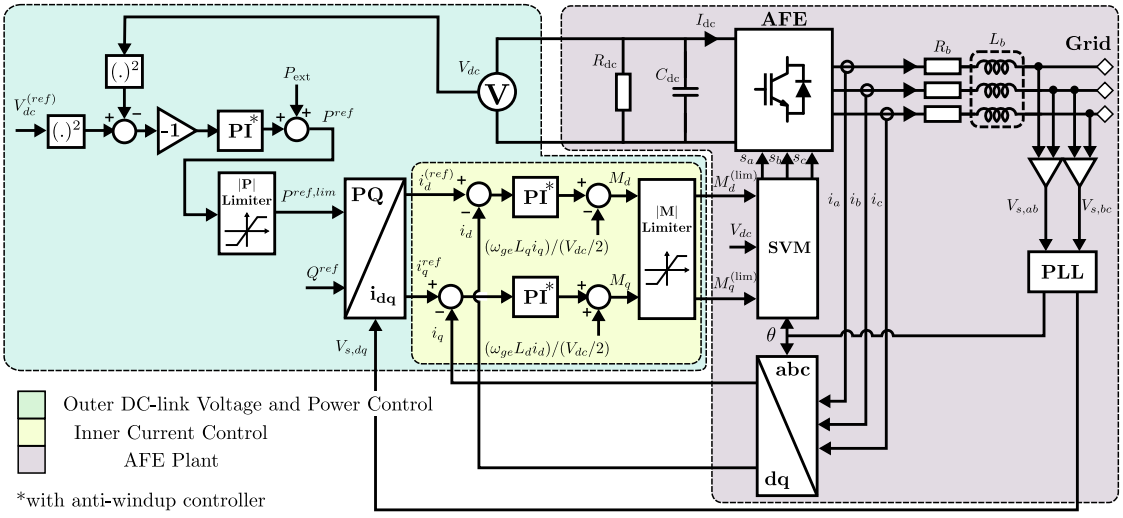


Figure 4.9: Structure of AFE control scheme, with inner current control and outer DC-link voltage control.

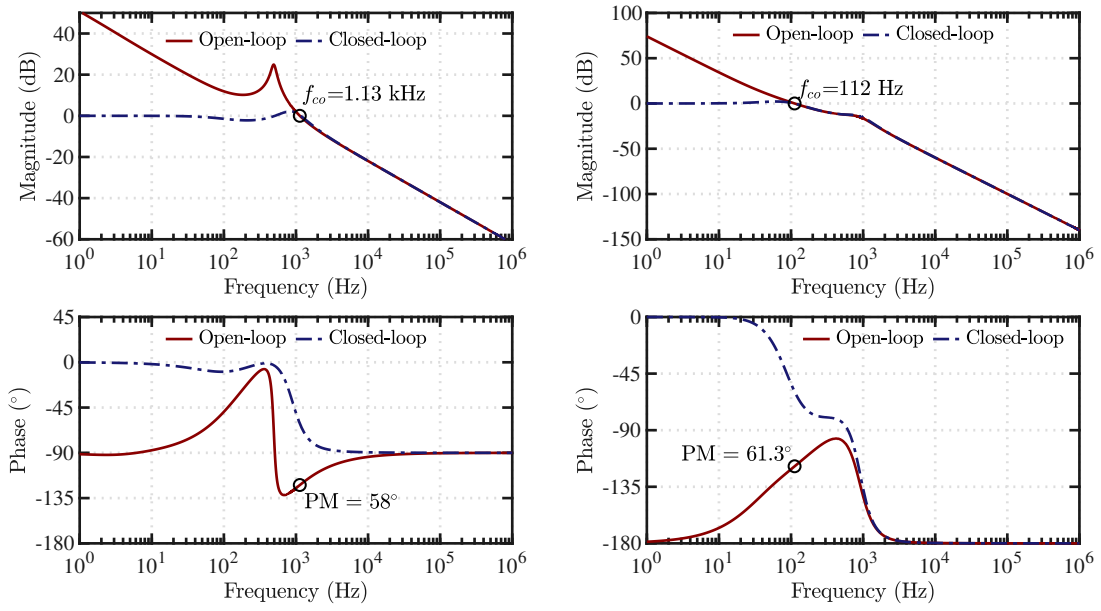


Figure 4.10: Examples of AFE open and closed-loop frequency response characteristics: (a) inner d-axis current control $i_d/i_d^{(\mathrm{ref})}$ (b) outer DC-link voltage control $V_{dc}^2/[V_{dc}^{(ref)}]^2$ with simplified DC-link plant.

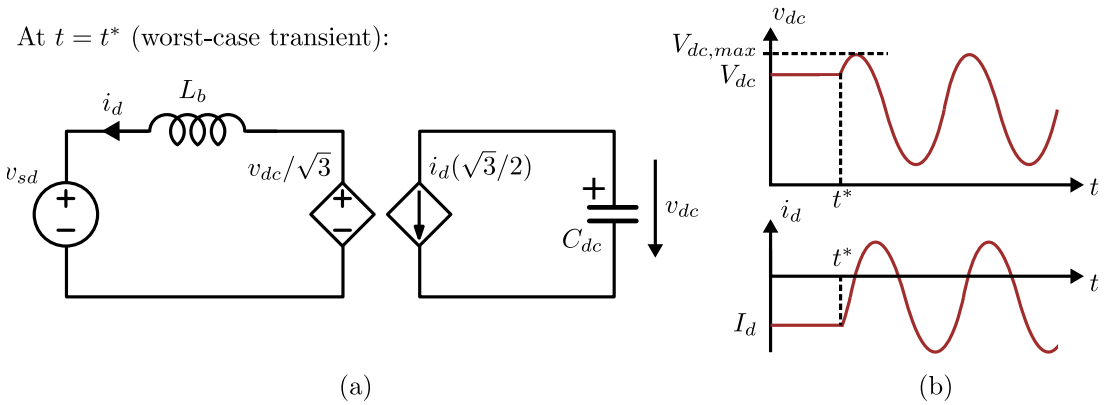


Figure 4.11: (a) Uncontrolled second-order LC-circuit formed by the boost inductors and DC-link capacitor, along with (a) corresponding voltage and current responses.

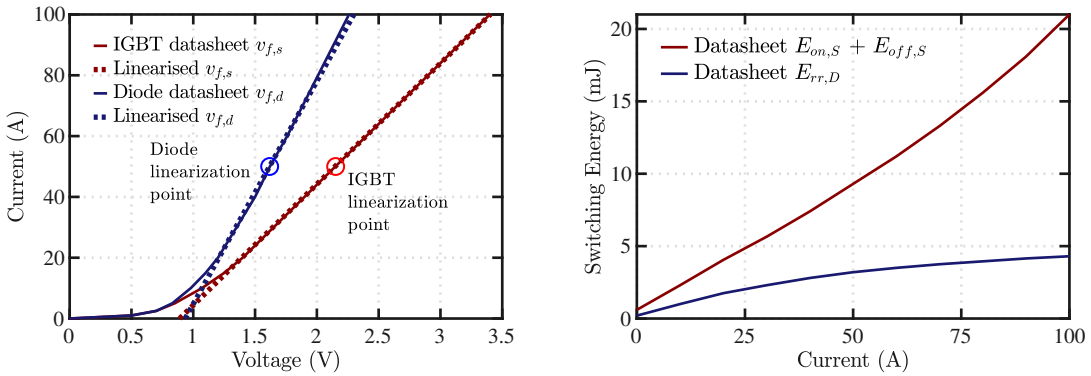
.

4.3 Semiconductor Losses and Heat-sink Model

In most motor drive applications, semiconductor switching devices produce the largest portion of losses in the converter, and an adequate cooling system is needed to dissipate these losses and avoid overheating [115]. This section first presents an analytical model to predict semiconductor losses, followed by descriptions of a simple heat-sink sizing model.

4.3.1 Semiconductor Losses

Despite increasing research attention towards silicon carbide Metal Oxide Semiconductor Field Effect Transistors (MOSFET), silicon Insulated Gate Bipolar Transistors (IGBT) remains the most popular device choice for low voltage (up to 1200 V) motor drive applications, mainly because of its cost and availability (as of 2018 [116]). The non-punch through concept with field-stop layer and trench-gate structure of Infineon IGBT4 devices enables higher current densities, lower conduction and switching losses, and higher breakdown voltages to be achieved, as compared to planar gate structures. For the mentioned reasons, this work considers Infineon IGBT4-T4 chips and EmCon4 diodes as the reference device technology.



(a) (b)

Figure 4.12: Infineon FS50R12KT4B15 power module device characteristics with V_{dc}=600 V and T_j=125°C: (a) on-state voltage drop (b) switching energies.

Semiconductor losses are typically divided into conduction and switching losses. Conduction losses occur during device on-state and are a function of its on-state resistance, while switching losses occur during device on-off switching transitions and are due to its parastic capacitance and inductance. Manufacturers typically provide device loss characteristics in their datasheets. For example, Fig. 4.12(a) shows the IGBT and diode on-state conduction characteristics for the Infineon FS50R12KT4B15 power module at junction temperature $T_j = 125°$. To model the device on-state characteristics, a linearisation is performed about its operating current, giving an approximate forward voltage drop V_f and on-state resistance R_{on} parameter. Thus, device on-state voltage drop is modelled as:

$$v_{f,S/D}(i) = V_{f,S/D} + R_{on,S/D} \cdot i \tag{4.34}$$

V_f and R_{on} parameters then allow device conduction losses, averaged over each fundamental period, to be calculated as:

$$P_{cond,S/D} = V_{f,S/D} \cdot I_{S/D,avg} + R_{on,S/D} \cdot I^2_{S/D,rms} \tag{4.35}$$

where $I_{S/D,avg}$ and $I^2_{S/D,rms}$ are obtained previously in Eq. (4.9).

Switching loss is the energy dissipated when the device voltage and current overlap during switching transitions. For IGBTs, both turn-on and turn-off energies ($E_{on,S}$ and $E_{off,S}$) are significant, but for diodes, turn-on energy is negligible and only turn-off energy $E_{rr,D}$ needs to be considered [117].

For the same junction temperature, the dissipated energies are a function of device current and blocking voltage. Their current dependency is usually provided in the manufacturers datasheet, as shown in Fig. 4.12(b) for the Infineon FS50R12KT4B15 power module, but their blocking voltage dependencies are not. Assuming a constant junction temperature, the following equations are used to model the blocking voltage dependency of the device switching energies:

$$E_{sw,S}(i,v) = \left[E_{on,S}(i) + E_{off,S}(i)\right] \cdot \left(\frac{v}{V_{ref}}\right)^{K_{v,S}} \tag{4.36}$$

$$E_{sw,D}(i,v) = E_{sw,D}(i) \cdot \left(\frac{v}{V_{ref}}\right)^{K_{v,D}} \tag{4.37}$$

where K_v is the blocking voltage dependency coefficients, V_{ref} is the rated blocking voltage, and $E_{on,S}$, $E_{off,S}$, and $E_{rr,S}$ are directly interpolated from manufacturer provided data, based on current i. Based on recommendations from the Semikron manual [117], $K_{v,S}$ and $K_{v,D}$ are set as 1.2 and 0.6, respectively. For improved accuracy, however, they can be calibrated for specific devices using experimental loss measurements.

Device switching losses averaged over each fundamental period can be determined as:

$$P_{sw,S} = \begin{cases} \frac{f_{sw}}{2\pi}\left[\int_0^{2\pi} E_{sw,S/D}(i_{ph}(\theta), V_{dc})\ \mathrm{d}\theta\right], & \text{for } i_{ph}(\theta) \geq 0; \\ 0, & \text{for } i_{ph}(\theta) < 0; \end{cases} \tag{4.38}$$

$$P_{sw,D} = \begin{cases} 0, & \text{for } i_{ph}(\theta) \geq 0; \\ \frac{f_{sw}}{2\pi}\left[\int_0^{2\pi} E_{sw,S/D}(i_{ph}(\theta), V_{dc})\ \mathrm{d}\theta\right], & \text{for } i_{ph}(\theta) < 0; \end{cases} \tag{4.39}$$

where f_{sw} is the switching frequency, i_{ph} is the instantaneous phase current, and V_{dc} is the DC-link voltage. For symmetrical SVM modulation, the devices are continuously switched and they thus dissipate switching energies all the time. For DPWM1 modulation, however, the devices are clamped for 60° intervals at every 120°, during which they do not dissipate switching energies. DPWM1 modulation switching energies are, therefore, discontinuous, as:

$$E_{sw,S/D}^{(\text{clamped})}(\theta) = \begin{cases} 0, & \text{if } (\theta - \phi) < \frac{\pi}{6} \text{ or } \frac{5\pi}{6} \leq (\theta - \phi) < \frac{7\pi}{6} \\ & \text{.. or } (\theta - \phi) \geq \frac{11\pi}{6}; \\ E_{sw,S/D}(\theta), & \text{else;} \end{cases} \tag{4.40}$$

where ϕ is the system power factor.

Finally, total losses in each fundamental period for a two-level voltage source converter can be calculated as a sum of conduction and switching losses, for all six IGBTs and diodes, as:

$$P_{tot} = 6 \cdot \left(P_{cond,S} + P_{cond,D} + P_{sw,S} + P_{sw,D}\right) \tag{4.41}$$

The loss models are verified with time-domain simulation software and experimental tests in Section 4.5.

4.3.2 Semiconductor Heat-sink Model

Heat generated within the power module due to semiconductor losses need to be efficiently dissipated, to prevent the semiconductor devices from overheating. A heat-sink can spread the heat flow at the device chip junction across an expanded surface, to facilitate good convection and radiation heat transfer to the ambient air. However, the heat-sink contributes to a significant portion of the total converter weight. In general, the larger the heat-sink, the better its heat dissipation capability, but at the cost of an overall system weight increase.

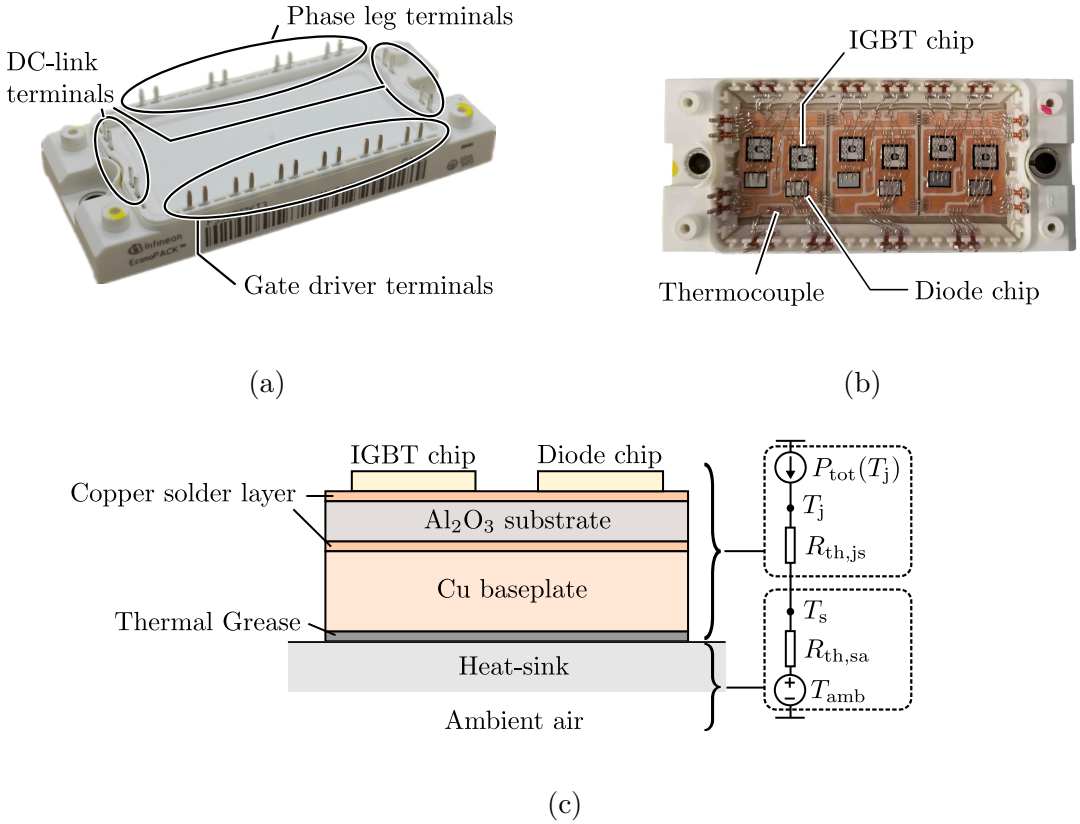


Figure 4.13: Photos of (a) outer view and (b) internal structure of Infineon FS50R12KT4B15 power module. (c) A simplified lumped parameter thermal network of the power module.

This work assumes that the semiconductor switching devices are housed in a power module with an Infineon EconoPACK2 packaging form factor, as shown in Fig. 4.13(a) and Fig. 4.13(b). Inside the modules, the semiconductor chips are soldered onto a direct-bonded copper aluminium dioxide Al_2O_3 substrate for electrical isolation. Heat is conducted away from the substrate via a standard copper baseplate, and dissipated through the heat-sink. The reason for selecting this module type is that six-pack IGBT devices for a wide power range of 15 to 100 A nominal current at 600/1200/1700 V are available as commercial products in EconoPACK2 from many packaging manufacturers, such as Infineon, LittleFuse, Fuji Electric etc., and it serves as a useful volumetric benchmark for the VSI or AFE realisation.

A simplified LPTN model, as shown in Fig. 4.13(c), is employed to describe the

power module's thermal behavior. Thermal resistances between chip-junction and heat-sink surface mainly depends on chip area, and they can be lumped together as $R_{th,js}$. Meanwhile, thermal resistances between the heat-sink surface and ambient air depends mostly on the cooling system, and they can also be lumped together as $R_{th,sa}$. The simplified model assumes that heat energy dissipates only in one direction and that thermal coupling between devices due to heat spreading across the surface is negligible, i.e. devices share the same junction temperature.

For a maximum steady-state junction temperature $T_{j,max}$, the maximum allowable cooling system thermal resistance $R_{th,sa,max}$ is:

$$R_{th,sa,max} = \left[\frac{T_{j,max} - T_{amb}}{P_{tot}}\right] - R_{th,js} \tag{4.42}$$

where T_{amb} is the ambient temperature, P_{tot} is the total semiconductor losses, and $R_{th,js}$ is the junction to heat-sink surface thermal resistance.

A forced-air convection setup is considered in this work, with ducted airflow from the fan through the heat sink channels, creating a self-contained cooling system. Compared to natural air convection systems, forced-air convection systems have thermal resistances typically up to 5-15 times lower for a similar weight and volume [117]. Liquid cooling systems, on the other hand, provide cooling capabilities superior to that of air-cooling but their main disadvantage is a need for maintenance, potential leaks, and extra weight of heat-pipes and external heat-exchangers.

The use of forced-air system with a electric fan in practical aerospace applications is usually avoided, due to reliability issues. Onboard an aircraft, forced air cooling may instead be provided to the heat loads by direct ram air ducting and direct air cycle Enviromental Cooling System (ECS) cooling. Further, hybrid cooling schemes are also commonly employed, for example: fan cooling might be provided for ground operations of normally ram air cooled heat loads [118]. Here, a forced-air convection, driven by electric fan, is only considered to get appropriate levels of airflow and is therefore representative.

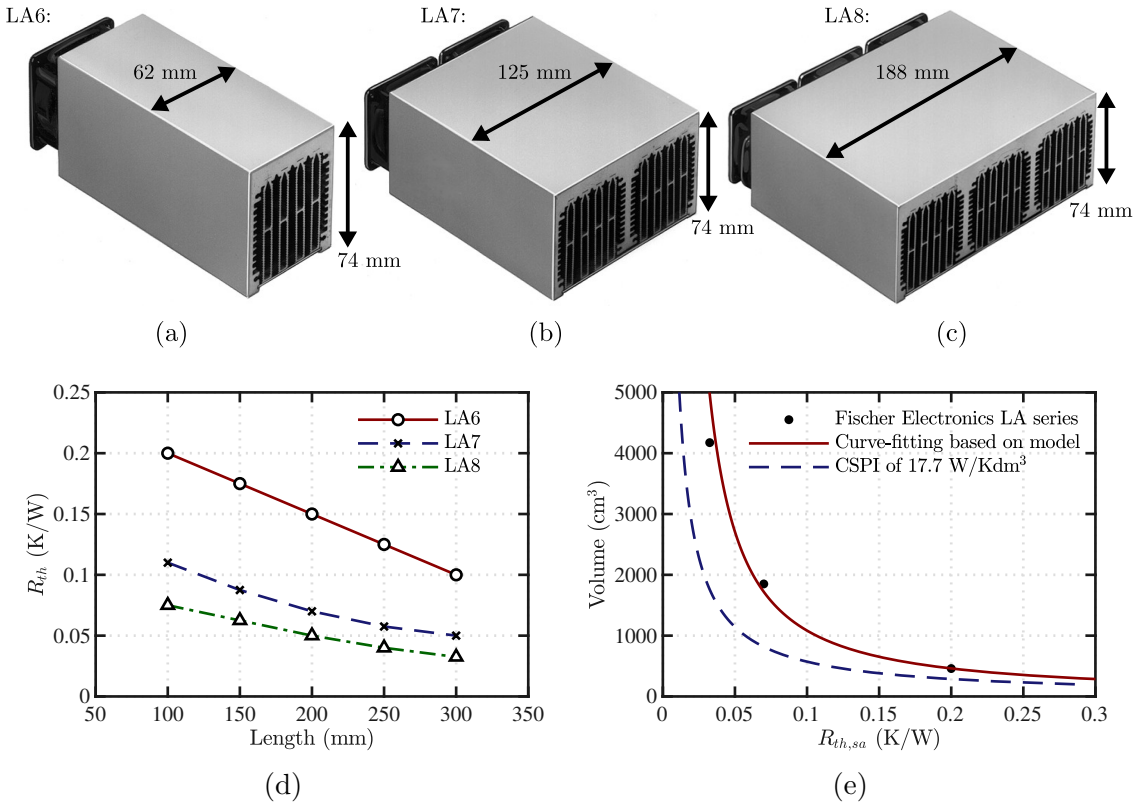


Figure 4.14: Forced-air convection cooling model based on Fischer Electronics (a) LA 6 (b) LA7 (c) LA8 cooling systems. (d) Plot of heat-sink thermal resistance against axial length. (e) Plot of heat-sink thermal resistance against volume for fixed height and length-width aspect ratio.

A simple forced-air convection model is developed based on commercially available LA 6, LA 7, and LA 8 forced-air convection cooling systems from Fischer Electronics [119]. As shown in Fig. 4.14(a-c), these systems employ a similar optimised air-flow channel design, but have different width and number of fans. Besides, they are also available in different axial lengths. In Fig. 4.14(d), the cooling systems' axial length are plotted against their thermal resistances, based on data provided by the manufacturer.

Based on the thermal relationships proposed by Drofenik et al. [120], the thermal resistance of a forced-air convection cooling system is modelled as:

$$R_{th,sa} = R_{th,bp} + R_{th,f} + R_{th,af} \tag{4.43}$$

where $R_{th,bp}$ is the baseplate thermal resistance, $R_{th,f}$ is the 'fins' thermal resistance, and $R_{th,af}$ is the thermal resistance to account for the average temperature rise of air, flowing from channel inlet to channel outlet. These thermal resistances are related to the heat-sink's geometry, in terms of height w_{hs}, width w_{hs}, and length l_{hs}, as:

$$R_{th,bp} \propto \frac{1}{A_{bp}} \propto \frac{1}{w_{hs} l_{hs}} \tag{4.44}$$

$$R_{th,f} \propto \frac{1}{A_f} \propto \frac{1}{l_{hs}} \tag{4.45}$$

$$R_{th,af} \propto \frac{1}{Vol_{af}} \propto \frac{1}{w_{hs} h_{hs}} \tag{4.46}$$

where A_{bp} is the baseplate surface area, A_f is the total fin area, and Vol_{af} is the volume of air flowing across the channel ducts. For a fixed height of $h_{hs} = 74$ mm and length-to-width ratio of $l_{hs} : w_{hs} = 1 : 0.6$, a thermal resistance against volume model is derived for the Fischer Electronics cooling systems:

$$R_{th,sa}(Vol_{hs}) = k_{1,hs} \frac{1}{Vol_{hs}} + k_{2,hs} \frac{1}{\sqrt{Vol_{hs}}} + k_{3,hs} \frac{1}{\sqrt{Vol_{hs}}} \tag{4.47}$$

where coefficients $k_{1,hs}$, $k_{2,hs}$, and $k_{3,hs}$ are determined to be 6.16×10^{-5}, 7.09×10^{-4}, and 7.09×10^{-4}, respectively, by performing a curve-fit on the manufacturers data. Figure 4.14(e) shows a plot of this relationship, and compares it against customised forced-air convection cooling systems with a Cooling System Performance Index (CSPI) of 17.7 WKdm^{-3}, reported by Drofenik et al. [121].

The minimum heat-sink volume can be interpolated from this figure, given a maximum allowable heat-sink thermal resistance. Finally, to calculate its weight, the heat-sink volume is multiplied by a mass density estimate of $\rho_{hs} = 0.86$ g/cm^3 [119].

4.4 Passive Components Modelling

Besides the semiconductor heat-sink, passive components also contribute to a significant portion of the total converter's weight and volume. For the back-to-back

converter, the main passive components are the input boost inductors and DC-link capacitor. In this section, sizing models for the boost inductor and DC-link capacitor are presented.

4.4.1 Boost Inductor

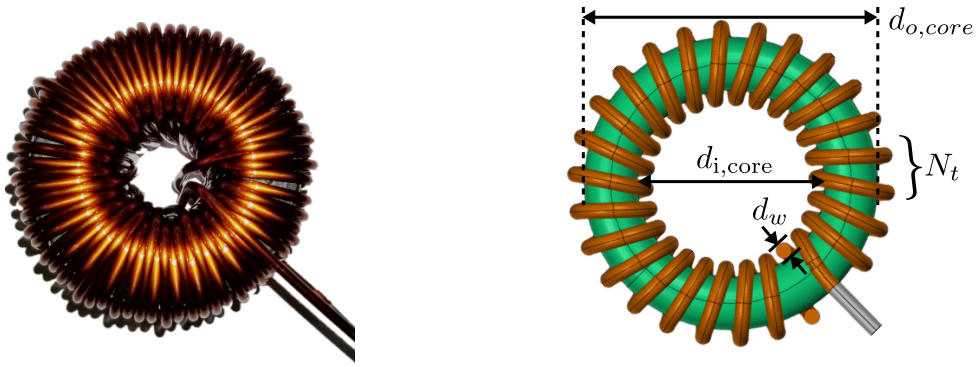
Popular inductor shape and architectures for boost inductor applications are mainly of two types: discrete-gap cores with laminated ferrite/iron-based alloys, or distributed-gap cores with powdered iron-based alloys. For different applications, it may be more important to select the correct type of technology rather than to optimise the size and weight of the inductor component.

Discrete-gap cores are often characterised with better inductance tolerance, lower core losses, and higher effective permeability under low bias conditions. For discrete-gap cores, amorphous alloys typically allow the highest saturation flux density, while nanocrystalline alloys feature very low hysteresis losses.

In comparison, distributed-gap cores have higher hysteresis losses but they offer the advantage of having soft magnetic saturation characteristics, allowing a gradual drop in inductance as DC-bias current is increased, allowing them to have a smaller physical size [122, 123]. Their soft saturation characteristics are also desirable regarding converter control [124]. They are, however, more difficult to wind and assemble, due to their physical geometry. In this thesis, only distributed-gap toroidal cores are modelled, as reference and to consider the different trade-offs in the sizing process.

Figure 4.15 shows a photo of the distributed-gap toroidal core inductor and its simplified geometrical model. The inductor design has to consider thermal, geometrical, and magnetic constraints, described as follows:

1. Thermal constraints: A minimum inductor wire diameter $d_{w,min}$ is required for



(a) (b)

Figure 4.15: (a) Hardware photo and (b) Simplified geometrical model of a distributed-gap toroidal core inductor.

acceptable winding losses and temperature, and it can be calculated as:

$$d_{w,min} = 2\sqrt{\frac{I_L}{\pi J_{rms}}} + 2h_{ins} \tag{4.48}$$

where I_L is the rms inductor current, J_{rms} is the rms current density of inductor winding, and h_{ins} is the winding insulation thickness. In this work, J_{rms} is chosen to be 5 A/mm^2, considering natural-convection cooled copper windings, while h_{ins} is 0.05 mm, assuming working AC voltages of no higher than 230 V RMS [125].

2. Geometrical constraints: The physical space of inner core window limits the number of winding turns allowed $N_{t,max}$ for a toroidal core inductor. If a single-layer winding approach is employed, $N_{t,max}$ is limited by the inner core circumference divided by wire diameter d_w, as:

$$N_{t,max} = \frac{\pi(d_{i,core} - d_w)}{\gamma_{spc} d_w} \tag{4.49}$$

where $d_{i,core}$ is the inner core diameter and γ_{spc} the wire spacing ratio (if γ_{spc} is 1, no spacing is allocated between wires). If a multi-layer winding approach is taken instead, $N_{t,max}$ is limited by a maximum winding factor k_{wf}, which is

defined as the ratio of total conductor cross-sectional area to the core window area. $N_{t,max}$ can be calculated as:

$$N_{t,max} = \frac{k_{wf} d_{i,core}^2}{d_{w,min}^2} \tag{4.50}$$

k_{wf} is typically set as 0.3 to 0.45 and it is a trade-off between fully utilizing the available inner core window area and having an excessive manufacturing cost. The advantages of using single-layer windings are lower parasitic capacitances and better cooling, but they have reduced power handling capability, as compared to multi-layer windings.

3. Magnetic constraints: As magnetic force H within the toroidal core increases, magnetic permeability μ drops due to saturation of the magnetic material. This relationship between permeability drop γ_μ and H is specific to the core material, and it can be found from the material data-sheet. For a maximum permeability drop of $\gamma_{\mu,max}$ (fixed as 0.8 in this work), the corresponding maximum magnetic force H_{max} can be found.

To design the inductor, manufacturer data of commercially available cores of a selected material are first compiled and stored inside a database. Custom cores are not considered here as they are more difficult to design and are more expensive to manufacture. For each commercial core, a nominal inductance factor $A_{L,0}$, which is often provided by the manufacturers, determines the required number of turns N_t to obtain an inductance L_r, as:

$$N_t = \sqrt{\frac{L_r}{A_{L,r}}} = \sqrt{\frac{L_r}{A_{L,0}\gamma_\mu}} \tag{4.51}$$

where $A_{L,r}$ is the inductance factor at rated current and γ_μ is the magnetic permeability drop. If $A_{L,0}$ is not given by manufacturers, it can be simply calculated as

follows, for a simplified case of a uniform magnetic circuit:

$$A_{L,0} = \frac{\mu_0 \mu_r A_c}{l_e} \tag{4.52}$$

where A_c is the core cross-sectional area and l_e is the magnetic path length. Permeability drop γ_μ is initially set to be 1, and the resulting magnetic force within the core is:

$$H = \frac{N_t I_L}{l_e} \tag{4.53}$$

where l_e is the magnetic path length, and I_L is the rms inductor current. Based on H, a new γ_μ can be interpolated from the material's $\gamma_\mu(H)$ relationship, and it is substituted into Eq. (4.51) to recalculate the required number of turns. After several iterations, the required core design's N_t and H are evaluated against constraints $N_{t,max}$ and H_{max}, respectively, to determine its feasibility. This process is repeated for all the commercially available cores, and the core with smallest volume is selected from the set of feasible designs.

For the Mega Flux 60 core material (Chang-Sung Corporation) [126] with single-layer windings, volumes of smallest core designs are plotted against inductance and current in Fig. 4.16(a). In this figure, the circled dots represent discrete core designs with the highest inductance-current product per volume LI/Vol. Assuming a thermally limited inductor design with fixed magnetic properties, the inductor volume Vol_L is modelled as a linear function of L_r and a squared function of $\hat{I}_L$, according to Friedli et al. [124], as:

$$Vol_L(\hat{I}_L, L) = (k_{1,vL}\hat{I}_L^2 + k_{2,vL}\hat{I}_L + k_{3,vL})L + (k_{4,vL}\hat{I}_L^2 + k_{5,vL}\hat{I}_L + k_{6,vL}) \tag{4.54}$$

where coefficients $k_{1-6,vL}$ are determined to be $k_{1,vL} = 1.0\times10^{-4}$, $k_{2,vL} = 5.2\times10^{-3}$, $k_{3,vL} = 13.3\times10^{-3}$, $k_{4,vL} = -2.3\times10^{-8}$, $k_{5,vL} = 6.4\times10^{-7}$, and $k_{6,vL} = -5.8\times10^{-7}$, by performing a least-square approximation fit on the discrete core designs with

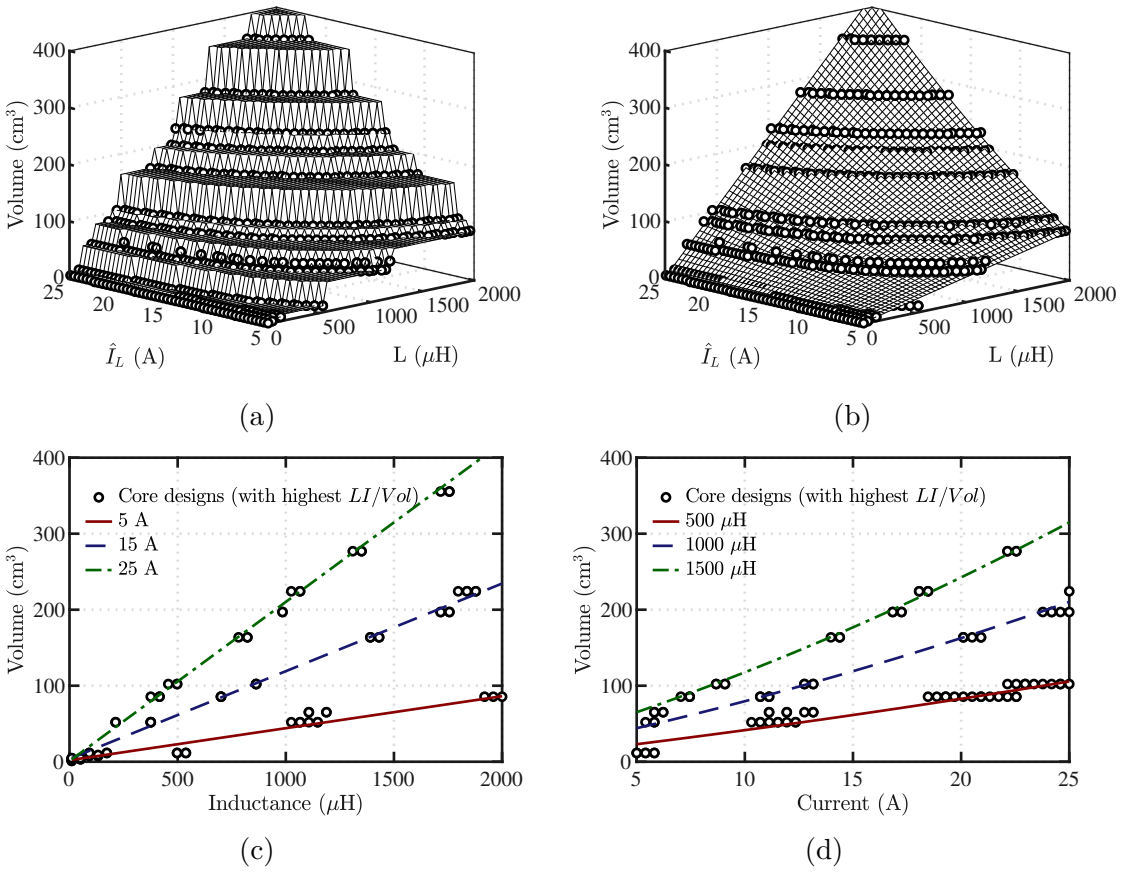


Figure 4.16: For single-layer toroidal inductors based on Mega Flux 60 core material, (a) volume against inductance and current for *discrete* core designs. The circled dots represent core designs with highest inductance-current per volume. For *continuous* model based on circled dots, volume against (b) inductance and current, (c) inductance and (d) current.

the highest LI/Vol. This allows a *continuous* model for the inductor volume to be derived based on the 'best' *discrete* core designs, as plotted in Fig. 4.16(b). As shown in Fig. 4.16(c) and (d), a good fit for volume against inductance and current is obtained.

Finally, inductor core weight is estimated by multiplying core volume with its material density ρ_{core}, usually provided by manufacturers.

4.4.2 DC-link Capacitor

For DC-link capacitor applications, the two most popular capacitor types are aluminium electrolytic capacitor and polypropylene film capacitor. The correct type of capacitor technology are often argued a priori. Although electrolytic capacitors feature a high energy density, they suffer from relatively high dielectric losses, making them a good choice for transient energy storage purposes. However, the voltage ratings of available electrolytic capacitors are currently limited to $\approx$ 450 V [127]. Film capacitors, on the other hand, are able to withstand higher voltages and have much lower dielectric losses, and hence better temperature characteristics and current ripples tolerance [128]. In this thesis, only physics-based models of film capacitors are provided, to estimate the minimum required weight in an efficient and quick manner and to describe the basic trade-offs in their sizing.

The physical size of a film capacitor is primarily a function of its energy storage requirement (capacitance and voltage), and an energy related scaling method can be employed to estimate its volume [129]. A simplified model for the parallel plate film capacitor is shown in Fig. 4.17(a), consisting of dielectric volume Vol_d, electrodes/plate surface volume Vol_e, isolation volume Vol_{iso} and interfaces volume Vol_i. Considering their individual dependencies on capacitance C and voltage V, the minimum capacitor volume, based on energy storage requirements, is modelled as:

$$\begin{aligned} Vol_{c,energy}(C,V) &= Vol_d(C,V) + Vol_e(C,V) + Vol_{iso}(C,V) + Vol_i(C,V) \\ &= k_{1,vC}CV^2 + k_{2,vC}CV + k_{3,vC}V + k_{4,vC} \end{aligned} \tag{4.55}$$

where coefficients $k_{1-4,vC}$ are found by performing a least mean square curve fit on commercially available capacitor data, as shown in Fig. 4.17(b). For the MKPB32778G film capacitors, these coefficients are found to be $k_{1,vC} = 4.54{\times}10^{-7}$, $k_{2,vC} = 1.5{\times}10^{-3}$, $k_{3,vC}$ = -2.51$\times10^{-8}$, and $k_{4,vC} = 3.03{\times}10^{-5}$.

Besides the energy storage requirement, the capacitor design is also thermally constrained and, therefore, its current-carrying capability needs also to be considered.

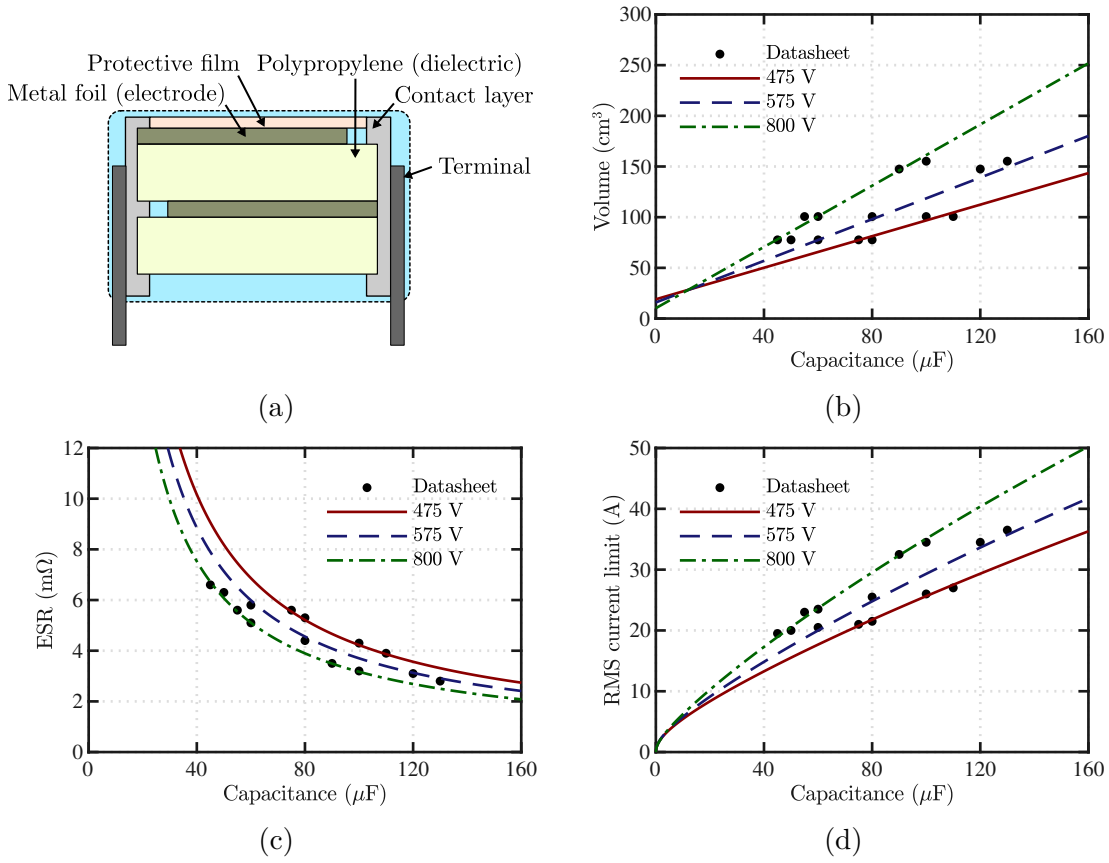


Figure 4.17: (a) Simplified model for parallel plate film capacitor. (b) Volume against capacitance and voltage, (c) Volume against equivalent series resistance and voltage, and (d) Volume against rms current limit modelled based on MKPB32778G film capacitors (TDK).

Resistive losses are generated in the capacitor due to its inherent parasitic equivalent series resistance R_{esr}. Keeping with the parallel plate capacitor model, its equivalent series resistance consists of the dielectric resistance R_d, electrodes/plate resistance R_e, and interfaces resistance R_i. Taking into account the individual dependencies of these resistances on capacitance C and voltage V, the total capacitor resistance R_{esr} is modelled as:

$$\begin{aligned} R_{esr}(C,V) &= R_d(C,V) + R_e(C,V) + R_i(C,V) \\ &= k_{1,rC}\frac{1}{C} + k_{2,rC}\frac{1}{CV} + k_{3,rC} \end{aligned} \tag{4.56}$$

where coefficients $k_{1-3,rC}$ are found by curve-fitting commercially available capacitor data, as shown in Fig. 4.17(c). For the MKPB32778G film capacitors, these coefficients are determined as: $k_{1,rC} = 1.55\times10^{-7}$, $k_{2,rC} = 1.08\times10^{-4}$, and $k_{3,rC} = 2.65\times10^{-4}$.

Power losses P_c in the capacitor is calculated as:

$$P_c = I_{c,rms,worst}^2 R_{esr} \tag{4.57}$$

where $I_{c,rms,worst}$ is the worst-case DC-link capacitor rms current calculated previously in Eq. (4.17). To ensure that sufficient heat dissipation is available, maximum power loss per surface area $P_{perArea}$ is fixed as 215 W/m^2, and it is used as a limiting parameter for the capacitor design. Considering a box-shaped capacitor, its surface area A_c is proportional to $Vol_c^{2/3}$, and capacitor rms current limit $I_{c,rms,lim}$ is calculated as:

$$P_{perArea} = \frac{I_{c,rms,lim}^2 R_{esr}}{A_c} \;\rightarrow\; I_{c,rms,lim}(C,V) = k_{iC} \cdot \sqrt{\frac{P_{perArea} \cdot [Vol_c(C,V)]^{2/3}}{R_{esr}(C,V)}} \tag{4.58}$$

where the coefficient k_{iC} is calculated from commercially available capacitor data, as shown in Fig. 4.17(d). For the MKPB32778G film capacitors, this coefficient $k_{1,rC} = 2.48$. Rearranging Eq. (4.58), the thermally constrained minimum capacitor volume is found to be:

$$Vol_{c,thermal}(C,V,I_{c,rms}) = \left(\frac{I_{c,rms}^2 R_{esr}(C,V)}{k_{iC}^2 P_{perArea}}\right)^{3/2} \tag{4.59}$$

To size the DC-link capacitor, the minimum capacitor volume due to energy storage requirements, $Vol_{c,energy}$, and minimum capacitor volume due to thermal constraints, $Vol_{c,thermal}$, are first calculated using Eq. (4.55) and Eq. (4.59), respectively. The final required capacitor volume is then taken as the larger of these two

constrained volumes, as:

$$Vol_c = \max([Vol_{c,energy}, Vol_{c,thermal}]) \tag{4.60}$$

Finally, capacitor weight is estimated by multiplying capacitor volume with average capacitor mass density ρ_{cap}, typically available in manufacturers data sheet.

4.5 Model Verifications

In this section, verifications of the converter modulation and control analysis using time-domain simulations are first described, followed by a discussion of the experimental prototype system used to validate the semiconductor loss models. Due to budget and time constraints, similar to the machine verifications, a standard power converter is employed for verifying the models, as opposed to an aerospace power converter. The main limitation with this test-rig is also its lower power density, lack of in-built reliability and fault-tolerance characteristics. However, considering the main objective of the verification, which is to check the assumptions in the models before using them in an optimisation-based design, these limitations are considered acceptable.

Besides, as the physical sizing models for heat-sink, inductors, and DC-link capacitor are derived from data of commercially available products, no further verifications are deemed necessary.

4.5.1 Time-domain Simulation Study

Time-domain simulations of the back-to-back converter driving a PM machine are carried out using PLECS standalone simulation tool. The purpose of the simulation study is to quickly verify the implemented control and modulation strategies, converter current ripple and transient performances, and also validate the analytical calculations for semiconductor losses dissipated during the converter operation. To

Table 4.1: System parameters for time-domain simulation study.

Parameter	**Value**	**Unit**
DC-Link Voltage	200	V
DC-Link Capacitance	0.5	mF
Input grid peak phase voltage	100	V
Input grid electrical frequency	50	Hz
Input grid resistance	0.01	Ω
Boost inductance	0.5	mH
Load torque	8.5	Nm
Output mechanical speed	1500	rpm
PM machine no. of pole pairs	5	-
PM machine dq inductance	2.2	mH
PM machine stator resistance	0.27	Ω
PM machine peak flux linkage	0.088	Ω
Combined shaft inertia	7.3×10^{-7}	kgm^2
Converter switching frequency	10	kHz
Converter modulation method	Symmetrical SVM	-

calculate average and total converter losses, thermal descriptions for the Infineon FS20R12KT4B15 power module are specified within the simulation tool, by means of look-up tables. Other parameters for this simulation study are provided in Table 4.1

Figure 4.18(a) shows the start-up response of the motor drive. Initially, at $t = 0.0$ s, all controllers are disabled, the modulating pulses to both VSI and AFE are blocked. The input grid voltage is ramped up from zero to 100 V, while the AFE operates in diode rectification mode, charging the DC-link capacitor to about 173 V. The AFE is enabled at $t = 0.1$ s, and it boosts the DC-link voltage to a reference value of 200 V. Subsequently, the VSI is enabled at $t = 0.2$ s, and it also controls

machine speed to a reference value of 1500 rpm. During this process, the current limit is briefly enforced, and the acceleration torque is limited, as shown in the figure. At $t = 0.3$ s, a load torque of 8.5 Nm is added to the PM machine in a step, and the converter controllers respond to maintain machine speed and DC-link voltage. Due to the limited control bandwidths, a slight dip in rotor speed and DC-link voltage is observed. Finally, the load is removed in a step at $t = 0.4$ s, simulating a trip of the VSI converter (worst-case transient).

At rated torque and speed, phase A and DC-link currents for the VSI and AFE are shown in Fig. 4.18(b) and Fig. 4.18(c), respectively, while current flowing into the DC-link capacitor is given in Fig. 4.18(d). In calculating average and rms currents for the switching devices and DC-link capacitor, the analytical model does not consider high-frequency switching harmonics. Therefore, a comparison between calculations from the analytical model and simulated results for the converters is made in Table 4.2. A good match is obtained, verifying the accuracy of the analytical calculations.

The analytical prediction of semiconductor losses is also compared to the simulation results in Table 4.2 and some discrepancies are observed. These discrepancies are expected because, in the simulation study, losses are calculated based on the instantaneous currents and on-state voltages, which are directly interpolated from the datasheet loss characteristics, while for the analytical model, average current over each switching period is employed, along with a linearised model to represent the device on-state voltage and current relationship.

At $t = 0.45$ s, when load is removed in a step, the simulated voltage overshoot and saturation of AFE modulation index are shown in Fig. 4.18(e). The converter analytical model computes a maximum overshoot of 202.30 V, while the recorded value in the simulation is 203.61 V. The small differences are due to PWM delays in the switching model, which are not considered in the analytical model.

Finally, the phase modulating signals and input phase A current waveform are analysed over one switching period in Fig. 4.18(f). The peak-to-peak current ripple

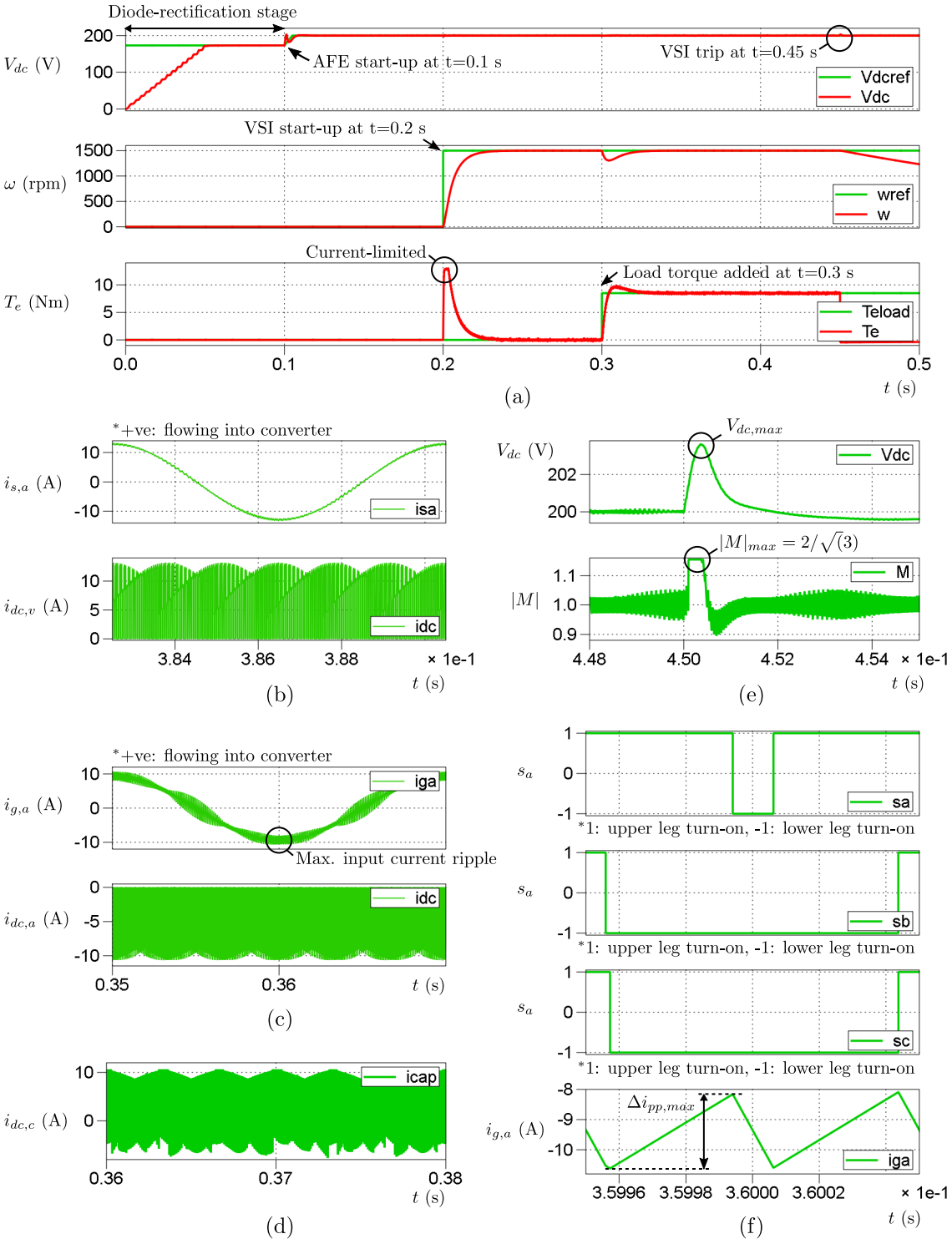


Figure 4.18: Simulated motor drive operation: (a) DC-link voltage, machine speed, and torque response. (b) VSI phase A and DC-link currents, (c) AFE phase A and DC-link currents, and (d) DC-link capacitor current, at rated torque and speed output. (e) DC-link voltage and AFE modulation index response to VSI trip at $t = 0.45$ s. (f) Modulating signals and maximum input current ripple at $t = 0.36$ s.

Table 4.2: Comparison of analytical against time-domain simulation results at rated operating point ($t = 0.4$ s).

Converter Parameters	**VSI**		**AFE**		**Unit**
	Ana.	**Sim.**	**Ana.**	**Sim.**	
IGBT average current	3.22	3.22	0.32	0.34	A
IGBT rms squared current	26.59	26.59	0.22	0.23	A
Diode average current	0.88	0.88	2.66	2.67	A
Diode rms squared current	1.78	1.77	18.00	18.01	A
DC-link average current	7.01	7.01	7.01	7.01	A
DC-link rms current	8.98	8.98	7.76	7.78	A
Conduction loss (per IGBT)	3.19	3.44	0.21	0.30	W
Switching loss (per diode)	0.67	0.83	2.33	2.41	W
Conduction loss (per IGBT)	2.57	2.56	2.02	2.05	W
Switching loss (per diode)	2.14	2.06	1.66	1.42	W

Other Parameters	**Analytical**	**Simulation**	**Unit**
Maximum input pk-pk current ripple	2.50	2.44	A
DC-link capacitor rms current	4.48	4.45	A
Maximum DC-link voltage overshoot at t =0.45 s	202.30	203.61	V

at 0° reference voltage vector angle, i.e. when $t = 0.36$ s, is determined as 2.50 A in the analytical model, matching well with simulation model calculations, which give 2.44 A.

4.5.2 Experimental Analysis

To experimentally verify the semiconductor loss and heat-sink thermal models, a prototype converter is constructed in the lab, based on a reference converter design from Texas Instrument [130].

The converter design employs current shunts to measure the phase currents, and has in-built hardware over-current and over-voltage protection. Instead of isolated gate-driver supplies, the gate drivers are powered by bootstrap power supplies, for lower cost and reduced board space. This gate driver configuration, however, poses a limitation on the converter modulation: the bootstrap capacitors do not have enough electrical charge to sustain the turn-on of upper leg switches during 'clamp-on' periods of the discontinuous DPWM1 modulation. This is not a problem for continuous Symmetrical SVM modulations, as there are no extended 'clamp-on' periods for the upper leg switches. For digital control, a C2000 Delfino F28379D micro-controller in a Texas Instrument LaunchPad is used.

The converter semiconductor switches are realised with an Infineon FS50R12KT4B15 power module directly mounted onto a Fischer Electronics LA6 high-performance forced-convection cooling system. These switching devices, rated at 50 A, are considerably oversized for the power levels considered in this work, but as the main objective of this experimental analysis is to validate losses and thermal models, this is not a significant concern. Photos of the converter hardware are shown in Fig. 4.19.

As the main objective of the experiment here is to characterise the converter semiconductor loss, a machine-load is not required at this stage and a simple Resistive-Inductive (RL)-load with representative inductance and resistance values are employed to represent the machine. The prototype converter is operated as a

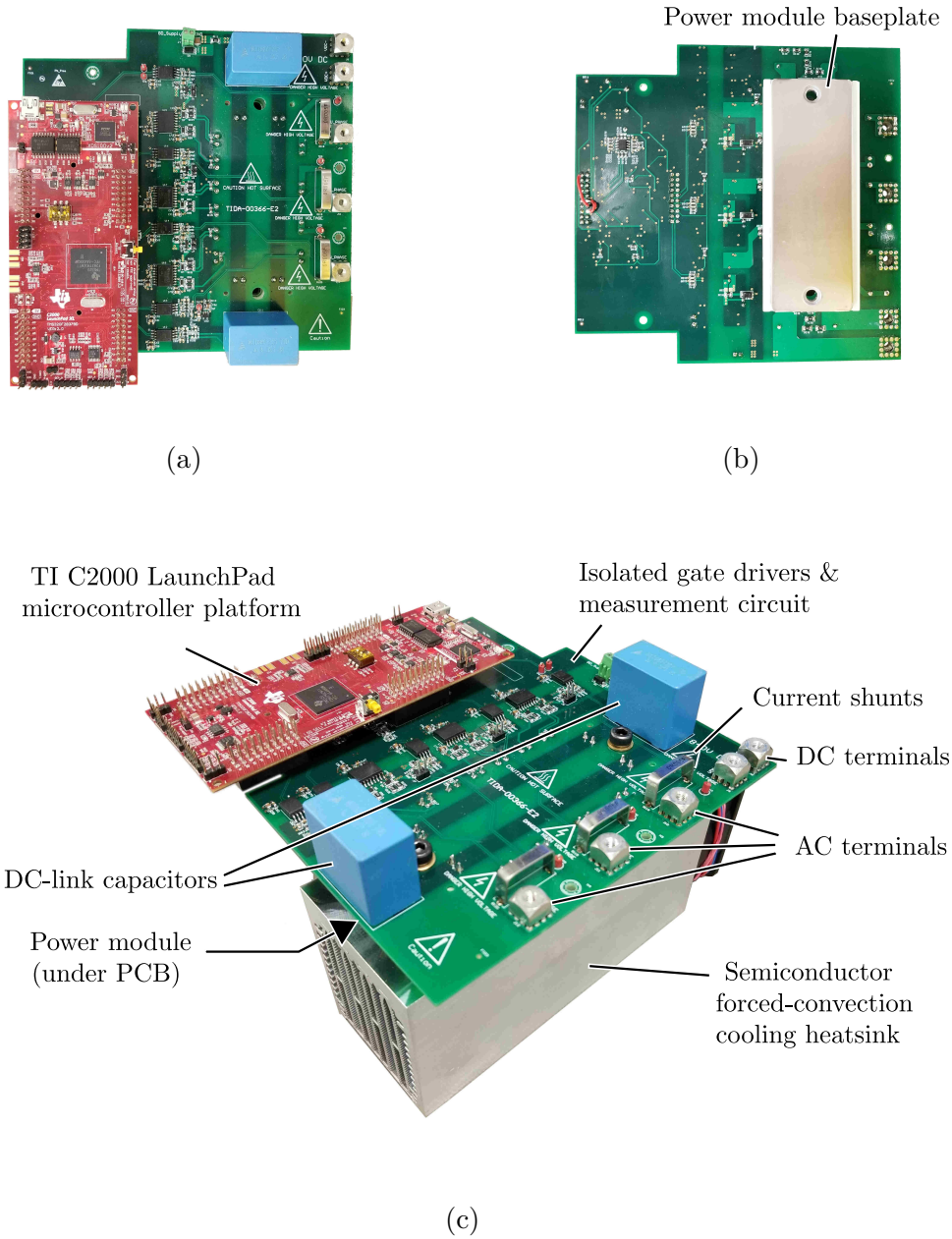


Figure 4.19: Photos of prototype two-level voltage source converter: (a) top view (b) bottom view (without heat-sink) (c) angled view.

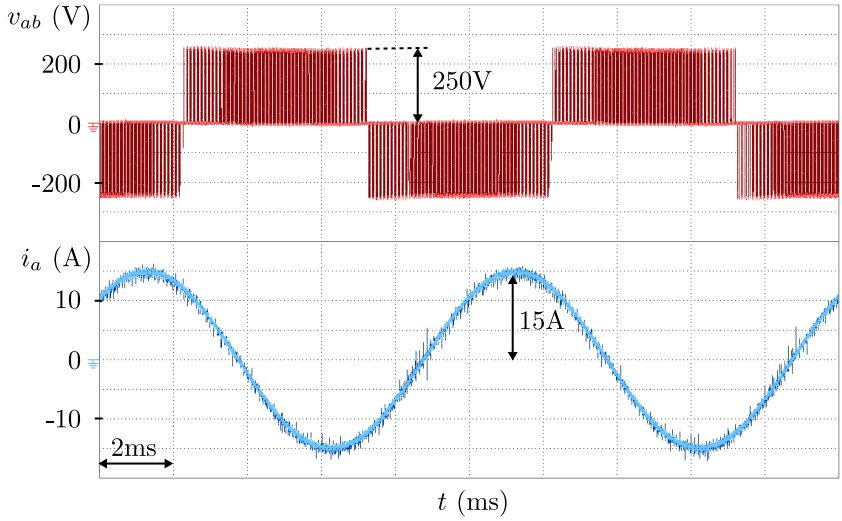


Figure 4.20: Measured line-to-line voltage v_{ab} and phase current i_a of VSI (with $V_{dc} = 250$ V, $f_e = 100$ Hz, and $\hat{i}_q = 15$ A).

VSI to power a RL-load (L_{ph} =3mH, $R_{ph} = 5.3\Omega$), and it is supplied by an EA-PS 9360-40 DC-power supply at its DC terminals.

For a DC-link voltage V_{dc} of 250 V, fundamental electrical frequency f_e of 100 Hz, q-axis current reference $\hat{i}_q^{ref}$ of 15 A, and using symmetrical SVM modulation, Fig. 4.20 shows the converter output line-to-line voltage v_{ab} and phase A current, analysed using a Yokogawa DLM2024 mixed signal oscilloscope with 200 MHz bandwidth.

Converter losses are measured at various DC-link voltages, switching frequencies, and currents using a Kinetiq PPA 2530 precision power analyser, with a bandwidth of 2 MHz and watts accuracy of 0.08%. These V_{dc}, f_{sw}, and $\hat{i}_{ph}$ parameters are modified in real-time, and the loss measurements are taken when junction temperature $T_j = 60 \pm 5°$C, monitored using the power module internal NTC thermistor.

The loss measurements are shown in Fig. 4.21. Initially, loss estimations from the analytical model were found to be lower than the measured values. There are several reasons to this: firstly, parasitic DC-link and emitter inductances in the commutation circuit greatly affect switching losses, and, consequently, real switching energy dissipated in the implemented converter circuitry can differ from the data-sheet specifications [117]. Secondly, the impact of junction temperature on switching

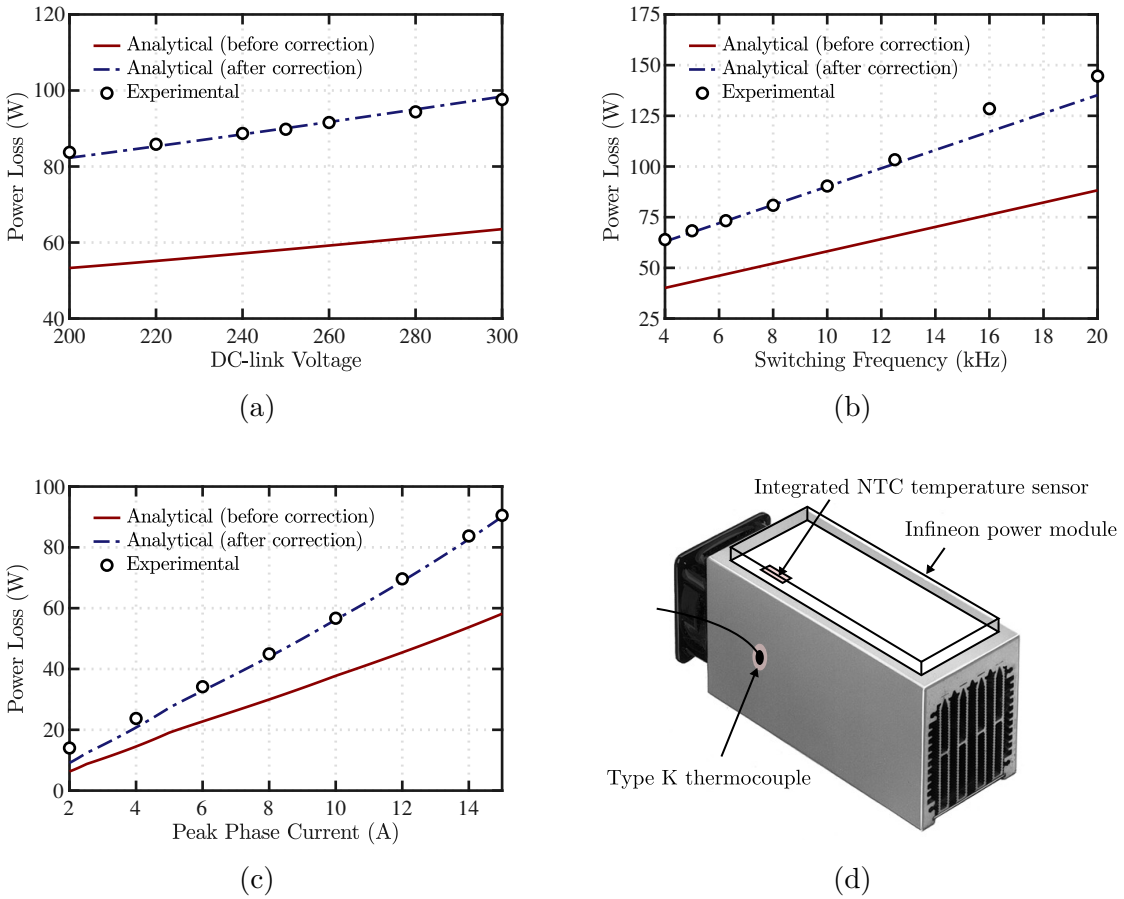


Figure 4.21: Comparison of losses predicted by the analytical model against measurements (before and after correction) for different (a) DC-link voltages V_{dc}, (b) switching frequencies f_{sw}, and (c) current references $\hat{i}_q^{ref}$ (at junction temperature $T_j = 60 \pm 5°$). (d) Temperature measurement locations of the converter system.

losses is not accounted for in the model. Lastly, the contact and cable resistances in the test setup can add to the ohmic losses measured.

To consider the extra switching and conduction losses, device switching energies calculated in Eqs. (4.36) and (4.37) are corrected with a correction factor of 1.5, and additional ohmic losses, due to an approximated contact resistance of 0.05 Ω, are included in the analytical loss calculations. The corrected loss model, as shown in Fig. 4.21, is more accurate in predicting the converter losses.

To verify the thermal model, the prototype converter cooling system's thermal

resistance is calculated from loss and temperature measurements as:

$$R_{th,hs} = (T_j - T_{hs})P_{loss} - R_{th,js} \tag{4.61}$$

where $R_{th,js}$ is the junction-to-baseplate thermal resistance provided by the device manufacturer, T_j is the junction temperature measured using the internal thermistor, and T_{hs} is the heat-sink surface temperature measured using a type-K thermocouple at a location shown in Fig. 4.21(d). A thermal resistance of 0.25 K/W is calculated from the analytical model, while experimentally, it is 0.28 K/W. This is a good match, considering the simplifications and assumptions made in the thermal model.

4.6 Chapter Summary

A comprehensive model for the evaluation of a back-to-back converter was presented in this chapter. The chapter began with an in-depth analysis of the converter modulation and control. Next, semiconductor loss models and a simplified cooling system sizing model were proposed. The cooling system model is based on commercially available products and it highlights the inverse relationship between cooling system thermal resistance and volume. To size the boost inductor and DC-link capacitor, different physics-based approximation methods were also introduced, considering toroidal core inductors and film capacitors. Finally, the converter modulation and control analysis, and semiconductor loss models were verified using a time-domain simulation study and experimental tests.

The combination of different analytical techniques in the model allows for a quick evaluation and sizing of the converter, taking only an average of approximately 1×10^{-4} seconds to run on a normal PC. Similar to the Chapter 3 machine model, the converter analytical model also has a simple framework and is very versatile. It can be, therefore, easily combined with the machine models for a holistic evaluation of the motor drive system, as will be discussed next in Chapter 5.

Chapter 5

System-level Motor Drive Modelling

The motor drive is a complex system composed of the machine and converter components, which are independently considered in the previous chapters. Due to the close and synergetic interactions between their operations, the motor drive components need to be modelled together to evaluate the motor drive performance holistically. This is particularly important for aerospace applications, where every bit of weight and efficiency has to be optimised.

When considering the motor drive performance at a system-level, detailed machine-converter effects, such as machine harmonic losses due to converter pulse width modulation (PWM) voltage waveforms, are important to model as they can be of the same order of magnitude as converter losses for low voltage applications under light loads. Compared to air-gap spatial harmonic losses due to fractional-slot concentrated winding machine slot-pole configurations, these machine PWM harmonic losses can be reduced by optimising the converter modulation parameters [42]. Besides, the converter voltage limitations need also to be considered, as it affects the operating range and field-weakening requirements of the machine.

This chapter begins by describing the implementation of a system-level model for

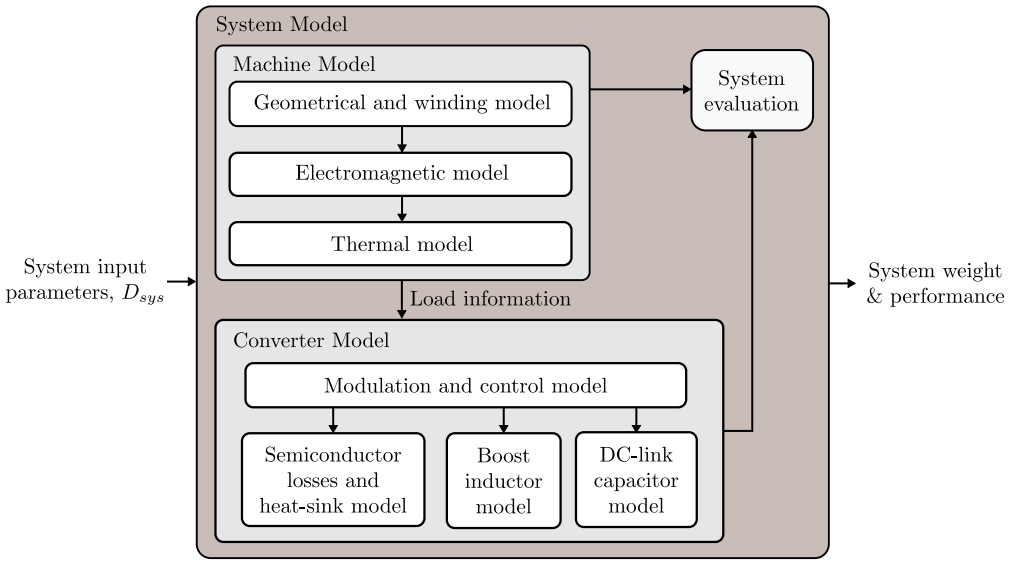


Figure 5.1: Organisation of system-level motor drive model.

the motor drive in Section 5.1. To account for machine harmonic losses due to the converter PWM, a harmonic loss model is proposed and validated experimentally in Section 5.2. Finally, the system-level model is employed to consider effects of converter modulation and machine operating point on system loss, and experimental tests are carried out on a back-to-back motor drive system to verify its findings in Section 5.2.

5.1 Motor Drive System-level Model

The individual machine and converter models are integrated into one system-level motor drive model, as shown in Fig. 5.1. This approach is rather simple and straightforward, where machine electrical properties are directly fed into the converter model as load parameters. The proposed system-level model accepts input parameters D_{sys}, consisting of elements from D_{mach} and D_{conv} (from Eqs. (3.1) and (4.1)), and it combines the machine and converters' performance and weight at the output.

More details of the motor drive system-level model, with links to its software

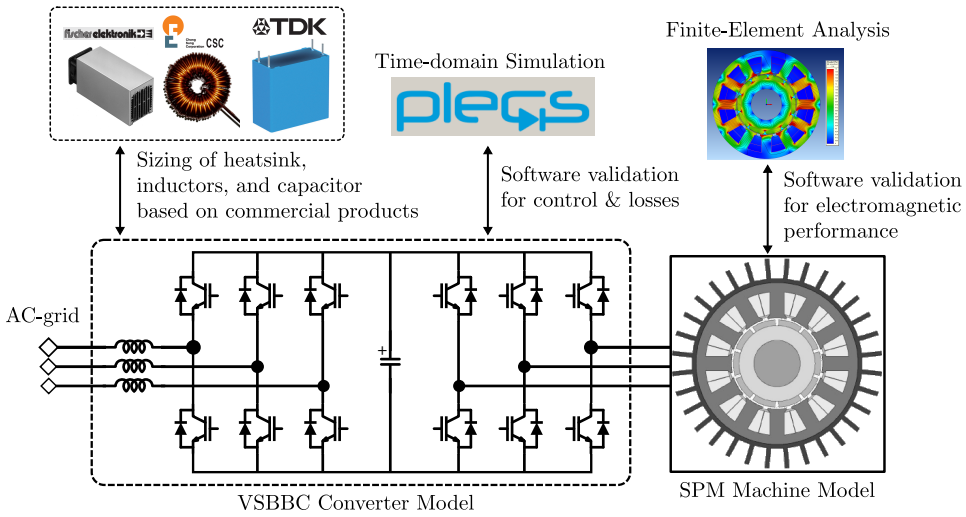


Figure 5.2: More details on system-level motor drive model, linking with relevant software validation tools.

validation tools, are shown in Fig. 5.2. As the analytical models are coded entirely in Matlab, the interfacing between the converter model and SPM machine model is done without significant effort.

The main feature of this system-level model is simplicity, ensuring that the speed and accuracy of the machine and converter component-level models are retained. The system-level model only takes, on average, approximately 3 to 4 $\times 10^{-2}$ seconds to run on a normal PC and its accuracy is validated using an experimental testbench in Section 5.3.

Prior to any further evaluations of the system-level model, it is important to also consider harmonic losses that occur in the machine, as a result of its system-level interactions with the converter. This effect is studied with more details in the following section.

5.2 Machine Harmonic Losses

When power converters are used to control the machine, pulsed voltages with high harmonic content are supplied to the machine. This results in distorted stator currents, which induce high frequency harmonic losses in the machine. This was shown by Boglietti et al. in [131], where iron losses in magnetic materials are compared for purely sinusoidal voltage and for PWM inverter output voltage excitation. The authors showed that losses measured for the latter setup are considerably higher, due to the high frequency harmonic losses.

To date, researchers have published different methods to model these PWM harmonic losses, and the majority of them is based on combining theoretical relationships with experimental coefficients calibrated for a specific machine.

Bradley et al. [132] presented a harmonic injection method to determine PWM harmonic losses for induction machines. In their paper, the authors assumed that eddy-current losses are dominant over conduction and hysteresis losses at high harmonic frequencies, and their method employs a 'loss-factor' curve, which is determined experimentally through a series of harmonic voltage injections. Harmonic losses at each frequency are first calculated by multiplying the square of harmonic voltage amplitudes with a loss-factor corresponding to its harmonic frequency, as obtained from the loss-factor curve. Assuming that harmonic loss can be superpositioned for a given stator voltage spectrum, the total harmonic losses $P_{h,tot}$ is calculated by summing the individual harmonic losses, as:

$$P_{h,tot} = \sum_{h>1}^{\infty} K_{lf}(f_h) \cdot V_h^2 \tag{5.1}$$

where $K_{lf}(.)$ is the loss-factor at a specific harmonic frequency f_h, and V_h is the harmonic voltage amplitude. The impact of different modulation techniques or converter topologies on machine harmonic losses can, thus, be quantified and compared using this method. Examples of its application can be found in [133] and [42] to

evaluate machine harmonic losses for matrix converters and three-level converters, respectively.

Boglietti et. al [134] proposed a different approach where the total machine iron losses $P_{ir,tot}$ (including both fundamental and harmonic loss components), with PWM excitation, is modelled as:

$$P_{ir,tot} = \left(\frac{V_{avg}}{V_{avg,fund}}\right)^{\beta} \cdot P_{hys,sin} + \left(\frac{V_{rms}}{V_{rms,fund}}\right)^{2} \cdot P_{eddy,sin} \tag{5.2}$$

where β is a Steinmetz coefficient of the material, $P_{hys,sin}$ and $P_{eddy,sin}$ are the hysteresis and eddy-current losses with a sinusoidal supply, respectively, V_{avg} and V_{rms} are the average and rms of stator voltage, respectively, and $V_{avg,fund}$, and $V_{rms,fund}$ are the average and rms of fundamental stator voltage, respectively. The losses $P_{hys,sin}$ and $P_{eddy,sin}$ are calculated with the same parameters from the modified Steinmetz equation in Eq. (3.6). It is later proven by Schweizer et al. in [42] that this approach gives the same result for PWM harmonic losses as the previous method in Eq. (5.1), if assumptions such as high switching frequency, dominant eddy-current losses, and negligible harmonic hysteresis and harmonic ohmic losses are valid.

The comprehensive set of work described thus far has considered only induction machines harmonic losses. In this thesis, a new model is proposed to approximate PM machine harmonic losses as a function of switching frequency and applied harmonic voltages. The theory and derivation of this model are first provided, followed by its experimental verifications.

5.2.1 Proposed Model

With a distorted stator winding current, eddy-current $I_{ac,h}$ induced in conductive parts of the machine is:

$$I_{ac,h} = -\frac{\mathrm{d}\Psi_h}{\mathrm{d}t} \cdot \frac{1}{R_{ac,h}} \quad \rightarrow \quad I_{ac,h} \propto -\frac{I_{h,rms} f_h}{R_{ac,h}} \tag{5.3}$$

where Ψ_h is the harmonic flux component created by stator winding harmonic currents $I_{h,rms}$ at frequency f_h and $R_{ac,h}$ is the AC resistance of these conductive parts at harmonic frequency f_h. Thus, eddy-current losses $P_{ac,h}$, due to $I_{ac,h}$, are:

$$P_{ac,h} = R_{ac,h} I_{ac,h}^2 \propto \frac{I_{h,rms}^2 f_h^2}{R_{ac,h}} \tag{5.4}$$

For a round conductor, $R_{ac,h}$ is proportional to $\sqrt{f_h}$ due to skin effect, as:

$$R_{ac,h} \propto \frac{1}{S_h} \propto \frac{1}{d_h} \propto \sqrt{f_h} \tag{5.5}$$

where S_h is the cross-sectional area of conduction, and d_h is the skin depth of the round conductor. For the complex geometry of machine conductive components, in which eddy-currents are induced, it is proposed to consider $R_{ac,h}$ to be proportional to f_h^x instead, where x is determined experimentally.

For different modulation methods, closed-form solutions for $I_{h,rms}$ of a two-level voltage source converter are derived by integrating the average squared value of instantaneous current ripples over a fundamental cycle. According to Holmes et al. [106], $I_{h,rms}$ can be calculated as:

$$I_{h,rms}^2 = \left(\frac{V_{dc}}{L_h f_h}\right)^2 \frac{1}{48} f(M) \tag{5.6}$$

where function $f(M)$ is the harmonic distortion factor specific to different modulation methods, M is the modulation index, L_h is the machine inductance at f_h, and V_{dc} is the DC-link voltage. For symmetrical SVM modulation, $f(M)$ is:

$$f(M) = \frac{3}{2}M^2 - \frac{4\sqrt{3}}{\pi}M^3 + \frac{9}{8}\left(\frac{3}{2} - \frac{9}{8}\frac{\sqrt{3}}{\pi}\right)M^4 \tag{5.7}$$

while for a DPWM1 modulation, it is:

$$f(M) = 6M^2 - \left(\frac{45}{2\pi} + \frac{4\sqrt{3}}{\pi}\right)M^3 + \left(\frac{27}{8} + \frac{27}{32}\frac{\sqrt{3}}{\pi}\right)M^4 \tag{5.8}$$

Substituting Eqs. (5.5) and (5.6) into Eq. (5.4) gives Eq. (5.9).

$$P_{ac,h} \propto \left(\frac{V_{dc}^2}{L_h^2 f_h}\right) \frac{1}{48} f(M) \left(\frac{f_h^2}{f_h^x}\right) \tag{5.9}$$

Simplifying Eq. (5.9) and considering only switching frequency harmonic components, the following harmonic loss model is proposed:

$$P_{ac,h} = K_a V_{dc}^2 f(M) f_{sw}^{K_b} + K_c \tag{5.10}$$

where coefficients K_a, K_b, and K_c are determined experimentally for a specific machine.

5.2.2 Experimental Analysis

To verify the proposed model, harmonic losses are measured for the prototype SPM machine from Chapter 3, in a no-load test setup, i.e. rotor shaft is allowed to rotate freely, with a power converter controlling its speed. A Kinetiq PPA2530 precision power analyser, with a bandwidth of 2 MHz and watts accuracy of 0.08%, is placed at the machine input terminals and it is programmed to calculate harmonic losses $P_{h,tot}$, by automatically subtracting fundamental input power P_{fund} from the total measured input power $P_{in,tot}$ [42]. The measurement window is set to 800 ms, and linear averaging over every ten measurement values is performed. The harmonic losses are measured for a range of converter switching frequency and DC-link voltage parameters, varied in real-time without stopping the machine's rotation, to ensure similar thermal conditions.

For a fixed speed of 1500 rpm and using symmetrical SVM modulation, the measured losses are plotted against switching frequency and DC-link voltage in Fig. 5.3. From the loss measurement points, a curve-fitting surface is then constructed based on the proposed model in Eq. (5.10) using a least-squares approximation technique. The resulting curve-fitting coefficients are K_a = 0.01943, K_b = -0.3168,

and K_c = -2.676 with an R-Square of 0.9973. The good fit verifies that the proposed model can accurately account for the effect of converter modulation parameters on machine harmonic losses.

This harmonic loss model is added to the machine model for the remaining motor drive system-level performance evaluations in this thesis.

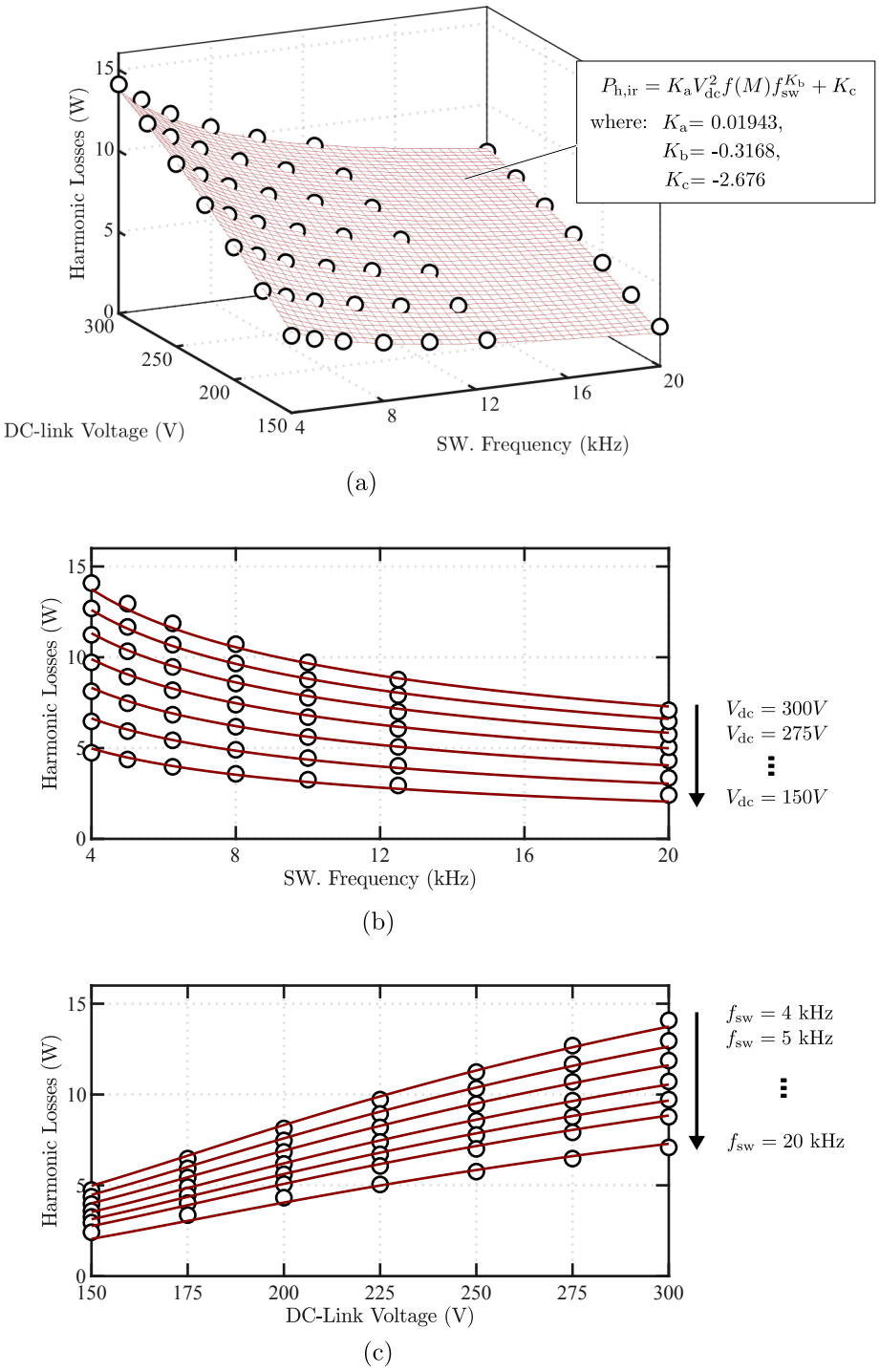


Figure 5.3: Plot of harmonic loss measurements for prototype PM machine: (a) against switching frequency and DC-link voltage, (b) against switching frequency, and (c) against DC-link voltage.

5.3 Analysis of System-level Model

The system-level model can be used to evaluate the comprehensive motor drive performance, including various machine-converter interactions. In this section, two specific aspects of these machine-converter interactions are studied using the model:

- Effects of converter modulation on system loss.
- Effects of load profile operating points on system loss, with different converter DC-link voltages and field-weakening enabled at higher machine speeds.

Additionally, experimental tests are also performed to verify and support the findings. The testbench setup is first discussed, followed by detailed analysis of the mentioned machine-converter interactions.

5.3.1 Experimental Setup

For the experimental tests, a pair of identical motor drive systems are connected at their electrical and mechanical interfaces (back-to-back), to form a closed-loop power transfer. The setup employs two 12-slot 10-pole SPM machines (from Chapter 3) and prototype converters (from Chapter 4). A photo of the experimental setup, along with its schematic diagram, is provided in Fig. 5.4.

At the DC-link connection, a DC supply supplies constant voltage power to Conv_1 which controls Mach_1. In turn, Mach_1 mechanically drives Mach_2, which is controlled by Conv_2, to regenerate power back to the DC-link. An advantage of this setup is that the DC supply effectively only supplies losses that occur in the power transfer loop, due to the converter, machine and mechanical drivetrain.

For loss measurements, Conv_1-Mach_1 pair is considered as the drive under test and it is operated under speed control to regulate shaft speed; while Conv_2-Mach_2 pair is considered as the loading drive and it is operated in current control to set the loading torque. Another advantage of this back-to-back motor drive test setup is

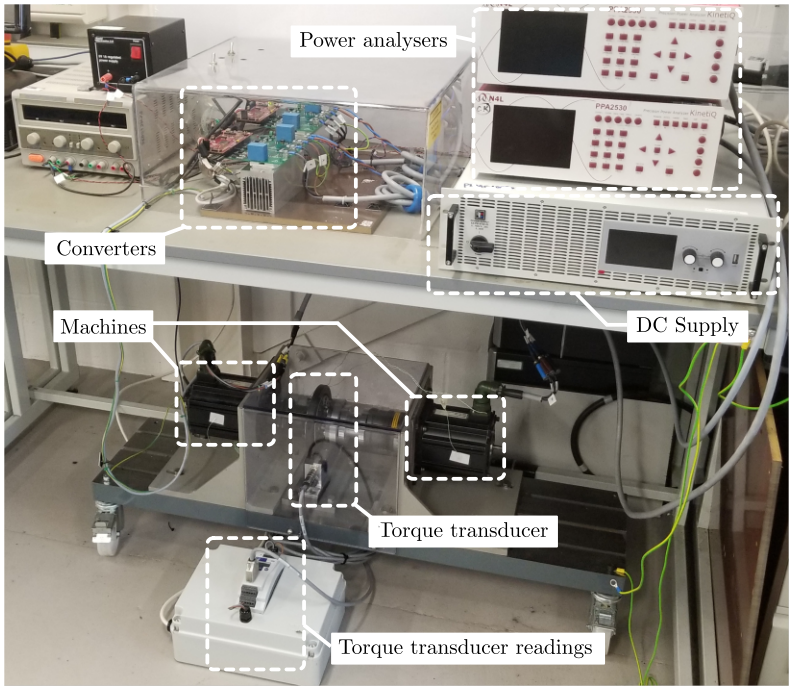
that the motor drive operating points can be easily varied, in real-time, by providing the converters with different current and speed references.

5.3.2 Impact of Converter Modulation

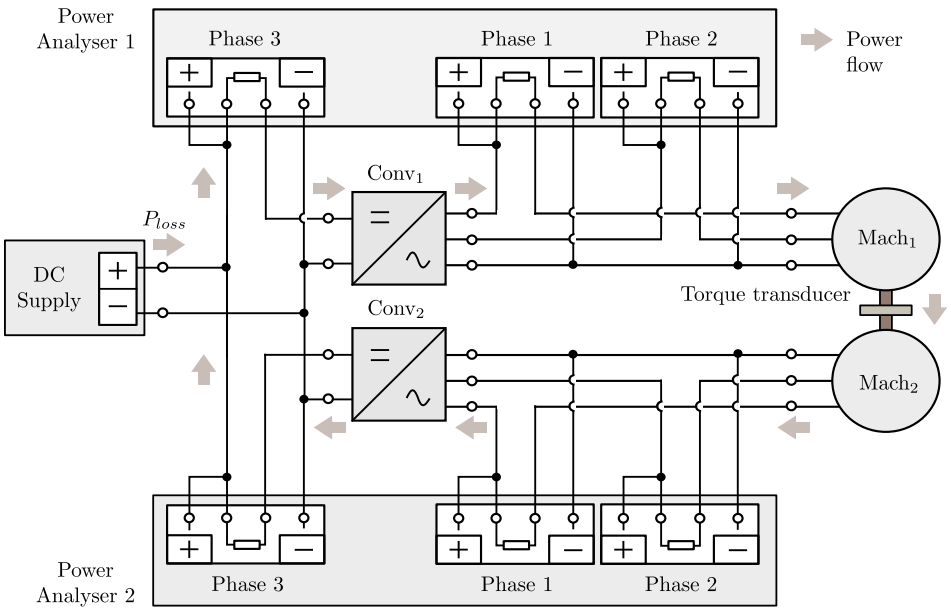
Assuming that the fundamental load current has negligible impact on machine harmonic losses, the system-level model considers the effects of converter modulation, under loaded conditions, using the harmonic loss analytical model described in the previous section.

With torque and speed of 8.5 Nm and 1500 rpm, losses predicted by the system-level model are plotted against DC-link voltage V_{dc} and switching frequency f_{sw} in Fig. 5.5(a). This figure shows that the least amount of system losses is produced when DC-link voltage is lowest, as expected because converter switching losses and machine harmonic losses are positively correlated to the DC-link voltage. A less obvious observation, however, is that the least amount of system losses is also produced when switching frequency is lowest despite the negative correlation between machine harmonic loss and switching frequency. This indicates that when switching frequency is increased, the increase in converter switching losses outweighs the decrease in harmonic machine losses, which is especially true for high-load conditions, as switching losses become more significant.

For experimental validation, nine combinations of V_{dc} (180, 230, 270 V) and f_{sw} (4, 8, 12.5 kHz) are selected, as indicated in Fig. 5.5(a). A similar loss measurement method to Section 5.2.2 is employed. The loss measurements are compared against the losses calculated by the system-level analytical model in Fig. 5.5(b), and they are tabulated in Table 5.1. An accurate match is obtained validating the assumption that no-load harmonic loss model coefficients are also applicable for rated-load conditions.



(a)



(b)

Figure 5.4: (a) Photo and (b) basic schematic diagram of back-to-back motor drive experimental setup.

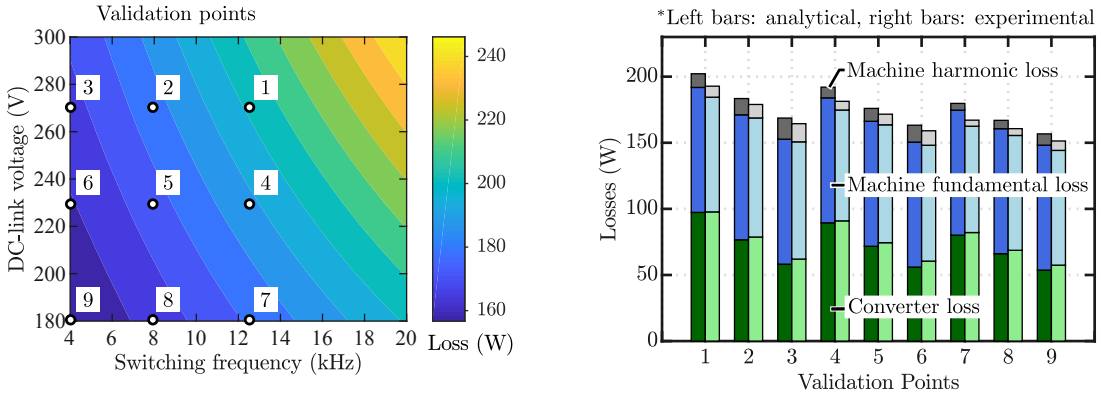


Figure 5.5: (a) Plot of total losses against DC-link voltage and switching frequency calculated by the system-level model. The circled dots represent the selected experimental validation points. (b) Comparison of system-level model losses against measured losses at the validation points.

Table 5.1: Comparison of losses calculated by system model and measured losses for different converter modulation parameters.

VP	Conv. loss		Mach. loss[1]		Mach. loss[2]		Total loss	
	Ana. (W)	Exp. (W)	Ana. (W)	Exp. (W)	Ana. (W)	Exp. (W)	Ana. (W)	Exp. (W)
1	97.34	97.73	94.52	86.74	10.34	8.32	202.20	192.79
2	76.60	78.71	94.52	90.05	12.32	10.20	183.44	178.97
3	58.17	62.03	94.52	88.67	16.00	13.73	168.69	164.43
4	89.44	90.94	94.52	83.83	8.11	6.58	192.07	181.35
5	71.71	74.42	94.52	89.16	9.75	8.04	175.99	171.61
6	55.95	60.49	94.52	87.63	12.80	10.95	163.28	159.07
7	80.13	82.09	94.52	80.41	5.13	4.59	179.77	167.09
8	66.12	68.68	94.52	86.86	6.31	5.14	166.95	160.68
9	53.67	57.44	94.52	86.79	8.52	7.12	156.71	151.35

[1] Fundamental losses [2] Harmonic losses

5.3.3 Impact of Load Profile Operating Points

The motor drive system is often expected to accommodate a wide range of operating points, defined in terms of torque and speed, as is specified in their load profiles. Considering a traction motor drive torque-speed curve, as illustrated in Fig. 5.6(a), constant torque is demanded up to a certain speed, at which point onwards, torque can be reduced as speed increases, to provide constant power. In the constant power region, field-weakening is typically required above a certain speed, determined by the converter voltage limit.

For the traction motor drive torque-speed curve, the choice of DC-link voltage is an interesting trade-off between system efficiencies in the constant torque and constant power region:

- In the constant torque region, it is desirable to operate with a low DC-link voltage to reduce converter switching losses.
- In the constant power region, however, a low DC-link voltage forces the motor drive to enter into field-weakening mode at lower speeds. Field-weakening requires an extra d-axis current component, and thus, increases machine and converter losses. For high efficiency in the constant power region, in contrast to the constant torque region, it can be desirable instead to have a high DC-link voltage, in order to avoid any field-weakening operation if possible.

System losses are evaluated for three operating points on the torque-speed curve in Fig. 5.6(a) and two DC-link voltages (200 and 300 V) to illustrate this trade-off. These operating points are analysed using the system-level model, and the findings are verified on the experimental setup. The losses are plotted in Fig. 5.6(b) and tabulated in Table 5.2.

For the 200 V system, total losses at operating points 1 and 2 are observed to be lower compared to that of the 300 V system. This is expected as significantly higher switching losses occur in the 300 V system due to higher device blocking voltages.

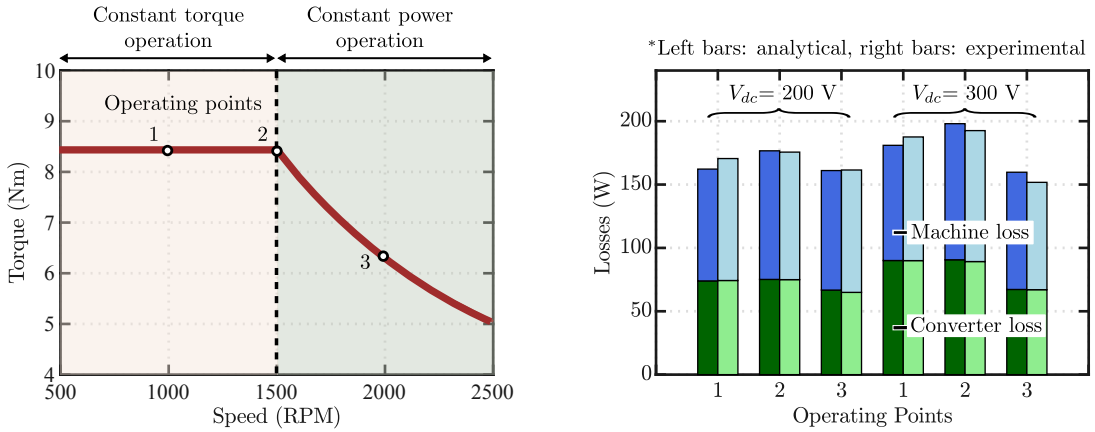


Figure 5.6: (a) Torque-speed curve for a traction motor drive application. (b) Comparison of system model losses against measured losses for each validation point, with different DC-link voltages.

Table 5.2: Comparison of losses calculated by system model and measured losses for different operating points and DC-link voltages.

OP	V_{dc} (V)	$\hat{i}_d$ (A)	$\hat{i}_q$ (A)	Conv. loss		Mach. loss		Total loss	
				Ana. (W)	Exp. (W)	Ana. (W)	Exp. (W)	Ana. (W)	Exp. (W)
1	200	0	14	73.96	74.29	88.25	96.24	162.21	170.53
2	200	0	14	75.14	74.97	101.49	100.64	176.63	175.61
3	200	-7.5	10.2	66.73	64.91	94.32	96.58	161.05	161.50
1	300	0	14	90.05	89.98	90.91	97.60	180.97	187.57
2	300	0	14	90.64	89.23	107.41	103.35	198.05	192.59
3	300	0	10.6	67.21	67.02	92.52	84.72	159.73	151.74

The opposite is true, however, for operating point 3. At this operating point, total losses for the 200 V system are higher compared to losses of the 300 V system, due to the field-weakening operation necessary only for the 200 V system.

These observations highlight the importance of selecting appropriate converter DC-link voltages, considering how they affect the average losses across the system's load-profile, instead of designing only for one operating point. For example, if the motor drive is operated for more extended periods in the constant power region, a higher DC-link voltage can reduce the total average losses.

The analysis in this section has assumed a fixed machine design, considering only the trade-off for converter DC-link voltage on the drive's losses depending on the operating point. Further improvements can be obtained if the machine's field-weakening capability, in terms of flux linkage and inductance, is also optimised in the design, alongside the converter DC-link voltage parameter.

5.4 Chapter Summary

This chapter has presented a system-level model, integrating individual models from previous chapters, to allow for a holistic and comprehensive evaluation of the motor drive system. As the system-level model retains the speed and accuracy of the individual models, it is suitable for use in an optimisation-based design.

Besides, a harmonic loss model has been proposed in this chapter to characterise machine high frequency harmonic losses that are due to converter PWM. To employ this model, harmonic loss coefficients are determined experimentally for a specific machine. By incorporating the machine harmonic loss model within the system-level model, the system-level impact of converter modulation parameters can be predicted.

Lastly, machine-converter interactions were analysed using the system-level model, and the findings are supported with experimental results. These results are obtained from experimental tests carried out on a testbench with an identical pair of motor drives connected back-to-back. Converter modulation parameters and machine

operating points were observed to have a significant impact on the motor drive loss distribution, which point to the need for system-level considerations during a motor drive design. The proposed system-level model forms the core of motor drive optimisation work carried out in Chapter 6.

Chapter 6

Evolutionary Multiobjective Optimisation

Engineering design process can generally be broken down into two independent parts: modelling and optimisation. Previous chapters have looked at developing fast and accurate component and system-level analytical models for the motor drive. This chapter addresses the practical application of multiobjective optimisation algorithms, with these models, for a motor drive design. In particular, the use of Evolutionary Multiobjective Optimisation (EMO) algorithms, namely the NSGA-II, SMPSO, and GDE3 algorithm, is investigated, considering the many design variables, constraints, and objectives involved for a motor drive optimisation. Here, the term 'evolutionary' refers to the gradual change of a population of solutions, to improve their merit.

The chapter outline is as follows: Section 6.1 firstly reviews working principles behind the mentioned EMO algorithms. Next, Section 6.2 provides practical guidelines for employing these algorithms in a motor drive optimisation. In Section 6.3, these concepts are illustrated using a multiobjective motor drive optimisation case study, considering the prototype machine from Chapter 3 and converter from Chapter 4 as benchmark. Finally, in Section 6.4, the EMO algorithms are compared, in terms of their performance and suitability, for a motor drive optimisation problem.

6.1 Description of EMO Algorithms

General search and optimisation techniques can be categorised as being either *deterministic* or *stochastic*. Deterministic optimisations rely on a systematic enumeration of all possible design variables. They are, however, generally not computationally efficient if an exhaustive search approach is employed, due to an inherent 'step-size' problem, and they can easily get stuck in local optimums if solution gradients are incorporated [12].

In contrast, stochastic optimisations do not have a step-size problem and allow a finer scan in more promising regions compared to areas with fewer prospects. Further, they are gradient-free and do not hang onto local optimums, due to their use of random variables and a continually evolving population.

Evolutionary algorithms are a family of stochastic algorithms that mimic the natural selection process. In evolutionary computation techniques, fitness values are assigned to partial solutions to guide the search towards optimal solutions, and random variables are used to significantly speed up the search process and prevent solutions from an early convergence towards local optimums.

Due to their stochastic nature, one can not 'prove' to have found the optimal solutions using evolutionary algorithms, but these algorithms are generally able to provide very competitive solutions to a wide range of optimisation problems, even those which deterministic algorithms are unable to solve, due to a limitation in computational power.

This section reviews the working principles of three popular EMO algorithms, namely the NSGAII, SMPSO, and GDE3 algorithm, which are multiobjective variants of the Genetic Algorithms (GA), Particle Swarm Optimisation (PSO), and Differential Evolution (DE) algorithm.

6.1.1 Non-dominated Sorting Genetic Algorithm II

GA is loosely based on natural evolution and Darwin's 'Survival of the Fittest' concept. In general, the algorithm consists of a population of *individuals*, which represent potential solutions and are controlled by a set of bio-inspired *operators*. These operators typically include *mutation*, *crossover*, *selection*, and *reproduction*. At any given *generation*, the *Parent* population is processed by the operators to produce a *Child* population. The combined Parent and Child population is evaluated via the objective function, and individuals in the population are assigned *fitness* values, which determine their survivability going into the next generation [135].

For engineering problems, real-parameter GA algorithms with Simulated Binary Crossover (SBX) and polynomial mutation operators are often preferred over their binary-parameter counterparts [136]. In real-parameter GA optimisation, the SBX and polynomial mutation operators function as the primary search mechanism. In the SBX operator, the Child population is created from the Parent population with the help of a randomised spread factor, which follows a probability distribution curve. The polynomial mutation operator further perturbs the Child population with two randomised parameters, also chosen based on a probability distribution curve. The shapes of the probability distribution curves for both SBX and polynomial mutation operators are determined by distribution indices, which can be tuned to control the algorithm's search characteristics.

The NSGAII, proposed by Deb et al. [137], is arguably the most popular multiobjective variation of GA. This algorithm uses a fast non-dominating ranking method and an extra *niching* operator to deal with multiobjective problems. This niching operator employs a crowding distance measure, which reflects the closeness of solutions to its neighbour in the performance space, and by sorting solutions based on crowding distances, the selection process can be guided towards a more diverse population and a better spread at the Pareto front. Algorithm 1 presents the pseudocode describing the NSGAII implementation.

Algorithm 1 Non-dominated Sorting Genetic Algorithm II

1: **procedure** NSGAII ($\vec{f}(\vec{x})$) ▷ to find Pareto-optimal solutions $\vec{x}^*$
2: Initialise and generate random population P of size $\mathcal{N}$.
3: Evaluate fitness $\vec{f}$ for all members.
4: Employ non-dominated sorting and assign rank to members based on Pareto dominance.
5: Do binary tournament selection based on rank to extract Parent population.
6: Crossover and mutate Parent population to generate Child population.
7: **for** i=1 to g_{max} number of generations **do**
8: Merge Parent and Child population.
9: Evaluate fitness $\vec{f}$ for members in the merged population.
10: Employ non-dominated sorting and assign rank to members based on Pareto dominance.
11: Compute and assign crowding distance index to members of each rank.
12: Do binary tournament selection based on rank and crowding distance index to extract *new* Parent population.
13: Crossover and mutate *new* Parent population to generate *new* Child population.
14: **end for**
15: **end procedure**

6.1.2 Speed Multiobjective Particle Swarm Optimisation

Unlike GA, PSO is a swarm-based optimisation algorithm developed by Kennedy et al. [138] that mimics the social behaviour of a flock of birds or school of fish, as it swarms towards and around food. The basic PSO concept is that individuals (also known as *particles*) move across the hyper-dimensional search space, changing their positions based on a social-psychological tendency to emulate the success of other individuals.

In each generation, the fitness of all individuals are evaluated and they are given new *velocity* and *position* values in the search space. Each individual's new velocity v_{n+1} and position x_{n+1} are determined based on their current positions relative to

positions of the fittest *personal* and *global* individual. They are updated as:

$$v_{n+1} = wv_n + c_1u_1(x_n^{(p)} - x_n) + c_2u_2(x_n^{(g)} - x_n) \tag{6.1}$$

$$x_{n+1} = v_{n+1}x_n \tag{6.2}$$

where n the generation number, u_1 and u_2 are random values between 0 and 1, v and x are the individual's current velocity and position, respectively, $x^{(p)}$ and $x^{(g)}$ are positions of the personal and global best individual, respectively, and w, c_1, and c_2 are user-defined parameters for inertia, personal 'atttraction', and global 'attraction', respectively.

A unique feature of the PSO is its use of memory, allowing the fittest personal and global individuals of previous generations to guide the search process. Thus, individuals can benefit from their and others' past experiences, to quickly converge towards an 'optimum'. This fast convergence speed, however, may be harmful especially as the algorithm is extended to handle multiple objectives.

A popular multiobjective variation of PSO is the SMPSO algorithm proposed by Nebro et al. [139]. This algorithm employs a secondary (external) repository to keep an archive of non-dominated individuals, and uses the NSGAII crowding distance measure to decide which individuals to keep when the archive becomes full. To prevent the optimisation from converging too quickly, the SMPSO algorithm also incorporates the NSGAII polynomial mutation operator.

A problem with directly using Eqs. (6.1) and (6.2) for multiobjective optimisation is that individual velocities can become too high, resulting in erratic movements towards upper and lower boundaries of the search space. To solve this issue, the SMPSO algorithm has a *constriction coefficient* and *velocity constriction* mechanism to limit the velocities of each individual. Algorithm 2 contains the pseudocode summarising the SMPSO implementation.

Algorithm 2 Speed Multi-objective Particle Swarm Optimisation

procedure SMPSO ($\vec{f}(\vec{x})$) ▷ to find Pareto-optimal solutions $\vec{x}^*$.
    Initialise and generate random population P of size $\mathcal{N}$.
    Evaluate fitness $\vec{f}$ for all individuals.
    Store individual positions as personal bests $\vec{x}^{(p)}$ in external repository R.
    Employ non-dominated sorting and store non-dominated individuals positions as global bests $\vec{x}^{(g)}$ in external repository R.
    Compute and assign crowding distance index C to global best individuals.
    for i=1 to g_{max} number of generations **do**
        Do roulette wheel selection to extract global bests $\vec{x}^{(g)}$ based on C.
        Calculate and update velocity and position for all individuals.
        Perform mutation on individuals.
        Evaluate fitness $\vec{f}$ for all individuals.
        Update personal best if $\vec{x}_i^{(p)}$ dominates previous personal best $\vec{x}_{i-1}^{(p)}$
        Employ non-dominated sorting and add *new* non-dominated particles to global bests $\vec{x}^{(g)}$.
        Compute and assign crowding distance index C to global bests.
        If R is full, keep only global bests with lower crowding distance indices.
    end for
end procedure

6.1.3 Generalised Differential Evolution 3

DE is a relatively recent evolutionary algorithm that has gained a lot of popularity within the community ever since it was proposed. The algorithm was initially developed by Price et al. [140] to be a reliable and versatile function optimiser that is also easy to use. DE shares many similarities with GA, in its use of a Parent and Child population, and bio-inspired operators to control the optimisation. However, the main difference is that DE combines both crossover and mutation characteristics into one unique operator, which perturbs the population members with scaled differences of randomly-selected and distinct population members.

The DE operator is simple to implement as it consists only of several equations. A mutation vector $v_{u,j}$ is firstly calculated from the population in each generation as

$$v_{u,j} = x_{r1,u,j} + F \cdot (x_{r2,u,j} - x_{r3,u,j}) \tag{6.3}$$

where F is a user-defined scaling factor, and $r1$, $r2$, and $r3$ are random vectors, selected such that $r1, r2, r3 \in 1, 2, ..., \mathcal{N}$, where $\mathcal{N}$ is the population size, and that $r1 \neq r2 \neq r3$. Population for the next generation is calculated next, using the mutation vector, as:

$$x_{n+1,u,j} = \begin{cases} v_{u,j}, & \text{if } u \leq CR \text{ or } j = k; \\ x_{n,u,j}, & \text{otherwise.} \end{cases} \tag{6.4}$$

where u is a random value between 0 and 1, k is a random integer between 1 and the total number of design variables n_d, and CR is the crossover rate.

GDE3 is an extension of the DE algorithm proposed by Kukkonen et al. [141] to handle multiobjective optimisation problems. The algorithm is very similar to the NSGAII, as it adopts the same non-dominating ranking method and crowding distance measure to decide which solutions survive into the next generation. Algorithm 3 provides the pseudocode summarising the GDE3 implementation.

Algorithm 3 Generalised Differential Evolution 3

procedure GDE3 ($\vec{f}(\vec{x})$) ▷ to find Pareto-optimal solutions $\vec{x}^*$.
    Initialise and generate random population P of size $\mathcal{N}$.
    Evaluate fitness $\vec{f}$ for all members.
    Employ non-dominated sorting and assign rank to members based on Pareto dominance.
    Do binary tournament selection based on rank to extract Parent population.
    Apply DE-operator on Parent population to generate Child population.
    for i=1 to g_{max} number of generations **do**
        Merge Parent and Child population.
        Evaluate fitness $\vec{f}$ for members in the merged population.
        Employ non-dominated sorting and assign rank to members based on Pareto dominance.
        Compute and assign crowding distance index to members of each rank.
        Do binary tournament selection based on rank and crowding distance index to extract *new* Parent population.
        Apply DE-operator on *new* Parent population to generate *new* Child population.
    end for
end procedure

6.2 Practical Guidelines for Applying EMO

The theoretical concept of multiobjective optimisation and EMO algorithms can be applied to a motor drive design optimisation. However, several important aspects of their implementations are first addressed in this section.

6.2.1 Modelling

Optimisation algorithms rely on a model for obtaining fitness values, implying that its successful use for design depends heavily on accurate modelling of the system. As many designs are typically evaluated to solve high-dimensional problems using EMO algorithms, the modelling has to also be computationally efficient.

The analytical motor drive models from previous chapters are especially suitable, as they are fast and have been verified to be accurate.

6.2.2 Search Space Definition

In an optimisation-based design, the model input parameters are pre-selected to be either fixed as requirements, or modifiable as design variables. Each possible combination of the design variables are subsequently allocated to a point in the search space. The pre-selection process for the design variables is often not straight-forward, and, therefore, several guidelines are provided as follows:

- Input parameters which are related to an external system, such as the grid or mechanical load for the motor drive, should be fixed and determined by the application under study.
- Limitations of the models should be taken into account. For example, if machine local saturations are not considered in the analytical model, the influence of machine stator tooth-tip profile is minimal and it should not be selected as a design variable.
- Compatibility of the optimisation algorithm with the input parameter type should also be considered. The EMO algorithms described in Section 6.1 are more suitable for *continuous* optimisation problems, and they are less efficient if discrete input parameters are selected as design variables.
- It is advantageous to have as many design variables as possible, to allow a wide range of solutions, even unconventional ones, to be evaluated. However, this requires an enormous amount of computing power, which is a practical concern. A compromise should, therefore, be made in the total number of design variables employed, based on the available computational resources.

Other important considerations when defining the search space include the selection of appropriate upper and lower boundaries. The designer has to ensure that the global optimum solutions are contained within these boundaries. Further, it is helpful to the algorithm's convergence speed, if the search boundaries are chosen

such that at least half of the search space contains feasible solutions. Fortunately, only crude estimates of these boundaries are needed with evolutionary algorithms, as not much is typically known about the optimal solutions for complex design problems at the start of the optimisation.

6.2.3 Performance Space Mapping

Potential solutions in the search space are evaluated with the models, and their output or performances can be mapped onto the performance space. For motor drives, performance measures such as weight, losses, and cost are typically chosen as objective functions for minimization [68].

To identify the Pareto optimal solutions for a multiobjective problem, aggregate selection techniques, such as weighted-sums method, are commonly employed [142, 56, 75]. With this method, each objective function is multiplied with a weighting factor, and solutions, which share the lowest scalar weighted sum, are considered to be Pareto optimal. Although this method is easy to implement, it has a significant drawback of being unable to find optimum solutions on a non-convex Pareto front. Further, the choice of weights using this method has a substantial impact on the optimality of the final design, according to Coello et al. [12].

The alternative approach, employed in this work, is to directly incorporate the Pareto dominance concept into the selection operator of the evolutionary algorithms, thus removing the need for any weighting factors.

6.2.4 Constraint Handling

System requirements or practical limitations can be considered as constraints in the optimisation if they are related to the output or performance of the model. There are several ways to handle these constraints in the evolutionary algorithm. The easiest way is the 'death penalty' method, where infeasible solutions are rejected and removed from the population. A serious limitation of this method is that infeasible

solutions do not offer insights nor contribute to the search for optimum solutions [135].

A more common approach towards constraint handling is the use of penalty functions, adding them to objective functions of infeasible solutions, to make them less *attractive* to the algorithm, as compared to feasible solutions [56, 143]. It is, however, challenging to tune the penalty factors that relate the constraint violations to objective functions [12]. If the penalty functions are too large, the search will struggle to explore the boundary between the feasible and infeasible region; if they are too small, too much time can be spent exploring the infeasible region.

To handle constraints without penalty factors, Deb et al. proposed a *constrained-domination* principle, which can be directly incorporated within the selection operator of the evolutionary algorithms. The modified selection process is based on the following principles:

1. If both individuals are feasible, the Pareto-dominance concept determines which individual is selected.

2. If one individual is feasible and the other is not, the feasible individual is selected.

3. If both individuals are infeasible, the individual with lower total constraint violation is selected.

In order to determine total constraint violation, individual constraint violations c_i are first normalised as:

$$c_i(\vec{x}) = \begin{cases} \min(1, g_{i,max}/g_i(\vec{x})), & \text{if } g_i(\vec{x}) \text{ has to be } \leq g_{i,max}; \\ \min(1, g_i(\vec{x})/g_{i,min}), & \text{if } g_i(\vec{x}) \text{ has to be } \geq g_{i,min}. \end{cases} \tag{6.5}$$

where g are the constrained variables. The total constraint violation c_{tot} is the sum

of the individual constraint violations, as:

$$c_{tot}(\vec{x}) = \sum_{i=1}^{o} c_i(\vec{x}) \tag{6.6}$$

where o is the total number of individual constraints. No penalty factors are needed using this constraint handling technique, and infeasible solutions are penalized in a way such that they still provide a search direction towards the feasible region. This technique is possible mainly due to the population approach of the evolutionary algorithms and their selection operators, and it is employed in this work.

6.3 Case Study: GDE3 Optimisation of Motor Drive

This section presents a case study looking at applying the GDE3 algorithm for a motor drive optimisation, in order to illustrate the concepts presented thus far.

6.3.1 Benchmark System

The benchmark for optimisation in this case study is a motor drive with the prototype surface PM machine rated at 1350 W and 1500 rpm (from Chapter 3) and two-level converters with Infineon IGBT4 FS50R12KT4 power modules, rated at 1200 V and 50 A (from Chapter 4). The 50 A switching devices are considerably oversized for the considered motor drive, but this is not a huge concern as the device loss characteristics are kept fixed throughout the optimisation. The associated heatsink is a Fischer Electronik LA6 forced-convection cooling system while the passive components are 0.5 mH toroidal-core single-layer inductors, made of Mega Flux 60 core material, and a 0.5 mF MKPB32778G polypropylene DC-link capacitors.

6.3.2 Optimisation Setup

The motor drive model from previous chapters is employed in this optimisation case study, and two objective functions are considered, i.e. the combined weight w_{tot} and total losses $P_{l,tot}$ of the motor drive.

Based on guidelines from Section 6.2.2, a total of 14 design variables are chosen from a combined set of input parameters provided in Chapter 3 and Chapter 4. The selected design variables are listed in Table 6.1, and three independent optimisation runs are performed for motor drive optimisations at both component and system-levels. For each optimisation run, a different set of these design variables is employed:

1. The first optimisation considers only machine-related design variables, leaving the converter-related ones fixed at their default values.

2. The second optimisation takes into account only converter-related design variables, keeping the machine-related ones fixed at their default values.

3. The third optimisation uses all machine and converter design variables.

Meanwhile, ten constraints are imposed onto the motor drive output performances, to ensure that the design solutions comply with the requirements and that they are feasible, i.e. temperature limits not exceeded, magnetic materials not saturated, etc. These constraints are listed in Table 6.2

The GDE3 algorithm employed in this case study is set up with a crossover rate and scaling factor of 0.2 and 0.5, respectively, according to the recommendations in [141]. For each optimisation run, a large population size of $\mathcal{N} = 200 \times n_d$ is used, where n_d is the number of design variables, and the optimisation is limited to a maximum number of g_{max}= 2000 generations.

For ease of integration, the motor drive analytical models and optimisation algorithm are coded entirely in Matlab. Besides, the Matlab Parallel Computing toolbox allows the use of multicore desktops to speed up the evaluation process incredibly. Calculations for this case study are performed on a High Performance

Table 6.1: Selected design variables for case study.

Symbol	Design Variables	Symbol	Design Variables
Machine-related		i_{do}:	d-axis machine current
l:	Axial length of machine	i_{qo}:	q-axis machine current
N_t:	No. of turns in series/phase	**Converter-related**	
w_{dia}:	Wire diameter	V_{dc}:	DC-link voltage
d_m:	Depth of permanent magnet	f_{swv}:	VSI switching frequency
d_{tb}:	Depth of stator tooth	f_{swa}:	AFE switching frequency
d_{sb}:	Depth of stator backiron	L_b:	Input boost inductance
α_t:	Stator tooth fraction	C_{dc}:	DC-link capacitance

Computing (HPC) facility at the University of Nottingham, on computer nodes equipped with 2 × Intel Xeon Gold 6138 20-core processors. The average time taken to run the full motor drive analytical model once is 0.03 seconds. Thus, for the third optimisation run, where 14 design variables are considered with a total of $14 \times 200 \times 2000 = 5.6$ million evaluations, the optimisation is typically completed in less than 1.5 hours.

Default input parameters for the benchmark motor drive are listed in Fig. 6.1, along with objective functions and constrained performances calculated using the motor drive analytical model. For this optimisation case study, the design variables' search space boundaries are chosen to be around the default input parameter values while the default constrained performances are enforced as constraints for a fair assessment of the final optimisation outcome. In other words, given the same machine output torque, slot packing factor, flux densities, temperatures, converter current ripple magnitudes, and DC-link voltage overshoot requirements, the optimisation has to seek for better design solutions.

Table 6.2: Constraints for case study.

Symbol	Constraints
$\tau_{e,min}$	Minimum machine output torque
$\%\Delta i_{pp,max}$	Maximum input current ripple percentage
$\%V_{dco,max}$:	Maximum DC-link voltage overshoot percentage
$k_{pf,max}$	Maximum machine slot packing factor
$T_{w,max}$	Maximum machine winding temperature
$T_{pm,max}$	Maximum permanent magnet temperature
$B_{st,max}$	Maximum stator tooth flux density
$B_{sb,max}$	Maximum stator backiron flux density
$M_{v,max}$	Maximum VSI modulation index
$M_{a,max}$	Maximum AFE modulation index

6.3.3 Analysis of Optimisation Results

The Pareto fronts from the optimisation runs are plotted together in the performance space in Fig. 6.2. The results reveal a wide range of design solutions, which offer good improvements over the default benchmark design, in terms of weight and losses, while maintaining the same constrained performances. These improvements are most significant with the system-level optimisation, where machine and converter-related design variables are simultaneously optimised, as compared to the component-level optimisations.

A general criticism of optimisation-based designs is that the engineer can easily lose track of the optimisation process and find it difficult to interpret the final solutions. For clarity and visibility of the design trends, two supplementary plots to visualise the optimisation process are recommended, in addition to the performance space plot:

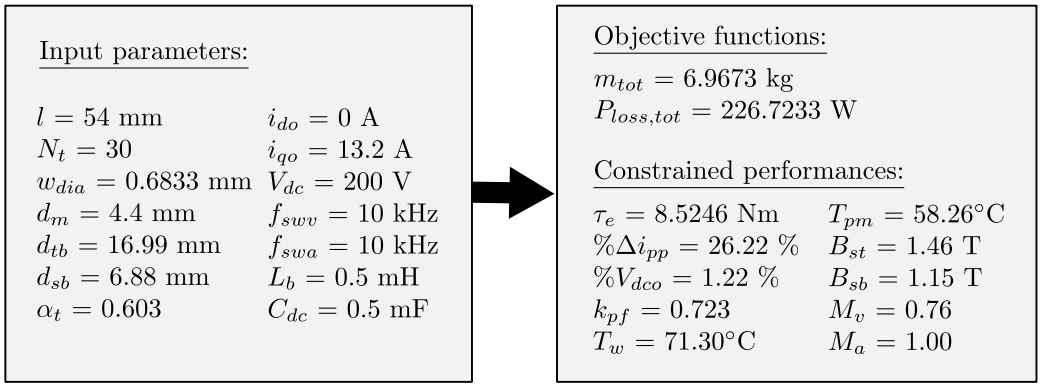


Figure 6.1: Default input parameters and performance-related outputs of benchmark motor drive.

- Plot of design variables for Pareto front solutions, as shown in Fig. 6.3(a), normalised to the upper and lower limits of their search space.
- Plot of constrained performances for Pareto front solutions, as shown in Fig. 6.3(b).

In both figures, the lower weight individuals are to the left in each window, while lower loss individuals are to the right.

In Fig. 6.3, it is observed for the machine optimisation (component-level) that there is a trend of increasing machine stator tooth depth and wire diameter, for lower loss solutions. This is because larger wire diameter results in lower winding resistances, but requires bigger slot areas to accommodate the windings without violating the slot packing factor constraint. This results in a larger machine diameter and improved cooling performance; therefore, lower winding and magnet temperatures are also obtained.

For machine component-level optimisation, the increase in output torque for lower loss solutions is, however, unexpected. This is due to the fixed converter current ripple percentage constraint, which is inversely proportional to its fundamental input current component. For machines with lower loss, despite the smaller stator currents required to produce the same output torque, the optimisation maintained

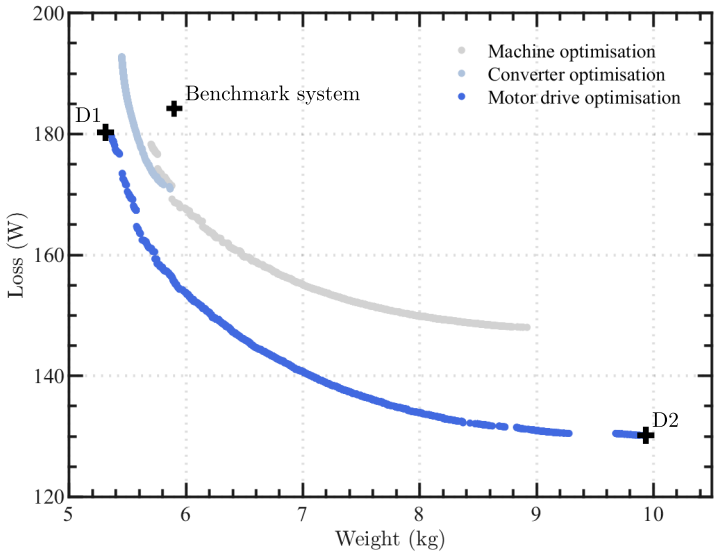


Figure 6.2: Pareto front solutions for the three optimisation runs with different set of design variables. D1 and D2 are two solutions chosen for further software verifications.

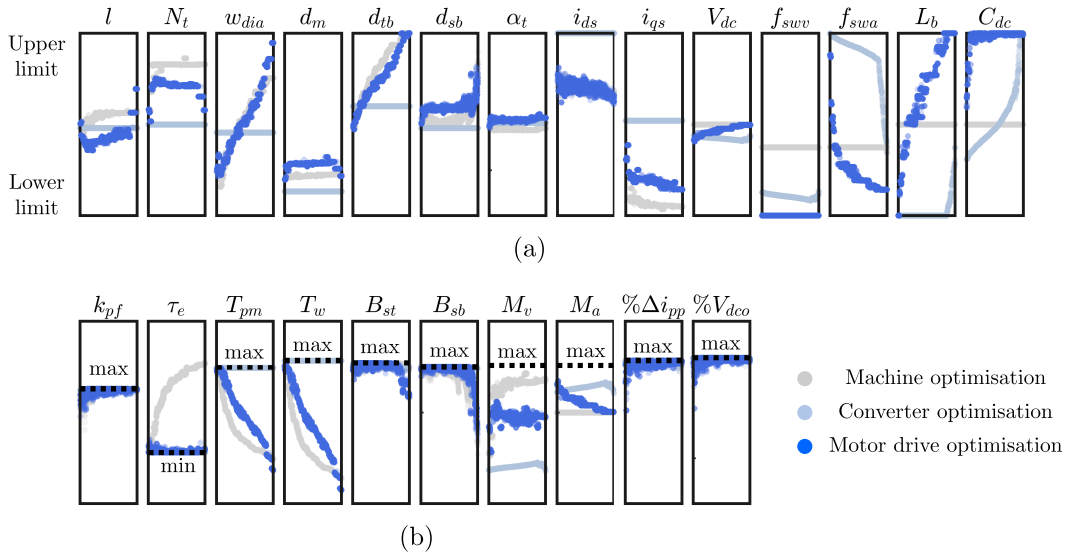


Figure 6.3: (a) Normalised design variable values and (b) constrained outputs of all Pareto front solutions (Left: lowest weight, Right: lowest loss).

the converter fundamental input and output currents, as to not violate the input current ripple constraint. Therefore, this leads to an increase in the output torque obtained.

For the converter optimisation (component-level), the inverse relationship of AFE switching frequency against boost inductance is observed. For lower loss solutions, the AFE switching frequency is reduced to decrease switching losses, but at the same time, boost inductance and DC-link capacitance are increased, as to not violate the current ripple and DC-link voltage overshoot constraint.

Unexpectedly, for converter component-level optimisation, it is observed that the VSI switching frequency is not set to the smallest possible value for this optimisation, despite switching losses being much more significant compared to machine harmonic losses under loaded conditions. This is because for a fixed machine design and machine current, increasing machine harmonic losses reduces the output torque. Thus, for low converter switching frequencies, the increased machine losses caused a violation in the torque constraint.

Finally, for motor drive optimisation (system-level), a similar increasing trend in machine stator tooth depth and wire diameter is observed for lower loss solutions, as with the inverse relationship between AFE switching frequency against boost inductance. However, the interactions between component parameters and constraints at a system-level can be better managed, especially in terms of the input current ripple and output torque constraints. Therefore, a significantly improved total weight and efficiency of the motor drive can be obtained.

The above illustrates the importance of plotting and visualising the design variable and constrained performances of the optimisation, to better understand the different phenomena that can arise and to explain design trends, that are sometimes unexpected.

6.3.4 Verification of Design Solutions

Two design solutions from the whole drive optimisation Pareto front are selected for further software verifications. They are the lowest weight (D1) and lowest loss (D2) solutions of the Pareto front, as indicated in Fig. 6.2. The design variables, constrained performances, and objective functions for the design solutions, as compared to the default benchmark solution, are listed in Table 6.3.

Figure 6.4 shows the weight and loss distributions of the two design solutions. It can be seen for D1 that the majority of weight savings are due to smaller boost inductors. For D2, inductor weight is increased significantly, compared to D1, as its AFE operates with lower switching frequencies, to improve efficiency while maintaining the input current ripple magnitudes. Machine weight is also slightly larger for D2 as it employs bigger magnets to ensure that sufficient flux linkage is created, despite its lower stator currents for higher efficiency.

Finite-element analysis and time-domain simulations are employed to validate the design solutions, in terms of the machine and converter performances. The results are reported in Table 6.4 and an accurate match is revealed, once again, highlighting the accuracy of the motor drive analytical models.

6.3.5 Effect of Fixed Input Parameters

To evaluate the impact of fixed input parameters of a discrete nature, their values are changed in steps and the optimisation process is repeated for a new set of fixed input parameters at each step. Six examples are considered in this section, as follows:

Machine operating points

Pareto front optimisation results for motor drive operating at different speeds in the constant power region are shown in Fig. 6.5. A comparison of their Pareto fronts reveal that higher speed motor drives are superior, in terms of weight but not in terms of efficiency.

Table 6.3: Input parameters, constraints, and objective functions of the benchmark, D1 (least weight), and D2 (least losses) design solutions.

Symbol	Benc.	D1	D2	Symbol	Benc.	D1	D2
Design Variables				**Constraints**			
l (mm)	54	55.3	64.7	τ_e (Nm)	8.52	8.53	8.53
N_t (-)	30	32.5	32.4	$\%\Delta i_{pp}$ (%)	26.22	26.04	26.12
w_{dia} (mm)	0.6822	0.5977	0.8790	$\%V_{dco}$ (%)	1.22	1.21	1.22
d_m (mm)	4.4	5.6	5.9	k_{pf} (-)	0.723	0.72	0.723
d_{tb} (mm)	16.99	14.7	25.0	T_w (°C)	71.4	70.21	42.86
d_{sb} (mm)	6.88	7.00	8.9	T_{pm} (°C)	58.3	58.07	36.88
α_t (-)	0.60	0.596	0.615	B_{st} (T)	1.47	1.46	1.41
i_{do} (A)	0	-1.30	-1.7	B_{sb} (T)	1.15	1.15	0.91
i_{qo} (A)	13.2	11.07	9.44	M_v (-)	0.76	0.95	0.99
V_{dc} (V)	200	183.14	199.50	M_a (-)	1.00	1.09	1.00
f_{swv} (kHz)	10	4	4	**Objective functions**			
f_{swa} (kHz)	10	18.1	6.29	w_{tot} (kg)	5.90	5.32	9.91
L_b (mH)	0.5	0.2	0.8	$P_{l,tot}$ (W)	184.21	180.07	130.15
C_{dc} (mF)	0.5	0.557	0.795				

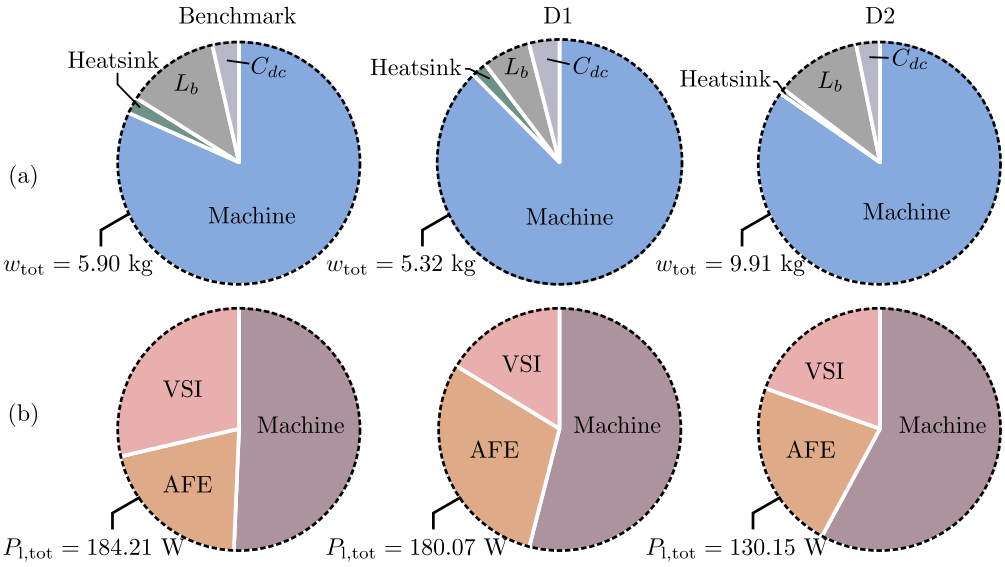


Figure 6.4: Plot of (a) weight and (b) losses distribution for the benchmark, D1 (least weight), and D2 (least losses) design solutions.

Table 6.4: Software verifications for the benchmark, D1 (least weight), and D2 (least losses) design solutions.

Symbol	Benc.		D1		D2	
	Ana.	**Sim.**	**Ana.**	**Sim.**	**Ana.**	**Sim.**
Phase resistance (mΩ)	238.3	217.4	340.4	308.7	176.8	161.6
Inductance (mH)	2.22	2.28	2.61	2.55	3.11	3.18
Rated speed open-circuit BEMF (V)	48.93	47.96	58.47	57.13	69.42	67.71
Rated output torque (Nm)	8.53	8.41	8.53	8.47	8.53	8.56
VSI total losses (W)	52.79	54.84	29.34	30.01	25.51	25.57
AFE total losses (W)	38.08	37.86	53.53	52.70	29.32	30.05
Maximum input pk-pk current ripple (A)	2.50	2.44	2.45	2.45	2.47	2.44
Maximum DC-link voltage overshoot (V)	202.4	203.73	185.4	185.98	201.9	203.26

According to the search space and constrained performance space plots in Fig. 6.6, weight improvements is mostly attributed to the smaller machine diameter and shorter axial length, enabled by the lower torque and flux linkage requirements.

It is interesting to observe that optimal winding currents, $\hat{i}_d$ and $\hat{i}_q$, vary only within a very small range for all the design solutions, despite variations in torque requirements for different operating points. This shows that, in the optimisation, machine winding currents of optimal design solutions are less dependent on torque requirements, as compared to other factors such as tooth thickness, temperature constraints, etc.

Machine slot-pole combinations

Pareto front optimisation results for machines with different slot-pole combinations are shown in Fig. 6.7. The comparison shows that motor drives with 18-slot 16-pole are the best designs in terms of weight, while the 12-slot 10-pole outperforms the other configurations in terms of efficiency.

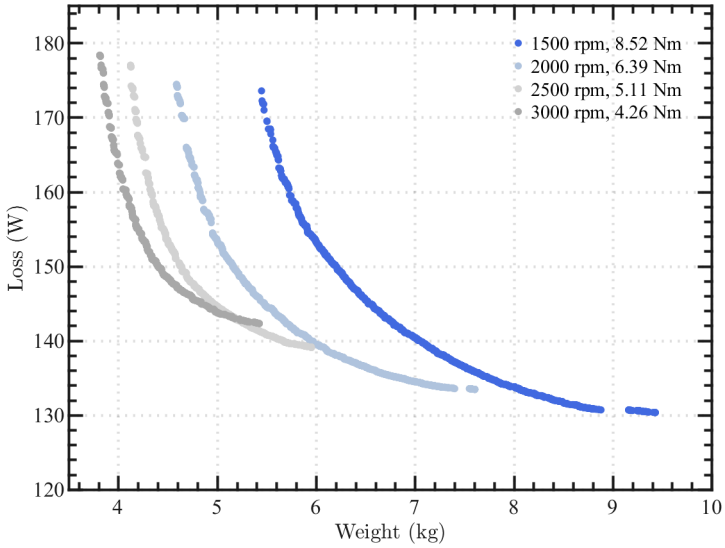


Figure 6.5: Pareto front solutions for motor drive optimisation with different machine operating points in the constant power region.

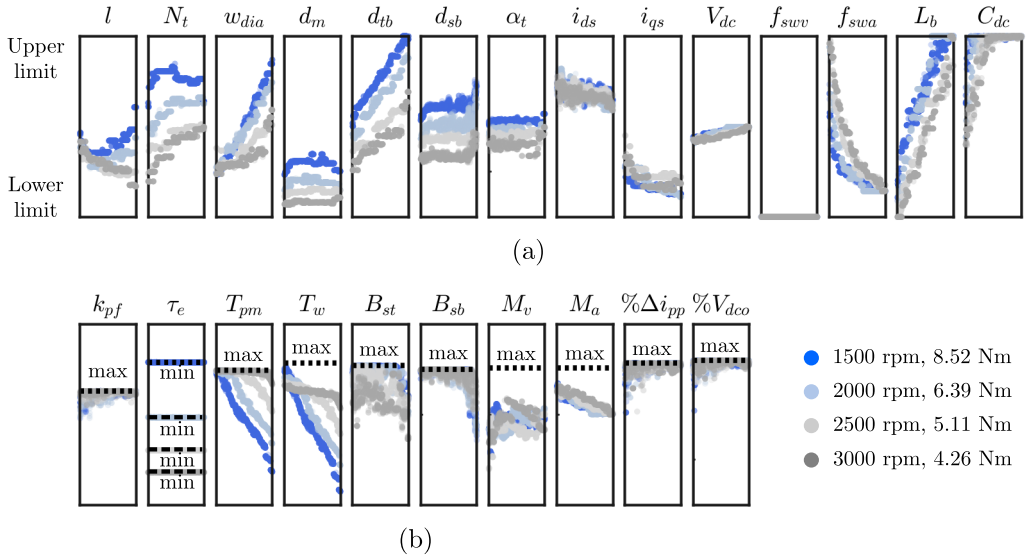


Figure 6.6: (a) Normalised design variable values and (b) constrained outputs of Pareto front solutions with different machine operating points in the constant power region (Left: lowest weight, Right: lowest loss).

This observation is further analysed by considering the search space and constrained performance space plots in Fig. 6.8. As the 18-slot 16-pole and 18-slot 20-pole configuration have the highest fundamental winding factor compared to the others, a smaller number of turns is required to achieve the same flux linkage in the machine. This allows the use of smaller slot areas and stator outer diameter, leading to a reduced machine weight. The 12-slot configurations, however, are able to accommodate winding conductors with larger wire diameters and lower resistances, because of its bigger slot-to-tooth area ratio, compared to the 18-slot configuration for the same machine diameter. Therefore, they are able to achieve higher efficiencies.

Devices current ratings

The impact of using switching devices with different current ratings can also be analysed using this optimisation-based design method. The Pareto front optimisation results for converters employing devices rated at 25, 50, and 75 A are shown in Fig. 6.9.

On the surface, machine and converter design parameters for all three Pareto optimal solutions are similar. However, taking a deeper look into the conduction and switching losses of the devices with different current ratings, the 25 A devices suffer from having high conduction losses while the 75 A devices have high switching losses. This is expected as the smaller current rating devices have small chip areas (higher on-state resistances), while the higher current rating devices have large chip areas (high parasitic capacitances), leading to higher switching energies. The comparison shows that the solutions using 50 A devices are the best, in terms of system weight and efficiency.

Converter modulation method

The impact of converter modulation method is also evaluated with this optimisation method. The Pareto front optimisation results for the Symmetrical SVM and DPWM1 methods are shown in Fig. 6.11.

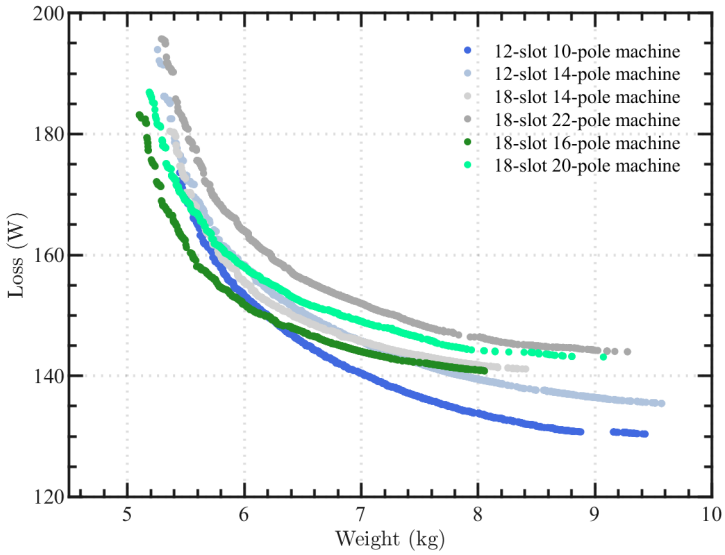


Figure 6.7: Pareto front solutions for motor drive optimisation with different machine slot-pole combinations.

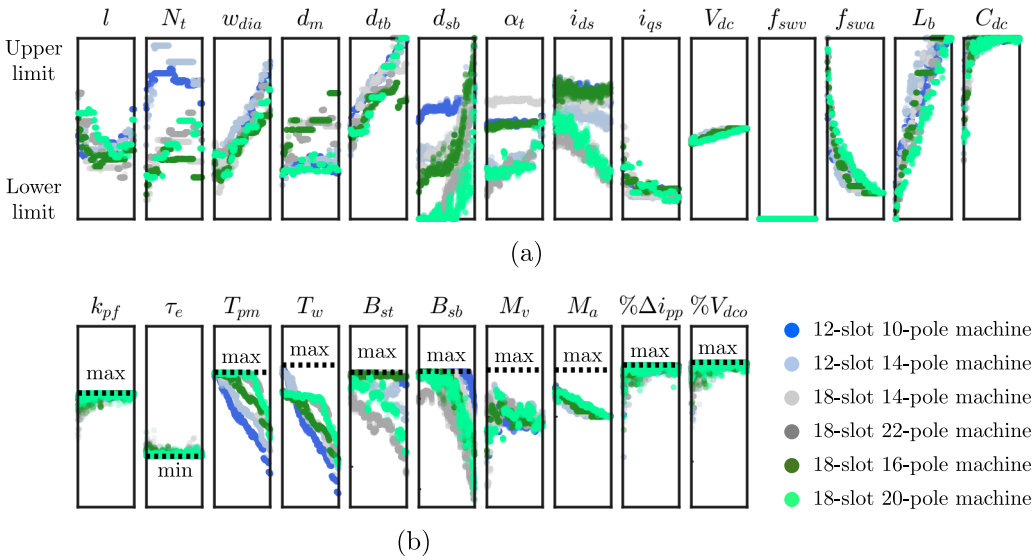


Figure 6.8: (a) Normalised design variable values and (b) constrained outputs of Pareto front solutions with different machine slot-pole combinations (Left: lowest weight, Right: lowest loss).

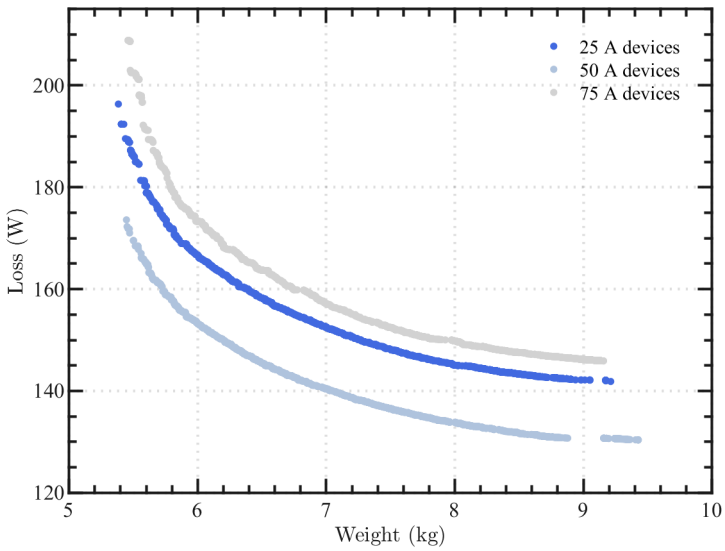


Figure 6.9: Pareto front solutions for motor drive optimisation with switching devices of different current ratings.

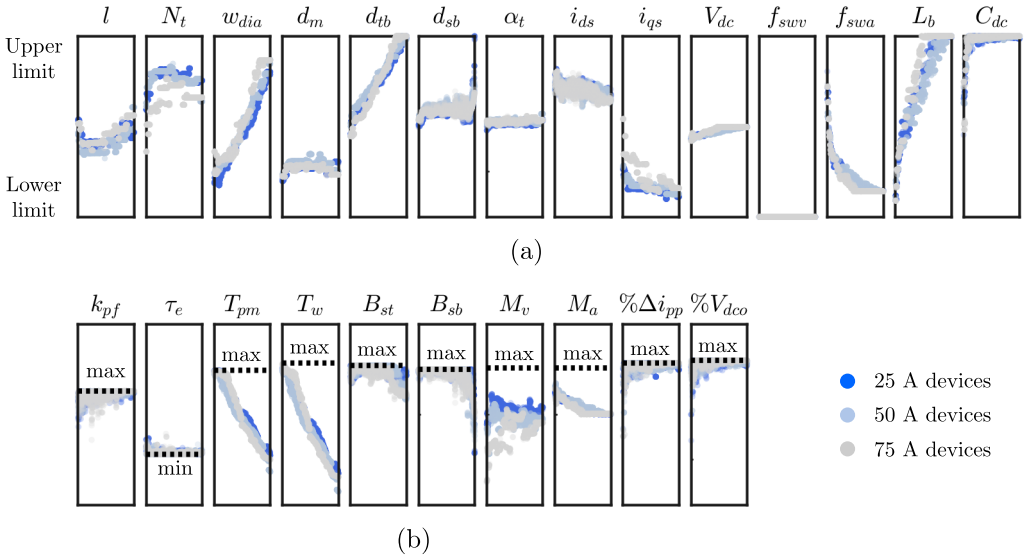


Figure 6.10: (a) Normalised design variable values and (b) constrained outputs of Pareto front solutions with switching devices of different current ratings (Left: lowest weight, Right: lowest loss).

For losses, as explained in Chapter 4, DPWM1 has significantly smaller switching losses, due to its periodic clamping of the switches, but this results in higher current ripple magnitudes. As observed in Fig. 6.12, the minimum AFE switching frequency is higher for DPWM1 method, as required for the design solution to not violate the current ripple constraint. This, subsequently, increases the switching instances of the converter. Nevertheless, the Pareto front comparison shows that the solutions using DPWM1 modulation still results in slightly better overall performances, especially in terms of efficiency.

Converter AC grid input voltage

Lastly, the influence of converter AC grid input voltage is studied and the Pareto front optimisation results for different grid input voltages are shown in Fig. 6.13. The results show that the best motor drive performance can be obtained when grid input voltage is either 100 or 120 V.

According to the design variables and constrained performances plots in Fig. 6.14, the optimal DC-link voltage is significantly influenced by the choice of grid input voltage. This subsequently influences machine voltage, which is a function of number of turns, and q-axis current. The 60 V grid input voltage system, due to higher input and output currents, suffers from more machine and converter conduction losses, while the 140 V grid input voltage system, due to its higher DC-link voltage, has higher converter switching losses.

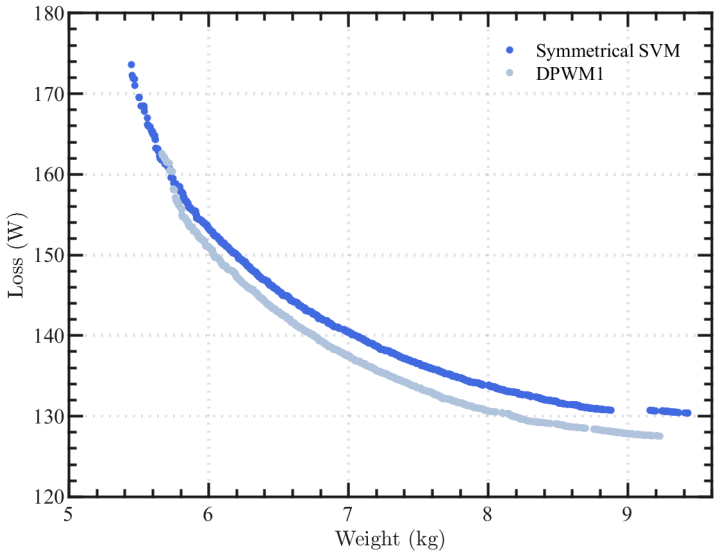


Figure 6.11: Pareto front solutions for motor drive optimisation with different converter modulation methods.

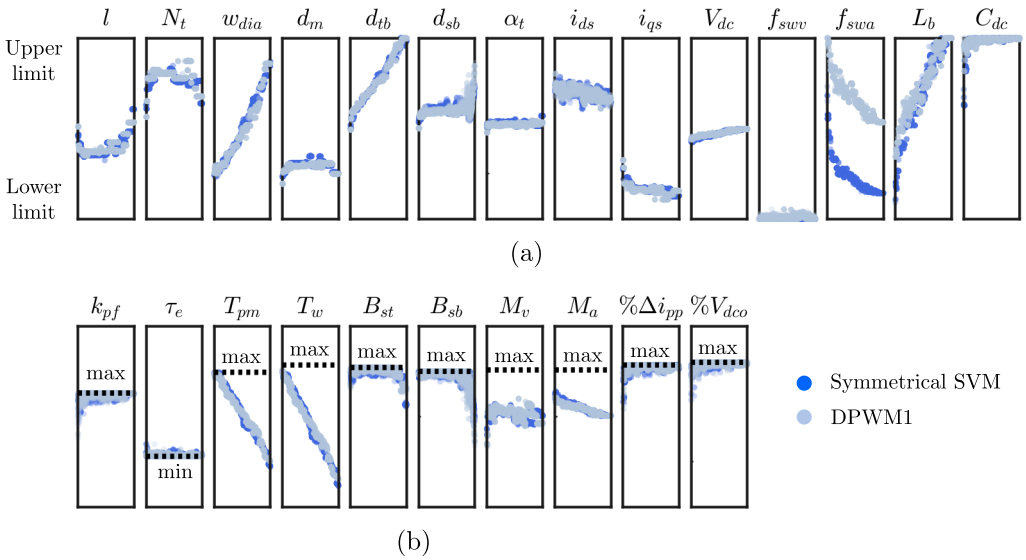


Figure 6.12: (a) Normalised design variable values and (b) constrained outputs of Pareto front solutions with different converter modulation methods (Left: lowest weight, Right: lowest loss).

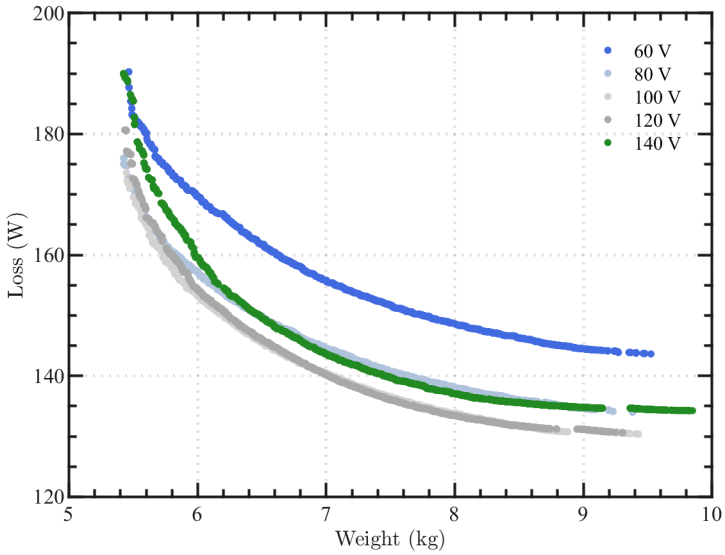


Figure 6.13: Pareto front solutions for motor drive optimisation with different converter AC grid input voltages.

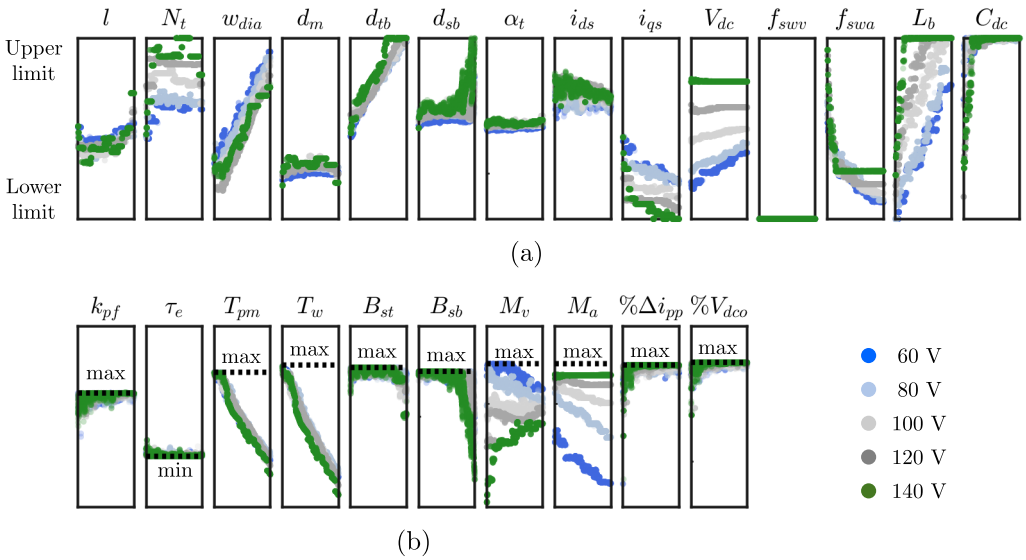


Figure 6.14: (a) Normalised design variable values and (b) constrained outputs of Pareto front solutions with different converter AC grid input voltages (Left: lowest weight, Right: lowest loss).

6.4 Comparison of EMO algorithms

In the field of evolutionary computing, different metrics or quality indicators are employed to capture the essential characteristics and compare the performance of different algorithms for specific problems [144]. In this section, the three EMO algorithms (NSGAII, SMPSO, and GDE3) are benchmarked against each other firstly using test functions, and then using the motor drive optimisation problem of Section 6.3, to compare their performances.

The metric or quality indicator employed is the Inverted Generational Distance (IGD), which reports the average distance between the approximated Pareto front and the 'true' Pareto front. The main advantage of using IGD is its computational efficiency. Given the approximated Pareto front and true Pareto front, IGD is calculated as follows:

$$IGD = \frac{1}{n}\sqrt{\sum_{i=1}^{n} d_i^2} \tag{6.7}$$

where n is the number of elements in the true Pareto front, and d_i is the Euclidean distance between each of these elements and the nearest member of the set of non-dominated solutions found by the algorithm.

6.4.1 Test Functions

Ten test functions (five unconstrained and five constrained), proposed by Zitzler et al. and Deb et al. [144, 145], are considered here.

The three optimisation algorithms are configured to run with a maximum number of 200 generations and population size of 200. For the NSGAII algorithm, the crossover and mutation probability indices are chosen to be 0.9 and $1/n_d$, respectively, where n_d is the number of design variables, and its crossover and mutation distribution factors are both set to 20, based on recommendations from [137]. For the SMPSO algorithm, the inertia constant is a random value between 0.1 and 0.5, while the

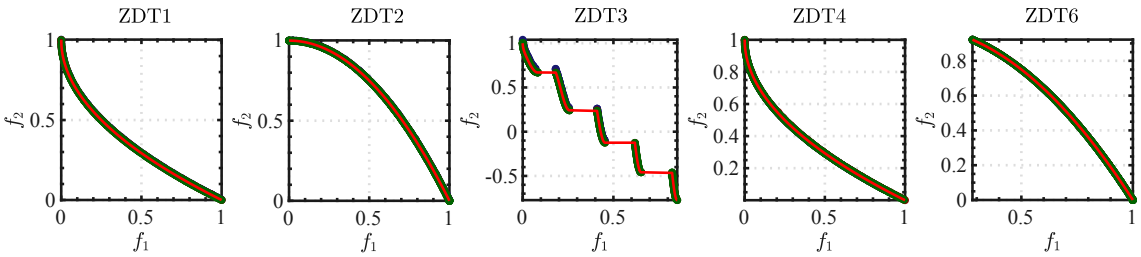
personal and global acceleration constants are also random values between 1.5 and 2.5, as recommended by [139]. For its polynomial mutation operator, the mutation probability index is set as $1/n_d$ with a distribution factor of 20. Finally, for the GDE3 algorithm, the crossover rate is set as 0.2 while the scaling factor is 0.5, based on guidelines in [141].

Due to the stochastic nature of the optimisation algorithm, the final solutions found in each run may not be the same. Therefore, ten independent optimisation runs are performed for each algorithm to provide a comparison with statistical confidence. From a qualitative point of view, the best Pareto-optimal results for each algorithm run for each test function are plotted in Fig. 6.15, and all optimisation algorithms are shown to be capable of solving the test functions. For a quantitative analysis, the IGDs calculated from ten independent optimisation runs are tabulated in Table 6.5, and, at first glance, the three optimisation algorithms appear to be very competitive. However, comparing their IGD values by highlighting the best performing algorithm for each test function, the GDE3 algorithm outperformed the other two algorithms in most of the test cases.

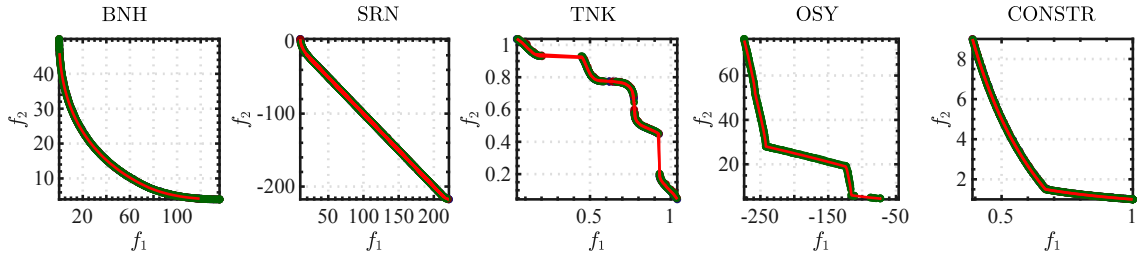
6.4.2 Motor Drive Optimisation Problem

The motor drive optimisation problem from Section 6.3 is also considered as a benchmark for the EMO algorithms. The optimisation algorithms are configured slightly different to run for a maximum number of 100 generations with have a population size of $100 \times n_d$ particles, where n_d is the number of design variables. The same optimisation parameters as before, for the NSGAII, SMPSO, and GDE3, are employed for this test.

For IGD calculations, it is important to note that as the 'true' Pareto front of the motor drive optimisation problem is unknown, a best-known Pareto front (BPF) is employed here instead. The BPF selected for this analysis is the Pareto front found by GDE3 in Section 6.3.3, obtained with 2000 generations and $200 \times n_d$ particles.



(a)



(b)

Figure 6.15: Plot of Pareto fronts for (a) unconstrained (b) constrained test functions solved by the EMO algorithms (red line indicates the true solution).

Table 6.5: Average IGD values for test functions.

Test Function	**NSGAII**		**SMPSO**		**GDE3**	
	Avg.	**Std.**	**Avg.**	**Std.**	**Avg.**	**Std.**
ZDT1	0.0039	7.96e-4	0.0024	1.17e-4	0.0020	5.94e-5
ZDT2	0.0060	0.0026	0.0024	4.96e-5	0.0022	2.78e-4
ZDT3	0.0784	0.0486	0.0025	8.24e-5	0.0035	1.73e-4
ZDT4	0.0482	0.0875	0.0025	8.30e-5	0.0019	5.57e-5
ZDT6	0.0027	0.0015	0.0019	1.28e-4	0.0024	8.73e-5
BNH	0.1935	0.0133	0.2127	0.0073	0.1895	0.0148
SRN	0.4293	0.0228	0.4946	0.0198	0.3704	0.0120
TNK	0.0024	1.24e-4	0.0048	2.94e-4	0.0027	1.83e-4
OSY	7.1591	6.6490	17.1206	3.6912	5.7891	5.9230
CONSTR	0.0104	2.60e-4	0.0087	2.1647	0.0083	1.6933e-4

* Best performing algorithm for each test function is highlighted in yellow.

This is a reasonable approach as all EMO algorithms are expected to converge towards the same Pareto front given a sufficiently large number of generations and particles.

Employing the same statistical approach, the optimisations are repeated ten times for each algorithm. The IGD results after 100 generations are tabulated in Table 6.6, and a plot of average IGD against number of generations is shown in Fig. 6.16. For the considered number of generations, the best performing algorithm is found to be the SMPSO algorithm, as it resulted in the lowest average IGD value (0.8126) with also the smallest standard deviation (0.2767), as compared to the NSGAII (avg: 1.0216, std: 0.6524) and GDE3 (avg: 1.3431, std: 0.4629).

Based on the above analysis, it is shown that the choice of optimisation algorithm does matter, due to their different working principles. For the motor drive optimisation problem, given a small maximum number of generations, the implemented SMPSO algorithm is the most suitable, due to its convergence speed, accuracy, and consistency.

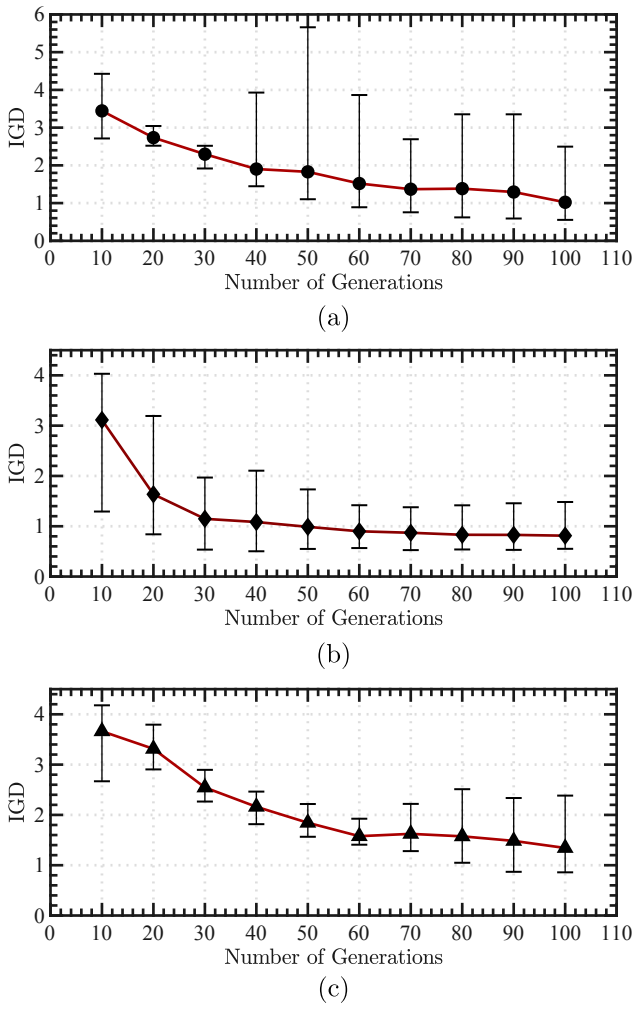


Figure 6.16: Plot of IGD values averaged over 10 independent runs against number of generations for motor drive optimisation problem with (a) NSGA2 (b) SMPSO (c) GDE3 algorithm.

Table 6.6: Average IGD values for the motor drive design problem.

Test Function	**NSGAII**		**SMPSO**		**GDE3**	
	Avg.	**Std.**	**Avg.**	**Std.**	**Avg.**	**Std.**
Motor drive design	1.0216	0.6524	0.8126	0.2767	1.3431	0.4629

* Best performing algorithm is highlighted in yellow.

6.5 Chapter Summary

This chapter demonstrated the use of the advanced models from previous chapters together with EMO algorithms for multiobjective motor drive design. Firstly, the working principles of three popular EMO algorithms (NSGAII, SMPSO, and GDE3) were reviewed, and the differences in their search and exploration approach were highlighted. GDE3 was the easiest to implement as it has the least number of optimisation parameters to tune. Next, practical guidelines for applying EMO to a motor drive design were given. In particular, selection criteria of design variables, identification methods for Pareto front solutions, and constraint handling techniques were discussed, for the effective use of EMO algorithms.

A case study was also carried out, looking at the multiobjective optimisation of a benchmark motor drive, consisting of the prototype machine and converter from Chapters 3 and 4. Optimisation results show that good improvements, in terms of weight and losses, are obtained. The improvements are especially significant when the machine and converter are optimised at a system-level, rather than individually as components. The lowest weight and lowest loss solutions of the Pareto front were further verified using software to check that the results are accurate.

Finally, the performance of the three EMO algorithms were compared with statistical confidence, to determine the most suitable algorithm for a multiobjective motor drive design problem. Results show that although the GDE3 algorithm outperformed the other two algorithms in the test function benchmarks, the SMPSO algorithm is the most competitive for the motor drive design problem, in terms of convergence and average IGD value, for the considered maximum number of generations.

Chapter 7

Conclusions

This chapter reviews the most important findings of this thesis and suggests potential future topics to be studied in this area of research.

With an expected growth in air travel over the next decade and increasingly stringent regulations for carbon emissions, the aerospace industry is looking at flight electrification as a means to reduce its environmental impact, improve fuel efficiency, and lower operating costs. A significant challenge concerning the realisation of many flight electrification concepts is to achieve light-weight and efficient motor drives, which are required for electromechanical power conversion on-board. This thesis presented an advanced modelling and multiobjective optimisation framework for motor drive designs using evolutionary algorithms, with a focus on minimising their weight and losses, with a system-level approach.

This work considers motor drives with a surface permanent magnet (SPM) machine and two-level voltage source back-to-back converter, for high power density aerospace applications. As discussed in Chapter 2, motor drive design and optimisation work available in the literature are found mostly to focus on either the machine or converter at a component-level, resulting in cross-coupling effects between components being neglected and, therefore, suboptimal system-level performance. Further, evolutionary algorithms are emerging, in terms of popularity for use in design optimisation, due to their effectiveness in handling complex problems. However,

the choice and proper setup of these algorithms are rarely considered in existing work, often leading to an inefficient utilisation of computational resources. This prevents the designer from considering many design input variables, constraints, and objectives. These observations formed the primary motivation of this research, to present a comprehensive system-level model for motor drives and to provide practical guidelines for optimising their design using EMO algorithms.

The analytical model developed for the SPM machine employs a combination of different techniques to represent its multiphysics operation in a fast and accurate manner, as described in Chapter 3. In particular, to evaluate its electromagnetic performance, a closed-form approach is employed to compute machine air-gap magnetic field distribution, which subsequently allows its back-EMF, inductance, and torque to be characterised. However, the limitation with this approach, as compared to a FE approach, is that local magnetic saturation effects are ignored and, therefore, it is only valid for SPM machines, where rotor saturations are negligible. To predict the machine's thermal behaviour, a simplified lumped parameter thermal network (LPTN) is implemented, exploiting stator slot symmetries to estimate machine winding and magnet temperatures. The main challenge with using LPTNs, however, is that they rely on thermal resistance values, which are difficult to accurately determine. Overall, this modelling approach is found to be simple and sufficiently accurate for SPM machines, as verified extensively using FE and experimental analysis.

The voltage source back-to-back converter, on the other hand, is modelled by first evaluating its modulation and control properties, as discussed in Chapter 4. Device current information, obtained from this analysis, then allows the converter semiconductor losses to be estimated. Physics-based sizing models for the associated cooling system and passive components are also proposed, with coefficients determined using data of commercially available products. Due to its simple structure, the modelling approach employed can be easily extended to consider other topologies, such as a multi-level converter, Vienna rectifier, etc. Similar to the machine model, accuracy of the converter model is validated using time-domain simulations and

experimental analysis.

For system-level designs, the complex and multiphysics interactions between the motor drive components are also important to consider. In Chapter 5, the extra high frequency harmonic losses in the PM machine, due to converter pulse-width modulation (PWM), are modelled, using a new physics-based machine harmonic loss model that assumes dominant eddy-current loss over conductor and hysteresis losses at high harmonic frequencies. As with other harmonic loss representations, this model requires experimental calibration, using machine harmonic loss data measured under rated speed no-load conditions. Another important system-level effect to consider is the impact of DC-link voltage on overall system efficiencies, especially for a back-to-back converter, where it can be optimised. It was shown that for operations in the constant torque region, it is desirable to have a low DC-link voltage, while for the constant power region, a high DC-link voltage is better, to avoid the need for field-weakening.

Based on the motor drive component and system-level analytical models, a multiobjective design optimisation was performed next. In Chapter 6, the working principles of popular EMO algorithms, namely the NSGAII, SMPSO, and GDE3 were discussed. The three algorithms are stochastic in nature, and although they are similar in their population-based approach and use of random variables, their search mechanisms are distinctive from each other. Practical guidelines for their application in a motor drive optimisation, in terms of search space definition, performance space mapping, and constraint handling, were presented. These concepts were illustrated in a practical motor drive optimisation case study, employing the prototype motor drive in Chapter 5 as a benchmark. Additional visualisation plots are proposed and discussed for the optimisation outcome, as it is very important that the designer understands the various trends that emerge, to gain further confidence in the results. Lastly, the EMO algorithms are benchmarked against each other, and it is shown, with statistical evidence, that SMPSO outperforms NSGAII and GDE3 for the motor drive optimisation problem, in terms of convergence for the selected number

of generations. As the analytical models and optimisation algorithms are all coded in Matlab, calculations were done utilising parallel cores in a high performance computing facility, allowing for significant savings in the amount of computational time required.

Returning to the problem statement posed at the beginning of this study, a system-level motor drive modelling and optimisation-based design approach has been presented in this work. The success of this approach, however, depends greatly on the modelling speed and accuracy, along with a correct implementation of the optimisation algorithms. The proposed methodologies should serve as a useful reference for engineers, not limited to the aerospace industry, to design weight and efficiency optimised motor drives, benefiting from the increasing availability and capability of modern computing.

7.1 Further Work

Due to a limitation of time, several aspects of this research were unfortunately not covered adequately, and further research can be done in the following areas:

- Many practical concerns of an aerospace-related motor drive, such as reliability, fault-tolerance, high-temperature operations, etc., were not considered in this model, as this thesis focused on establishing a generic framework for power density and efficiency optimisations. Consequently, a standard motor drive test rig, as opposed to an aerospace one, was employed to verify the analytical models used. To take this work forward, more advanced models, which are specific to certain aerospace applications and verified using real aerospace hardware, can be developed and 'plugged' into this optimisation framework.

- The closed-form analytical machine model employed in this work is fast, but it does not account for magnetic saturation effects. To consider saturation, magnetic reluctance networks or FE models are typically used. However, they

are considerably slower and are hence not suitable for large-scale optimisations. Future research could look into developing 'hybrid' analytical models to consider machine saturation, without losing much modelling speed.

- Thermal limitations and constraints have a significant influence on the achievable power density of the motor drive, as shown in the optimisation. However, this work has only considered one type of cooling for the machine and converter, along with a basic validation of the thermal models. For high power density, alternative cooling systems and more advanced thermal models, along with their validations, are needed.

- Although this thesis has briefly discussed the coupling effects between operating points and system efficiency in Chapter 5, the optimisation part has only looked at individual operating points. To account for multiple operating points across a load profile, the electromagnetic and thermal models employed in the optimisation need also to include thermal capacitances, peak output power requirements, etc.

- While weight and losses are important, especially for aerospace applications, additional objective functions, such as cost, dynamic performance, and reliability, should also be considered in the multiobjective optimisation for a practical and 'truly' competitive system.

Appendix A

Machine Model

A.1 Geometrical and Winding Model

Detailed equations for the machine geometrical and winding model are provided in this section:

Table A.1: Geometrical relationships for SPM machine (Part 1 of 3).

Rotor back-iron outer radius:	$r_{rb} = r_{rs} + d_{rb}$	(A.1.1)
Rotor air-gap radius:	$r_{rg} = r_{rb} + d_m$	(A.1.2)
Stator air-gap radius:	$r_{st} = r_{rg} + g$	(A.1.3)
Stator tooth-tip inner radius:	$r_{si} = r_{st} + d_{ttc}$	(A.1.4)
Slot pitch at r_{st}:	$\tau_s = \frac{2\pi r_{st}}{S_s}$	(A.1.5)
Pole pitch at r_{st}:	$\tau_p = \frac{2\pi r_{st}}{P}$	(A.1.6)

Table A.2: Geometrical relationships for SPM machine (Part 2 of 3).

Angle per slot:	$\theta_{st} = \frac{2\pi}{S_s}$	(A.2.1)
Angle per pole:	$\theta_p = \frac{2\pi}{P}$	(A.2.2)
Tooth-base angle at r_{st}:	$\theta_t = \frac{2\pi\alpha_t}{S_s}$	(A.2.3)
Tooth-tip angle at r_{st}:	$\theta_{tt} = \frac{2\pi\alpha_{tt}}{S_s}$	(A.2.4)
Slot opening angle at r_{st}:	$\theta_{so} = \frac{2\pi}{S_s - \theta_{tt}}$	(A.2.5)
Tooth-base width:	$w_{tb} = 2r_{st}\sin\frac{\theta_t}{2}$	(A.2.6)
Tooth-tip width:	$w_{tt} = 2r_{st}\sin\frac{\theta_{tt}}{2}$	(A.2.7)
Slot opening width:	$w_{so} = 2r_{st}\sin\frac{\theta_{so}}{2}$	(A.2.8)
Stator back-iron inner radius:	$r_{sb} = \sqrt{\left(\frac{w_{tb}}{2}\right)^2 + \left[r_{st}\cos\left(\frac{\theta_t}{2}\right) + d_{tb} + d_{ttc}\right]^2}$	(A.2.9)
Tooth-base angle at r_{sb}:	$\theta_{tb} = 2\,\mathrm{asin}\left(\frac{w_{tb}}{2r_{sb}}\right)$	(A.2.10)
Tooth-base angle at r_{si}:	$\theta_{ti} = 2\,\mathrm{asin}\left(\frac{w_{tb}}{2r_{si}}\right)$	(A.2.11)
Stator slot depth:	$d_{st} = r_{sb} - r_{st}$	(A.2.12)
Stator back-iron outer radius:	$r_{ss} = r_{sb} + d_{sb}$	(A.2.13)

Table A.3: Geometrical relationships for SPM machine (Part 3 of 3).

Area of stator slot:	$a_{\text{slot}} = \frac{\pi(r_{sb}^2 - r_{si}^2)}{S_s} - \frac{r_{sb}[r_{sb}\theta_{tb} - w_{tb}\cos\left(\frac{\theta_{tb}}{2}\right)]}{2} \cdots - w_{tb}d_{tb} + \frac{r_{si}[r_{si}\theta_{ti} - w_{tb}\cos\left(\frac{\theta_{ti}}{2}\right)]}{2}$	(A.3.1)
Area of tooth-tip:	$a_{tt} = \frac{1}{2}\Big[2w_{tt}d_{tte} - r_{st}^2\theta_{tt} + r_{si}^2\theta_{ti} + w_{tt}r_{st}\cos\left(\frac{\theta_{tt}}{2}\right) \cdots + (w_{tb} + w_{tt})(d_{ttc} - d_{tte}) - w_{tb}r_{si}\cos\left(\frac{\theta_{ti}}{2}\right)\Big]$	(A.3.2)
Area of tooth-base:	$a_{tb} = \frac{\pi(r_{sb}^2 - r_{si}^2)}{S_s} - a_{\text{slot}}$	(A.3.3)
Volume of teeth:	$Vol_{st} = S_s(a_{tt} + a_{tb})l$	(A.3.4)
Volume of stator back-iron:	$Vol_{sb} = \pi(r_{ss}^2 + r_{sb}^2)l$	(A.3.5)
Volume of stator core:	$Vol_{sl} = Vol_{st} + Vol_{sb}$	(A.3.6)
Volume of rotor back-iron:	$Vol_{rb} = \pi(r_{rb}^2 - r_{rs}^2)l$	(A.3.7)
Volume of magnets:	$Vol_{pm} = \pi(r_{rg}^2 - r_{rb}^2)\alpha_{pm}l$	(A.3.8)
Mass of stator core:	$m_{sl} = K_{sf}Vol_{sl}\rho_{sl}$	(A.3.9)
Mass of rotor back-iron:	$m_{rb} = K_{sf}Vol_{rb}\rho_{rb}$	(A.3.10)
Mass of magnets:	$m_{pm} = Vol_{pm}\rho_{pm}$	(A.3.11)

where K_{sf} is the core lamination stacking factor, and ρ_{sl}, ρ_{rb}, and ρ_{pm} are the stator core, rotor core, and magnet mass densities respectively.

Table A.4: Winding model equations for SPM machine.

No. of conductors per slot:	$z_Q = 2N_t$	(A.4.1)
No. of conductor turns in series per phase:	$N_{ts} = \frac{N_t S_s}{3}$	(A.4.2)
Cross-sectional area of conductor:	$a_c = \frac{n_{\text{wpc}} \pi w_{\text{dia}}^2}{4}$	(A.4.3)
Area of wire:	$a_w = \frac{n_{\text{wpc}} \pi (w_{\text{dia}} + 2w_{\text{ins}})^2}{4}$	(A.4.4)
where w_{ins} is the wire insulation thickness.		
Slot fill-factor:	$K_{\text{fill}} = \frac{a_w z_Q}{a_{\text{slot}}}$	(A.4.5)
Length of end-winding per conductor per side:	$l_{ew} = \frac{\pi}{2}\left(\frac{r_{st} + r_{sb}}{2}\right)\theta_{st} + 2l_{eo}$	(A.4.6)
where l_{eo} is the end-winding offset.		
Total length of winding per phase:	$l_{c,ph} = N_{ts}(2l + 2l_{ew})$	(A.4.7)
Volume of active winding:	$Vol_{scd} = 2N_{ts} l a_c$	(A.4.8)
Volume of end winding:	$Vol_{ecd} = 2N_{ts} l_{ew} a_c$	(A.4.9)
Volume of total winding:	$Vol_{cd} = Vol_{scd} + Vol_{ecd}$	(A.4.10)
Mass of total winding:	$m_{cd} = Vol_{cd} \rho_{cd}$	(A.4.11)
where ρ_{cd} is the winding mass density.		
Phase resistance:	$R_{ph}(T) = \frac{1}{\sigma_c(T)}\left(\frac{l_{c,ph}}{a_c}\right)$	(A.4.12)
where T is the winding temperature.		

A.2 Electromagnetic Model

Detailed equations for the machine electromagnetic model are provided in this section:

Table A.5: Open-circuit air-gap flux density for slotless SPM machine [88].

Radial and tangential air-gap flux density (B_r and B_t), due to flux from the rotor magnets, are calculated as a function of radius r and angle θ, as:

$$B_{r,\mathrm{PM}}(r,\theta) = \sum_{n=1,3,5\cdots}^{\infty} K_B(n) \cdot f_{Br}(r) \cdot \cos(np\theta) \tag{A.5.1}$$

$$B_{t,\mathrm{PM}}(r,\theta) = \sum_{n=1,3,5\cdots}^{\infty} K_B(n) \cdot f_{B\theta}(r) \cdot \sin(np\theta) \tag{A.5.2}$$

where p is the number of pole pairs. $K_B(n)$ is determined as:

$$K_B(n) = \frac{\mu_0 M_n}{\mu_r} \frac{np}{(np)^2 - 1} \cdot \left\{ \frac{(A_{3n}-1) + 2\left(\frac{r_{rb}}{r_{rg}}\right)^{np+1} - (A_{3n}+1)\left(\frac{r_{rb}}{r_{rg}}\right)^{2np}}{\frac{\mu_r+1}{\mu_r}\left[1 - \left(\frac{r_{rb}}{r_{st}}\right)^{2np}\right] - \frac{\mu_r-1}{\mu_r}\left[\left(\frac{r_{rg}}{r_{st}}\right)^{2np} - \left(\frac{r_{rb}}{r_{rg}}\right)^{2np}\right]} \right\} \tag{A.5.3}$$

where for parallel magnetisation:

$$A_{1n} = \frac{\sin\left[(np+1)\alpha_{pm}\frac{\pi}{2p}\right]}{(np+1)\alpha_{pm}\frac{\pi}{2p}};\ A_{2n} = \frac{\sin\left[(np-1)\alpha_{pm}\frac{\pi}{2p}\right]}{(np-1)\alpha_{pm}\frac{\pi}{2p}};\ M_{rn} = \frac{B_r}{\mu_0}\alpha_{pm}(A_{1n}+A_{2n});$$

$$M_{tn} = \frac{B_r}{\mu_0}\alpha_{pm}(A_{1n}-A_{2n});\ M_n = M_{rn} + npM_{tn};\ A_{3n} = \left(np - \frac{1}{np}\right)\frac{M_{rn}}{M_n} + \frac{1}{np}$$

Meanwhile, $f_{Br}(r)$, and $f_{B\theta}(r)$ are determined as:

$$f_{Br}(r) = \left(\frac{r}{r_{st}}\right)^{np-1}\left(\frac{r_{rg}}{r_{st}}\right)^{np+1} + \left(\frac{r_{rg}}{r}\right)^{np+1} \tag{A.5.4}$$

$$f_{B\theta}(r) = -\left(\frac{r}{r_{st}}\right)^{np-1}\left(\frac{r_{rg}}{r_{st}}\right)^{np+1} + \left(\frac{r_{rg}}{r}\right)^{np+1} \tag{A.5.5}$$

Table A.6: Complex relative air-gap permeance function at slot-opening and open-circuit air-gap flux density for slotted SPM machine [89].

The following parameters are firstly defined:

$$b'_o = \theta_{tt2} - \theta_{tt}; \qquad g' = \log\left(\frac{r_{st}}{r_{rb}}\right); \qquad b = \left[\frac{b'_o}{2g'} + \sqrt{\left(\frac{b'_o}{2g'}\right)^2 + 1}\right]^2; \qquad a = \frac{1}{b};$$

where θ_{tt} and θ_{tt2} are angles of the starting and ending points for the slot-opening, respectively. Using conformal transformation, the slot-opening's z-plane coordinates z_o and z_c are determined as:

$$z_o(r,\theta) = \log(r) + j\theta \tag{A.6.1}$$

$$z_c = j\frac{g'}{\pi}\left[\ln\left|\frac{1+p_1}{1-p_1}\right| - \ln\left|\frac{b+p_1}{b-p_1}\right| - 2\left(\frac{b-1}{\sqrt{b}}\right)\tan^{-1}\left(\frac{p_1}{\sqrt{b}}\right)\right] + C_1 \tag{A.6.2}$$

where $p_1 = \sqrt{\dfrac{w-b}{w-a}}$ and $C_1 = \ln(r_{st}) + j\theta_{tt2}$.

At each θ, Eq.(A.6.1) and (A.6.2) are solved to obtain w when $z_c = z_o$. Using the solutions for w, the relative air-gap permeance at the slot-opening is computed as a function of radius r and angle θ, according to:

$$\lambda(r,\theta) = \frac{k(r,\theta)}{s}\left[\frac{w(r,\theta)-1}{(w(r,\theta)-a)^{\frac{1}{2}}(w(r,\theta)-b)^{\frac{1}{2}}}\right] \tag{A.6.3}$$

where $k = r_{st}\exp\left\{j\left[\dfrac{g'}{\pi}\ln(w(r,\theta)) + \dfrac{\theta_{st}}{2}\right]\right\}$ and $s = \exp(z_o(r,\theta))$.

In a complex form ($\lambda = \lambda_{\text{real}} + j\lambda_{\text{imag}}$), the real and imaginary components of λ are:

$$\lambda_{\text{real}}(r,\theta) = \lambda_0 + \sum_{n=1}^{\infty}\lambda_{\text{an}}\cos(nS_s\theta); \;\; \lambda_{\text{imag}}(r,\theta) = \sum_{n=1}^{\infty}\lambda_{\text{bn}}\sin(nS_s\theta); \tag{A.6.4}$$

where λ_0, λ_{an}, and λ_{bn} are Fourier coefficients.

Lastly, radial and tangential components of the slotted open-circuit air-gap flux density function can be written as:

$$\begin{aligned} B_{r,\text{PM}}^{(\text{slotted})}(r,\theta) &= B_{r,\text{PM}}(r,\theta)\lambda_{\text{real}}(r,\theta) + B_{t,\text{PM}}(r,\theta)\lambda_{\text{imag}}(r,\theta) \\ B_{t,\text{PM}}^{(\text{slotted})}(r,\theta) &= B_{r,\text{PM}}(r,\theta)\lambda_{\text{real}}(r,\theta) - B_{t,\text{PM}}(r,\theta)\lambda_{\text{imag}}(r,\theta) \end{aligned} \tag{A.6.5}$$

Table A.7: PM magnetic flux, flux linkage, and back electromotive force under open-circuit conditions [89].

At any time instant t, the magnetic flux entering stator tooth is:

$$\phi_{\mathrm{PM}}(t) = r_{st} l \int_{-\frac{\theta_{st}}{2}}^{\frac{\theta_{st}}{2}} B_{r,\mathrm{PM}}^{(\mathrm{slotted})}(r_{st}, \theta, t) \mathrm{d}\theta \tag{A.7.1}$$

The induced phase flux linkage can subsequently be derived as:

$$\Psi_{\mathrm{PM,ph}}(t) = N_{ts} k_{\mathrm{dn}} k_{\mathrm{on}} k_{\mathrm{pn}} \phi_{\mathrm{PM}}(t) \tag{A.7.2}$$

where k_{dn} is the winding distribution factor, k_{pn} is the winding pitch factor, and k_{on} is the slot-opening factor. The formulation of the three winding factors k_{dn}, k_{pn}, and k_{on} are given in [27]. Finally, an expression for the back electromotive force can be written as:

$$\begin{aligned} E_{\mathrm{PM,ph}}(t) &= -\frac{\mathrm{d}}{\mathrm{d}t}\Psi_{\mathrm{PM,ph}} \\ &= -\omega_{\mathrm{rm}} N_{ts} k_{\mathrm{dn}} k_{\mathrm{on}} r_{st} l \sum_{n=1,3,5,\ldots}^{\infty} \Bigg\{ 2\lambda_0 B_{r,\mathrm{PM}} k_{\mathrm{pn}} \cdots \\ &\quad + \sum_{m=1}^{\infty} (B_{r,\mathrm{PM}} \lambda_{\mathrm{am}} - B_{t,\mathrm{PM}} \lambda_{\mathrm{bm}}) \frac{\sin\left[(np + mS_s)\frac{\tau_c}{2}\right] np}{np + mS_s} \cdots \\ &\quad + \sum_{m=1}^{\infty} (B_{r,\mathrm{PM}} \lambda_{\mathrm{am}} + B_{t,\mathrm{PM}} \lambda_{\mathrm{bm}}) \frac{\sin\left[(np - mS_s)\frac{\tau_c}{2}\right] np}{np - mS_s} \Bigg\} \sin(np\omega_{\mathrm{rm}} t) \end{aligned} \tag{A.7.3}$$

where ω_{rm} is the rotor mechanical speed and τ_c is the stator coil pitch.

Table A.8: Complex winding air-gap permeance function and armature-reaction air-gap flux density [92].

Firstly, the following parameters have to be defined:

$$b'_o = \theta_{tt2} - \theta_{tt}; \qquad g' = \log\left(\frac{r_{st}}{r_{rb}}\right); \qquad a = \left(\frac{2g\prime}{b'_o}\right)^2;$$

where θ_{tt} and θ_{tt2} are angles of the starting and ending points for the slot-opening, respectively. Using conformal transformation, the slot-opening's z-plane coordinates z_o and z_c are determined as:

$$z_o(r,\theta) = \log(r) + j\theta \tag{A.8.1}$$

$$z_c = 2A\left[\frac{1}{\sqrt{a}}\arctan\left(\frac{p_2}{\sqrt{a}}\right) + \frac{1}{2}\ln\left(\frac{1+p_2}{1-p_2}\right)\right] + C_2 \tag{A.8.2}$$

where $p_2 = \sqrt{\dfrac{w-a}{w+1}}$, $C_2 = \ln(R_r) + j\dfrac{\theta_s}{2}$ and $A = -j\dfrac{g'}{\pi}$.

At each θ, Eq.(A.8.1) and (A.8.2) are solved to obtain w when $z_c = z_o$. Using the solutions for w, winding permeance function at the slot-opening of current-carrying conductors is computed as:

$$\lambda_w(r,\theta) = \frac{1}{s}\sqrt{\frac{w(r,\theta)-a}{w(r,\theta)+1}} \tag{A.8.3}$$

where $s = \exp[z_o(r,\theta)]$. In a cylindrical coordinate form:

$$\begin{aligned}\lambda_{w,r}(r,\theta) &= \mathrm{Re}(\lambda_w(r,\theta))\cos\theta + \mathrm{Im}(\lambda_w(r,\theta))\sin\theta \\ \lambda_{w,t}(r,\theta) &= -\mathrm{Re}(\lambda_w(r,\theta))\sin\theta + \mathrm{Im}(\lambda_w(r,\theta))\cos\theta\end{aligned} \tag{A.8.4}$$

For a slot with conductors carrying a peak winding current of $\hat{i}_{ph}$, the air-gap flux density function at the slot-opening is:

$$\begin{aligned}B_{r,\mathrm{arm,so}}(r,\theta) &= \mu_0\left(\frac{N_c}{2g'}\right)\hat{i}_{ph}\lambda_{w,r}(r,\theta) \\ B_{t,\mathrm{arm,so}}(r,\theta) &= \mu_0\left(\frac{N_c}{2g'}\right)\hat{i}_{ph}\lambda_{w,t}(r,\theta)\end{aligned} \tag{A.8.5}$$

Armature-reaction air-gap flux density for a winding coil $B_{\text{arm,coil}}$ is assembled from a $B_{\text{arm,so}}$, at the positive current slot-opening, and its inverted copy $-B_{\text{arm,so}}$, at the negative current slot-opening, and the full waveform is shifted in amplitude so that the average radial flux density across the circumference is equal to zero. Relative air-gap permeance functions from Eq.(A.6.4) are employed for slots without currents. Radial and tangential components of air-gap flux density, due to phase A coils, are:

$$B^{(\text{slotted})}_{r,\text{arm,A}}(r,\theta,t) = \sum_{s=1}^{S_s} B^{(\text{slotted})}_{r,\text{arm,coil(s)}}(r,\theta)\cos(\omega t)W_A(s) \tag{A.8.6}$$
$$B^{(\text{slotted})}_{t,\text{arm,A}}(r,\theta,t) = \sum_{s=1}^{S_s} B^{(\text{slotted})}_{t,\text{arm,coil(s)}}(r,\theta)\cos(\omega t)W_A(s)$$

where $B^{(\text{slotted})}_{\text{arm,coil(s)}}$ is the armature-reaction air-gap flux density for winding coil s and W_A is the phase winding function. Subsequently, the 3-phase armature-reaction air-gap flux density is:

$$B^{(\text{slotted})}_{r,\text{arm}}(r,\theta,t) = B^{(\text{slotted})}_{r,\text{arm,A}}(r,\theta,t) + B^{(\text{slotted})}_{r,\text{arm,B}}(r,\theta,t) + B^{(\text{slotted})}_{r,\text{arm,C}}(r,\theta,t) \tag{A.8.7}$$
$$B^{(\text{slotted})}_{t,\text{arm}}(r,\theta,t) = B^{(\text{slotted})}_{t,\text{arm,A}}(r,\theta,t) + B^{(\text{slotted})}_{t,\text{arm,B}}(r,\theta,t) + B^{(\text{slotted})}_{t,\text{arm,C}}(r,\theta,t)$$

Table A.9: Stator magnetising flux, flux linkage and inductance.

Magnetising self-inductance of phase A is:

$$L_{\text{ms,A}} = \left\{ r_{st} l N_t \sum_{s=1}^{S_s} \left[\int_{\frac{(s-1)\pi}{S_s}}^{\frac{s\pi}{S_s}} W_A(s) B^{\text{slotting}}_{r,\text{arm,A}}(r_{st},\theta,t) \right] \mathrm{d}\theta \right\} \frac{1}{\hat{i}_A} \tag{A.9.1}$$

Magnetising mutual-inductances of phase A, due to flux from phase B and C, are:

$$L_{\text{mm,AB}} = \left\{ r_{st} l N_t \sum_{s=1}^{S_s} \left[\int_{\frac{(s-1)\pi}{S_s}}^{\frac{s\pi}{S_s}} W_B(s) B^{\text{slotting}}_{r,\text{arm,A}}(r_{st},\theta,t) \right] \mathrm{d}\theta \right\} \frac{1}{\hat{i}_A} \tag{A.9.2}$$
$$L_{\text{mm,AC}} = \left\{ r_{st} l N_t \sum_{s=1}^{S_s} \left[\int_{\frac{(s-1)\pi}{S_s}}^{\frac{s\pi}{S_s}} W_C(s) B^{\text{slotting}}_{r,\text{arm,A}}(r_{st},\theta,t) \right] \mathrm{d}\theta \right\} \frac{1}{\hat{i}_A}$$

Finally, the total magnetising inductance of phase A is:

$$L_{\text{m,A}} = L_{\text{ms,A}} + L_{\text{mm,A}} = L_{\text{ms,A}} + L_{\text{mm,AB}} + L_{\text{mm,AC}} \tag{A.9.3}$$

Table A.10: Machine leakage inductances.

Inner slot leakage inductance (Path 1):

$$L_{\text{stin}} = \frac{S_s z_Q^2}{3}\left[\mu_0 L\left(\frac{d_{stR}}{3w_{siR}}\right)\right] \tag{A.10.1}$$

Tooth-tip leakage inductance (Path 2):

$$L_{\text{tt}} = \frac{S_s z_Q^2}{3}\left[\mu_0 L\left(\frac{d_{ttR}}{w_{soR}}\right)\right] \tag{A.10.2}$$

Tooth-tip fringing leakage inductance (Path 3):

$$L_{\text{ttf}} = \frac{S_s z_Q^2}{3}\left\{\frac{\mu_0 L}{2\pi}\left[\log\left(\frac{g\prime^2}{w_{soR}^2}+\frac{1}{4}\right)+\frac{4g\prime}{w_{soR}}\operatorname{atan}\left(\frac{w_{soR}}{2g\prime}\right)\right]\right\} \tag{A.10.3}$$

Total slot leakage inductances:

$$L_{\text{st}} = L_{\text{tt}} + L_{\text{stin}} + L_{\text{ttf}} \tag{A.10.4}$$

End-winding leakage inductance (Path 4):

$$L_{\text{ew}} = \frac{S_s}{3}\left[\frac{2\mu_0(\frac{z_Q}{2})^2\pi r_{ew}^2}{d_{siR}}\right] \tag{A.10.5}$$

Table A.11: Maximum flux and flux densities in the machine.

Rotor back-iron flux is dominated by the magnet flux, and average rotor flux is determined by integrating radial rotor back-iron surface flux density $B_{r(PM)}(r_{rb},\theta)$ over half a magnet length:

$$\phi_{\text{rb,max}} = r_{rb} l \int_0^{\frac{\theta_{pm}}{2}} B_{r(PM)}(r_{rb},\theta)\mathrm{d}\theta \tag{A.11.1}$$

Flux flowing through stator tooth k, due to magnets, is found by integrating the radial open-circuit air-gap flux density over the stator slot pitch, as:

$$\phi_{\mathrm{stpm,k}}(t) = r_{\mathrm{rst}} l \int_{\frac{(k-1)\pi}{S_s}}^{\frac{k\pi}{S_s}} B_{r,\mathrm{PM}}^{\mathrm{slotting}}(r_{\mathrm{rst}}, \theta, t)\mathrm{d}\theta \tag{A.11.2}$$

Armature-reaction and slot leakage flux produced by each phase coil is calculated as:

$$\phi_{\mathrm{coil,ph}}(t) = \frac{(L_{\mathrm{m,ph}} + L_{\mathrm{st}})i_{\mathrm{ph}}(t)}{N_{ts}} \tag{A.11.3}$$

Flux flowing through stator tooth k, due to winding coils, is:

$$\phi_{\mathrm{stcoil,k}}(t) = W_A^* \phi_{\mathrm{coil,A}}(t) + W_B^* \phi_{\mathrm{coil,B}}(t) + W_C^* \phi_{\mathrm{coil,C}}(t) \tag{A.11.4}$$

where $W_{(\,\cdot\,)}^*$ are modified phase winding functions, considering flux flowing in stator teeth on both sides of each coil. Total flux in stator tooth k is:

$$\phi_{\mathrm{st,k}}(t) = \phi_{\mathrm{stpm,k}}(t) + \phi_{\mathrm{stcoil,k}}(t) \tag{A.11.5}$$

Considering a time instant t^* when magnet's d-axis is middle-aligned with stator tooth 1, maximum stator tooth flux is:

$$\phi_{\mathrm{st,max}} = \max(\phi_{\mathrm{st,k}}(t^*)) \tag{A.11.6}$$

Assuming that $\phi_{\mathrm{st,max}}$ splits tangentially in opposite directions as it enters the stator back-iron, maximum stator back-iron flux is:

$$\phi_{\mathrm{sb,max}} = \frac{\phi_{\mathrm{st,max}}}{2} \tag{A.11.7}$$

Finally, maximum stator teeth, stator back-iron, and rotor back-iron flux densities can be computed as:

$$B_{\mathrm{st,max}} = \frac{\phi_{\mathrm{st,max}}}{l k_{sf} w_{st}}, \qquad B_{\mathrm{sb,max}} = \frac{\phi_{\mathrm{sb,max}}}{l k_{sf} d_{sb}}, \qquad B_{\mathrm{rb,max}} = \frac{\phi_{\mathrm{rb,max}}}{l k_{sf} d_r} \tag{A.11.8}$$

Appendix B

Converter Model

B.1 Phase Average Duty-cycle Reference

To consider how modulation strategies achieve an average sinusoidal commanded voltages across the load, the duty-cycle reference for each phase, averaged over each switching period, is analysed. Average duty-cycle reference can be calculated as:

$$d_{ph,ref} = \frac{M_{ph,ref} + 1}{2} \tag{B.1}$$

where $M_{ph,ref}$ is the phase modulation index, also averaged over each switching period.

To calculate $M_{ph,ref}$ for each phase, the phase-leg pulse patterns are evaluated based on the switching state relative turn-on times, and their pre-determined sequences. Based on the derivations given in [106], analytical solutions for phase A modulation index $M_{A,ref}$ in each sector are provided in Table B.1, as a function of target output voltage vector angle θ.

Table B.1: Solution for phase A modulation index reference, $M_{A,ref}$.

With symmetrical SVM modulation:			
$0 \leq \theta < \frac{\pi}{3}$:	$\frac{\sqrt{3}}{2}\hat{M}\cos\left(\theta - \frac{\pi}{6}\right)$,	$\frac{\pi}{3} \leq \theta < \frac{2\pi}{3}$:	$\frac{3}{2}\hat{M}\cos(\theta)$
$\frac{2\pi}{3} \leq \theta < \pi$:	$\frac{\sqrt{3}}{2}\hat{M}\cos\left(\theta + \frac{\pi}{6}\right)$,	$\pi \leq \theta < \frac{4\pi}{3}$:	$\frac{\sqrt{3}}{2}\hat{M}\cos\left(\theta - \frac{\pi}{6}\right)$
$\frac{4\pi}{3} \leq \theta < \frac{5\pi}{3}$:	$\frac{3}{2}\hat{M}\cos(\theta)$,	$\frac{5\pi}{3} \leq \theta < 2\pi$:	$\frac{\sqrt{3}}{2}\hat{M}\cos\left(\theta + \frac{\pi}{6}\right)$
With DPWM1 modulation:			
$-\frac{\pi}{6} \leq \theta < \frac{\pi}{6}$:	$+1$,	$\frac{\pi}{6} \leq \theta < \frac{\pi}{2}$:	$-1 - \sqrt{3}\hat{M}\cos\left(\theta + \frac{5\pi}{6}\right)$
$\frac{\pi}{2} \leq \theta < \frac{5\pi}{6}$:	$+1 + \sqrt{3}\hat{M}\cos\left(\theta + \frac{\pi}{6}\right)$,	$\frac{5\pi}{6} \leq \theta < \frac{7\pi}{6}$:	-1
$\frac{7\pi}{6} \leq \theta < \frac{3\pi}{2}$:	$+1 - \sqrt{3}\hat{M}\cos\left(\theta + \frac{5\pi}{6}\right)$,	$\frac{3\pi}{2} \leq \theta < \frac{11\pi}{6}$:	$-1 + \sqrt{3}\hat{M}\cos\left(\theta + \frac{\pi}{6}\right)$

B.2 Device Average and RMS Currents

Based on the phase duty-cycle references from Section B.1, mathematical expressions for the device average and rms squared currents can also be derived. Firstly, the instantaneous phase A current can be found as:

$$i_A(\theta) = \hat{i}_{ph} \cos(\theta - \phi) \tag{B.2}$$

where $\hat{i}_{ph}$ is the peak phase current, and ϕ is the power factor. Next, analytical solutions for current going through the phase A upper-leg IGBT and diode, averaged over each sector are determined separately.

For example, the average IGBT current for sector 1 with symmetrical SVM modulation is:

$$I_{S,A,avg(\mathrm{s1})} = \int_0^{\pi/3} d_{A,ref(\mathrm{s1})}(\theta) \cdot i_A(\theta) \mathrm{d}\theta \tag{B.3}$$

$$= \int_0^{\pi/3} \left\{ \frac{1}{2} \left[\frac{\sqrt{3}}{2} \hat{M} \cos\left(\theta - \frac{\pi}{6}\right) + 1 \right] \cdot \hat{i}_{ph} \cos(\theta - \phi) \right\} \mathrm{d}\theta \tag{B.4}$$

Similarly, the rms squared solution for IGBT current, averaged over each sector, are also found separately. For sector 1 with symmetrical SVM modulation, it is:

$$I^2_{S,A,rms(\text{sector 1})} = \int_0^{\pi/3} [d_{A,ref(\text{sector 1})}(\theta) \cdot i_A(\theta)]^2 \mathrm{d}\theta \tag{B.5}$$

$$= \int_0^{\pi/3} \left\{ \frac{1}{2} \left[\frac{\sqrt{3}}{2} \hat{M} \cos\left(\theta - \frac{\pi}{6}\right) + 1 \right] \cdot \hat{i}_{ph} \cos(\theta - \phi) \right\}^2 \mathrm{d}\theta \tag{B.6}$$

When the average and rms squared IGBT current solutions are found for each sector, they are combined and the average and rms squared IGBT current for the

whole fundamental period are:

$$I_{S,A,avg} = \frac{1}{2\pi} \sum_{n=1}^{\mathrm{N}} I_{sA,avg(\mathrm{sn})} \tag{B.7}$$

$$I^2_{S,A,rms} = \frac{1}{2\pi} \sum_{n=1}^{\mathrm{N}} I^2_{sA,rms(\mathrm{sn})} \tag{B.8}$$

where N is the total number of sectors. Equations (B.7) and (B.8) can then be simplified using Mathematica into the analytical equations, as shown in Table B.2 for the example of a VSI motoring operation. The same analysis is carried out to determine the diode average and rms squared currents ($I_{D,A,avg}$ and $I^2_{D,A,rms}$) and the resulting equations are also tabulated in Table B.2.

Table B.2: Analytical solutions for IGBT and diode average and rms squared currents (over a fundamental period) for VSI motoring operation.

With symmetrical SVM modulation:

$$I_{S,A,avg} \quad \frac{\hat{i}_{ph}}{8\pi}(\pi\hat{M}\cos(\phi)+4) \tag{B.2.1}$$

$$I^2_{S,A,rms} \quad \frac{\hat{i}^2_{ph}}{768\pi}\Big[-9\sqrt{3}\hat{M}^2+30\pi\hat{M}^2+384\hat{M}\cos(\phi)- \Big(9\sqrt{3}\hat{M}-12\pi\hat{M}+32\sqrt{3}\Big)\hat{M}\cos(2\phi)-48\sqrt{3}\hat{M}+48\pi\Big] \tag{B.2.2}$$

$$I_{D,A,avg} \quad -\frac{\hat{i}_{ph}}{8\pi}(\pi\hat{M}\cos(\phi)-4) \tag{B.2.3}$$

$$I^2_{D,A,rms} \quad \frac{\hat{i}^2_{ph}}{768\pi}\Big[-9\sqrt{3}\hat{M}^2+30\pi\hat{M}^2-384\hat{M}\cos(\phi)- \Big(9\sqrt{3}\hat{M}-12\pi\hat{M}-32\sqrt{3}\Big)\hat{M}\cos(2\phi)+48\sqrt{3}\hat{M}+48\pi\Big] \tag{B.2.4}$$

With DPWM1 modulation:

$$I_{S,A,avg} \quad \frac{\hat{i}_{ph}}{8\pi}(\pi\hat{M}\cos(\phi)+4) \tag{B.2.5}$$

$$I^2_{S,A,rms} \quad \frac{\hat{i}^2_{ph}}{768\pi}\Big[72\hat{M}^2\phi-45\hat{M}^2\sin(2\phi)+18\sqrt{3}\hat{M}^2\phi\sin(2\phi)+ 18\hat{M}^2\phi\cos(2\phi)-36\sqrt{3}\hat{M}^2\cos(2\phi)+12\pi\hat{M}^2\cos(2\phi)+ 18\sqrt{3}\hat{M}^2+48\pi\hat{M}^2-128\sqrt{3}\hat{M}\sin(\phi)+64\sqrt{3}\hat{M}\sin(2\phi)+ 384\hat{M}\cos(\phi)-96\hat{M}\cos(2\phi)-288\hat{M}+192\phi-96\sin(2\phi)+ 96\sin\left(\frac{1}{3}(6\phi+\pi)\right)+96\cos\left(2\phi+\frac{\pi}{6}\right)+64\pi\Big] \tag{B.2.6}$$

$$I_{D,A,avg} \quad -\frac{\hat{i}_{ph}}{8\pi}(\pi\hat{M}\cos(\phi)-4) \tag{B.2.7}$$

$$I^2_{D,A,rms} \quad \frac{\hat{i}^2_{ph}}{768\pi}\Big[72\hat{M}^2\phi-45\hat{M}^2\sin(2\phi)+18\sqrt{3}\hat{M}^2\phi\sin(2\phi)- 6\left(\hat{M}^2\left(-3\phi+6\sqrt{3}-2\pi\right)-64\hat{M}+16\sqrt{3}\right)\cos(2\phi)+ 18\sqrt{3}\hat{M}^2+48\pi\hat{M}^2-768\hat{M}\cos(\phi)+128\pi\Big] \tag{B.2.8}$$

Bibliography

[1] Air Transport Action Group (ATAG). (2018) Facts & figures. [Online]. Available: https://www.atag.org/facts-figures.html

[2] Directorate-General for Research and Innovation, "Flightpath 2050 europe's vision for aviation," European Commission, Tech. Rep., 2011.

[3] Aerospace Technology Institute, "Insight07 electrical power systems," Aerospace Technology Institute (ATI), Tech. Rep., 2018.

[4] J. Rosero, J. Ortega, E. Aldabas, and L. Romeral, "Moving towards a more electric aircraft," *IEEE Aerospace and Electronic Systems Magazine*, vol. 22, no. 3, pp. 3–9, mar 2007.

[5] R. Thomson, M. Nazukin, N. Sachdeva, and N. Martinez, "Think:act, aircraft electrical propulsion - the next chapter of aviation?" Roland Berger GMBH., Tech. Rep., 2017.

[6] Roland Berger GMBH, "Aircraft electrical propulsion - the next chapter of aviation?" 2017.

[7] Liebherr-Aerospace Lindenberg GmbH. (2019) Flight control and actuation systems. [Online]. Available: https://www.liebherr.com/en/usa/products/aerospace-and-transportation-systems/aerospace/products-and-solutions/flight-control-and-actuation-systems/flight-control-and-actuation-systems.html

[8] Safran Landing Systems. (2017) Boeing 787 electric brake: an advanced technology that meets airline requirements. [Online]. Available: https://www.safran-landing-systems.com/media/boeing-787-electric-brake-advanced-technology-meets-airline-requirements-20170622

[9] Pipstrel d.o.o. Ajdovščina. (2016) Most powerful hybrid electric powertrain powers up. [Online]. Available: http://www.hypstair.eu/most-powerful-hybrid-electric-powertrain-powers-up/

[10] Siemens. (2016) Electric motor from siemens sets new world climb record. [Online]. Available: https://press.siemens.com/global/en/pressrelease/electric-motor-siemens-sets-new-world-climb-record

[11] S. D. Sudhoff, *Power Magnetic Devices*, S. D. Sudhoff, Ed. John Wiley & Sons, feb 2014.

[12] C. A. Coello, D. A. Veldhuizen, and G. B. Lamont, *Evolutionary Algorithms for Solving Multi-Objective Problems*. Springer-Verlag GmbH, 2007.

[13] L. T. Bui, *Multi-Objective Optimization in Computational Intelligence*. Information Science Reference, 2008.

[14] X.-S. Yang, *A Brief History of Optimization*. John Wiley & Sons, Inc., sep 2010.

[15] G.-J. Park, D. Lee, J.-W. Kim, and S.-Y. Jung, "Intelligent simplex method for optimal design of electric machine," in *9th IET International Conference on Computation in Electromagnetics (CEM 2014)*. Institution of Engineering and Technology, 2014.

[16] D.-D. Nguyen, K. Yukita, A. Katou, and S. Yoshida, "Design optimization of a three-phase dual-active-bridge converter for charging stations," in *2019 IEEE Vehicle Power and Propulsion Conference (VPPC)*. IEEE, oct 2019.

[17] S.-B. Yoon, J. Hur, and D.-S. Hyun, "A method of optimal design of single-sided linear induction motor for transit," *IEEE Transactions on Magnetics*, vol. 33, no. 5, pp. 4215–4217, 1997.

[18] L. N. Tutelea, T. Staudt, A. A. Popa, W. Hoffmann, and I. Boldea, "Line start 1 phase-source split phase capacitor cage-pm rotor-relsyn motor: Modeling, performance, and optimal design with experiments," *IEEE Transactions on Industrial Electronics*, vol. 65, no. 2, pp. 1772–1780, feb 2018.

[19] S. Safi and J. Bumby, "Design optimisation of a superconducting AC generator," *IEE Proceedings B Electric Power Applications*, vol. 140, no. 4, p. 267, 1993.

[20] S. Sudhoff, J. Cale, B. Cassimere, and M. Swinney, "Genetic algorithm based design of a permanent magnet synchronous machine," in *IEEE International Conference on Electric Machines and Drives, 2005.* IEEE, 2005.

[21] S. Ho, S. Yang, H. Wong, and G. Ni, "A simulated annealing algorithm for multiobjective optimizations of electromagnetic devices," *IEEE Transactions on Magnetics*, vol. 39, no. 3, pp. 1285–1288, may 2003.

[22] R. M. Burkart, "Advanced modeling and multi-objective optimization of power electronic converter systems," Ph.D. dissertation, ETH Zurich, 2016, dissertation. ETH-Zürich. 2016. No. 23209.

[23] C. Gerada, M. Galea, and A. Kladas, "Electrical machines for aerospace applications," in *2015 IEEE Workshop on Electrical Machines Design, Control and Diagnosis (WEMDCD).* IEEE, mar 2015.

[24] Maxon Motor AG. (2019) Taking to the high skies with maxon motors. [Online]. Available: https://www.maxongroup.com/maxon/view/application/Taking-to-the-high-skies-with-maxon-motors

[25] R. Krishnan, D. Blanding, A. Bhanot, A. Staley, and N. Lobo, "High reliability SRM drive system for aerospace applications," in *IECON'03. 29th Annual Con-*

ference of the IEEE Industrial Electronics Society (IEEE Cat. No.03CH37468). IEEE, 2003.

[26] MOOG Inc. (2019) Moog electrohydrostatic actuators. [Online]. Available: https://www.moog.com/news/blog-new/electrohydrostaticactuators.html

[27] T. A. Lipo, *Introduction to AC Machine Design*. John Wiley and Sons Ltd, 2017.

[28] M. Galea, Z. Xu, C. Tighe, T. Hamiti, C. Gerada, and S. Pickering, "Development of an aircraft wheel actuator for green taxiing," in *2014 International Conference on Electrical Machines (ICEM)*. IEEE, sep 2014.

[29] W. Cao, B. C. Mecrow, G. J. Atkinson, J. W. Bennett, and D. J. Atkinson, "Overview of electric motor technologies used for more electric aircraft (MEA)," *IEEE Transactions on Industrial Electronics*, vol. 59, no. 9, pp. 3523–3531, sep 2012.

[30] C. Gammeter, "Multi-objective optimization of power electronics and generators of airborne wind turbines," Ph.D. dissertation, ETH Zurich, 2018.

[31] J. H. Pyrhonen, T. Jokinen, and V. Hrabovcova, *Design of Rotating Electrical Machines (2nd edition)*. John Wiley & Sons, 2013.

[32] D. Ishak, Z. Zhu, and D. Howe, "Comparison of PM brushless motors, having either all teeth or alternate teeth wound," *IEEE Transactions on Energy Conversion*, vol. 21, no. 1, pp. 95–103, mar 2006.

[33] A. EL-Refaie, "Fractional-slot concentrated-windings synchronous permanent magnet machines: Opportunities and challenges," *IEEE Transactions on Industrial Electronics*, vol. 57, no. 1, pp. 107–121, jan 2010.

[34] C. R. Avery, S. G. Burrow, and P. H. Mellor, "Electrical generation and distribution for the more electric aircraft," in *2007 42nd International Universities Power Engineering Conference*. IEEE, sep 2007.

[35] G. Whatt and L. Chick, "Electrical generation for more-electric aircraft using solid oxide fuel cells," 2012.

[36] T. Nelson, "787 systems and performance," *The Boeing Company*, 2005.

[37] T. Yang, S. Bozhko, P. Wheeler, S. Wang, and S. Wu, "Generic functional modelling of multi-pulse auto-transformer rectifier units for more-electric aircraft applications," *Chinese Journal of Aeronautics*, vol. 31, no. 5, pp. 883–891, may 2018.

[38] M. Hartmann, "Ultra-compact and ultra-efficient three-phase pwm rectifier systems for more electric aircraft," Ph.D. dissertation, ETH Zurich, 2011, diss., Eidgenössische Technische Hochschule ETH Zürich, Nr. 19755, 2011.

[39] RTCA, "Do-160e environmental conditions and test procedures for airborne equipment," 2004.

[40] J.-C. Maré and J. Fu, "Review on signal-by-wire and power-by-wire actuation for more electric aircraft," *Chinese Journal of Aeronautics*, vol. 30, no. 3, pp. 857–870, jun 2017.

[41] P. Wheeler, A. Trentin, S. Bozhko, and J. Clare, "Regeneration of energy onto an aircraft electrical power system from an electro-mechanical actuator," in *2012 Electrical Systems for Aircraft, Railway and Ship Propulsion*. IEEE, oct 2012, pp. 1–6.

[42] M. Schweizer, T. Friedli, and J. W. Kolar, "Comparative evaluation of advanced three-phase three-level inverter/converter topologies against two-level systems," *IEEE Transactions on Industrial Electronics*, vol. 60, no. 12, pp. 5515–5527, dec 2013.

[43] J. W. Kolar, T. Friedli, J. Rodriguez, and P. W. Wheeler, "Review of three-phase PWM ac-ac converter topologies," *IEEE Transactions on Industrial Electronics*, vol. 58, no. 11, pp. 4988–5006, nov 2011.

[44] A. Boglietti, A. Cavagnino, D. Staton, M. Shanel, M. Mueller, and C. Mejuto, "Evolution and modern approaches for thermal analysis of electrical machines," *IEEE Transactions on Industrial Electronics*, vol. 56, no. 3, pp. 871–882, mar 2009.

[45] M. Mirjafari and R. S. Balog, "Survey of modelling techniques used in optimisation of power electronic components," *IET Power Electronics*, vol. 7, no. 5, pp. 1192–1203, may 2014.

[46] N. Bianchi, "Brushless DC motor design: an optimisation procedure based on genetic algorithms," in *Eighth International Conference on Electrical Machines and Drives*. IEE, 1997.

[47] J. Wieczorek, O. Gol, and Z. Michalewicz, "An evolutionary algorithm for the optimal design of induction motors," *IEEE Transactions on Magnetics*, vol. 34, no. 6, pp. 3882–3887, 1998.

[48] F. Messine, B. Nogarede, and J.-L. Lagouanelle, "Optimal design of electromechanical actuators: a new method based on global optimization," *IEEE Transactions on Magnetics*, vol. 34, no. 1, pp. 299–308, 1998.

[49] E. Fitan, F. Messine, and B. Nogarede, "A general analytical model of electrical permanent magnet machine dedicated to optimal design," *COMPEL - The international journal for computation and mathematics in electrical and electronic engineering*, vol. 22, no. 4, pp. 1037–1050, dec 2003.

[50] ——, "The electromagnetic actuator design problem: A general and rational approach," *IEEE Transactions on Magnetics*, vol. 40, no. 3, pp. 1579–1590, may 2004.

[51] B. N. Cassimere, S. D. Sudhoff, and D. H. Sudhoff, "Analytical design model for surface-mounted permanent-magnet synchronous machines," *IEEE Transactions on Energy Conversion*, vol. 24, no. 2, pp. 347–357, jun 2009.

[52] B. N. Cassimere and S. D. Sudhoff, "Population-based design of surface-mounted permanent-magnet synchronous machines," *IEEE Transactions on Energy Conversion*, vol. 24, no. 2, pp. 338–346, jun 2009.

[53] Y. Duan, R. Harley, and T. Habetler, "Multi-objective design optimization of surface mount permanent magnet machine with particle swarm intelligence," in *2008 IEEE Swarm Intelligence Symposium*. IEEE, sep 2008.

[54] S. A. Semidey, Y. Duan, J. R. Mayor, R. G. Harley, and T. G. Habetler, "Optimal electromagnetic-thermo-mechanical integrated design candidate search and selection for surface-mount permanent-magnet machines considering load profiles," *IEEE Transactions on Industry Applications*, vol. 47, no. 6, pp. 2460–2468, nov 2011.

[55] C. Gammeter, Y. Drapela, A. Tuysuz, and J. W. Kolar, "Weight optimization of a machine for airborne wind turbines," in *IECON 2014 - 40th Annual Conference of the IEEE Industrial Electronics Society*. IEEE, oct 2014.

[56] S. G. Min, G. Bramerdorfer, and B. Sarlioglu, "Analytical modeling and optimization for electromagnetic performances of fractional-slot PM brushless machines," *IEEE Transactions on Industrial Electronics*, vol. 65, no. 5, pp. 4017–4027, may 2018.

[57] S. G. Min and B. Sarlioglu, "Fast and systematic design optimization of surface-mounted PM machines using advanced analytical models and subharmonic elimination methods," *IEEE Transactions on Magnetics*, vol. 55, no. 1, pp. 1–16, jan 2019.

[58] M. Rottach, C. Gerada, T. Hamiti, and P. W. Wheeler, "A computationally efficient design procedure for actuator motors using magnetic reluctance-and thermal resistance network models," in *2012 XXth International Conference on Electrical Machines*. IEEE, sep 2012.

[59] M. E. Beniakar, A. G. Sarigiannidis, P. E. Kakosimos, and A. G. Kladas, "Multiobjective evolutionary optimization of a surface mounted PM actuator with fractional slot winding for aerospace applications," *IEEE Transactions on Magnetics*, vol. 50, no. 2, pp. 665–668, feb 2014.

[60] G. Y. Sizov, D. M. Ionel, and N. A. O. Demerdash, "Modeling and parametric design of permanent-magnet AC machines using computationally efficient finite-element analysis," *IEEE Transactions on Industrial Electronics*, vol. 59, no. 6, pp. 2403–2413, jun 2012.

[61] G. Y. Sizov, P. Zhang, D. M. Ionel, N. A. O. Demerdash, and M. Rosu, "Automated multi-objective design optimization of PM AC machines using computationally efficient FEA and differential evolution," *IEEE Transactions on Industry Applications*, vol. 49, no. 5, pp. 2086–2096, sep 2013.

[62] P. Zhang, G. Y. Sizov, M. Li, D. M. Ionel, N. A. O. Demerdash, S. J. Stretz, and A. W. Yeadon, "Multi-objective tradeoffs in the design optimization of a brushless permanent-magnet machine with fractional-slot concentrated windings," *IEEE Transactions on Industry Applications*, vol. 50, no. 5, pp. 3285–3294, sep 2014.

[63] A. Fatemi, D. M. Ionel, N. A. O. Demerdash, and T. W. Nehl, "Fast multi-objective CMODE-type optimization of PM machines using multicore desktop computers," *IEEE Transactions on Industry Applications*, vol. 52, no. 4, pp. 2941–2950, jul 2016.

[64] D. Zarko, S. Stipetic, M. Martinovic, M. Kovacic, T. Jercic, and Z. Hanic, "Reduction of computational efforts in finite element-based permanent magnet

traction motor optimization," *IEEE Transactions on Industrial Electronics*, vol. 65, no. 2, pp. 1799–1807, feb 2018.

[65] M. Van der Geest, H. Polinder, J. A. Ferreira, and D. Zeilstra, "Optimization and comparison of electrical machines using particle swarm optimization," in *2012 XXth International Conference on Electrical Machines*. IEEE, sep 2012.

[66] F. Blaabjerg and J. Pedersen, "Optimized design of a complete three-phase PWM-VS inverter," *IEEE Transactions on Power Electronics*, vol. 12, no. 3, pp. 567–577, may 1997.

[67] S. Busquets-Monge, J.-C. Crebier, S. Ragon, E. Hertz, D. Boroyevich, Z. Gurdal, M. Arpilliere, and D. Lindner, "Design of a boost power factor correction converter using optimization techniques," *IEEE Transactions on Power Electronics*, vol. 19, no. 6, pp. 1388–1396, nov 2004.

[68] J. Kolar, J. Biela, and J. Minibock, "Exploring the pareto front of multi-objective single-phase pfc rectifier design optimization - 99pc efficiency vs. 7kw/dm3 power density," in *2009 IEEE 6th International Power Electronics and Motion Control Conference*. IEEE, may 2009.

[69] R. M. Burkart and J. W. Kolar, "Comparative eta-rho-sigma pareto optimization of si and sic multilevel dual-active-bridge topologies with wide input voltage range," *IEEE Transactions on Power Electronics*, vol. 32, no. 7, pp. 5258–5270, jul 2017.

[70] Q. Wang, V. Turriate, R. Burgos, D. Boroyevich, J. Sagona, and M. Kheraluwala, "Towards a high performance motor drive for aerospace applications: Topology evaluation, converter optimization and hardware verification," in *IECON 2017 - 43rd Annual Conference of the IEEE Industrial Electronics Society*. IEEE, oct 2017.

[71] Q. Wang, X. Zhang, R. Burgos, D. Boroyevich, A. M. White, and M. Kheraluwala, "Design and implementation of a two-channel interleaved vienna-type rectifier with >99% efficiency," *IEEE Transactions on Power Electronics*, vol. 33, no. 1, pp. 226–239, jan 2018.

[72] I. Laird, X. Yuan, J. Scoltock, and A. J. Forsyth, "A design optimization tool for maximizing the power density of 3-phase dc ac converters using silicon carbide (sic) devices," *IEEE Transactions on Power Electronics*, vol. 33, no. 4, pp. 2913–2932, April 2018.

[73] F. Wang, G. Chen, D. Boroyevich, S. Ragon, M. Arpilliere, and V. Stefanovic, "Analysis and design optimization of diode front-end rectifier passive components for voltage source inverters," *IEEE Transactions on Power Electronics*, vol. 23, no. 5, pp. 2278–2289, sep 2008.

[74] M. Mirjafari, S. Harb, and R. S. Balog, "Multiobjective optimization and topology selection for a module-integrated inverter," *IEEE Transactions on Power Electronics*, vol. 30, no. 8, pp. 4219–4231, aug 2015.

[75] M. DAntonio, C. Shi, B. Wu, and A. Khaligh, "Design and optimization of a solar power conversion system for space applications," *IEEE Transactions on Industry Applications*, vol. 55, no. 3, pp. 2310–2319, may 2019.

[76] E. Lovelace, T. Jahns, and J. Lang, "Impact of saturation and inverter cost on interior PM synchronous machine drive optimization," *IEEE Transactions on Industry Applications*, vol. 36, no. 3, pp. 723–729, 2000.

[77] F. Roos, "Towards a methodology for integrated design of mechatronic servo systems," Ph.D. dissertation, KTH, Machine Design (Div.), 2007, qC 20100816.

[78] A. Sarikhani and O. A. Mohammed, "Multiobjective design optimization of coupled PM synchronous motor-drive using physics-based modeling approach," *IEEE Transactions on Magnetics*, vol. 47, no. 5, pp. 1266–1269, may 2011.

[79] J. Aubry, H. B. Ahmed, and B. Multon, "Sizing optimization methodology of a surface permanent magnet machine-converter system over a torque-speed operating profile: Application to a wave energy converter," *IEEE Transactions on Industrial Electronics*, vol. 59, no. 5, pp. 2116–2125, may 2012.

[80] A. De Andrade, A. Lesage, B. Sareni, T. Meynard, X. Roboam, R. Ruelland, and M. Couderc, "Integrated optimal design for power systems of more electrical aircraft," in *MEA 2012 - More Electric Aircraft*, 2012.

[81] M. Rottach, "Drive-system optimisation for a helicopter electromechanical actuation system," Ph.D. dissertation, 2014.

[82] G. Lei, T. Wang, Y. Guo, J. Zhu, and S. Wang, "System-level design optimization methods for electrical drive systems: Deterministic approach," *IEEE Transactions on Industrial Electronics*, vol. 61, no. 12, pp. 6591–6602, Dec 2014.

[83] G. Lei, T. Wang, J. Zhu, Y. Guo, and S. Wang, "System-level design optimization method for electrical drive systems—robust approach," *IEEE Transactions on Industrial Electronics*, vol. 62, no. 8, pp. 4702–4713, aug 2015.

[84] D. Zarko, M. Kovacic, S. Stipetic, and D. Vuljaj, "Optimization of electric drives for traction applications," in *2017 19th International Conference on Electrical Drives and Power Electronics (EDPE)*. IEEE, oct 2017.

[85] A. Mitcham, G. Antonopoulos, and J. Cullen, "Favourable slot and pole number combinations for fault-tolerant PM machines," *IEE Proceedings - Electric Power Applications*, vol. 151, no. 5, p. 520, Sept 2004.

[86] M. Farshadnia, R. Dutta, J. E. Fletcher, K. Ahsanullah, M. F. Rahman, and H. C. Lovatt, "Analysis of mmf and back-emf waveforms for fractional-slot concentrated-wound permanent magnet machines," in *2014 International Conference on Electrical Machines (ICEM)*, Sept 2014, pp. 1976–1982.

[87] Z. Q. Zhu, D. Howe, E. Bolte, and B. Ackermann, "Instantaneous magnetic field distribution in brushless permanent magnet dc motors. i. open-circuit field," *IEEE Transactions on Magnetics*, vol. 29, no. 1, pp. 124–135, Jan 1993.

[88] Z. Q. Zhu, D. Howe, and C. C. Chan, "Improved analytical model for predicting the magnetic field distribution in brushless permanent-magnet machines," *IEEE Transactions on Magnetics*, vol. 38, no. 1, pp. 229–238, Jan 2002.

[89] D. Zarko, D. Ban, and T. Lipo, "Analytical calculation of magnetic field distribution in the slotted air gap of a surface permanent-magnet motor using complex relative air-gap permeance," *IEEE Transactions on Magnetics*, vol. 42, no. 7, pp. 1828–1837, jul 2006.

[90] K. Ramakrishnan, M. Curti, D. Zarko, G. Mastinu, J. J. H. Paulides, and E. A. Lomonova, "Comparative analysis of various methods for modelling surface permanent magnet machines," *IET Electric Power Applications*, vol. 11, no. 4, pp. 540–547, apr 2017.

[91] Z. Q. Zhu and D. Howe, "Instantaneous magnetic field distribution in brushless permanent magnet dc motors. ii. armature-reaction field," *IEEE Transactions on Magnetics*, vol. 29, no. 1, pp. 136–142, Jan 1993.

[92] D. Zarko, D. Ban, and T. Lipo, "Analytical solution for electromagnetic torque in surface permanent-magnet motors using conformal mapping," *IEEE Transactions on Magnetics*, vol. 45, no. 7, pp. 2943–2954, jul 2009.

[93] D. Hanselman, *Brushless Motors: Magnetic Design, Performance, and Control of Brushless DC and Permanent Magnet Synchronous Motors.* E-man PR LLC., 2012.

[94] P. Ponomarev, Y. Alexandrova, I. Petrov, P. Lindh, E. Lomonova, and J. Pyrhonen, "Inductance calculation of tooth-coil permanent-magnet synchronous

machines," *IEEE Transactions on Industrial Electronics*, vol. 61, no. 11, pp. 5966–5973, nov 2014.

[95] T. Cox, F. Eastham, and J. Proverbs, "End turn leakage reactance of concentrated modular winding stators," *IEEE Transactions on Magnetics*, vol. 44, no. 11, pp. 4057–4061, nov 2008.

[96] Infolytica Corporation. (2018) Magnet 2d/3d electromagnetic field simulation software. [Online]. Available: https://www.mentor.com/products/mechanical/magnet/magnet/

[97] K. Yamazaki and Y. Fukushima, "Effect of eddy-current loss reduction by magnet segmentation in synchronous motors with concentrated windings," *IEEE Transactions on Industry Applications*, vol. 47, no. 2, pp. 779–788, mar 2011.

[98] E. Brancato, "Insulation aging a historical and critical review," *IEEE Transactions on Electrical Insulation*, vol. EI-13, no. 4, pp. 308–317, aug 1978.

[99] C. Sciascera, P. Giangrande, L. Papini, C. Gerada, and M. Galea, "Analytical thermal model for fast stator winding temperature prediction," *IEEE Transactions on Industrial Electronics*, vol. 64, no. 8, pp. 6116–6126, aug 2017.

[100] E. Cheever. (2018) Symbolic circuit analysis in matlab (scam). [Online]. Available: http://www.swarthmore.edu/NatSci/echeeve1/Ref/mna/MNA6.html

[101] A. Boglietti, A. Cavagnino, M. Lazzari, and M. Pastorelli, "A simplified thermal model for variable-speed self-cooled industrial induction motor," *IEEE Transactions on Industry Applications*, vol. 39, no. 4, pp. 945–952, jul 2003.

[102] A. Bejan, *Heat Transfer Handbook*. John Wiley & Sons, 2003. [Online]. Available: https://www.ebook.de/de/product/3673409/adrian_bejan_heat_transfer_handbook.html

[103] Motor Design Limited. (2018) Motor-cad software. [Online]. Available: https://www.motor-design.com/motor-cad-software/

[104] J. R. Hendershot and T. J. E. Miller, *Design of Brushless Permanent-Magnet Motors*. Magna Physics Publishing, 1994.

[105] A. Al-Timimy, G. Vakil, M. Degano, P. Giangrande, C. Gerada, and M. Galea, "Considerations on the effects that core material machining has on an electrical machine's performance," *IEEE Transactions on Energy Conversion*, vol. 33, no. 3, pp. 1154–1163, sep 2018.

[106] D. G. Holmes and T. A. Lipo, *Pulse Width Modulation for Power Converters: Principles and Practice*. John Wiley & Sons, Inc., 2003.

[107] R. W. Erickson and D. Maksimovic, *Fundamentals of Power Electronics*. Springer Us, 2007.

[108] J. Kolar and S. Round, "Analytical calculation of the RMS current stress on the DC-link capacitor of voltage-PWM converter systems," *IEE Proceedings - Electric Power Applications*, vol. 153, no. 4, p. 535, 2006.

[109] L. Shen, S. Bozhko, G. Asher, C. Patel, and P. Wheeler, "Active DC-link capacitor harmonic current reduction in two-level back-to-back converter," *IEEE Transactions on Power Electronics*, pp. 1–1, 2015.

[110] P.-Y. Lin and Y.-S. Lai, "Voltage control technique for the extension of DC-link voltage utilization of finite-speed SPMSM drives," *IEEE Transactions on Industrial Electronics*, vol. 59, no. 9, pp. 3392–3402, sep 2012.

[111] H.-B. Shin, "New antiwindup PI controller for variable-speed motor drives," *IEEE Transactions on Industrial Electronics*, vol. 45, no. 3, pp. 445–450, jun 1998.

[112] C. Wildrick, F. Lee, B. Cho, and B. Choi, "A method of defining the load impedance specification for a stable distributed power system," *IEEE Transactions on Power Electronics*, vol. 10, no. 3, pp. 280–285, may 1995.

[113] A. Yazdani and R. Iravani, *Voltage-Sourced Converters in Power Systems*. John Wiley & Sons, Inc., jan 2010.

[114] Y. Ye, M. Kazerani, and V. Quintana, "Modeling, control and implementation of three-phase PWM converters," *IEEE Transactions on Power Electronics*, vol. 18, no. 3, pp. 857–864, may 2003.

[115] F. Blaabjerg, J. Pedersen, S. Sigurjonsson, and A. Elkjaer, "An extended model of power losses in hard-switched igbt-inverters," in *IAS 96. Conference Record of the 1996 IEEE Industry Applications Conference Thirty-First IAS Annual Meeting*. IEEE, 1996.

[116] System Plus Consulting, "1200v silicon igbt vs sic mosfet comparison 2018 (product code sp18388)," 2018. [Online]. Available: www.systemplus.fr/reverse-costing-reports/1200v-silicon-igbt-vs-sic-mosfet-comparison-2018/

[117] A. Wintrich, U. Nicolai, W. Tursky, and T. Reimann, *Application Manual Power Semiconductors*. Semikron International GmbH, 2015. [Online]. Available: https://www.semikron.com/service-support/application-manual.html

[118] SAE International, "Aerospace standard air1277b (cooling of military avionic equipment)," 2015.

[119] Fischer Elektronik, "Quotations for fischer elektronik 3," Fischer Elektronik, Tech. Rep., 2014.

[120] U. Drofenik and J. W. Kolar, "Sub-optimum design of a forced air cooled heat sink for simple manufacturing," in *2007 Power Conversion Conference - Nagoya*, April 2007, pp. 1189–1194.

[121] U. Drofenik, G. Laimer, and J. W. Kolar, "Theoretical converter power density limits for forced convection cooling," in *Proceedings of the International PCIM Europe 2005 Conference*, 2005.

[122] Magnetics Inc., "Powder cores," 2017. [Online]. Available: www.mag-inc.com

[123] Hitachi Metals, "High performance amorphous powder core hlm50 series," 2017.

[124] T. Friedli, "Comparative evaluation of three-phase si and sic ac-ac converter systems," Ph.D. dissertation, ETH Zurich, 2010, diss., Eidgenössische Technische Hochschule ETH Zürich, Nr. 19194, 2010.

[125] SAE International, "Aerospace standard as50881g (wiring aerospace vehicle)," aug 2019. [Online]. Available: https://doi.org/10.4271/AS50881G

[126] Chang Sung Corporation, "Magnetic power cores (ver. 13)," 2018.

[127] Panasonic Industry, "Aluminium electrolytic capacitors: Products catalog," 2019.

[128] TDK. (2018) Capacitor selection guide. [Online]. Available: https://product.tdk.com/info/en/products/capacitor/technote/selection-guide.html

[129] D. Christen, "Analysis and performance evaluation of converter systems for ev-ultra-fast charging stations with integrated grid storage," Ph.D. dissertation, 2017.

[130] Texas Instrument, "Tida-00366 reference design for reinforced isolation 3-phase inverter with current, voltage and temp protection," Texas Instrument, Tech. Rep., 2016. [Online]. Available: http://www.ti.com/tool/tida-00366

[131] A. Boglietti, P. Ferraris, M. Lazzari, and M. Pastorelli, "Influence of the inverter characteristics on the iron losses in PWM inverter-fed induction motors," *IEEE Transactions on Industry Applications*, vol. 32, no. 5, pp. 1190–1194, 1996.

[132] K. Bradley, W. Cao, J. Clare, and P. Wheeler, "Predicting inverter-induced harmonic loss by improved harmonic injection," *IEEE Transactions on Power Electronics*, vol. 23, no. 5, pp. 2619–2624, sep 2008.

[133] P. W. Wheeler, J. C. Clare, M. Apap, and K. J. Bradley, "Harmonic loss due to operation of induction machines from matrix converters," *IEEE Transactions on Industrial Electronics*, vol. 55, no. 2, pp. 809–816, 2008.

[134] A. Boglietti, A. Cavagnino, and M. Lazzari, "Fast method for the iron loss prediction in inverter-fed induction motors," *IEEE Transactions on Industry Applications*, vol. 46, no. 2, pp. 806–811, 2010.

[135] Z. Michalewicz and D. B. Fogel, *How to Solve It: Modern Heuristics*. Springer, 2004.

[136] R. B. Agrawal, "Simulated binary crossover for continuous search space," *Complex systems*, vol. 9, no. 2, pp. 115–148, 1995.

[137] K. Deb, A. Pratap, S. Agarwal, and T. Meyarivan, "A fast and elitist multi-objective genetic algorithm: NSGA-II," *IEEE Transactions on Evolutionary Computation*, vol. 6, no. 2, pp. 182–197, apr 2002.

[138] J. Kennedy and R. Eberhart, "Particle swarm optimization," in *Proceedings of ICNN 95 International Conference on Neural Networks*. IEEE, 1995.

[139] A. Nebro, J. Durillo, J. Garcia-Nieto, C. C. Coello, F. Luna, and E. Alba, "SMPSO: A new PSO-based metaheuristic for multi-objective optimization," in *2009 IEEE Symposium on Computational Intelligence in Milti-Criteria Decision-Making*. IEEE, mar 2009.

[140] K. V. Price, J. Lampinen, and R. Storn, *Differential Evolution*. Springer-Verlag GmbH, 2005.

[141] S. Kukkonen and J. Lampinen, "GDE3: The third evolution step of generalized differential evolution," in *IEEE Congress on Evolutionary Computation*. IEEE, 2005.

[142] L. Guo, H. Zhang, M. Galea, J. Li, and C. Gerada, "Multiobjective optimization of a magnetically levitated planar motor with multilayer windings," *IEEE Transactions on Industrial Electronics*, vol. 63, no. 6, pp. 3522–3532, jun 2016.

[143] Y. Duan and D. M. Ionel, "A review of recent developments in electrical machine design optimization methods with a permanent-magnet synchronous motor benchmark study," *IEEE Transactions on Industry Applications*, vol. 49, no. 3, pp. 1268–1275, May 2013.

[144] E. Zitzler, K. Deb, and L. Thiele, "Comparison of multiobjective evolutionary algorithms: Empirical results," *Evolutionary Computation*, vol. 8, no. 2, pp. 173–195, jun 2000.

[145] K. Deb, A. P. Mathur, and T. Meyarivan, "Constrained test problems for multi-objective evolutionary optimization," in *First International Conference on Evolutionary Multi-criterion Optimization*. Springer Verlag, 2000, pp. 284–298.